High lights: stellar flares as probes of magnetism in stars and star-planet systems

Ekaterina Ilin

Universitätsdissertation
zur Erlangung des akademischen Grades

doctor rerum naturalium
(Dr. rer. nat.)

in der Wissenschaftsdisziplin
Astrophysik

eingereicht an der
Mathematisch-Naturwissenschaftlichen Fakultät Institut für Physik und Astronomie
der Universität Potsdam

Potsdam, den 15. Juni 2022

Hauptgutachterin

Prof. Dr. Katja Poppenhäger
Leibniz-Institut für Astrophysik Potsdam (AIP), University of Potsdam

Gutachter:innen

Prof. Dr. Ruth Angus
American Museum of Natural History, Center for Computational Astrophysics

Prof. Dr. Martin M. Roth
Leibniz-Institut für Astrophysik Potsdam (AIP), University of Potsdam

Published online on the
Publication Server of the University of Potsdam:
https://doi.org/10.25932/publishup-56356
https://nbn-resolving.org/urn:nbn:de:kobv:517-opus4-563565

Abstract

Flares are magnetically driven explosions that occur in the atmospheres of all main sequence stars that possess an outer convection zone. Flaring activity is rooted in the magnetic dynamo that operates deep in the stellar interior, propagates through all layers of the atmosphere from the corona to the photosphere, and emits electromagnetic radiation from radio bands to X-ray. Eventually, this radiation, and associated eruptions of energetic particles, are ejected out into interplanetary space, where they impact planetary atmospheres, and dominate the space weather environments of young star-planet systems.

Thanks to the Kepler and the Transit Exoplanet Survey Satellite (TESS) missions, flare observations have become accessible for millions of stars and star-planet systems. The goal of this thesis is to use these flares as multifaceted messengers to understand stellar magnetism across the main sequence, investigate planetary habitability, and explore how close-in planets can affect the host star.

Using space based observations obtained by the Kepler/K2 mission, I found that flaring activity declines with stellar age, but this decline crucially depends on stellar mass and rotation. I calibrated the age of the stars in my sample using their membership in open clusters from zero age main sequence to solar age. This allowed me to reveal the rapid transition from an active, saturated flaring state to a more quiescent, inactive flaring behavior in early M dwarfs at about 600-800 Myr. This result is an important observational constraint on stellar activity evolution that I was able to de-bias using open clusters as an activity-independent age indicator.

The TESS mission quickly superseded Kepler and K2 as the main source of flares in low mass M dwarfs. Using TESS 2-minute cadence light curves, I developed a new technique for flare localization and discovered, against the commonly held belief, that flares do not occur uniformly across their stellar surface: In fast rotating fully convective stars, giant flares are preferably located at high latitudes. This bears implications for both our understanding of magnetic field emergence in these stars, and the impact on the exoplanet atmospheres: A planet that orbits in the equatorial plane of its host may be spared from the destructive effects of these poleward emitting flares.

AU Mic is an early M dwarf, and the most actively flaring planet host detected to date. Its innermost companion, AU Mic b is one of the most promising targets for a first observation of flaring star-planet interactions. In these interactions, the planet influences the star, as opposed to space weather, where the planet is always on the receiving side. The effect reflects the properties of the magnetosphere shared by planet and star, as well as the so far inaccessible magnetic properties of planets. In the about 50 days of TESS monitoring data of AU Mic, I searched for statistically robust signs of flaring interactions with AU Mic b as flares that occur in surplus of the star's intrinsic activity. I found the strongest yet still marginal signal in recurring excess flaring in phase with the orbital period of AU Mic b. If it reflects true signal, I estimate that extending the observing time by a factor of 2-3 will yield

a statistically significant detection. Well within the reach of future TESS observations, this additional data may bring us closer to robustly detecting this effect than we have ever been.

This thesis demonstrates the immense scientific value of space based, long baseline flare monitoring, and the versatility of flares as a carrier of information about the magnetism of star-planet systems. Many discoveries still lay in wait in the vast archives that Kepler and TESS have produced over the years. Flares are intense spotlights into the magnetic structures in star-planet systems that are otherwise far below our resolution limits. The ongoing TESS mission, and soon PLATO, will further open the door to in-depth understanding of small and dynamic scale magnetic fields on low mass stars, and the space weather environment they effect.

Zusammenfassung

Flares sind magnetisch getriebene Explosionen. Sie treten in den Atmosphären aller Hauptreihensterne mit einer äußeren Konvektionszone auf, und sind auf den magnetischen Dynamo zurückzuführen, der tief im Sterninneren arbeitet. Das entstehende Magnetfeld durchdringt alle Schichten der Atmosphäre von der Korona bis zur Photosphäre und sendet elektromagnetische Strahlung vom Radio- bis in den Röntgenbereich aus. Diese Strahlung und die damit verbundenen Eruptionen energiereicher Teilchen werden anschließend in den interplanetaren Raum geschleudert, wo sie auf die Planetenatmosphären treffen und das Weltraumwetter junger Stern-Planeten-Systeme bestimmen.

Die Kepler und die Transiting Exoplanet Survey Satellite (TESS) Missionen haben in den letzten Jahren die systematische Beobachtung von Flares auf Millionen von Sternen ermöglicht. Das Ziel dieser Dissertation ist es, Flares in jungen Sternen und Stern-Planeten-Systemen als vielseitige Werkzeuge zur Sondierung des stellaren Magnetismus auf der Hauptreihe zu etablierten, ihre Rolle bei der Bewohnbarkeit von Planeten zu untersuchen und zu erforschen, wie die Wechselwirkung mit nahen Planeten die magnetische Aktivität des Wirtssterns beeinflusst.

Anhand von weltraumgestützten Beobachtungen der Kepler/K2-Mission habe ich herausgefunden, dass die Flare-Aktivität mit dem Alter des Sterns abnimmt, wobei dieser Rückgang entscheidend von der Masse und der Rotation des Sterns abhängt. Ich kalibrierte das Alter der Sterne in meiner Stichprobe anhand ihrer Zugehörigkeit zu offenen Sternhaufen von der Nullalter-Hauptreihe bis zum Zustand der heutigen Sonne. Auf diese Weise konnte ich den schnellen Übergang von einer aktiven, gesättigten Flare-Aktivität zu einem ruhigeren, inaktiven Zustand bei frühen M-Zwergen bei etwa 600-800 Millionen Jahren aufdecken. Dieser Zeitpunkt ist eine wichtige Randbedingung für die Entwicklung der Sternaktivität, die ich Dank der offenen Sternhaufen als aktivitätsunabhängigem Altersindikator eindeutig bestimmen konnte.

Die TESS-Mission hat Kepler und K2 bereits als Hauptquelle von Flares in M-Zwergen abgelöst. Anhand der zeitlich hochaufgelösten Lichtkurven von TESS entwickelte ich eine neue Technik zur Lokalisierung von Flares und entdeckte, dass – entgegen der allgemeinen Annahme – Flares nicht gleichmäßig über die Sternoberfläche verteilt sind: Bei schnell rotierenden, vollkonvektiven Sternen sind die energiereichsten Flares bevorzugt bei hohen Breitengraden zu finden. Das Ergebnis hat Auswirkungen sowohl auf unser Verständnis der Magnetfeldentstehung in diesen Sternen als auch auf die Auswirkungen auf die Atmosphären von Planeten, die in deren Äquatorebene kreisen. Die jungen Welten könnten durch die Lage ihrer Orbits den zerstörerischen Auswirkungen dieser polwärts strahlenden Flares entkommen.

AU Mic ist ein früher M-Zwerg und der bisher magnetisch aktivste Stern mit bekannten Planeten. Sein innerster Begleiter, AU Mic b, ist eines der vielversprechendsten Ziele für eine erste Beobachtung der Wechselwirkungen zwischen Stern und Planet. Dabei beeinflusst der

Planet den Stern, und nicht, wie bei Weltraumwetter, andersherum. In diesem Effekt spiegeln sich die Eigenschaften der von beiden geteilten Magnetosphäre, sowie beispielsweise die bisher unzugänglichen magnetischen Eigenschaften von Planeten. In den vorhandenen etwa 50 Tagen von TESS-Beobachtungsdaten von AU Mic suchte ich nach statistisch robusten Anzeichen für magnetische Wechselwirkungen mit AU Mic b, die sich als Flares offenbaren, die im Überschuss zur Eigenaktivität des Sterns auftreten. Das stärkste, aber doch vorläufige Signal fand ich in mit der Umlaufperiode von AU Mic b wiederkehrenden, überzähligen Flares. Wenn es sich hierbei um ein wahres Signal handelt, schätze ich anhand der Daten, dass eine Verlängerung der Beobachtungszeit um einen Faktor 2-3 einen statistisch signifikanten Nachweis erbringen wird. Die Anforderung liegt in Bereich zukünftiger TESS-Beobachtungen, und bringt uns somit womöglich näher an eine robuste Detektion dieses Effekts heran, als wir es jemals waren.

Die Untersuchungen in dieser Arbeit sind nur durch das Eintreten ins Zeitalter der Flare-Statistik möglich geworden. Diese Arbeit demonstriert den immensen wissenschaftlichen Wert der weltraumgestützten, wochen- und monatelangen Beobachtung von Flares, als auch die Vielseitigkeit von Flares als Informationsträger über den dynamischen Magnetismus in Stern-Planeten-Systemen. In den riesigen Archiven, die Kepler und TESS im Laufe der Jahre angelegt haben, schlummern noch viele Entdeckungen. Flares werfen kontrastreiche Schlaglichter auf magnetische Strukturen in Stern-Planeten-Systemen, die sonst weit unterhalb der modernen Auflösungsgrenze liegen. Die laufenden Beobachtungen von TESS, und bald PLATO, werden die Tür zu einem tiefen Verständnis der kleinen und dynamischen Magnetfelder in diesen Systemen weiter öffnen.

Contents

Part I

Introduction

1 A spotlight on flares

Somewhere in the universe, out in a spiral arm of the Milky Way disk, lies our home. Our Sun, several billion years old, burning hydrogen in its core, and surrounded by a small number of gaseous and rocky planets, is one among millions of similar stars in our galaxy. And like most of them, it sustains a magnetic field that is sustained by its rotation and the convection of ionized plasma in the interior.

The Sun's magnetic field stores energy, but it can only hold a limited amount of it locally. If this limit is exceeded, the field becomes unstable and a flare occurs, a magnetically driven explosion in the Sun's atmosphere millions of times more powerful than the most powerful modern thermonuclear bombs. Much of the stored energy is released in the form of radiation. Particularly energetic flares are also accompanied by so-called coronal mass ejections (CMEs), gigantic eruptions of hot, charged particles.

When the mixture of radiation and particles reaches the Earth, it causes a geomagnetic storm. The Earth's magnetic field is compressed and some particles spiral into the Earth's magnetosphere. We see them as breathtaking auroras at northern latitudes, but in Earth's orbit their influence also disrupts satellite communications and endangers the health of humans working in space. However, even during the strongest flares, Earth's great distance from the Sun and the Earth's magnetic field protect us from most of the blast.

The most actively flaring stars, however, are much smaller and cooler than our Sun [Ger72; Wes+11]. They are called M dwarfs or red dwarfs, and make up about 75% of all stars. They are also orbited by planets, even more frequently than Sun-like stars [DC15]. The presence of flares and planets around red dwarfs is a similarity with the Solar System, but there are two important differences:

First, the magnetic field that produces the flares is stronger than the Sun's over much longer cosmic times. Red dwarfs are born with strong magnetic fields [Shu+17; Shu+19]. Their internal physical processes preserve and amplify it. The Sun possessed a similarly active field in its youth several billion years ago. But stars like the Sun lose this activity within a few hundred million years, while red dwarfs remain magnetically active for billions of years. In the process, they produce a large number of flares whose energies can exceed those of solar flares by a factor of a thousand and more.

Second, the habitable zone [KWR93] is much closer to these extremely active stars. Liquid water is crucial for the emergence of life as we know it. The Earth orbits the Sun at a distance so that just enough light reaches its surface for liquid water to exist. In the case of cool and relatively dim red dwarfs, this zone is much closer to the star. So close, in fact, that the thrust of flare radiation may be enough to vaporize the atmospheres and oceans of exoplanets in this zone, turning them into radioactively irradiated desert planets [Air+17; LB15]. The presumably habitable zone turns out to be a hellish place. Life might still find a way [Taj08], but the conditions are very different from Earth's without a doubt.

If we are eager to find life, we might want to focus on stars that are more like the Sun

than red dwarfs. And astronomers have indeed set out to find a twin of the Solar System as they came up with the Kepler mission [Bor+10]. But it remains to be found – which does not indicate that the Solar System is special. The most efficient methods we use to find exoplanets are not well suited to detect small planets that take more than around about a hundred days to orbit their host. Instead, they discovered thousands of cool, highly magnetized red dwarfs with close-in planets of all varieties. Red dwarfs make up the majority of stars in our galaxy and the solar neighborhood, and each of them hosts at least one planet on average. Can we somehow tell if life on these apparently unpleasant exoplanets can and does exist?

If we want to assess habitability and unambiguously identify the signatures of biological life, we need to understand how the stars (Chapter 2), their planets (Chapter 3) and their interactions work together over the millions and billions of years of these systems' existence. At the end of this introduction I hope to convince you that flares are not only an important constituent of the environments in which habitable planets reside, but that Kepler and the Transiting Exoplanet Survey Satellite [Ric+15] have enabled them as great tools to study the magnetism of star-planet systems (Chapter 4). The bulk of this thesis consists of three scientific studies (Chapters 6-8), which I will briefly summarize in Chapter 5, as well as a software (Chapter 9) that was used extensively in all these studies. In the final Chapter 10, we will look ahead into future prospects of flares.

2 Low mass stars

To a first approximation, most stars, most of the time, are well described as hot, partially ionized balls of hydrogen, and a few other elements. They are symmetric spheres, fusing hydrogen to helium in their cores for billions of years. The Sun possesses an atmosphere comprised of a photosphere, which typically defines the boundary between the in- and outside of a star; a chromosphere, and a corona, with a transition region between the latter two [KWW12]. The photosphere emits light at a blackbody temperature that increases with stellar mass. The Sun emits at about 6,000 K at the photosphere [Chr21], the smallest stars at about 2,500 K [PM13]. In the chromosphere above, dynamic collisional and radiative ionization and excitation form the characteristic temperature dependent spectra [CS02; WC11]. In the corona, the gas density drops rapidly, and the temperature rises to several million Kelvin.

2.1 Stellar rotation

The story could end here with the depiction of a stack of concentric layers given above. However, the spherical symmetry is broken by rotation. The Sun has been known to rotate since the invention of telescopes in the early 17th century [CVV06]. Stellar rotation became accessible only as late as the first half of the 20th century, when the rotational broadening of spectral lines was established as an unambiguous measure of projected rotation velocity (e.g., [Car33; MS81; Str30]). The rotation of stars is increasing during formation, when a cloud of gas collapses into the proto-star [Shu77] collecting its angular momentum like ballet dancers who pull in their arms in to spin faster. When the star is fully collapsed, it ends up with only a small fraction of the birth cloud's angular momentum. A lion's share is lost by processes that are not yet fully understood, but involve the removal of angular momentum from the protostar via magnetized jets [Lee+17; Lee+18; Pud+07], and the circumstellar disk [Bou+14; Reb+06; RWS04]. The spin-up of young stars ends on the zero age main sequence (ZAMS), where they land at a broad range of rotation periods from $\sim$ 0.1 to 10 d [Reb+16]. From this moment, most stars, except for those with close stellar or sub-stellar companions that can transfer angular momentum back to the star via tidal interaction [Hut81; LM16; MR13; Zah77], begin to spin down again, and continue to do so throughout their main-sequence lifetimes. To understand how and why this happens, we need to add magnetic fields to the picture.

2.2 Stellar magnetic dynamo

Rotation is not all the star inherits from its birthplace. In its formation process, the collapsing star collects the magnetic field that penetrates the protostellar cloud. Just as with angular

momentum, a majority is lost before the star arrives on the ZAMS. But for what is about to happen, only a small seed field is needed.

Earlier, we glossed over a detail of stellar rotation that now becomes important: The stellar rotation periods quoted were merely average values. The Sun and solar-type stars experience differential rotation. Instead of rotating as a solid body the rotation period depends on the surface latitude, and the distance to the rotation axis [Ben+18; Sch+98]. The presence of differential rotation and convection in the conducting plasma of the stellar convective envelope induces the amplification and sustenance of a strong and stable field that converts the kinetic energy of the motion into magnetic energy [Par55; Spr02]. The induction equation, in the perfectly conducting limit, is the basic physical process underlying the stellar magnetic dynamo:

$$\frac{\partial \vec{B}}{\partial t} = \nabla \times (\vec{v} \times \vec{B}). \tag{2.1}$$

The field strength B is amplified by the motion v of the nearly perfectly conducting plasma. The stellar dynamo is, in fact, a subclass of magnetic dynamos that generate magnetic fields on both smaller and larger astrophysical scales, which draw on other sources of kinetic energy to generate strong magnetic fields in planetary bodies [Jon11], and even entire galaxies [Bec15].

The magnetic field properties that the stellar dynamo produces are much more difficult to understand and reproduce than Eq. 2.1 suggests. The two main reasons are a., the large range of spatial and temporal scales involved, which makes it computationally infeasible to trace the process from large scale convectional flows to the emergence of individual magnetic features on the stellar surface, and b., the fact that we cannot observe the inside of the star directly, which makes it difficult to test the model directly as parts of it remain an observational black box [BB17; Str+16]. Lacking information about the interior magnetic field, observational evidence of dynamo action from the outside is even more important.

2.3 Stellar magnetic fields

Ideally, we could measure the magnetic fields predicted by the dynamo theory directly. This is possible, albeit to a limited extent. Plasma embedded in a magnetic field experiences the energy splitting of certain quantum mechanical states, called the Zeeman effect [Zee97]. The split states add new transitions, and hence new spectral lines at wavelengths close – but not equal to – the previously unmagnetized line. In the magnetic field regimes of low mass stars of $\sim 10^0 - 10^4$ G in sunspots and in the average total surface field strengths of stars [BB55; Hal08; Mor+08a; Mor+10; Rei12; Saa94; See+17; See+19], the frequency shift is proportional to the magnetic field strength, and the polarization of the lines reveals the orientation of the magnetic field [DL09; Hal08]. Combined with the rotational broadening of these lines, one can measure the total field strength, and reconstruct the large scale field configuration of a sufficiently magnetized star. Among low mass stars, active G and K types were most amenable to the technique [Don+97; SR98]. Later, the method could be extended to M dwarfs [Mor+08b; Mor+10; See+19]. The Zeeman effect provides low resolution large

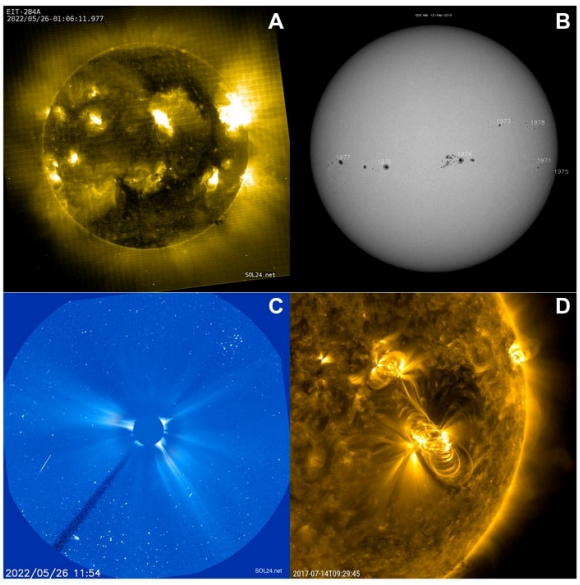

Figure 2.1: Panel A: Solar corona at 2 million Kelvin (284 Å) on May 26, 2022. Courtesy of ESA/NASA/NRL (SOHO) **Panel B**: Sunspot regions during solar maximum in 2014, observed in broadband optical light by the Helioseismic and Magnetic Imager (mid wavelength 6,173 Å). Courtesy of SDO, SOHO (NASA) and the HMI consortium. **Panel C**: Large Angle Spectrometric Coronagraph image of the solar wind, taken on the same day as Panel A. The extent of the image is about half the orbit of Mercury. Courtesy of ESA/NASA/NRL (LASCO). **Panel D**: Particles accelerated along magnetic field loops are observed in extreme ultraviolet light after a medium-sized (M2) solar flare and a coronal mass ejection occurred in a large active region of the Sun on July 14, 2017. Courtesy of NASA/GSFC/Solar Dynamics Observatory.

scale magnetic field structure, and an estimate of the total surface field strength. However, it cannot capture the dynamic, small-scale magnetic fields, the importance of which will become clear in the course of this introduction. Luckily, we do not have to guess their whereabouts. These fields make themselves known through activity in the magnetized stellar atmosphere.

2.4 Stellar activity

Stellar flaring is part of an entourage of magnetic phenomena called stellar magnetic activity, or stellar activity for short. We refer to stellar activity when we talk about phenomena caused by small-scale variable magnetic fields in stellar atmospheres, such as chromospheric and coronal emission, starspots, faculae, flares, coronal mass ejections, and stellar winds (Fig. 2.1).

In the photosphere, emergent stellar magnetic fields suppress the sub-surface convection, causing cool regions that show up as dark spots on the stellar surface. We can see them directly on the Sun, a small telescope is usually enough to see the largest regions. Sunspot groups cover areas between 10^{-6} and 10^{-2} of the solar hemisphere, with smaller groups

being much more common than large ones [Muñ+15]. Stars appear as point sources, so evidence of spots is indirect. Starspots manifest as variations in the total stellar flux periodic with stellar rotation, or rotational variations in the line profiles of spectral lines that are sensitive to magnetic fields or temperature changes [AB15; Deu58; RWK89; SR98]. These methods typically only recover the general distribution of dark and bright (or magnetically strong and weak) regions. An alternative technique are small brightenings during exoplanet transits when the planet covers the spots. Such spot crossings cannot map the entire stellar surface, but they provide size estimates for individual spots or spot groups. On G stars [NV20; San+13; Sil+10; Zal+19], and some K and M dwarfs [Mor+17; Zal+20], observed starspot sizes are of the order of the largest sunspots and up to about an order of magnitude larger than the Sun's.

Faculae, magnetic flux clumped together into bright features between surface convection granules [Wij+09], are the bright counterparts of star- and sunspots. While easy to tell apart on the solar surface, the coexistence of spots and faculae complicates the picture in the stellar case. In the presence of both spots and faculae, a decrease in the total stellar flux can mean either the presence of spots or the absence of faculae. Sometimes bright spots fit the observations better than dark spots [Mor+18], and it is difficult (but not impossible) to disambiguate the two [Ama+20; Sha+20; Zal+19; Zal+20].

In the chromosphere and corona, the atmosphere becomes increasingly tenuous, radiative and collisional equilibrium is disturbed, and the stratification becomes more and more complex [CBE07; CS02]. The heating supply is magnetohydrodynamic, and comes in the form of dissipation of kinetic energy either moving along as acoustic waves on top of magnetic fields, or as energy released when tension in the magnetic field is relaxed in very small, unresolved flares [Kho+04; TA22]. In the chromosphere, line emission, such as the H and K lines of singly ionized calcium, the Balmer series including Hα, and various lines in the ultraviolet (UV) part of the stellar spectrum show increasing departure from radiative and collisional equilibrium by gradually reversing from absorption to emission [Lin17]. The corona is reached when the cooling capacity of chromospheric line emission is exhausted, while additional magnetic heating is still present. Energy deposited in this region is dissipated through X-ray emission, ejected kinetically in the form of steady solar wind, and eruptive coronal mass ejections. The partition between the three is difficult to measure, and solar scaling relations don't hold for active M dwarfs [Dra+13; SMD06; Woo+21]. The process, or rather processes (including flares), that heat the corona are still poorly understood [PD12; TA22; TSD15].

So far, flares only appeared as a potential heating mechanism of the corona. In the following Section, we shall see that flares are, in fact, a prominent indicator of stellar activity, but unlike most others they cannot be constrained to one or even two layers of the atmosphere.

2.5 Flares

Let us now finally cast a spotlight on the protagonist of this story. Flares are strong and impulsive eruptions of electromagnetic energy that is stored as tension of the magnetic

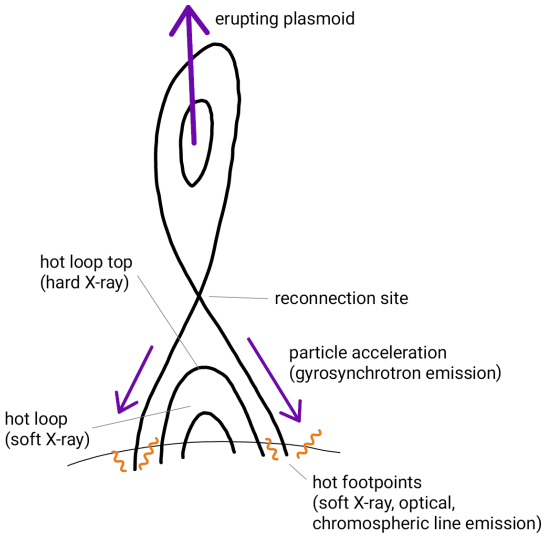

Figure 2.2: Simplified sketch of a flare loop (black lines) after re-connection. The magenta arrows indicate particles accelerated up- and downwards from the re-connection site in the corona.

field, and released by re-connection and subsequent relaxation of field lines [Sve76]. In the standard picture of a solar flare ([BG10; PF02], Fig. 2.2), a magnetic loop emerges from the stellar interior and rises into the corona. For some time, magnetic force holds it back from rising any further. Meanwhile, the subsurface convective motion moves the photospheric footpoints around, depositing energy in the loop as additional magnetic tension. At sufficiently high tension, the loop structure becomes unstable. In fully ionized and magnetized plasma, the Maxwell equations dictate that the plasma moves along with the magnetic field, and vice versa, depending on which carries more energy at any given point. This so-called "frozen-in condition" is locally violated at the onset of the flare. For a brief moment, plasma and field are no longer tied to each other. Driven towards the lowest possible energy state, the fields under tension seize the opportunity, and by splitting and re-connecting magnetic field lines rapidly release magnetic energy into the kinetic energy of the plasma that surrounds them [Par57; Swe58].

A part of the reorganized field is ejected out into space, while the other is relaxed and accelerated downwards (see Fig. 2.2). Particles precipitating downwards heat the atmospheric layers locally as they pass. When they finally hit the photosphere and lower chromosphere at the loop's footpoints, most energy is dissipated thermally through evaporation and thermal emission (see Fig. 2.1, panel D). This in turn heats up the chromospheric layer above, so that during the late stages of a flare, Balmer line emission can dissipate up to $\sim 30\%$ of the flare flux [Kow+13].

We can observe flares in nearly all electromagnetic wavelengths available to astronomers – from centimeter and decimeter radio bands to the soft and hard X-ray regime [Ben16; BG10]. Each wavelength regime traces different dissipation processes, both thermal and non-thermal. Particle acceleration causes bremsstrahlung and gyrosynchrotron emission

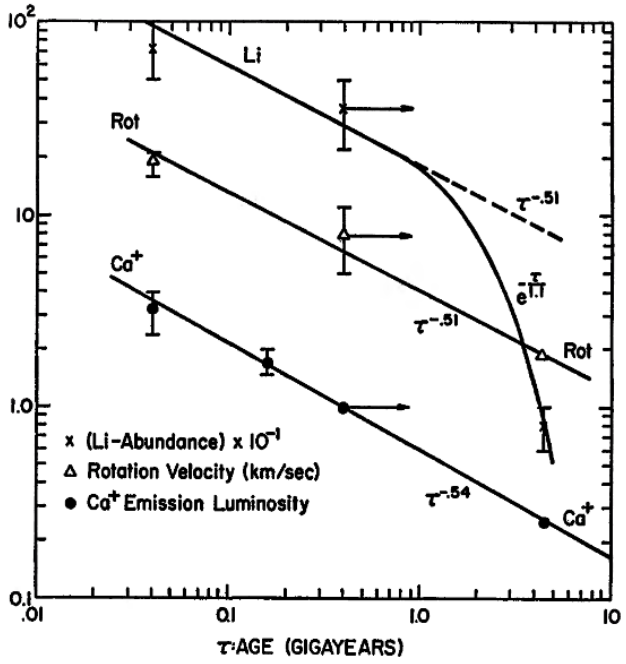

Figure 2.3: Ca II H & K abundance, Li abundance, and equatorial velocities of stars in the Ursa Major moving group of coeval stars, the Pleiades and Hyades open clusters, and the Sun, as a function of stellar age, from [Sku72].

which is seen in hard X-rays and radio bands; thermal dissipation is observed in soft X-ray, broadband optical and UV radiation, and chromospheric line emission [Ben16]. Except for the hard X-ray regime, flare emission in the various bands observed on the Sun has also been detected on other stars. As we will see in Section 2.7, this gives flares a major advantage as probes of stellar magnetism.

The majority of the total flare energy is released as blackbody radiation at temperatures of typically about 9,000 K [Asc+17; Kre11], but both higher and lower temperatures have been observed [Fro+19; Giz+13; Kow+13]. Solar observations of thermal emission focus on the highest energies, which provide the best contrast against the 6,000 K photosphere. M dwarfs are much cooler, and optical signatures of flares stick out from the quiescent photosphere, so that their blackbody radiation can be observed even in very faint stars. In recent years, the surge in large-scale optical monitoring campaigns has enabled us to find and characterize flares across all spectral types, and move on from studies of individual flares to ensembles (Chapter 4). To better appreciate the impact of this development, and its role for the studies presented in Chapters 6-8, we will now look at the role of flares in the magnetic main-sequence evolution of low mass stars.

2.6 Magnetic main-sequence evolution

In Section 2.1 I left you with the question as to how and why stellar rotation slows down on the main sequence. With our understanding of stellar dynamos (Section 2.2), magnetic field measurements (Section 2.3), and activity (Section 2.4), we now have everything in place to give an answer to the best of our current knowledge, and delineate the gaps in our understanding of this process. Nearing the end of this chapter (Section 2.7) we will come to see why flares play a special role in addressing those gaps.

From the perspective of nuclear reactions, the main sequence is an uneventful place. For billions of years, Sun-like and low mass stars spend their core hydrogen on helium fusion before they run out of fuel. While rotation and magnetism do not change this basic stellar evolution fact, they themselves evolve greatly throughout their main sequence lifetime.

[Sku72] synthesized the observational efforts of the preceding half-century in a now famous(ly simple) diagram, reproduced in Fig. 2.3. It shows that stellar activity (in the form of Ca II H & K emission) and rotation (in the form of equatorial velocities) decline with the square root of stellar age – $\sim \tau^{-1/2}$. The decline in lithium, the third observable in Fig. 2.3, later turned out to be caused by processes largely independent of the other two (e.g., [SP15]). However, the relation between age, rotation, magnetic fields and activity has since been confirmed as highly correlated in numerous studies of stellar rotation as a function of age [Bar+16; Bar03; Cur+13; Cur+19; Fri+21; Lu+21; Mei+15], and activity indicators such as spot lifetimes [GCH17] and sizes [Mae+17; Mor20], chromospheric [New+17; Rei+22] and coronal emission [Jef+11; Rei+22; Wri+11; Wri+18], and flares [Fei+20; Gün+20; How+20; Ili+19; Ili+21a; Rae+20; Shi+13b].

The consensus idea is firmly established: The initial rotation and magnetic field gained during formation fires up the stellar dynamo. The faster the rotation velocity, the stronger the magnetic field (see Eq. 2.1). At the same time, strong magnetic fields cause strong stellar winds, which carry away angular momentum from the star like the ballet dancer who extends their arms to slow down while spinning. How much torque the arms of the ballet dancer exert on the body depends on their weight and length. In the stellar picture this corresponds to the amount of mass expelled from the stellar atmosphere along the large scale magnetic field lines that connect to the star, and the co-rotation radius, also called the Alfvén radius, out to which they remain attached to the star [Sch62; WD67].

The Alfvén radius is the distance out to which the velocity v of the stellar wind is slower than the Alfvén velocity v_A. This velocity,

$$v_A = \frac{B}{\sqrt{\mu_0 \rho}}, \tag{2.2}$$

depends on the density ρ of the plasma and the strength B of magnetic field that pervades it. μ_0 denotes the vacuum permeability constant. Perpendicular waves, called Alfvén waves, can travel along the lines with speed v_A. Particles that are frozen-in to the magnetic field lines provide the mass, and the magnetic field tension the restoring force for the oscillation. If $v_A > v$, energy can be transported by these waves along the field lines back to the star. This situation is relevant not only to stellar wind and angular momentum loss, but, as we

will see in Section 3.3, also to the magnetic interactions between planets and their host stars. If, however, $v_A < v$ the bulk motion of the plasma carries away the magnetic field and the Alfvén waves with it. What also leaves the system for good at this point is the angular momentum of the escaping plasma.

In summary, torque on the star, exhibited by the Alfvén radius-long magnetic lever arm, slows its rotation, which in turn weakens its magnetic field. Weaker magnetic fields can only produce weaker stellar winds, which results in less angular momentum loss. Decrease in rotation and decrease in stellar activity, the proxy for magnetic field strength, will go hand in hand as the star ages. Eventually, the feedback loop wears itself out, and the star is left with slow rotation, a very weak field and low stellar activity.

2.6.1 The stellar mass factor

We now need to take an important mental note on the masses of cool stars. Mass is not part of the feedback loop itself because it changes very little over the main sequence lifetime compared to high mass stars. It has a strong influence on its magnetic evolution regardless. At a fixed rotation rate, higher mass stars have weaker magnetic fields because their convection zone is shallower [Noy+84]. Without a convective envelope, stars of spectral F5 or earlier cannot generate strong magnetic fields, and thus have no efficient way of dissipating angular momentum [Kra67]. The largest of the stars relevant to this work are about the size of the Sun. Their interiors consist of an inner radiative core, and an outer convective envelope. The envelope becomes larger in smaller stars until the radiative zone disappears completely at about $0.35 M_\odot$, and the star becomes fully convective [CB97]. This transition from partially to fully convective stars marks a difference in stellar interior structure that is also believed to change the mechanism of the stellar dynamo ([Gue+16; Irw+11], see also Section 2.6.4). Finally, the lowest mass stars at the bottom of the main sequence have increasingly neutral atmospheres that appears to change the dissipation pathways for magnetic energy [Ber06; Bou+17; Mur+22].

In other words, stars with different masses follow different magnetic evolutionary tracks in the activity-rotation-age space. Mass is incorporated into stellar rotational evolution models via the characteristic timescale of convection within the outer envelope of the star [Bar10; Mat+15; SP13], or, perhaps more intuitively, via the kinetic energy available from convection [Rei+22]. The fully convective regime, in particular the lowest mass stars, are a much less well explored territory. Historically, dynamo models were anchored on the solar case, which has a radiative core, and hence leaves the smallest stars neglected. Only few dynamo models exist in their mass regime [Bro08; Gas+13; WB16; Yad+15]. Moreover, their low luminosity complicates observations, and some observations clearly deviate from a simple extrapolation from higher masses (Section 2.6.4). It is clearly important to distinguish different stellar mass regimes, and Chapter 6 will serve as an instructive example later on. For now, when we talk about magnetic evolution, we shall bear in mind the mass of the stars in question to avoid confusion.

2.6.2 Measuring the rotation-activity relation

Rotation drives activity through *magnetic field generation*, activity decreases rotation through *angular momentum loss*. Isolated stars on the main sequence can therefore only spin down over time, but the two processes' observational inaccessibility hampers progress of the quantitative kind.

First, the uncertainties and unknowns of our understanding of stellar dynamos (Section 2.2) propagate directly to stellar magnetic evolution. We still cannot look directly inside the star, although asteroseismology may partly overcome this limitation in higher mass stars by measuring their radial differential rotation [Bec+12; Sch+16b]. Second, measuring stellar winds, which define the Alfvén radius, and ultimately the torque on the star, is challenging. In situ measurements of stellar winds are impossible, and proxies like evaporating exoplanet atmospheres [VB17], astrospheric Lyα [Woo+14; Woo+21] and slingshot prominences [Don+00; JC19] are indirect and so far only available for a small number of stars [Vid21]. Another problem is the Sun, which is often used as a calibrator for scaling relations in stellar activity, and in magnetic evolution and dynamo models. It is tricky to measure the relatively slow local tangential movement of particles in the solar wind, and from that to infer global torques exerted on the Sun [Fin+20]. Moreover, the solar angular momentum loss is variable on timescales of thousands of years, which limits the Sun's use as an etalon in the first place [Fin+19].

Lacking direct observables, astronomers resorted to rotation (combined with mass) as a proxy for the dynamo, and to magnetic fields and stellar activity in lieu of mass loss to establish the rotation-activity relation – and successfully so! There is a clear link between stellar rotation (measuring which has improved tremendously in the recent past [MMA14], see Section 2.1), and practically all known stellar activity indicators. Stars that rotate faster show stronger Balmer line emission [Dou+14; New+17], stronger Ca II H & K lines [Rei+22], more and hotter X-ray emission [Jef+11; Ste+16; Wri+11; Wri+18], more rotational variability in the optical regime [BLP16; Mae+17], and more frequent and more energetic flares [Dav+19; How+20; Rae+20]. Measurements of magnetic field strength show that higher stellar activity is due to stronger magnetic fields in faster rotating stars [Fol+18; See+17; See+19; Vid+14].

2.6.3 Following stars as they age: open clusters and other independent stellar time stamps

One of the best objects to look at if we want to know how this feedback loop plays out over time across the main sequence are open clusters, groups of order of $\sim 10^3$ stars born at the same time from the same cloud of gas. Their more massive evolved stellar population provides an independent age measurement for all of the low mass members.

As we would expect from the magnetic main sequence evolution, data from about a dozen open clusters has shown over and over that rotation periods increase over time, and that the spin-down rates depend on their mass [Bar03; Cur+13; Cur+19; Cur16; Fri+21]. Magnetic field strength [Fol+18] and stellar activity indicators such as X-ray [Boo+17; JBG21] and chromospheric lines [Agü+18; Dou+14; Fri+21] also weaken over time. At ages older than the Sun's, most open clusters have dispersed. Kinematic ages [Lu+21], which are based on

the velocity of stars relative to the Galactic disk, and asteroseismic ages [Hal+21] provide an alternative.

In Chapter 6, we will explore how the flaring activity declines in five different open clusters from ZAMS to solar age, as a function of their mass and rotation period. Studying stars with open clusters, kinematic or asteroseismic time stamps allows us to track the interplay between rotation, magnetic fields, and activity, piecing together the full picture of magnetic main sequence evolution ...which turns out to be abundant with puzzles.

2.6.4 Deviations from "standard" magnetic main sequence evolution

As the observations of stellar rotation periods, activity, and magnetic fields across masses and ages are growing more precise and complete, we begin to see some major shortcomings in our understanding of magnetic main sequence evolution.

All known activity indicators, and the results in Chapter 6, show that below rotation periods of about 10 days, or Rossby numbers of ~ 0.1, activity and magnetic field strength no longer increases with faster rotation. This is one of the best and most consistently observed, yet poorly understood, constraints for magnetic dynamo models [Bru+17; Wri+18]. Wide binaries, which should be magnetic twins, sometimes show strikingly different magnetic structure [Bar+17]. Solar scaling relations for mass loss rates produce nonphysically high values in actively flaring low mass stars [Dra+13; OW15].

Rotational evolution in old F stars [Sad+16] is faster than predicted in standard models. Evidence for such weakened magnetic braking has also come from asteroseismic observations [Hal+21]. K dwarfs also appear to rotate faster than predicted at about 1 Gyr of age [Cur+19], but resume spinning down later [Cur+20]. There is no consensus as to if and how the magnetic field causes these deviations from standard expectations, but there certainly is more substructure in rotational evolution than we currently understand [Lor+19; ME19]

Fully convective stars are another interesting mass regime. On the one hand, their activity-rotation relation is no different from that of partly convective stars [Wri+11; Wri+18], although the lack of a radiative core suggests a difference in the dynamo mechanism [Bar10; Gue+16; Irw+11]. On the other hand, flaring seems to be partially suppressed in the most rapidly rotating fully convective stars [Doy+22; Ram+22], and the strong correlation between radio and X-ray emission that holds for more massive stars (Güdel-Benz relation [BG94; GB93]) breaks down in late M dwarfs [Ber06; Cal+21b]. Changes in the dynamo or the atmospheric conditions could both be responsible for the deviations, and disentangling the two is a matter of active research.

All these recent findings point towards hidden processes that cause deviations from solar-type dynamo behavior, and Skumanich-type spin-down relations (Fig. 2.3). Some important clues to these puzzles can be delivered by flares.

2.7 The special role of flares

So far, flares have appeared beside other photometric, chromospheric and coronal activity indicators. However, their *spatio-temporal confinement*, and simultaneous *appearance in all atmospheric layers* gives them a unique advantage over global, "mono-layer" activity measures. During each flare, the injection of energy into the magnetized stellar atmosphere spotlights its local characteristics. This has been exploited in the numerous multiwavelength studies of stellar flares that cover combinations of bands across the electromagnetic spectrum from X-ray to radio [Dav+12; Hil+10; Kan+22; Kow+13; Mac+21; Mae+21; MOH20; Nam+20; Vid+16].

Because different parts of the atmosphere emit at different wavelength during a flare, every additional observing window resolves a different altitude in the atmosphere. Optical spectroscopy of flares allows us to infer densities and temperatures in the heated plasma [Fuh+08; Kow+10; Kow+13], follow its movement within the atmosphere [Hon+18; Wu+22], and even trace its escape in the form of CMEs [HFR90; Nam+21]. Inversions of time resolved spectroscopy can locate the flares on the stellar surface, in longitude, latitude, or both, probing the topology of small-scale fields [Gar+03; Joh+21; Wol+08]. Spectroscopically resolved X-ray observations of flares reveal the structure and size of flaring coronal loops ([LFS10; Pil+22; Ser+91], see Section 10.2 for an example from our current work). We can use stellar flaring properties to estimate the magnetic field strengths required in these regions to produce them, confine the sizes of active regions on the stellar surface [How+19; How+20; Not+19; Shi+13a; Stu+84], and measure the ability of flares to heat the corona [Car+07; Jes+19; Kas+02]. If conducted systematically on a sufficiently large sample of stars, these observations can tremendously improve our models of small scale magnetic fields. These in turn constrain stellar dynamo models, and angular momentum loss. They provide direct insight into individual, localized events that are consequence of the former and driver of the latter.

A main drawback in using flares as probes of magnetic dynamos and mass loss is their random occurrence in time. This makes multiwavelength observations and campaigns with time-constrained instruments such as X-ray satellites expensive, often prohibitively so, adding to the difficulty of coordinating multiple independent instruments in some cases [Mac+21; Mac22; MOH20]. Except for particularly active objects that have been the favored targets in many of the studies mentioned above, most stars are not guaranteed to flare within a night or even several nights of observations. We thus did not know whether the flaring properties of active stars also apply to quiet, more Sun-like objects, and generally less active stars. However, as we will see at the end of this introduction in Section 4, this is rapidly changing. Large numbers of flares on all stars across the lower main sequence, and beyond, have become available in the optical domain as a fortunate byproduct of the surge in exoplanet surveys in the recent decade (Section 4.1). The observational connection between flares and exoplanets is a coincidence, but the astrophysical relations between them have proven crucial for the understanding of both the planets and their hosts. So before we some back to flares as probes in Section 4, let us first draw a more holistic picture of the star-planet systems in which they occur.

3 Star-planet systems

Perhaps one of the most exciting astronomical discoveries in the last few decades was that there are planets that orbit stars other than the Sun. In 2019, Michel Mayor and Didier Queloz were awarded the Nobel Prize for their discovery of the first *exo*-planet around a Sun-like star, 51 Pegasi b, in 1995 [Com19]. 51 Pegasi b was a surprising find, because it had no analog in the Solar System. It was called a Hot Jupiter because, although it had the radius typical of gas giant planets that live in the outskirts of the Solar System, it orbited its solar type star in only 4.23 days, far inside Mercury's orbit [MQ95]. In the last few decades, thousands of extrasolar star-planet systems were discovered with properties that overturned our concept of a canonical Solar System. Their peculiarities present a fundamentally new path to understanding the origin and fate of our own world.

3.1 Exoplanet demographics

No star-planet system we found so far looks like our home. This is less surprising than the exotic new worlds we discovered in the past few decades. The techniques used to detect and verify the presence of one or more exoplanets around a particular star inevitably bias what kinds of planets we can detect. The first exoplanets were discovered using the radial velocity variations measured as shifts in the stellar spectrum as the orbiting planet causes the star to wobble back and forth with respect to the observer (e.g. [Vog+00; Vog+02]). However, with the launch of space missions like Kepler [Bor+10] and the Transiting Exoplanet Survey Satellite [Ric+15] the detection of transits in time series observations have become the most productive method.

The search for dips in stellar brightness that repeat each time the planet passes in front of the star and blocks a part of the stellar disk account for the majority of discoveries. This method strongly favors large planets in close orbits, preferably around small stars. The larger the planet compared to its host, the deeper the dip in brightness. The closer the orbit, the more transits are observed per time. These detection biases as well as the instruments' limitations and astrophysical confounders like stellar multiplicity and activity have to be accurately accounted for. To infer what fraction of stars is orbited by each kind of planet at every possible distance established the field of exoplanet demographics [GCM21]. There are over 5,000 exoplanets confirmed to date in around 3,700 star-planet systems [Arc22; Enc22]. Within this growing archive, two types of exoplanets are of special interest for where this introduction is leading us.

First, planets in the habitable zone. Because the search for a second Earth is of key interest for both researchers and the public, the demographics of planets in orbits that receive the right amount of stellar irradiation to keep water in its liquid form have been extensively studied. For the Sun, the distance of the habitable zone is about 1 AU, with its outer and inner

edges marked approximately by the orbits of Mars and Venus, respectively. For smaller stars that are less bright, the habitable zone is closer to the star. Eventually, going to smaller and smaller stars, we arrive in the sub-stellar regime where most brown dwarfs are so cool that the habitable zone, if we still want to call it that, would eventually end up inside the dwarf's atmosphere. The frequency of potentially habitable Earth-like planets around Sun-like stars is still uncertain, about 5 – 50%, because the number of known planets in such wide 365 day orbits is still small [Bry+20; GCM21; PHM13; SGW15]. The planet occurrence rate increases for smaller stars, in particular for terrestrial planets in the habitable zone, suggesting that, on average, every other M dwarf might have one planet at the required separation [BB22; DC15; Har+19; Pin+22]. How habitable these planets really are, however, is significantly influenced by their hosts' flaring activity (Section 3.2).

The second demographic of interest here are very close-in planets orbiting their hosts at around 10 days or less. They have less of a public spotlight compared to habitable zone planets, but their demographics overlap, especially for the lowest mass stars. TRAPPIST-1 is a famous example of this, an M8 dwarf with an unbeaten seven planets in orbits between 1.5 and 12.5 days, on several of which liquid water can exist [Gil+17]. The closest ultra-short period planets with orbits < 1 d occur in only 1-4 out of a thousand GK stars, are perhaps an order of magnitude more common in M dwarfs, and are usually rocky and smaller than planets in wider orbits [San+14; URP21; WSR18; ZD21]. Hot Jupiters, gaseous giant planets at periods below 10 d, are a little more common. About 1% of stars host planets like 51 Pegasi b [MQ95], that have surface temperatures heated by stellar irradiation up to about 1,00-2,000 K [May+11; Wri+12]. In the intermediate radius regime between Jupiter- and Earth-sized planets, Neptunes in short orbits are a particularly curious population. Their extreme rarity at periods below 5 days coined the term Hot Neptune Desert [MHF16], and is believed to be caused by the combined effect of radial planet migration and efficient atmosphere evaporation due to stellar activity [MK16; OL18]. AU Mic b [Mar+21; Pla+20] is such a young Neptune in an orbit of about 8.6 days, and will appear prominently in Chapter 8. These four types – close-in habitable zone planets, ultra-short period planets, Hot Jupiters and Neptunes – can find themselves within the Alfvén zones of their magnetically active hosts. This can can lead to interactions between star and planet wherein the planet influences the star, which are impossible at lager separations (Section 3.3).

3.2 Exo-space weather

Liquid water atop a rocky surface alone is not enough to make a planet habitable. There are factors that can play a role, such as an inefficient carbon cycle [Fol15], or the absence of ocean convection [OJA20], which could preclude life. A certain reason for concern, however, is the ability of low mass stars to alter and erode planetary atmospheres with their magnetism [SBJ16]. Since they all operate a dynamo in their interior, the planets will be exposed to their magnetic main sequence evolution over millions and billions of years.

The Sun is, of course, no exception. In the Solar System, the Sun's influence on the planets is not limited to its 6,000 K blackbody irradiation. Solar magnetic activity affects us in the

form of high energy irradiation from flares, and storms of energetic and magnetized plasma that hit Earth's magnetosphere, collectively called "space weather".

Space weather consists of a range of phenomena. Incoming particles, radiation, and electric currents pose a threat to the sensitive technology of spacecraft [22] and the health of space travelers [DC11]. Usually, charged particles are deflected by the magnetic field, and do not make it to Earth's surface. What we see as auroras at higher latitudes are particles channeled back into the magnetosphere from the night side, where they are accelerated after re-connection occurs in the magnetospheric tail [Dun61].

However, sufficiently strong disturbances in Earth's magnetic field, classified as geomagnetic storm [Gon+94], can reach the Earth's surface with detrimental effects on the infrastructure. The intensity of a geomagnetic storm is determined by the distance of Earth from the Sun, the structure of the terrestrial magnetic field, its orientation with respect to the magnetic field of the incoming plasma, the kinetic energy of the plasma and its magnetic field strength, and the frequency with which smaller storms occurred in the immediate past [DC11]. Other types of space weather are called solar radiation storms and radio blackouts. Solar radiation storms refer to unusually high amounts of energetic particles arriving from the Sun. Radio blackouts are the direct effects of strong solar flares. Its intense X-ray and UV radiation ionizes the air around spacecraft in low orbits, disrupting communication. Today's extensive space weather monitoring and preparedness prevents most - but not all [Wal22] - negative effects of space weather, so that large scale power outages [Bot19], accidentally exploding mines [Let18], or misinterpretations of communication loss as adversary attacks [TL18] are no longer likely to occur.

Compared to younger and smaller stars, the Sun is only weakly active and Earth is at a "safe" distance from most of its whims. Earth's magnetic field shields our atmosphere from being eroded, and our atmospheric ozone efficiently absorbs most high energy radiation. M dwarfs, the prime targets for exoplanet discovery, and the most common and long-lived type of stars, have their habitable zones in very close orbits [KWR93]. And as we have seen in the previous section, every other M dwarf is likely to host a planet in that zone. The youngest planets probably experience the most extreme space weather conditions [Alv+22]. Stellar winds and high energy radiation at ultraviolet (UV), extreme ultraviolet and X-ray wavelength in young systems can evaporate their atmospheres [Ehr+15; Kul+14; SOH21], which are the favored explanations for a lack of planets with intermediate radii [Ful+17] and the Hot Neptune Desert [MHF16]. Evaporation is observed spectroscopically during transits [VB17], and reconstructed in numerical simulations [Har+21; Kho+07; Lam+03; OM16; Owe19; Vid+15]. The combination of both is likely more than the sum of the two [Har+21], but the relative contributions from each, winds and radiation, are not yet well understood.

3.2.1 Flares and habitability

As we have seen in Section 2.6.1, flaring activity in low mass stars is much stronger than in the solar case [Sch+14b; Sch+15a; Wes+11; Xin+21]. This bears important consequences for the planets in their orbits.

On the one hand, flares could be an agent that enables UV chemistry that is required for the synthesis of prebiotic molecules [Rim+18]. On the other hand, it can affect both the short-term [Seg+10; Ven+16] and long-term [Che+21; Joh+15] evolution of planetary atmospheres. Flaring significantly contributes to their X-ray, UV and energetic particle influx [Air+17; AM20; Loy+18b] to an extent that it can destroy the protective ozone layer of an Earth-like atmosphere if the flare is accompanied by energetic particles [Cha+17; Seg+10; Til+19]. Particularly, the association of flares with energetic particle events and CMEs is expected to have a large impact on the planetary atmosphere's mass and composition [Haz+22; Vid+13].

Energetic particle events can push a planet's atmospheric conditions out of the habitable zone, but also into it [Sch+20]. The flux of such particles is difficult to constrain in both theory [Fra+19] and observations [Her+19]. Observing CMEs is similarly difficult [Lei+20]. The majority of the most energetic flares on the Sun are accompanied by CMEs [CRZ17]. However, this relation is not established on other stars [Dra+13; OW15]. Observations and simulations suggest that CMEs may carry the same amount of energy but at lower velocities because the strong magnetic field suppresses the ejection, increasing the required escape velocity [Mos+19]. The slow speed can make them invisible for solar-like CME indicators [Alv+20], but need not reduce their impact on planets [Tsu+04].

An important aspect of solar CMEs is their ejection direction. CMEs are launched in a cone radially outward from the location of the flare [How+85; St +00]. If this is true for stellar CMEs, the latitude at which flares occur will affect the mass loss induced in the planet. Many simulations assume that flares and CMEs are launched in a direction close to the orbital plane of the planet [Alv+22; Til+19], but if this is not the case, the CME may simply miss the planet. In Chapter 7, we will see that some of the most energetic flares in fully convective stars indeed occur at high latitudes, in contrast to the usually modeled case of Sun-like stars.

3.3 Star-planet interactions

The term space weather usually marks a one sided-relationship – the planet deals with the radiation and particles received from the star, but the star itself is not affected by the presence of the planet. However, planetary companions that are in sufficiently close orbits can interact with their host stars, and leave transient or even permanent traces in their behavior. We distinguish two main types of such interactions – tidal and magnetic.

Tidal interactions are caused by gravitational force similar to the Moon's influence on Earth, albeit with reverse direction of angular momentum transfer [LM16; MR13]. A massive, fast orbiting planet may transfer angular momentum onto the star, slowing down until the stellar rotation period is equal to the planetary orbital period, spinning up the star in the process, and subsequently increasing its overall activity level [IPH22; SL18].

Magnetic star-planet interactions can most unambiguously be traced as a periodic signal of magnetic activity in phase with the orbit of the planet. If a planet is sufficiently close and large enough it can directly transfer energy and matter from its atmosphere onto the star, a phenomenon observed in close stellar binary systems [Mas+08; MMN02], and planet-moon systems like Jupiter and Io [Big64; Sau+13; Zar98]. Plasma expelled from Io can spiral along

these magnetic fields and hit Jupiter's atmosphere, where it creates a hot spot visible in UV light [Cla+02]. The necessary conditions for this interaction are a. that the planet orbits within the Alfvén zone of the star (see Section 2.6), and b. that the planet is conductive or even possesses an intrinsic magnetic field.

In the case of Sun and Earth, tidal effects are negligible, and magnetic effects are absent because Earth is outside the Sun's Alfvén radius. The solar wind carries away any particles or magnetic field perturbations that Earth can expel or cause. But as we have seen in Section 3, the relative masses, distances, and magnetic field strengths and configurations in other star-planet systems are nothing like in the Solar System. For those, planetary conductivity and magnetism are observationally out of reach, but the extent of the Alfvén zone can be modeled. And indeed, many planets are found close enough to their hosts to be considered sub-Alfvénic [Fol+20].

When magnetic star-planet interaction occurs, it may manifest itself as chromospheric hot spots [Cau+19; Kle+22; Shk+05], coherent radio emission [Ved+20], or flares in excess of intrinsic activity [Mag+15; Pil+11; Pil+14; Pil+22]. However, the shape of the temporal modulation caused by the interaction is easier to constrain than its amplitude [Lan18; Str+15; Str+19]. Many studies searching for modulation with orbital period either find no signal or periodic variability with rotation period instead [PS11; Sca+13; Shk+08], and the observational evidence so far is tentative at most. The interaction can also temporarily cease due to the randomness of flare occurrence [Shk+08], activity cycles that influence the stellar wind and affect the extent of the Alfvén zone [Kav+19], and variability inherent in the accretion mechanism of magnetized plasma from the planet onto the star [Col+22]. These effects hamper even the definition of upper limits on the amplitude of the interaction signal. However, in Chapter 8, we will find that might be just a few light curves away from a statistically robust detection of flaring star-planet interaction in the most actively flaring planet host known to date, AU Mic.

4 Observing flares as probes of magnetism

In the previous Chapters we gained an overall idea of stars, planets, and their magnetism, understood how flares emerge in this landscape, and what role they play in investigating main sequence magnetic evolution, space weather in star-planet systems, and magnetic star-planet interactions. We have seen how the studies that will follow in Chapters 6-8 fit this context. To complete the picture, the following pages take a more practical observer's perspective on the study of flares to sketch the circumstances that enabled this thesis.

In Section 4.1, I will lay out how the surge in exoplanet hunting missions, and the flood of observational data that came with it, has tremendously improved our access to flares. With it came the demand for new tools for the fast and reliable analysis of centuries worth of observations (Section 4.2). In the final two Sections, 4.3 and 4.4, I will lay out how these efforts are beginning to pay off.

4.1 Exoplanet transit surveys find flares in abundance

Flares can be extremely energetic, sometimes enhancing the (bolometric) stellar flux by orders of magnitude [Pau+19; Sch+14b] (Fig. 4.1). In fact, most stellar flares observed so far are more energetic than the Carrington event [Car59], the most energetic solar flare to hit Earth in recorded history. This makes them more accessible than other magnetic features of the star, particularly in small stars where the blue-hot flare temperature appears in strong contrast against the cool-red spectrum of the star (see Section 2.5). Why has the bright-and-high-contrast advantage of flares not been exploited earlier?

The main downside of studying flares is the stochastic nature of their occurrence. An active region produces flares following a Poisson process with a mean flare rate such that flare occurrence times appear randomly distributed in time [Whe00; Whe04]. In a fully emerged active region, the waiting times between flares follow an exponential distribution, which is cut off at the short end by the detection threshold of small but abundant flares [Whe01]. If my observing time is short, catching a flare is a matter of chance. To study flares on stars that are typical of low mass stars and not the most vigorously active young M dwarfs like AU Mic (Chapter 8), YZ CMi (Fig. 4.1), or the flare prototype star UV Ceti [Luy49], one needs to stare at stars for days and weeks on end, and produce hundreds or thousands of light curves. An optical light curve is a time series of photometric observations, ideally uninterrupted and taken at a steady cadence. In such light curves, flares typically appear as sudden outbursts in flux with a fast rise and exponential decay, which takes between minutes and hours (Fig 4.1).

Until recently, the required amount of observations with sufficiently high cadence and long enough baselines for the study of typical low mass stars was unattainable. Smaller numbers of light curves of flares were regularly obtained from the ground since the cataloging of the

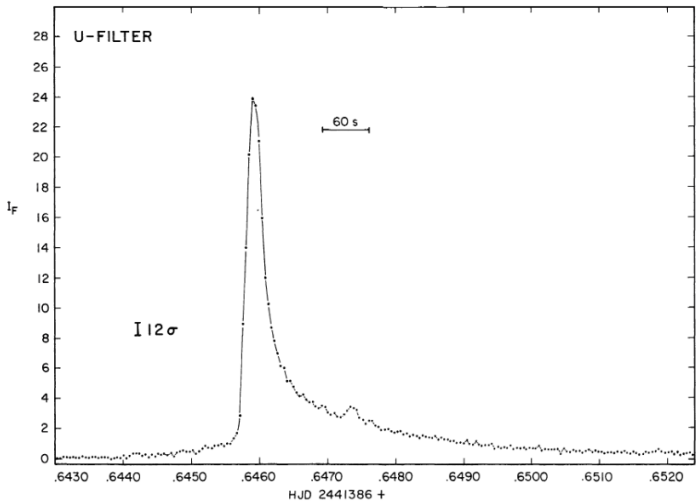

Figure 4.1: Flare with a typical time evolution observed photoelectrically with a U band filter on YZ CMi by [Mof74]. I_F is the flare flux relative to the quiescent flux level of the star, and the time is denoted in Heliocentric Julian Date. The flare shows a rapid rise, sharp peak at which YZ CMi becomes 25 times a bright as usual in the U band, and an exponential decay returning the stellar flux to the pre-flare level after a few minutes. The bump in the decay portion of the flare could be a small flare superimposed on the large one.

prototype flare star UV Ceti [Ger72; Luy49; Mof74], but were not worthwhile for the less active stars. The Convection, Rotation et Transits planétaires (CoRoT [Auv+09]) mission took 60 day long light curves from space aimed mostly at massive but also some solar type stars, some of which captured flares [Bag+09; Fla+18]. However, only with the launch of the Kepler satellite in 2009 [Bor+10] did long-baseline high precision optical light curves become available for large numbers of low mass stars. Designed to search for transits of exoplanets in short orbits, they have produced several millions of light curves, each between three and twelve weeks long. Kepler, and its extension, called K2 [How+14], retired in 2018, but the Transiting Exoplanet Survey Satellite (TESS, [Ric+15]), launched in the same year, continues watching the entire sky and producing high cadence stellar monitoring data suitable for flare hunting. In the near future, this archive will grow even further with the expected launch of the PLATO mission in 2026 [Rau+14]. Modern-day ground based flare observations with the Evryscope [Law+15], the Next Generation Transit Survey (NGTS, [Jac+20; Jac+21; Whe+18]), or the ExoEarth Discovery and Exploration Network (EDEN, [Gib+20; Lin+21]) step in where the rather large detector pixels or the lack of long term or flexible monitoring for many stars in Kepler and TESS are lacking, but they cannot replace the unprecedented volume of their observations: Flare catalogs obtained by Kepler and TESS [Dav16; Gün+20; YL19] each contain $10^3 - 10^4$ stars and $10^4 - 10^6$ flares, instead of the dozens and hundreds in the past century [Ger72; Ish+91; Mof74]. This is the first enabling factor for this thesis. The second is fast and automated data processing techniques.

4.2 Searching for flares in large archives

Kepler and TESS detected the most flares, but they were not intentionally designed to do so. In the hunt for exoplanets, any kind of stellar activity, such as flares, is a source of noise to be eliminated. Data reduction pipelines designed for transit surveys aim to preserve the transit signal, and flare signal is often removed in early stages of the analysis as it biases the quiescent flux level towards higher values or even appears during a transit dip, directly interfering with the fitting of the planetary signal.

Flare studies thus have to develop their own pipelines to automatically and reliably detect events. Manual inspection is no longer feasible with a thousand or more light curves per study. They need to account for instrumental and astrophysical false positives such as satellite movement, cosmic rays and Solar System objects that create spikes in flux that can mimic flare signals, as well as non-flaring stellar variability such as rotational modulation, or, ironically, planetary transits. A variety of (semi-)automated algorithms have been developed to efficiently detect and characterize true flare signatures in the cumulative centuries of observations amassed to date [Dav16; Fei+20; Gün+20; VR18; VSD17; Wal+11]. They all face different trade-offs between the rate of false positives and false negatives, and achieve similar results.

In Chapters 6, 7 and 8, I made use of the `AltaiPony` algorithm that I designed to search for flares in Kepler and TESS light curves. Beyond the flare finding pipeline, it includes methods to quantify the efficiency and biases of the flare detection, and perform the standard statistical analysis of flares [Ili21]. Several studies have made use of `AltaiPony` so far (e.g., [Bou+22; Ram+22; RDD20; Zel+21]) since it is an open source software with an instructive online documentation[1]. The peer-reviewed software paper is reproduced in Chapter 9.

4.3 Individual flares

Because flares are so self-similar, unusual flare shapes contain information about the stellar system that goes beyond the flare itself. The large amount of flares in the Kepler and TESS archives allows us to search for and study rare flares that deviate from the classic flare shape (Fig. 4.1, [Dav+14; HM22]). Ground based observations of the most energetic stellar flares in nearby active stars revealed early on that light curves of the more energetic but less common flares sometimes show irregularities [Mof74]. Less energetic flares more often conform to the typical shape [Dav+14; Haw+14]. High cadence TESS observations (like in the bottom panel in Fig. 4.2) allowed us to find structure in the regularity, most of which are pending a convincing explanation [HM22].

Multi-peaked flares are the most common type of complex flares. They can often be modeled as superposition of 2-10 classical flares occurring within a short time frame [Dav+14; Gün+20]. The clustering in time can either be physical, in which case the flares triggered one another in a cascade within an active region, or coincidental, when two flares in two spatially distinct regions occur almost at the same time. However, when a large number of

1 altaipony.readthedocs.io, accessed on April 21st, 2022

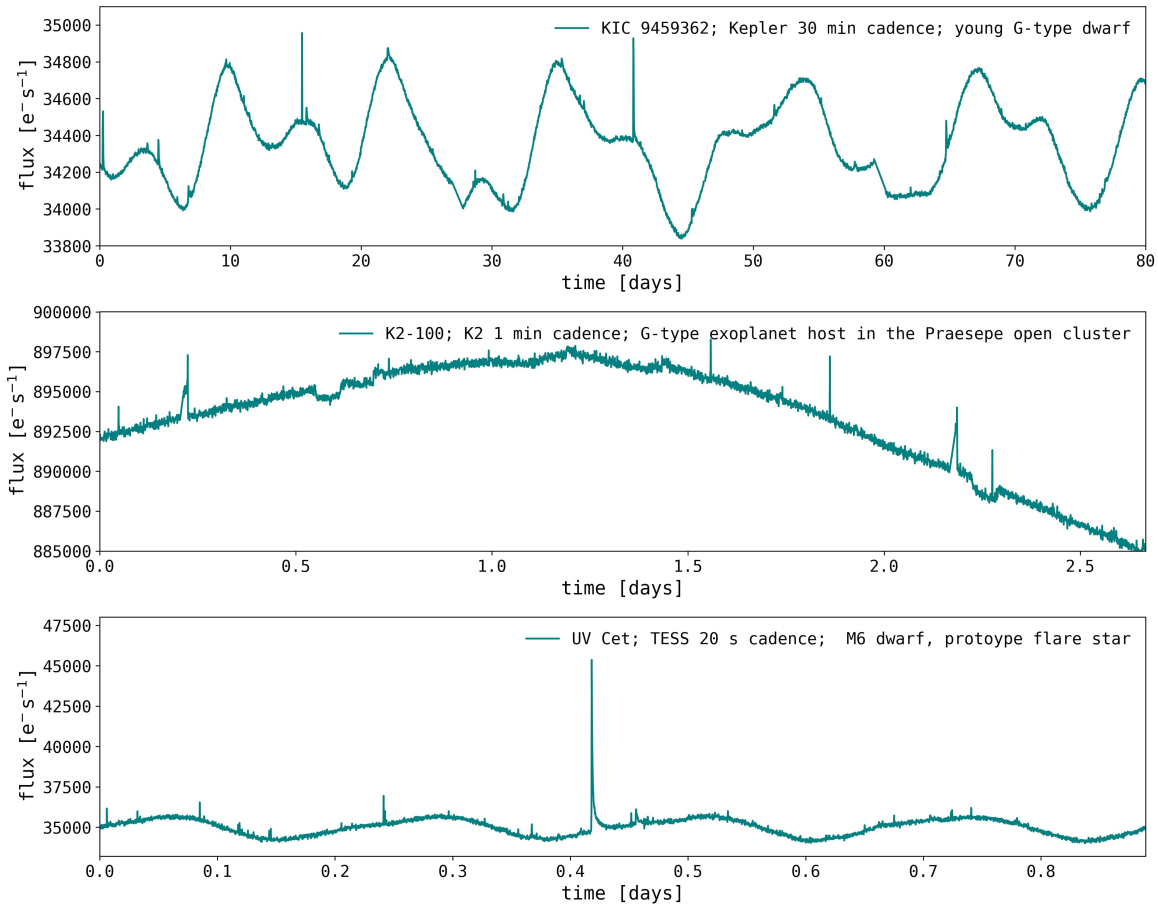

Figure 4.2: Selected sections of light curves of actively flaring stars, observed by Kepler (top panel), K2 (middle panel), and TESS (bottom panel). The time axis is offset to compare the different lengths of the selections. All selections encompass the same number of data points, which were taken with increasing temporal resolution from top to bottom. All three stars show rotational variability and flares. KIC 9459362 (top panel) has a rotation period of 12.5 d, and shows clear signs of spot evolution, seen in the changing shape of the light curve rotation after rotation. The light curve of K2-100 (middle panel) shows very low amplitude flares at around $t \approx 1.4 - 1.5$ d, the transits of K2-100 b at $t \approx 0.6$ d and $t \approx 2.2$ d, and systematic errors at $t \approx 0.2$ d and $t \approx 2.1$ d. They are common sources of false positive flare detections in the handicapped K2 mission [Van+16]. UV Ceti (bottom) is a fully convective, rapidly rotating, nearby M dwarf, after which actively flaring stars have been historically named. It shows the flare with the highest amplitude in this figure, which temporarily brightened the star by $\sim 30\%$.

flares is required to reproduce the shape of the flare light curve, it becomes more likely that an additional process modulates the shape of the light curve.

The high cadence of observations achieved with Kepler (1 min) and TESS (2 min and 20 s) allows us to access relatively subtle substructure in flares, and establish new categories. Additions to the flare zoo are peaked flares followed by a bump, flares that reach the peak and keep emitting at peak flux for several minutes before decay, or flares with substructure in the rise phase [HM22]. A particularly interesting complex type of flare is one that exhibits quasi-periodic pulsations (QPPs) in the decay portion of the light curve. QPPs are commonplace on the Sun [Asc+99; Nak+99], and shown to follow similar physics in stars [Cho+16]. Although stellar QPPs have been known to occur in the optical regime for a long time [MHB92; Rod74], Kepler and TESS revealed that they are regular events on a variety of stars [HM22; Kol+21; Ram+21]. The frequency of oscillations can be interpreted as waves traveling at Alfvén speeds along the flaring loops. The frequency implies a wavelength that can be used to estimate the size of the magnetic coronal loops [CP06; Nak+06], which appear to reach heights from a fraction and up to several stellar radii [Anf+13; Jac+19; Ram+21]. However, not all oscillations turn out to be QPPs. In Chapter 7, you will see light curves of flares that occur only about once every 120 years. They appear periodically modulated, but not because of QPPs, but because the flaring region on the star rotates in and out of view of the observer. They can easily be distinguished from QPPs: The frequency of the oscillation is both longer than the longest QPP periods known so far, and perfectly matches the stellar rotation period seen in the light curve outside the flare. Without anticipating the result from Chapter 7, I can already say this much: These flares are a prime example of how complex flares encode unique information about stellar magnetism that goes beyond the flare itself.

4.4 The age of flare statistics

Equipped with large samples of flare light curves of all kinds of flaring stars (Section 4.1), and efficient software to search for and characterize flares (Section 4.2), we have overcome the two major obstacles thwarting the rise of flare statistics, without which this thesis could not exist. We can now count, stack, and sum up flares, calculate their amplitudes, durations, waiting times and energies. Since flares are a stochastic phenomenon, statistical analysis is the appropriate approach to understanding their underlying causes and global effects. And even in the study of individual events (Section 4.3), we have to rely on a body of reference flares to decide whether the particular event is within the norm, an expected outlier, or a truly new category.

Flare statistics with Kepler and TESS have confirmed the universal properties of flares across more than ten orders of magnitude in flare energy [Fei+22; Ili+21a; Not+19], down the entire main sequence from the onset of a convective envelope at spectral type F5, and into the brown dwarf regime [Fei+20; Olá+21; Pau+20; SPZ22]. They can be used to quantify the magnetic main sequence evolution of stars, such as we will explore in Chapter 6 for main sequence stars in open clusters (see also [Ili+19]), as a function of spectral type [Dav16; Wal+11] or rotation [Mae+15] or both [Rae+20], or in pre-main sequence stars [Fei+20]. The distributions of flare energies constrain the impact of flaring

activity on the onset of abiogenesis and ozone depletion [BSR22; Gün+20; Til+19]. Finally, magnetic interactions (Section 3.3) between planet and star can show up as a statistical uptick of flare events at certain orbital phases of the planet [CPM22; FS19], as we will shortly explore in Chapter 8.

5 Overview

The following Chapters contain three astrophysical stories [Ols15] that I hinted at here and there in the previous parts, and that should now fall readily into place within the fascinating landscape of low mass star-planet systems. The first is about stellar magnetic evolution, the second about the dynamic small-scale magnetic fields of the smallest stars and their relation to space weather, and the last one is about the magnetic interaction between a planet and its young, dangerous host. The main characters will, of course, be flares.

In the first story (Chapter 6), we will comprise the largest catalog of flares observed by the Kepler/K2 mission in main sequence open clusters with ages ranging from ZAMS to solar. The frequencies and energies of the flares in this catalog will reveal that stellar mass, rotation, and flaring activity are intimately connected, but that their relation is far from linear. It will become clear that age is not the fundamental characteristic that defines a star. We will see that flaring drops by 1-2 orders of magnitude when a star reaches a certain *rotation* period, and not when it reaches a certain *age*. This indicates a drastic change in how the dynamo generates the star's magnetic field, in particular the strong small-scale fields close to the surface. We will identify the stars caught in transition from the saturated into the unsaturated activity regime – early M dwarfs in the Praesepe and Hyades open clusters – as objects of high interest for further investigation. Their magnetic field configuration may reveal an intermediate state between young stars with saturated activity and stars that have already spun down to Sun-like, slow rotation periods.

The second story (Chapter 7) is about a discovery that could only be made in the age of flare statistics. Four peculiar, highly energetic flares occurred on stars that rotate so fast that their individual light curves with their fast rise and exponential decay shapes are modulated as the flaring region on the stellar surface moves in and out of view while the star rotates. Their morphology, captured by TESS with high temporal resolution, cannot be confused with any other type of irregularity that flare light curves exhibit. These rare flares can occur about once in 120 years in fully convective, rapidly rotating M dwarfs – an observational baseline that has been out of reach before Kepler and TESS. But what makes them truly remarkable protagonists is the shape of the modulation. It can be systematically used to infer the location of the flaring region on the stellar surface – a crucial piece of information about the small-scale magnetic fields of these stars. These flares appeared at high latitudes, closer to the rotational poles of the stars than to the equator, consistent with the predictions of several dynamo models, models of flux emergence, and magnetic measurements that suggest large magnetic field concentrations in the polar regions of these stars.

The last story (Chapter 8) features AU Mic, a young, pre-main sequence M-type dwarf, and its innermost planet, AU Mic b. AU Mic has long been known to be actively flaring, but only in recent years did exoplanet hunters find its planetary companions, one of them in a close-by orbit of less than 9 days, making this star the most actively flaring exoplanet host known to date. This system, emerged from its protoplanetary disk only about a dozen years

ago, represents the youth of many star-planet systems we have detected and will continue discovering in the near future. The close orbit of AU Mic b could, depending somewhat on the yet unknown wind speed in the system, reside inside the Alfvén zone of the host star, and experience magnetic star-planet interactions. We developed a reliable and straightforward statistical test to show that most of the 189 flares we found in the system's TESS light curves are intrinsic. However, a small number might have been caused by the disturbance AU Mic b caused within the stellar magnetosphere. Encouragingly, we could estimate that another 2-4 TESS light curves, which can be obtained within the next few years during the satellite's second extended mission, will be sufficient to conclusively confirm or refute this tentative finding.

Finally, in Chapter 10, after highlighting `AltaiPony` (Chapter 9) as the software that is the work horse behind all these studies, I will invite you to take a look ahead. Some of the stories presented here have a sequel: New observations are underway, new techniques are ready to be applied. I will extrapolate the scientific revenue of TESS, but also take a peek at future small- and large-scale missions. In the end, it shall become clear why we have only just begun to uncover the full potential of flares as probes of magnetism in star-planet systems.

Part II

Flare Stories

6 Flares in Open Clusters with K2. II. Pleiades, Hyades, Praesepe, Ruprecht 147, and M67

Ilin, E.; Schmidt, S. J.; Poppenhäger, K.; Davenport, J. R. A.; Kristiansen, M. H.; Omohundro, M.
Astronomy & Astrophysics. Volume 645, A42 (2021).
DOI: 10.1051/0004-6361/202039198

Abstract

Magnetic fields are a key component in the main sequence evolution of low mass stars. Flares, energetic eruptions on the surfaces of stars, are an unmistakable manifestation of magnetically driven emission. The occurrence rates and energy distributions of flares trace stellar characteristics such as mass and age. However, before flares can be used to constrain stellar properties, the flaring-age-mass relation requires proper calibration. This work sets out to quantify the flaring activity of independently age-dated main sequence stars for a broad range of spectral types using optical light curves obtained by the Kepler satellite.

Drawing from the complete K2 archive, we searched 3435 ~ 80 day long light curves of 2111 open cluster members for flares using the open-source software packages K2SC to remove instrumental and astrophysical variability from K2 light curves, and AltaiPony to search and characterize the flare candidates.

We confirmed a total of 3844 flares on high probability open cluster members with ages from zero age main sequence (Pleiades) to 3.6 Gyr (M67). We extended the mass range probed in the first study of this series to span from Sun-like stars to mid-M dwarfs. We added the Hyades (690 Myr) to the sample as a comparison cluster to Praesepe (750 Myr), the 2.6 Gyr old Ruprecht 147, and several hundred light curves from the late K2 Campaigns in the remaining clusters. We found that the flare energy distribution was similar in the entire parameter space, following a power law relation with exponent $\alpha \approx 1.84 - 2.39$.

We confirm that flaring rates decline with age, and decline faster for higher mass stars. Our results are in good agreement with most previous statistical flare studies. We find evidence that a rapid decline in flaring activity occurred in M1-M2 dwarfs around the ages of the Hyades and Praesepe, when these stars spun down to rotation periods of about 10 d, while higher mass stars had already transitioned to lower flaring rates and lower mass stars still resided in the saturated activity regime. We conclude that some discrepancies between our results and flare studies that used rotation periods for their age estimates could be explained by sample selection bias toward more active stars, but others may point to the limitations of using rotation as an age indicator without additional constraints from stellar activity.

6.1 Introduction

Flares are explosions that occur on the surfaces of practically all low mass stars down to the very bottom of the main sequence. We know that flares are magnetic reconnection events that lead to a change in field line topology and subsequent energy releasePriest and Forbes [PF02]. We can observe flares in nearly all electromagnetic bands, from radio to X-ray, and on all stars that possess a convection zone, from late F type stars to ultracool dwarfs [BG10; Giz+13; SKD00].

Stellar flares on cool stars can enhance the optical flux by multiple orders of magnitude within minutes or seconds [HSR91; Sch+19], and release energies up to $\sim 10^{37}$ erg [Dav16; Mae+12]. They typically exhibit blackbody emission at about 10 000 K [HF92; Kow+13], which is significantly hotter than the photospheres of these stars (2500 − 6500 K). The high intensity, strong contrast, and broad energy distributions allow us to measure magnetic activity as traced by flares for a great variety of time resolved observations.

Statistical flare studies were pioneered from the ground [LME76], but it was not until space missions like Kepler [Koc+10] that investigating stellar ensembles that were not preselected for their activity became possible [Wal+11]. Today, the ground based all-sky surveys ASAS-SN [Sha+14] and Evryscope [Law+15], as well as the Transiting Exoplanet Survey Satellite (TESS, [Ric+15]), are following in the footsteps of Kepler (see works by [Fei+20; Gün+20; How+19; How+20; Rod+20; Sch+19]). Statistical studies of stellar flaring activity can help us understand the underlying physical processes of flares [BG10], the nature and strength of stellar magnetic fields [Ber06; Ode+17], starspots [Dav15; How+20; Not+19], how flares relate to stellar angular momentum evolution [How+20; Mon+19], and how they affect the atmospheres of exoplanets [How+19; Lec+12; Loy+18b; Til+19].

The present study focuses on the relation between flares and the age of low mass stars on the main sequence. To this end, we set out to quantify how flaring activity changes as a function of stellar mass and age.

In cool main sequence stars, the fraction of stars found flaring in the optical is known to increase down to spectral type M5 [CWO20; Yan+17]. Even beyond M5, and down to L dwarfs, flaring is ubiquitous [Giz+13; Pau+18; Pau+20; RPS10; Sch+15a; Sch+16a; Ste+06]. In fact, the prototype flare star, UV Ceti, is an M6 dwarf [KHM91]. Flaring activity also decays with age, but stellar ages can only be determined indirectly. Using galactic latitude as a proxy for age, flaring activity appeared to decline with higher galactic latitude, that is, older age, for M dwarfs [Hil+10; How+19; Wal+11]. In gyrochronology, fast rotation indicates young age [Bar03], and as the star ages rotation periods grow longer. Therefore, the relation between rotation and flaring can be used to calibrate a flaring-age relation [Dav+19].

In M dwarfs, the fraction of stellar luminosity emitted in flares is correlated with the fraction emitted in Hα in quiescence [Yan+17]. Quiescent Hα emission was also explored as an age tracer in the past [LPS16; Pac13; SDJ91]. More recent work has focused on stars older than a gigayear and calibrated the Hα-age relation using isochronal [Lor+18] and asteroseismic ages [Boo+17; Boo+20], suggesting that an age calibration of flaring activity is possible.

While absolute stellar ages are difficult to assess, they can be differentially controlled for

in coeval groups of stars. Flaring-age studies in binaries have shown consistent activity for both components in the majority of targets [Cla+18; Lur+15]. Open clusters are also coeval groups of stars with well-determined isochronal ages that have been used as a laboratory for flare studies on stars with a fixed age [CBH15; Mir93]. [Ili+19] investigated the flaring activity of late-K to mid-M dwarfs in three open clusters, the Pleiades, Praesepe, and M67, using K2 time domain photometry. We analyzed flare frequency distributions (FFDs) broken down by the stars' effective temperatures $T_{\rm eff}$ and ages. We found that flaring activity declined with both increasing mass and age, and that the trend was more pronounced for higher mass stars.

This study extends the results in [Ili+19] to the age of Ruprecht 147 (2.6 Gyr), and both higher and lower masses than in the previous study. We used the now complete K2 data set, supplemented all three open clusters in [Ili+19] with improved versions of already treated light curves in Campaigns 4 and 5, and added light curves from later Campaigns. The light curve catalog, and the determination of cluster membership and effective temperature for the investigated stars are detailed in Section 6.2. We describe how we used a semi-automated flare finding procedure, how we estimated flare energies, and how we parametrized the statistical properties of flares in Section 6.3. We present our findings in Section 6.4. We place our results in the context of recent flare studies, and reflect on the power law nature of FFDs in Section 6.5. Recently, [Dav+19] proposed an empirical parametrization of the flaring-mass-age relation based on FFDs of stars with gyrochronologically determined ages, which we also put to test in the discussion. The summary and conclusions can be found in Section 6.6.

6.2 Observations and data analysis

This work is based on K2 long cadence light curves with an integration time of 30 minutes that were provided by the Kepler archives hosted at the Barbara A. Mikulski Archive for Space Telescopes (MAST) (Section 6.2.1). To select a sample with independently derived ages we began by gathering open cluster membership information from the literature (Section 6.2.2). An overview over the cluster sample is presented in Table 6.1 and illustrated in Figure 6.1. To characterize the stars in the resulting catalog for the analysis that followed, we used multiband photometry from several all-sky surveys to assign $T_{\rm eff}$ (Fig. 6.2) and determine stellar radii (Fig. 6.3) using empirical relations, and eventually calculated stellar luminosities in the Kepler band (Section 6.2.3).

6.2.1 K2 light curves

The Kepler [Koc+10] spacecraft finished its follow-up mission K2 [How+14] in September 2018, after having completed nearly 20 80-day observing campaigns. With the full archive at hand, we selected and analyzed a total of 3435 light curves of high confidence members of five open clusters. Each light curve contained up to 80 uninterrupted days of 30 min cadence observations in white light ($4,200 - 9,000\,\mathring{A}$).
As K2 was conducted on the two-wheeled Kepler satellite, it was subjected to substantial

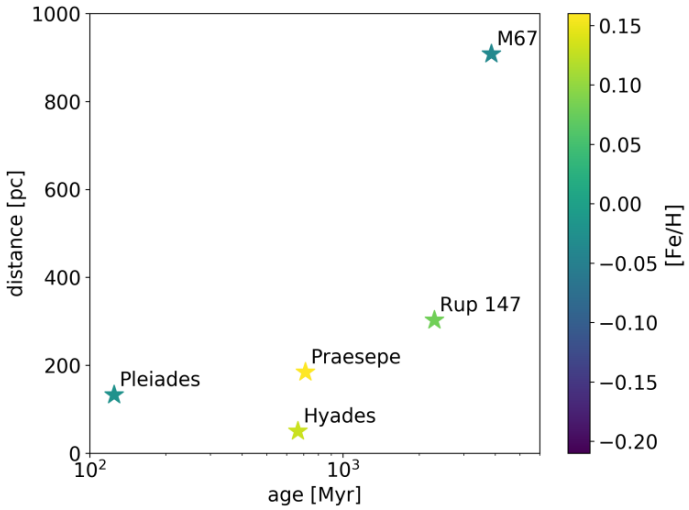

Figure 6.1: Distance as a function of age for open clusters (star symbols) that we searched for flares, colored by [Fe/H]. Age, distance, and [Fe/H] are approximate values from a compilation of existing literature, see Appendix 6.7.2.

drift motion (spacecraft roll, [Van+16]) and had an overall reduced pointing accuracy. To mitigate these effects, various solutions were developed [APP16; Lug+16; Lug+18; VJ14]. We used the K2 Systematics Correction (K2SC) pipeline [APP16] with minor modificiations to de-trend the 36th data release of the K2 data products. This data release was final, and included a uniform, global reprocessing of most K2 campaigns using an improved data reduction pipeline[2].

6.2.2 Open cluster membership

For each open cluster, we obtained membership information from a selection of catalogs which we cross-matched on right ascension and declination within 3 arcsec against the full K2 archive. One part of the membership catalogs provided membership probabilities [Can+18; Dou+14; Gao18; Oli+18; Rei+18b]. For the other part no probability was quoted [Col+18b; Dou+17; Reb+16], or qualitative classifiers were given [Cur+13; Gon16; Reb+17]. In the latter cases we assigned approximate probabilities anchored to the set threshold for inclusion into our final sample (Appendix 6.7.1). Absence in a catalog did not decrease the likelihood of membership, as each catalog had different selection biases which we did not address in this study. We set the threshold mean membership probability p for a target in our sample to 0.8. All in all, we identified 2111 low mass stars in five open clusters spanning ages from zero age main sequence (ZAMS) to roughly solar. Table 6.1 provides an overview over the final sample of stars and flares, and the adopted open cluster properties. Membership probability histograms of the final sample are displayed in Figure 6.14 in Appendix 6.7.1. A literature overview of age, distance, and metallicity determinations for the open clusters from which

2 https://keplergo.github.io/KeplerScienceWebsite/k2-uniform-global-reprocessing-underway.html, accessed June 4, 2022

Table 6.1: Open clusters. The values for age, [Fe/H], and distance d are approximate values arrived at by a comparison of existing literature (see Table 6.6 in the Appendix). The uncertainties are noted in parentheses. "stars" denotes the number of cluster members with membership probability $p > 0.8$. "LCs" and "campaigns" are the numbers of available light curves, and the K2 campaigns during which they were observed, respectively. "flares" is the number of confirmed flares found in each cluster. The quoted Hyades distance is the mean Gaia DR parallax distance. [1] [Can+18], [2] [Gos+18], [3] [Con+14], [4] [Col+18b], [5] [Net+16], [6] [Bos+19], [7] [Tor+18], [8] [Bra+18], [9] [Dia+12]

	d [pc]	stars	LCs	flares	campaigns	age [Myr]	[Fe/H]
Pleiades	135.6 [1]	741	741	1583	4	$135\binom{25}{25}$ [2]	$-0.04(0.03)$ [3]
Hyades	46.0	170	179	402	4, 13	$690\binom{160}{100}$ [4]	$0.13(0.02)$ [5]
Praesepe	185.5 [1]	913	1965	1849	5, 16, 18	$750\binom{3}{7}$ [6]	$0.16(0.00)$ [5]
Ruprecht 147	305.0 [1]	53	53	9	7	$2650\binom{380}{380}$ [7]	$0.08(0.07)$ [8]
M67	908.0 [9]	234	497	1	5, 16, 18	$3639\binom{17}{17}$ [6]	$-0.10(0.08)$ [3]

we adopt the values for this study is given in Table 6.6 in Appendix 6.7.2[3]. Below, we provide additional details on the final samples of each cluster.

Pleiades

The Pleiades, a nearby ZAMS cluster with age estimates ranging from 87 Myr to 141 Myr [Bel+12; Bos+19; Dah15; Gos+18; Sch+15b; Yen+18], was observed in Campaign 4, and treated in [Ili+19]. Here, we used 741 reprocessed K2 light curves from this open cluster, and our methodological improvements to [Ili+19] to repeat the analysis. We revisited the members from [Reb+16], which were used in [Ili+19], and merged the catalog with lists of members determined by [Col+18b; Oli+18]; and [Can+18].

Hyades

The Hyades are a 625 − 690 Myr old open cluster [Col+18b; Gos+18; Per+98; SWP98] that was observed during Campaigns 4 and 13 with K2. We merged membership tables obtained from [Dou+14; Rei+18b]; and [Col+18b] to select 170 high confidence members, nine of which were observed in both K2 campaigns.

Praesepe

Compared across different studies, Praesepe (590 − 830 Myr, [Bos+19; Bou+12; Gos+18; Sch+15b; SWP98; Yen+18]) is a little older than the Hyades on average. The open cluster was observed during Campaign 5, and was also treated in [Ili+19]. It was observed again during campaigns 16 and 18. We revisited the membership catalog from [Dou+14], and matched it to the members identified in [Can+18; Dou+17; Reb+17]; and [Col+18b]. This was the richest sample with over 900 stars and nearly 2000 light curves.

3 The analysis code for this section can be found at https://github.com/ekaterinailin/flares-in-clusters-with-k2-ii in the "Membership_Matching" directory (accessed June 4, 2022).

Ruprecht 147

Ruprecht 147 is an open cluster with estimated ages from 2.0 Gyr to 3.1 Gyr [Col+18b; Cur+13; Sch+15b; Tor+18] observed during Campaign 7 with K2. We used the mean membership probabilities obtained from [Can+18; Cur+13; Oli+19], and [Col+18b] to identify the 53 most likely members with K2 light curves as described above.

M67

M67 is an old open cluster that has 234 members which were observed during campaigns 5, 16 and 18. Its age is about solar, with estimates ranging from 3.4 Gyr to 4.3 Gyr [Bar+16; Bos+19; Dia+12; Öne+11; Sch+15b; SWP98]. The relatively large distance of about 900 pc [Dia+12] limited the number of observable low mass stars in this otherwise rich cluster. We did not find any flares in M67 in Campaign 5 [Ili+19] light curves of members identified by [Gon16]. Campaigns 16 and 18 delivered both additional observations, and new targets to our previous sample, yielding almost 500 light curves for this open cluster. We merged the members from [Gon16] with a recent study based of Gaia DR2 data [Gao18].

6.2.3 Effective temperatures, stellar radii, and luminosities

To study the flaring-age-mass relation, we needed to determine effective temperatures ($T_{\rm eff}$, Section 6.2.3), and the luminosities in the Kepler band ($L_{\rm Kp,*}$, Section 6.2.3) of the investigated stars. $L_{\rm Kp,*}$ was required to determine the flare energies, and $T_{\rm eff}$ was used as a proxy to stellar mass. Since our catalog of stars spanned a wide variety of observables, no reliable Gaia parallaxes were available for a significant fraction of the targets, no single photometric survey covered all stars with broadband observations, and there was no emprical relation available that could have been used to derive $T_{\rm eff}$ for the entire range of spectral types. Empirical color-temperature relations (CTRs) suffer from systematic errors that stem both from the different methods applied, and from sample selection biases. We therefore used several empirical relations in their appropriate ranges to obtain $T_{\rm eff}$ from each, and draw a more reliable mean. Targets that were lacking sufficient photometric data to derive $T_{\rm eff}$, or that were too hot to be expected to have a convective envelope ($T_{\rm eff} \geq 7000\,{\rm K}$), were removed from the sample. We dropped all targets where the uncertainty on the weighted mean $T_{\rm eff}$ was greater than 10 %. Only targets that were assigned a $T_{\rm eff}$ were searched for flares. To eventually derive $L_{\rm Kp,*}$ from $T_{\rm eff}$ and model spectra we also required stellar radii as an intermediate step (Section 6.2.3).

Effective temperatures $T_{\rm eff}$

We determined $T_{\rm eff}$ using broadband photometry from the Two Micron All Sky Survey (2MASS; [Skr+06]), the Panoramic Survey Telescope and Rapid Response System Data Release 1 (PanSTARRS DR1; [Cha+16]), and Gaia Data Release 2 (Gaia DR2; [Col+16b; Col+18b]) with the following quality cuts: We required the 2MASS measurements for J, H, and K to be "A." "A" meant that measurements had $S/N > 10$ and $\sigma < 0.11$. For PanSTARRS photometry, we required that the QF_OBJ_GOOD quality filter flag was set. SDSS and PanSTARRS *ugrizy*

bands were similar but not identical. They could be converted using Table 2 in [Fin+16]. And for Gaia photometry, we cut at `flux/flux_error` ≥ 10 in the G, BP, and RP bands. Gaia astrometry solutions were only used when the Renormalized Unit Weight Error (RUWE) was < 1.4. We also removed foreground stars using Gaia DR2 parallaxes. We corrected the 2MASS and PanSTARRS photometry from the distant clusters M67 and Ruprecht 147 for extinction using the most recent version of the `dustmaps` [Gre18] package that provides 3D dust maps derived from 2MASS and PanSTARRS photometry together with Gaia distances [Gre+19]. When no Gaia parallax was available we used the cluster median distance instead. If an extinction value was not available for a given star we used the average extinction value of the respective cluster. We accounted for extinction in Gaia BP and RP bands using the reddening $E(B_P - R_P)$ derived from Gaia photometry and parallax from Gaia DR2 [And+18]. We dropped targets that were too bright and would saturate the detector (Kepler magnitude $K_\mathrm{p} \leq 9$). Faint targets were not filtered out by a threshold but were removed from the sample when T_eff did not meet the quality criteria described above.
To determine robust T_eff (Fig. 6.2), we used CTRs from [Boy+13] and [Man+16] (erratum to [Man+15]), T_eff derived from Gaia DR2 using the StarHorse algorithm [Que+18], and T_eff inferred from Gaia DR2 using the Apsis pipeline [And+18; Bai+13]. [Boy+13] determined CTRs from a range of interferometrically characterized stars using $g-r$, $g-i$, $g-z$, $g-J$, $g-H$, and $g-K$ colors from SDSS and Johnson magnitudes for A to K stars. Their sample was centered on solar metallicity, so we constained the use of these CTRs to stars with $-0.25 <$ [Fe/H] < 0.25. Following [Boy+13], we transformed 2MASS JHK to $J-H$, $H-K$, and $J-K$ in the Johnson system from 2MASS to the Bessell-Brett sytem [Car01], and from Bessell-Brett to Johnson using the relations in [BB88].
[Man+15] derived CTRs from absolutely calibrated spectra to which they fit atmospheric models to obtain T_eff. They provided transformations for SDSS/2MASS $r-z$ and $r-J$, or Gaia $BP-RP$ where extra information could be added from metallicity or 2MASS $J-H$. The relations in [Man+15] were only valid if metallicity was sufficiently close to solar, which was satisfied for the open clusters in this paper (see Table 6.1).
We supplemented our estimates with T_eff estimates from [And+19] who determined distances, extinctions, and various stellar parameters for 137 million stars in Gaia DR2 using the StarHorse pipeline [Que+18]. Gaia DR2 published T_eff for over 160 million sources [Col+18b]. The typical uncertainty was quoted at 324 K, but it was lower for stars above ~4100 K and below ~6700K, so that we adopted 175 K which was above the quoted root-median-squared error in this T_eff range, and used provided values only in this range, as the pipeline systematically overestimated the temperatures for M dwarfs [And+18; Kes+19].
Finally, we plotted color-magnitude diagrams in all aforementioned colors, and flagged outliers from the main sequence. These stars were excluded from the analysis.[4].

4 The analysis code for this section can be found at https://github.com/ekaterinailin/flares-in-clusters-with-k2-ii in the "StellarParameters" directory (accessed June 4, 2022)

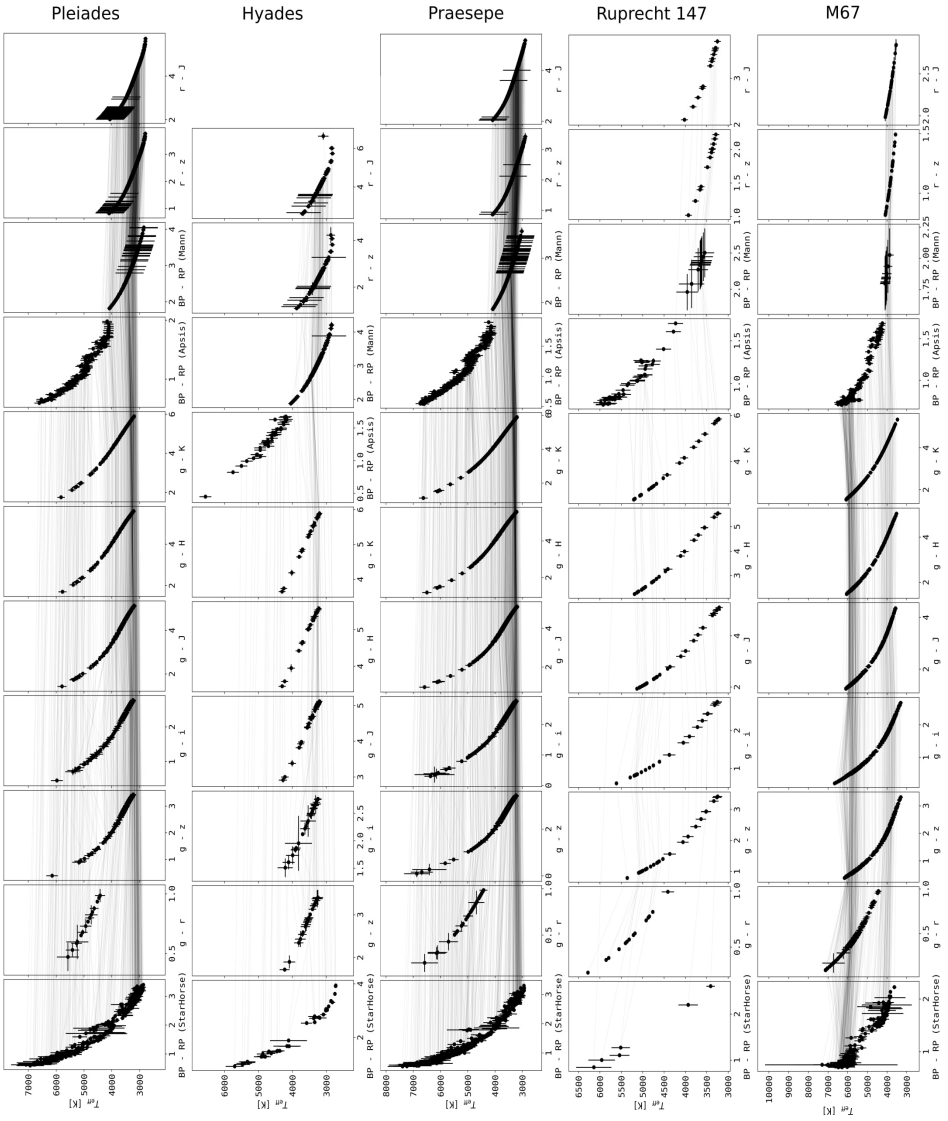

Figure 6.2: Empirical color-$T_{\rm eff}$ relations applied to high probability members of the five open clusters in this study. Individual stars are connected with lines between subplots to illustrate differences in the relations. We used PanSTARRS *griz*, 2MASS *JHK*, and Gaia DR2 *BP* and *RP* photometry with the following relations: $BP - RP$ (StarHorse, [And+19]); $g - r$, $g - i$, $g - z$, $g - J$, $g - H$, $g - K$ [Boy+13]; $BP - RP$ (Apsis, [And+18]); $BP - RP$ (Mann), $r - z$, and $r - J$ [Man+16]. The majority of connecting lines show very little slope, indicating that different CTRs are consistent with one another when applied to our sample. As expected, some relations show noticeable systematic differences, especially at the high and low temperature ends of their scopes of validity. We did not count results from Apsis with $T_{\rm eff} < 4100$ K because the pipeline systematically overestimated the temperatures for M dwarfs [And+18; Kes+19].

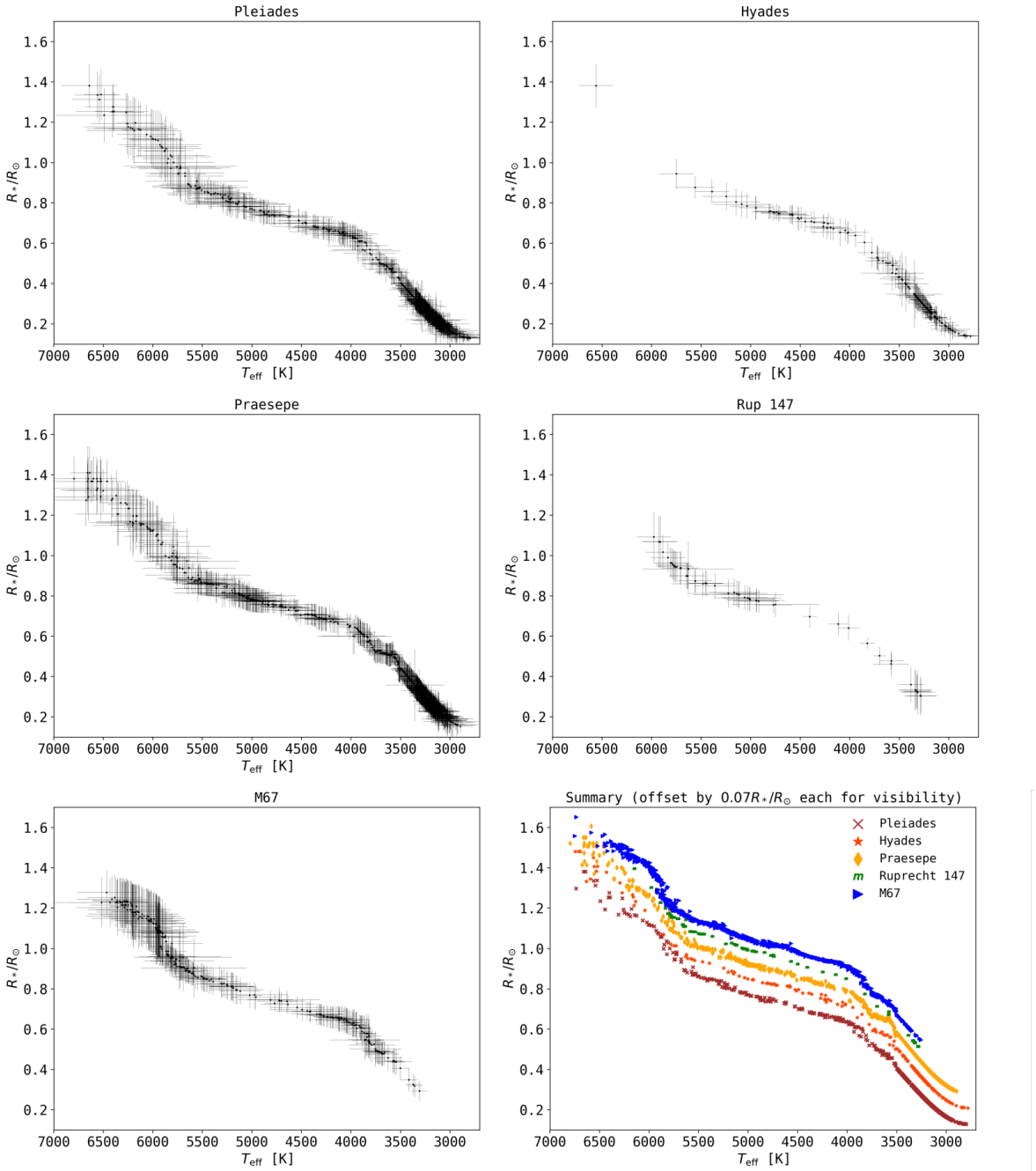

Figure 6.3: $T_{\rm eff} - R_*$ distributions for all clusters in this study. Each panel shows the distribution of high probability members of the open cluster indicated in the panel title. Stellar radii R_* are given in units of solar radii. Uncertainties on $T_{\rm eff}$ and R_* (gray error bars) were propagated from the photomety, the color-$T_{\rm eff}$ relations, and empirical $T_{\rm eff} - R_*$ relations. The uncertainties on R_* were typically $\sim 10 - 15$ %, which matches the scatter in the empirical $T_{\rm eff} - R_*$ relations. The uncertainties on $T_{\rm eff}$ roughly correspond to the size of the temperature bins that we chose in this work (see, for example, Fig. 6.4). The bottom right panel shows all five cluster samples together for comparison.

Stellar radii

We used a catalog of empirically characterized stars [YPB17] and empirical $T_{\rm eff} - R_*$ relations derived by [YPB17] compiled 404 stars with high-resolution spectra from the literature, and performed their own observations of mid to late K-dwarfs, achieving a coverage of low mass stars from 7000 K down to 3000 K. For these stars, the resulting catalog was accurate to 100 K in $T_{\rm eff}$, 15 % in R_*, and 0.09 dex in [Fe/H]. We interpolated between stars from the catalog to our derived $T_{\rm eff}$, and propagated the resulting scatter to the uncertainty in R_* if $T_{\rm eff} > 3500$ K. For stars with $T_{\rm eff} < 3500$ K we used $T_{\rm eff} - R_*$ relations derived by [Man+15; Man+16].

Stellar spectra and luminosities

We assigned spectra to our targets from the SpecMatchEmp[5] [YPB17] and the FlareSpecPhot[6] libraries [BM06; Boc+07; Boc+10; Bur+04; Bur+07; Bur+08; Bur+10; Cru+03; Cru+04; Doi+10; Fil+15; Kir+10; Man+15; RCV09; Sch+10; Sch+14a; Sch+15a; Sch14; Wes+11]. When a spectrum was available for the derived spectral type in FlareSpecPhot, we preferred it over SpecMatchEmp, which was the case for all stars cooler than M0, where we mapped spectral type to effective temperature [PM13]. We then combined R_*, $T_{\rm eff}$, and spectra to projected bolometric luminosities $L_{\rm bol,*}$, and projected luminosities in the Kepler band $L_{\rm Kp,*}$ following [Shi+13b] and [Ili+19]. For $L_{\rm bol,*}$, we integrated the convolution of the template spectrum with the blackbody spectral energy distribution at $T_{\rm eff}$ over wavelength to derive the flux per stellar surface area, and then integrated over the visible stellar hemisphere with radius R_*. To arrive at $L_{\rm Kp,*}$, we included the Kepler response function [VC16] in the convolution. Uncertainties on $L_{\rm Kp,*}$ ranged from 9 % to 52 % with a median value of 17 %. The full table of stellar properties is available in electronic form at CDS.

6.3 Methods

We developed the open source software `AltaiPony`[7] [Ili21] as a toolbox for statistical flare studies tailored but not limited to time series observations obtained by Kepler, K2, and TESS. Its functionality includes light curve de-trending, flare finding and characterization, injection- and recovery of synthetic flares, visualization commands, and methods for the statistical analysis of flare samples. We used `AltaiPony` to detect flare candidates (Section 6.3.1), and determine their equivalent durations (Section 6.3.2). We validated all events by eye, and calculated their energies in the Kepler band (Section 6.3.3). The flare rates are believed to follow a power law distribution that spans multiple orders of magnitude in energy. We used `AltaiPony`'s `FFD.fit_powerlaw()` method to fit the power law parameters simultaneously using the Markov Chain Monte Carlo (MCMC) method to sample from the posterior distribution (Section 6.3.4).

5 https://specmatch-emp.readthedocs.io/en/latest/,accessedJune4,2022
6 https://github.com/sjschmidt/FlareSpecPhot, accessed June 4, 2022
7 altaipony.readthedocs.io, accessed June 4, 2022

6.3.1 Flare finding

We used the open source software `AltaiPony` to automatically detect and characterize flares in our sample that relied on K2SC[8] [APP16] to remove instrumental and astrophysical variablity from K2 light curves. We did not use the de-trended light curves available in MAST[9]. Instead, we used K2SC to de-trend light curves from the high quality, uniformly processed and documented final K2 data release ourselves. We clipped outliers at 3σ iteratively, as compared to the original work, where outliers were clipped at 5σ [APP16]. We also masked $\sqrt{n}$ data points before and after the sequences of outliers with lengths $n > 1$ because these regions often showed physically elevated flux levels below the 3σ threshold.
After de-trending, the flare finder algorithm searched for continuous observing periods, defined as time series that were longer than 10 data points at a minimum cadence of 2 h. All further routines were run on these observing periods. We estimated the scatter in the de-trended flux using a rolling standard deviation with a 7.5 h window excluding the outliers. In the next step, the finder iteratively clipped excursions from the median value at 3σ. After each iteration, outliers were replaced with the last median value. Either after convergence, or 50 iterations, the resulting median value was adopted.
The previously masked outliers in the light curve were assigned the mean uncertainty from the remainder of the light curve. Thus we used the non-flaring parts of the light curve to define the scatter in the flaring parts. This procedure assumed that the scatter of the 80 day light curve was stable throughout the observation. In K2, stability could not be guaranteed, leading to false positive detections in regions of light curves where the uncertainty was underestimated due to strong systematic effects that K2SC could not compensate. These false positives were later removed manually.
Using the iteratively derived median as quiescent flux and the estimated scatter, we flagged all outliers above 3σ in the residual light curve. For flare candidates, we required at least three consecutive data points to fulfill the 3σ-criterion. We merged the candidates into single candidate events if they were less than four data points apart.
With the automated procedure we detected 6916 flare candidates. However, the Kepler flare sample has shown to be difficult to treat in a fully automated way. Without manual vetting, the event samples remained significantly contaminated [YL19]. As K2 was subject to severe technical difficulties, we expected that the contamination would be even higher. Some light curves could not be de-trended using K2SC alone. Light curves with extreme astrophysical signal, such as deep transits, rotational modulation on time scales of a few hours or passages of bright solar system objects (SSOs) had to be masked or fit with an additional sinusoidal component to the K2SC-treated time series. Other SSOs mimicked the fast rise and exponential decay shape of flares, and could only be identified using an extension to the Virtual Observatory (VO) tool sky body tracker (SkyBoT, [Ber+06; Ber+16]). We identified 144 SSOs using SkyBot and visual inspection with `lightkurve` [Lig+18], that is 3.6 % of all confirmed flare candidates (see Appendix 6.7.3). A number of light curves were excluded from the flare search because they saturated the detector (~ 0.2% of all light

8 github.com/OxES/k2sc, accessed June 4, 2022
9 archive.stsci.edu/prepds/k2sc/, accessed June 4, 2022

curves), or because the target aperture overlapped with broken pixels (one case). Some very faint targets and extreme variables could not be searched because the de-trending procedure did not terminate successfully ($\sim$ 0.1% of all light curves). The online version of the final flare sample (Table 6.2) includes explanatory flags, and notes on the excluded targets. Eventually, we vetted all candidates manually and confirmed 3844 events.

6.3.2 Equivalent duration

For each candidate, flaring time, amplitude and equivalent duration (*ED*) were returned. The equivalent duration is the area between the light curve and the quiescent flux, that is, the integrated flare flux divided by the median quiescent flux F_0 of the star, integrated over the flare duration [Ger72]:

$$ED = \int \mathrm{d}t \, \frac{F_{flare}(t)}{F_0}. \tag{6.1}$$

This is a quantity independent of stellar calibration and distance that is suited to compare flaring activity on stars where these properties are uncertain. Equivalent duration describes the time during which the non-flaring star releases as much energy as the flare itself. This time can be shorter or longer than the actual flare duration. The uncertainty in *ED* depends on the light curve noise properties, time sampling, spacecraft roll, and potentially other systematic effects introduced by the de-trending procedure.

6.3.3 Kepler flare energy

Multiband time-resolved observations of active M dwarfs have shown that thermal continuum flux accounts for the majority of the energy radiated by flares at optical wavelengths [Kow+13]. The effective temperature of this blackbody varies: While solar flares are relatively cool, with $T_{\mathrm{eff}} \approx 5\,000 - 7\,000$ K [KF14; Kle+16; Mae+17; Wat+13], most stellar events emit in the blue, and exhibit temperatures of about $9\,000 - 10\,000$ K [Dav+12; HF92; Kre11; Shi+13b]. However, in ultraviolet time resolved spectral observations, one superflare was reported at a blackbody temperature of 15 500 K [Loy+18a], and another could even be fit with a single 40 000 K spectral energy distribution [Fro+19]. A dependence of flare temperature on stellar age, or mass, or both, would additionally bias our analysis. For example, at about 6 200 K, the Kepler pass band captures the largest flux fraction, at 10 000 K 72 %, at 40 000 K only 4% of this value is transmitted. Given the uncertainties on stellar luminosity in the Kepler band (see Section 6.2.3) and on equivalent duration, the flare energies

$$E_{\mathrm{Kp}} = L_{\mathrm{Kp},*} \cdot ED \tag{6.2}$$

will substantially deviate from the true released energy. If these uncertainties did not affect all flares in a similar fashion, the present analysis will have suffered from nonuniform biases that affected the FFDs on stars of different ages and temperatures, and skewed the flare distributions within each subsample. However, the comparison to other studies (see Section 6.5.1) suggested that our results were mostly consistent with studies based on similar

data (see Fig. 6.11, and [Lin+19] therein for an example), albeit using different methods to infer E_{flare}.

6.3.4 Power law fits

Flare frequency distributions (FFDs) follow power law relations that cover several orders of magnitude, from solar microflares to stellar superflares (see Fig. 9 in [Shi+13b]). In the cumulative distribution the frequency $f(>E)$ of flares above a certain energy E is defined as

$$f(>E) = \frac{\beta}{\alpha - 1} E^{-\alpha+1}, \tag{6.3}$$

and, analogously, for ED [Ger72]. We used and compared two approaches to fitting α and β to the data. The first was a modified maximum likelihood estimator (MMLE) for power law distributions [MK09]. The second approach was more specifically tailored to flaring activity. Following [Whe04], we used the MCMC method to sample from the predictive distribution of flares from a prototype flare source. This source has two characteristics. Firstly, it produces flare events as a homogeneous Poisson process in time. Secondly, the flare energies are power law distributed. While the MMLE was computationally efficient, and useful to obtain first results (see Appendix 6.7.4), only the predictive distribution allowed us to fit for α and β simultaneously, and determine their uncertainties, so we adopted the latter. The posterior distribution in [Whe04] captured both the Poissonian distribution of flare events in time, and their power law distribution in energy, simultaneously. The authors derived this model to be able to predict the flaring rate above a given energy for any active region on the Sun including changes in flaring activity rates as the active region evolves, and also characteristics of the active region itself, such as sunspot classifiers. In our simplification of the model, we assumed that the flare generating process did not change within the observation time span in any star in our sample ($M = M'$ in Eq. 24 in [Whe04]). Another assumption was that this process was the same for all stars in the sample ($\Lambda_{MC} = 1$ in aforementioned Eq. 24). Under these assumptions, the samples of flares found in the light curves of different stars and light curves obtained during different campaigns could be stacked together. With these simplifications to Eq. 24, we defined the joint posterior distribution for the probability ϵ that a flare with ED or E_{Kp} above some value S_2 would occur within a time period ΔT:

$$\begin{aligned} p(\epsilon, \alpha) \quad = \quad & C \cdot \left(-\ln(1-\epsilon)^M\right) \\ & \cdot (\alpha - 1)^M \cdot \Gamma(\alpha) \left[\frac{(S_2/S_1)^{M+1}}{\pi}\right]^{\alpha} \\ & \cdot (1-\epsilon)^{(T/\Delta T)\cdot (S_2/S_1)^{\alpha-1}-1}. \end{aligned} \tag{6.4}$$

C was the normalization constant, M was the number of events, T the total observation time. Γ contained the prior distribution for α, and S_1 denoted the detection threshold above

which all flares were detected. π encapsulated the flare energies as

$$\pi = \prod_{i=1}^{M} \frac{s_i}{S_1}, \tag{6.5}$$

where $\{s_1, s_2, ...s_m\}$ were the flare energies $E_{\rm Kp}$ or ED. We chose ΔT to be equal to the total observation time of the FFD, and S_2 was set to be ten times the maximum observed energy in that FFD.
From the posterior distribution of ϵ we derived β by combining Poisson statistics

$$\epsilon = 1 - \mathrm{e}^{(-f \cdot \Delta T)} \tag{6.6}$$

and the cumulative power law function in Eq. 6.3:

$$\beta = -\frac{\ln(1-\epsilon) \cdot (\alpha - 1)}{\Delta T} \cdot S_2^{\alpha - 1} \tag{6.7}$$

With a uniform prior for α the results from the MMLE and MCMC sampling from the posterior distribution were consistent within uncertainties (see Appendix 6.7.4). However, the MCMC method allowed us to fit for both ϵ and α simultaneously, and to use more informative priors.
The power law exponent determined for FFDs has consistently been found to be independent of age [Dav+19], and spectral type for solar-type and low mass dwarfs (e.g., [CBH15; How+19; Lin+19]; see Fig. 6.13 for an overview). We chose our prior to reflect this result: Starting from a uniform prior for α and ϵ, we found a Gaussian distribution to be an excellent fit to the posterior distribution for α for the full sample of flares in $E_{\rm Kp}$ and ED space. We then used this Gaussian distribution as a prior for the FFDs in individual age and $T_{\rm eff}$ bins.

6.3.5 Injection and recovery of synthetic flares

Energies of flares found in Kepler 30 minute cadence light curves are underestimated by about 25 % compared to 1 minute cadence [Yan+18]. Moreover, the low energy end of FFDs is incomplete because not all small flares of a given energy are recovered [Dav16]. In [Ili+19] we injected and recovered synthetic flare signal based on the empirical flare template from [Dav+14] to determine the energy bias, and the recovery probability as a function of energy. We injected flares into the K2 light curves after de-trending them with K2SC to test the performance of the flare finding and characterization algorithms. Here, we performed this procedure on a random selection of light curves from our sample before applying K2SC. The injected flare candidates thus had to survive the K2SC de-trending in addition to flare search prescription. As this procedure was computationally very expensive, we did not repeat the process for all light curves in our sample. We noted that both energy bias and recovery probability were better described as a function of amplitude and duration than of energy alone, and that they varied strongly from light curve to light curve. Therefore, energy bias and recovery probability should be quantified light curve by light curve. While this was not

possible here, we recommend using the `FlareLightCurve.sample_flare_recovery()` method and associated visualization functions in `AltaiPony` with light curves from the original Kepler mission, and TESS, to assess the effects of light curve quality, and de-trending and flare search methods on the detected ensembles of flares[10]. We mitigated the lack of such an assessment by cutting our FFDs at the incomplete low energy tail, but we have to acknowledge that the reported energies remain underestimated [Yan+18]. [Asc15] suggested that the observed incompleteness may be partly canceled by background contamination from, for instance, cosmic rays, or SSOs. While the effect of cosmic rays is currently not well constrained [Ili+19], we could quantify the contamination by cataloged SSOs to 3.6 % (see Section 6.3.1).

6.4 Results

The core objective of this work was to quantify how the previously noted decline in flaring activity with age would unfold for different spectral types. To this end, we searched the long cadence light curves of stars across a broad range of spectral types in five different open clusters for flares, and measured their energies and occurrence rates. We found 3844 flares on 2111 stars in five open clusters for $T_{\rm eff}$ between 2500 K and 6000 K. The flares' amplitudes a, start and end cadence numbers c_0 and c_1, ED, energies $E_{\rm Kp}$, along with the stars' EPIC ID, $T_{\rm eff}$, and projected bolometric and Kepler band luminosities $L_{\rm bol,*}$ and $L_{\rm Kp,*}$ are listed in Table 6.2. We fit power law relations to the FFDs of stars binned by age, and $T_{\rm eff}$ (Section 6.4.1, Figs. 6.4, 6.5 and Table 6.3). We found that flaring activity decreased with increasing age from ZAMS to 3.6 Gyr, and from mid-M to G dwarfs (Sections 6.4.2 and 6.4.3, Figs. 6.6 and 6.7). Except for the stars in the coolest temperature bin (M5.5-M8, 2 500-3 000 K), stellar flaring activity at a given age was higher for cooler stars. The stars in our sample indicated a mass- and rotation-dependent threshold age above which they were no longer found on the saturated activity branch which was characterized by fast rotating and actively flaring stars. Stars above this threshold showed much lower flaring rates (Sections 6.4.4 and 6.4.5, Fig. 6.9). In the old clusters Ruprecht 147 and M67 we found very few flares, and suggest that a significant fraction of those found on higher mass stars may stem from unresovled low mass companions (Section 6.4.6).

6.4.1 Flare frequency distributions

The aim of this work was to investigate the effects of age on the flaring activity for low mass stars. We therefore split up the full sample into $T_{\rm eff}$ bins and constructed the FFDs cluster by cluster (Figs. 6.4 and 6.5). We used a broad Gaussian prior for α with mean 1.9 and standard deviation .4 that covered the range of α values obtained in past studies (see Fig. 6.13 in the discussion). The power law fit parameters to these FFDs, broken down by cluster and $T_{\rm eff}$, are summarized in Table 6.3. In the table, α and β are the power law parameters from Eq. 6.3. The number of flares $n_{\rm tot}$ in the distribution is higher than the number $n_{\rm fit}$ of flares

10 Examples of usage can be found in the software documentation.

Table 6.2: Confirmed flare candidates detected in open cluster stars observed by K2, sorted by amplitude a.

EPIC	C	cluster	c_0	c_1	a	$T_{\rm eff}$ [K]	ED [s]	$L_{\rm bol,*}$ [erg/s]	$L_{\rm Kp}$ [erg/s]
211079830	4	Pleiades	105984	105993	15.330194	3097(87)	63340(63)	$8.29(3.34)10^{29}$	$3.32(1.34)10^{29}$
210720772	4	Pleiades	107181	107184	9.674757	3104(86)	19901(7)	$8.66(3.45)10^{29}$	$3.48(1.38)10^{29}$
247523445	13	Hyades	143106	143109	8.260956	2964(49)	16615(11)	$4.33(1.09)10^{29}$	$1.69(0.43)10^{29}$
212021131	5	Praesepe	108974	108980	7.421916	3215(68)	19828(175)	$2.01(0.65)10^{30}$	$8.22(2.65)10^{29}$
210978953	4	Pleiades	106762	106770	6.769888	3050(95)	39467(125)	$6.20(2.63)10^{29}$	$2.46(1.04)10^{29}$
211913613	16	Praesepe	156845	156849	6.690356	3218(66)	21632(147)	$2.05(0.65)10^{30}$	$8.37(2.63)10^{29}$
211127297	4	Pleiades	106754	106759	6.449569	3147(86)	20830(5)	$1.13(0.45)10^{30}$	$4.59(1.81)10^{29}$
211681193	5	Praesepe	108116	108120	5.570804	3182(76)	11198(95)	$1.64(0.58)10^{30}$	$6.68(2.37)10^{29}$
211024798	4	Pleiades	104822	104826	5.394897	3290(62)	12524(63)	$2.58(0.75)10^{30}$	$1.06(0.31)10^{30}$
211134185	4	Pleiades	103891	103896	4.951629	3127(96)	17459(33)	$9.99(4.33)10^{29}$	$4.03(1.75)10^{29}$
211095280	4	Pleiades	106283	106287	4.796979	3138(93)	12186(10)	$1.06(0.45)10^{30}$	$4.32(1.82)10^{29}$
211022535	4	Pleiades	104262	104267	3.994973	2953(76)	15164(57)	$3.50(1.10)10^{29}$	$1.37(0.43)10^{29}$
211010517	4	Pleiades	106680	106685	3.968907	3252(70)	16241(171)	$2.09(0.68)10^{30}$	$8.59(2.77)10^{29}$
210846442	4	Pleiades	104410	104415	3.959977	3311(79)	13515(10)	$2.88(0.96)10^{30}$	$1.18(0.40)10^{30}$
212017838	5	Praesepe	111183	111192	3.671037	3307(89)	10274(10)	$3.35(1.22)10^{30}$	$1.38(0.50)10^{30}$
211984058	5	Praesepe	109952	109965	3.320636	3124(97)	16063(149)	$1.17(0.51)10^{30}$	$4.73(2.06)10^{29}$
211912899	5	Praesepe	110700	110706	3.257997	3133(81)	7967(16)	$1.24(0.47)10^{30}$	$5.01(1.89)10^{29}$
211151674	4	Pleiades	106457	106467	3.166323	3072(93)	17843(106)	$7.10(2.99)10^{29}$	$2.84(1.19)10^{29}$
211822895	5	Praesepe	107809	107812	3.164494	3005(177)	6883(31)	$5.68(3.98)10^{29}$	$2.25(1.57)10^{29}$
211760567	5	Praesepe	109962	109965	3.061417	3245(58)	7838(9)	$2.39(0.69)10^{30}$	$9.84(2.83)10^{29}$
211939350	16	Praesepe	155018	155022	2.892939	3149(150)	9542(68)	$1.36(0.86)10^{30}$	$5.52(3.49)10^{29}$
211137806	4	Hyades	106768	106775	2.482828	3127(58)	9208(8)	$1.16(0.35)10^{30}$	$4.69(1.40)10^{29}$
210674207	13	Hyades	141708	141711	2.419586	3210(74)	5343(3)	$1.90(0.65)10^{30}$	$7.78(2.66)10^{29}$
211994910	5	Praesepe	109858	109864	2.401426	3325(95)	7807(14)	$3.71(1.40)10^{30}$	$1.53(0.58)10^{30}$
211010517	4	Pleiades	106561	106564	2.341076	3252(70)	4838(36)	$2.09(0.68)10^{30}$	$8.59(2.77)10^{29}$
211984058	5	Praesepe	108584	108587	2.155468	3124(97)	4817(13)	$1.17(0.51)10^{30}$	$4.73(2.06)10^{29}$
211983544	18	Praesepe	162792	162798	2.096077	3159(98)	6924(55)	$1.44(0.63)10^{30}$	$5.88(2.55)10^{29}$
210988354	4	Pleiades	106012	106017	2.057812	3661(144)	5725(1)	$1.40(0.31)10^{31}$	$6.06(1.32)10^{30}$
210886447	4	Pleiades	103871	103877	2.057490	3048(105)	8710(49)	$6.13(2.83)10^{29}$	$2.43(1.12)10^{29}$
211098921	4	Pleiades	105254	105262	2.041041	3300(101)	7499(5)	$2.72(1.10)10^{30}$	$1.12(0.45)10^{30}$

The full table is available in electronic form at CDS. EPIC and C denote the K2 ID and observing campaign. a – relative flare amplitude, c_0 and c_1 – flare start and end cadence numbers, $T_{\rm eff}$ – stellar effective temperature, ED – equivalent duration, $L_{\rm bol,*}$ – projected stellar bolometric luminosity, $L_{\rm Kp}$ - projected stellar luminosity in the Kepler band. Uncertainties are given in parentheses.

used to fit the power law because we omitted the low energy tail of the distribution where the detection probability decreased. Our approximation to the detection threshold was the highest minimum detected energy from all FFDs of individual stars in a given bin. This was equivalent to using only the part of the FFD that was above the detection threshold for all stars in that bin. The indices s and erg to α and β indicate the fits to the FFDs in ED (Fig. 6.4) and $E_{\rm Kp}$ (Fig. 6.5), respectively. For the single flare detection in M67 we give the power law parameters obtained directly from Eq. 6.3 using the prior value and uncertainty for α. We provide Table 6.3 to enable future science to build a comprehensive flare rate evolution model.

6.4.2 Flaring activity measure β_{100s}

Relative flaring activity levels are best described by β_s, that is, the power law fit intercept β (see Eq. 6.3) for the FFDs in ED space (equivalent to R_{1s} in [Dav+19]). Because of the definition of ED as relative to the quiescent flux of the star (Eq. 6.1), β_s is a measure of flaring activity in which the different energy budgets of stars are controlled for, in contrast to $\beta_{\rm erg}$, which uses the absolute flare energies. However β_s is defined as the flaring rate at $ED > 1$ s which is below the detection threshold for most $T_{\rm eff}$-age bins. To reduce errors arising from extrapolation we chose β_{100s} (analogous to R_{100s}), that is, Eq. 6.3 evaluated at $ED = 100$ s where most FFDs overlap to compare across both $T_{\rm eff}$ and age at the same time. Fig. 6.6 can be interpreted as a synthesis of the FFDs presented in Fig. 6.4. Overall, β_{100s} tended to be lower for hotter stars at a given age. This general trend is consistent with the flaring rates found in nearby young moving groups, open clusters, OB associations, and star forming regions with ages between 1 and 800 Myr in TESS [Fei+20]. β_{100s} declined with age in all investigated $T_{\rm eff}$ bins, and it declined stronger in the hotter stars, a trend also observed in the transition from 125-300 Myr to 300-800 Myr in the TESS study. An exception to this rule is the $2500 - 3000$ K bin, where β_{100s} marginally increased from ZAMS to Hyades age. A slight increase in activity is also seen for stars < 4000 K at ages between 1-20 Myr and 30-45 Myr in [Fei+20]. This uptick in activity was also present in comparing fast and slow rotators in a K2 short cadence K7-M6 dwarf flaring study [Rae+20]. In the lowest mass bin (M5-M6) the authors measured higher flaring activity for relatively slow rotators ($P_{\rm rot} > 2$ d) than for their fast counterparts ($P_{\rm rot} < 2$ d).
[Mon+19] found evidence of increased flaring activity at intermediate rotation rates between fast and slow sequence [Bar03]. This finding could not be reproduced in the data obtained from the all-sky EvryFlare survey [How+20]. We found β_{100s} to decrease with age from ZAMS to 700 Myr for all stars except those with spectral types later than M5 (Fig. 6.6 a.). But this does not exclude that β_{100s} in fact increased between these two ages before decreasing relatively rapidly within a short period of time.

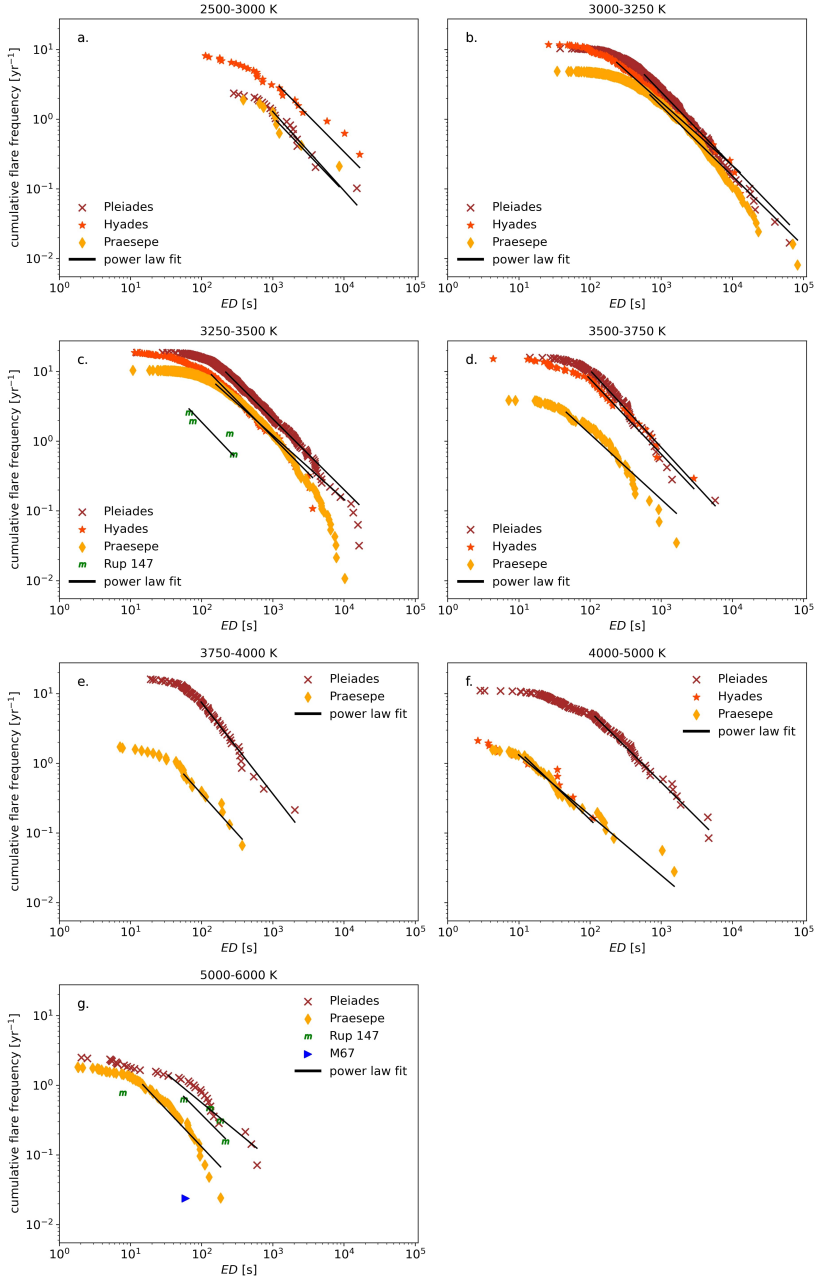

Figure 6.4: Cumulative FFDs (scatter) in *ED*, and respective power law fits to the portion of the FFDs where we considered our sample not be affected by reduced detection efficiency of low energy flares (black lines), in log-log representation. In each of the panels a.-g. the distributions of flares are shown for different open clusters for samples of stars in the $T_{\rm eff}$ bin that is given in the panel title. The different clusters are the Pleiades (maroon crosses), the Hyades (orange stars), Praesepe (yellow diamonds), Ruprecht 147 (green "m"s), and M67 (blue triangles). The extension of the black lines in *ED* indicates the low energy threshold adopted for every fit. When no distribution is shown, either no flares were found in the subsample, or no stars in that $T_{\rm eff}$ bin were observed by K2. The overview of all power law fit parameters including uncertainties is given in Table 6.3.

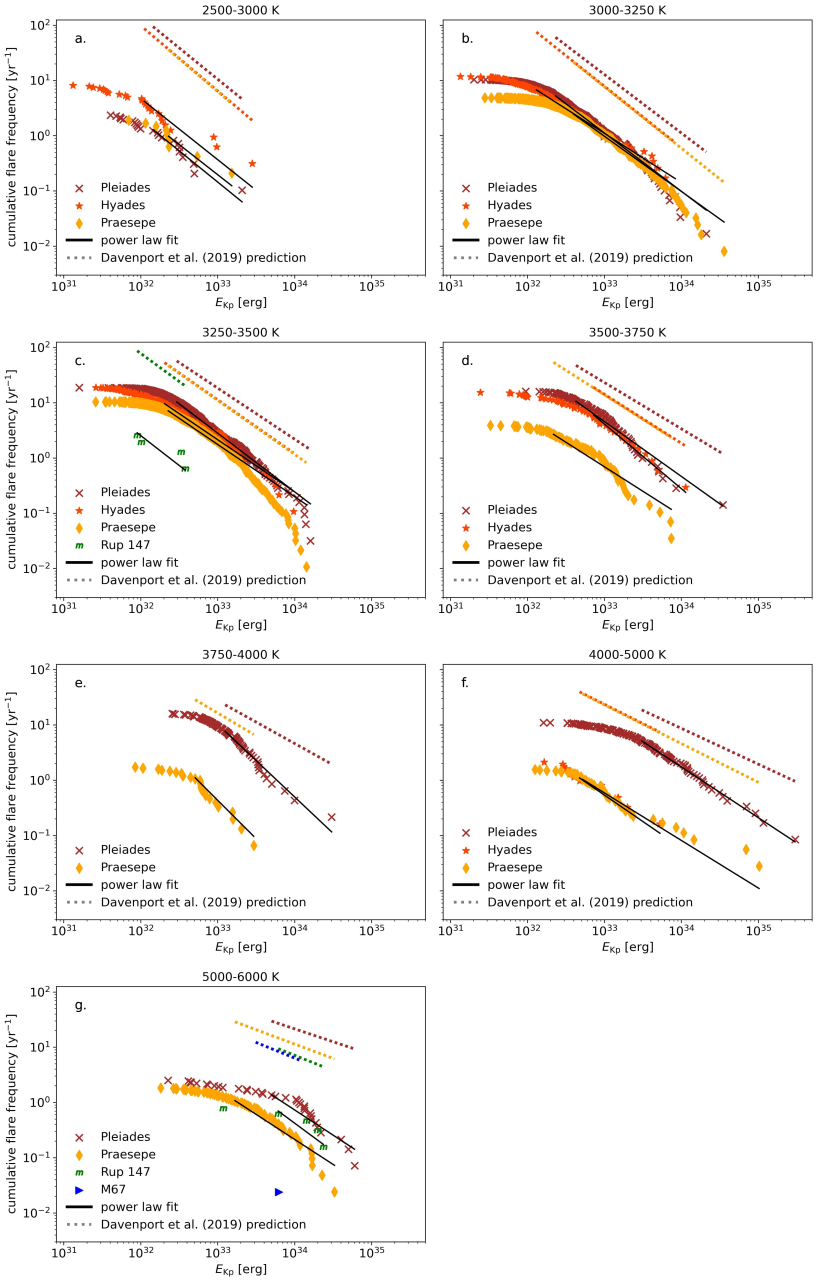

Figure 6.5: Same as in Fig. 6.4 but for E_{Kp} instead of *ED*. Additionally, predictions from the [Dav+19] gyrochronology-calibrated FFD parametrization with stellar age and mass were added in the colors that denote the different open clusters (see discussion in Section 6.5.2). To calculate the predictions, we used the mean of each T_{eff} bin to determine the mass [PM13], and open cluster ages from the literature.

Table 6.3: Power law fit parameters α and β for all clusters and $T_{\rm eff}$ bins in $E_{\rm Kp}$ and ED FFDs.

Teff	cluster	$\alpha_{\rm s}$	$\beta_{\rm s}$ [yr^{-1}]	$ED_{\rm min}$ [s]	$ED_{\rm max}$ [s]	$n_{\rm tot,s}$	$n_{\rm fit,s}$	$\alpha_{\rm erg}$	$\beta_{\rm erg}$ [yr^{-1}]	$E_{\rm Kp,min}$ [erg]	$E_{\rm Kp,max}$ [erg]	$n_{\rm tot,erg}$	$n_{\rm fit,erg}$
2500-3000	Hyades	$2.03^{(0.27}_{0.24)}$	$4707^{(37065}_{4086)}$	$1.24 \cdot 10^{3}$	$1.66 \cdot 10^{4}$	26	9	$2.11^{(0.25}_{0.23)}$	$1.4 \cdot 10^{36}{}^{(1.5\cdot10^{44}}_{1.4\cdot10^{36})}$	$1.11 \cdot 10^{32}$	$2.82 \cdot 10^{33}$	26	13
	Pleiades	$2.13^{(0.26}_{0.23)}$	$3668^{(23493}_{3102)}$	$0.99 \cdot 10^{3}$	$1.52 \cdot 10^{4}$	23	12	$2.13^{(0.26}_{0.24)}$	$3.3 \cdot 10^{36}{}^{(6.6\cdot10^{44}}_{3.3\cdot10^{36})}$	$1.45 \cdot 10^{32}$	$2.08 \cdot 10^{33}$	23	12
	Praesepe	$2.07^{(0.32}_{0.30)}$	$1883^{(22416}_{1727)}$	$1.13 \cdot 10^{3}$	$0.86 \cdot 10^{4}$	9	4	$2.09^{(0.32}_{0.30)}$	$2.1 \cdot 10^{35}{}^{(8.8\cdot10^{45}}_{2.1\cdot10^{35})}$	$2.3 \cdot 10^{32}$	$1.53 \cdot 10^{33}$	9	4
3000-3250	Hyades	$1.91^{(0.10}_{0.10)}$	$865^{(832}_{413)}$	$2.37 \cdot 10^{2}$	$1.29 \cdot 10^{4}$	137	76	$1.89^{(0.10}_{0.09)}$	$2.3 \cdot 10^{29}{}^{(3.8\cdot10^{32}}_{2.3\cdot10^{29})}$	$1.31 \cdot 10^{32}$	$0.84 \cdot 10^{34}$	137	78
	Pleiades	$2.06^{(0.06}_{0.06)}$	$3809^{(2338}_{1431)}$	$0.58 \cdot 10^{3}$	$0.63 \cdot 10^{5}$	616	258	$2.06^{(0.06}_{0.06)}$	$8.1 \cdot 10^{34}{}^{(7.4\cdot10^{36}}_{8.0\cdot10^{34})}$	$2.32 \cdot 10^{32}$	$2.11 \cdot 10^{34}$	616	311
	Praesepe	$2.00^{(0.06}_{0.06)}$	$1605^{(935}_{573)}$	$0.7 \cdot 10^{3}$	$0.82 \cdot 10^{5}$	601	275	$2.00^{(0.06}_{0.05)}$	$8.8 \cdot 10^{32}{}^{(6.9\cdot10^{34}}_{8.6\cdot10^{32})}$	$0.4 \cdot 10^{33}$	$0.36 \cdot 10^{35}$	601	302
3250-3500	Hyades	$2.04^{(0.11}_{0.10)}$	$1545^{(1434}_{714)}$	$1.37 \cdot 10^{2}$	$0.36 \cdot 10^{4}$	174	83	$1.94^{(0.10}_{0.09)}$	$2.8 \cdot 10^{31}{}^{(4.5\cdot10^{34}}_{2.8\cdot10^{31})}$	$2.04 \cdot 10^{32}$	$0.97 \cdot 10^{34}$	174	90
	Pleiades	$2.02^{(0.06}_{0.06)}$	$2367^{(1063}_{713)}$	$2.19 \cdot 10^{2}$	$1.62 \cdot 10^{4}$	590	310	$2.06^{(0.06}_{0.06)}$	$3.3 \cdot 10^{35}{}^{(2.9\cdot10^{37}}_{3.3\cdot10^{35})}$	$2.95 \cdot 10^{32}$	$1.61 \cdot 10^{34}$	590	327
	Praesepe	$1.92^{(0.04}_{0.04)}$	$626^{(164}_{127)}$	$1.59 \cdot 10^{2}$	$1.03 \cdot 10^{4}$	970	612	$1.95^{(0.04}_{0.04)}$	$2.6 \cdot 10^{31}{}^{(3.8\cdot10^{32}}_{2.4\cdot10^{31})}$	$2.28 \cdot 10^{32}$	$1.42 \cdot 10^{34}$	970	663
	Rup 147	$2.07^{(0.32}_{0.30)}$	$283^{(1232}_{228)}$	$0.67 \cdot 10^{2}$	$2.81 \cdot 10^{2}$	4	4	$2.08^{(0.33}_{0.30)}$	$1.0 \cdot 10^{35}{}^{(3.6\cdot10^{45}}_{1.0\cdot10^{35})}$	$0.9 \cdot 10^{32}$	$0.38 \cdot 10^{33}$	4	4
3500-3750	Hyades	$2.08^{(0.19}_{0.17)}$	$1216^{(2144}_{754)}$	$0.93 \cdot 10^{2}$	$2.88 \cdot 10^{3}$	52	28	$2.17^{(0.22}_{0.21)}$	$1.9 \cdot 10^{39}{}^{(5.6\cdot10^{46}}_{1.9\cdot10^{39})}$	$0.72 \cdot 10^{33}$	$1.14 \cdot 10^{34}$	52	20
	Pleiades	$2.11^{(0.13}_{0.12)}$	$1882^{(2020}_{943)}$	$1.06 \cdot 10^{2}$	$0.57 \cdot 10^{4}$	113	69	$1.99^{(0.11}_{0.11)}$	$2.7 \cdot 10^{33}{}^{(1.6\cdot10^{37}}_{2.7\cdot10^{33})}$	$0.43 \cdot 10^{33}$	$0.35 \cdot 10^{35}$	113	75
	Praesepe	$1.94^{(0.11}_{0.10)}$	$88^{(63}_{35)}$	$0.46 \cdot 10^{2}$	$1.63 \cdot 10^{3}$	111	74	$1.89^{(0.10}_{0.09)}$	$1.1 \cdot 10^{29}{}^{(2.2\cdot10^{32}}_{1.1\cdot10^{29})}$	$2.19 \cdot 10^{32}$	$0.74 \cdot 10^{34}$	111	76
3750-4000	Pleiades	$2.31^{(0.20}_{0.18)}$	$3990^{(7449}_{2512)}$	$0.98 \cdot 10^{2}$	$2.05 \cdot 10^{3}$	75	35	$2.32^{(0.20}_{0.18)}$	$3.4 \cdot 10^{44}{}^{(1.2\cdot10^{51}}_{3.4\cdot10^{44})}$	$1.25 \cdot 10^{33}$	$3.03 \cdot 10^{34}$	75	36
	Praesepe	$2.13^{(0.27}_{0.25)}$	$76^{(213}_{55)}$	$0.56 \cdot 10^{2}$	$0.37 \cdot 10^{3}$	26	10	$2.39^{(0.27}_{0.24)}$	$4.4 \cdot 10^{45}{}^{(3.4\cdot10^{54}}_{4.4\cdot10^{45})}$	$0.51 \cdot 10^{33}$	$2.95 \cdot 10^{33}$	26	16
4000-5000	Hyades	$1.98^{(0.28}_{0.25)}$	$14^{(24}_{8)}$	$1.22 \cdot 10^{1}$	$1.1 \cdot 10^{2}$	13	7	$1.96^{(0.29}_{0.26)}$	$2.0 \cdot 10^{31}{}^{(6.1\cdot10^{40}}_{2.0\cdot10^{31})}$	$0.48 \cdot 10^{33}$	$0.53 \cdot 10^{34}$	13	6
	Pleiades	$2.02^{(0.13}_{0.12)}$	$603^{(681}_{312)}$	$1.17 \cdot 10^{2}$	$0.46 \cdot 10^{4}$	131	55	$1.92^{(0.12}_{0.11)}$	$2.3 \cdot 10^{31}{}^{(2.4\cdot10^{35}}_{2.3\cdot10^{31})}$	$3.06 \cdot 10^{33}$	$3.01 \cdot 10^{35}$	131	59
	Praesepe	$1.86^{(0.12}_{0.11)}$	$8.2^{(4.5}_{2.8)}$	$0.99 \cdot 10^{1}$	$1.52 \cdot 10^{3}$	56	47	$1.86^{(0.14}_{0.12)}$	$1.3 \cdot 10^{28}{}^{(4.1\cdot10^{32}}_{1.3\cdot10^{28})}$	$0.52 \cdot 10^{33}$	$1.03 \cdot 10^{35}$	56	37
5000-6000	M67	$1.90^{(0.40}_{0.40)}$	$0.9^{(5.4}_{0.8)}$	$0.6 \cdot 10^{2}$	$0.6 \cdot 10^{2}$	1	1	$1.90^{(0.40}_{0.40)}$	$5.6 \cdot 10^{28}{}^{(2.7\cdot10^{42}}_{5.6\cdot10^{28})}$	$0.62 \cdot 10^{34}$	$0.62 \cdot 10^{34}$	1	1
	Pleiades	$1.84^{(0.18}_{0.16)}$	$22^{(30}_{12)}$	$0.34 \cdot 10^{2}$	$0.6 \cdot 10^{3}$	35	19	$1.91^{(0.19}_{0.17)}$	$6.9 \cdot 10^{30}{}^{(2\cdot10^{37}}_{6.9\cdot10^{30})}$	$0.5 \cdot 10^{34}$	$0.6 \cdot 10^{35}$	35	19
	Praesepe	$2.08^{(0.16}_{0.14)}$	$20^{(15}_{8)}$	$1.49 \cdot 10^{1}$	$1.85 \cdot 10^{2}$	76	42	$1.91^{(0.13}_{0.12)}$	$1.2 \cdot 10^{30}{}^{(3.2\cdot10^{34}}_{1.2\cdot10^{30})}$	$1.68 \cdot 10^{33}$	$0.33 \cdot 10^{35}$	76	44
	Rup 147	$2.03^{(0.32}_{0.29)}$	$45^{(182}_{36)}$	$0.56 \cdot 10^{2}$	$2.16 \cdot 10^{2}$	5	4	$2.03^{(0.32}_{0.29)}$	$4.3 \cdot 10^{34}{}^{(3.6\cdot10^{45}}_{4.3\cdot10^{34})}$	$0.61 \cdot 10^{34}$	$2.36 \cdot 10^{34}$	5	4

This table is available in electronic form at CDS. Uncertainties are given in parentheses. Indices $_{\rm s}$ and $_{\rm erg}$ refer to the units of ED and $E_{\rm Kp}$ FFDs. $E_{\rm Kp,min}/ED_{\rm min}$ and $E_{\rm Kp,max}/ED_{\rm max}$ are minimum and maximum detected flare ED/energy, $n_{\rm tot}$ is the total number of flares in the sample. $n_{\rm fit}$ is the number of flares used for the power law fit.

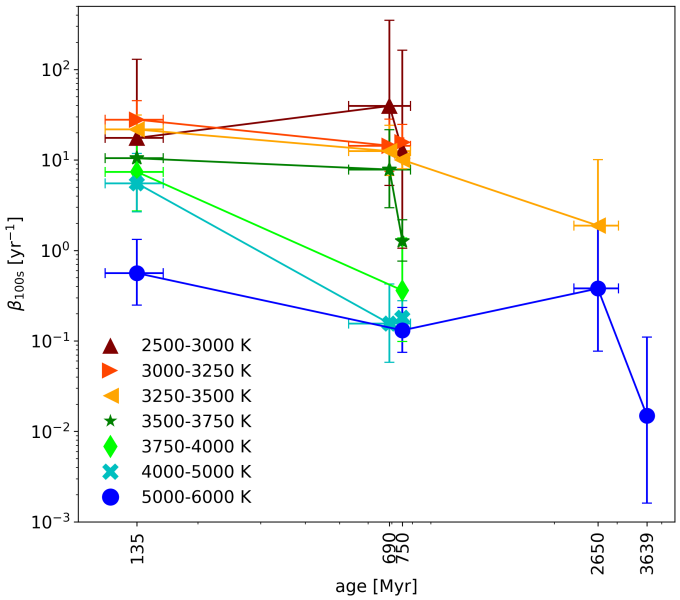

Figure 6.6: Flaring activity measure β_{100s} for the FFDs in Fig. 6.4 as a function of age. The values are grouped by $T_{\rm eff}$ (different colors and symbols in the legend), and presented on a log-log scale. β_{100s} indicates the occurrence rate of flares with $ED > 100$ s (see Eq. 6.3). It is controlled for stellar luminosity, so that we can compare flaring activity across both age, and $T_{\rm eff}$, at the same time. The age labels correspond to the open cluster ages in Table 6.1.

6.4.3 Flaring luminosity FA

We can relate the luminosity in flares in the Kepler band to the quiescent bolometric luminosity of the star, and by this define the fractional flare luminosity FA (similar to [Ili+19]):

$$FA = \frac{E_{\rm Kp,flare,tot,}}{t \cdot L_{\rm bol,*,}} \tag{6.8}$$

$E_{\rm Kp,flare,tot,}$ is the total energy released in flares, and t is the total observing time of the star. We determined $L_{\rm bol,*}$ from R_* and $T_{\rm eff}$, as described in Section 6.2.3. The energy released in flares was inferred using our derived stellar luminosities. By definition, FA is a useful measure of relative stellar activity as long as the flux portion of the quiescent star in the Kepler band is roughly constant. One can compare FA across age, but comparisons across $T_{\rm eff}$ bins should be interpreted with caution. FA declines with age for every $T_{\rm eff}$ bin considered for both the total luminosity and relative to the quiescent flux (Fig. 6.7). However, we found that FA remained high ($> 10^{-5}$) in early to mid M dwarfs for several hundred Myr after Pleiades age.
[Lur+15] analyzed the flares on GJ 1245 A and B, two M5 dwarfs in a triple system with another M8 dwarf, that were observed in 1 minute cadence during the original Kepler mission. GJ 1245 A and B both fall roughly into the $3000 - 3250$ K bin, and rotate at periode < 1 d. The authors calculated $FA \approx 10^{-4}$ for both components, consistent with the FA value

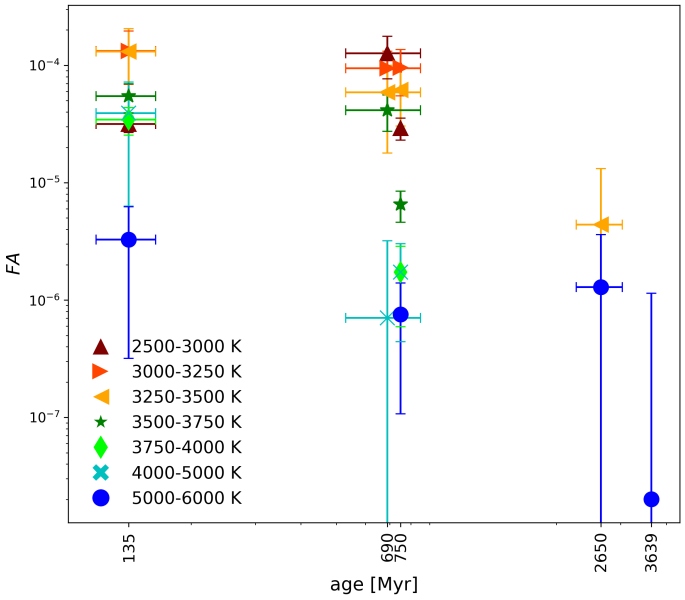

Figure 6.7: Median fraction of stellar luminosity emitted in flares (*FA*), and standard deviation plotted against age. The values are grouped by $T_{\rm eff}$, and presented on a log-log scale. The colors and shapes are the same as in Fig. 6.6. We calculated the shared energy detection threshold $3.31 \cdot 10^{32}$ erg using the method described in Section 6.4.1 to derive *FA* with Eq. 6.8. *FA* is a useful measure of relative stellar activity as long as the flux portion of the quiescent star in the Kepler band is roughly constant. It is therefore more meaningful to compare *FA* across age than across $T_{\rm eff}$.

in the 135 Myr old Pleiades in this $T_{\rm eff}$. But as the activity remains high at least up to the ages of Hyades and Praesepe, GJ 1245 could also be older.

6.4.4 Hyades and Praesepe: Rotating differently

We expected the flaring activity in the Hyades and Praesepe to be very similar because they are nearly coeval clusters with ages around 700 Myr, and comparable metallicities ([Fe/H](Praesepe) = 0.16, [Fe/H](Hyades) = 0.13, [Net+16]). We found this reflected in all our FFDs, except for the 3500 − 3750 K temperature bin, where the Hyades appeared almost as active as the Pleiades (135 Myr), while Praesepe showed flare frequencies about ten times lower than the Pleiades. This effect is not captured by the [Dav+19] model that predicts consistent flaring rates in all mass bins for Hyades and Praesepe (Fig. 6.5). This discrepancy could be explained by the rotation period distribution in that bin.
In Fig. 6.8 we show rotation periods derived from K2 light curves for the Pleiades [Reb+16], the Hyades and Praesepe [Dou+19], to illustrate the $P_{\rm rot}$ distributions that correspond to our $T_{\rm eff}$ bins. In all but the 3500 − 3750 K temperature bin the rotation period distributions of the Hyades and Praesepe were similar, while the Pleiades showed shorter periods on average. Only in this bin the rotation periods found in the Hyades and the Pleiades were more alike than in the Hyades and Praesepe. In this temperature regime, the majority of Praesepe stars had rotation periods > 10 d, while in the Hyades and the Pleiades rotation periods were more evenly distibuted in the 0.3 − 30 d range. A distinct transition in stellar activity was previously detected in various observables, including flaring luminosities and amplitudes, at the $P_{\rm rot}$ = 10 d boundary [Lu+19; Ste+16]. Assuming that Praesepe is truly older than the Hyades (see [Dou+19] for an indication of the opposite), the rotation period distribution appears to have made a jump between the ages of Hyades and Praesepe, and the flaring rates echoed this decrease. Considering the small sample size for the Hyades in this $T_{\rm eff}$ bin, a large spread in flaring activity levels is a second conceivable interpretation. In both cases, the results suggest a transition that occurred at the 10 d boundary in the 3500 − 3750 K regime around the ages of the two clusters. A similar transition would then have already passed for hotter stars (Fig. 6.5 f.), and has yet to happen in lower mass stars (Fig. 6.5 b. and c.).

6.4.5 A mass- and rotation-dependent flaring activity transition: Leaving the saturated regime

To further explore the dependence of the flaring-age-mass relation on stellar rotation, we compared the distributions of rotation periods to $\beta_{100\rm s}$ in different age and $T_{\rm eff}$ bins (Fig. 6.9). Up to Praesepe age, all stars below 3500 K showed a gradual decline in rotation speed with increasing $T_{\rm eff}$ while the flaring activity declined only marginally. These stars can be interpreted as residing in the saturated activity regime that is populated by young and rapidly rotating stars. This is consistent with age-rotation studies of surface magnetic field strengths [Vid+14], and a number of activity indicators, including coronal X-ray emission [Piz+03; Wri+11], and chromospheric Hα and Ca II H and K lines [MH08; New+17;

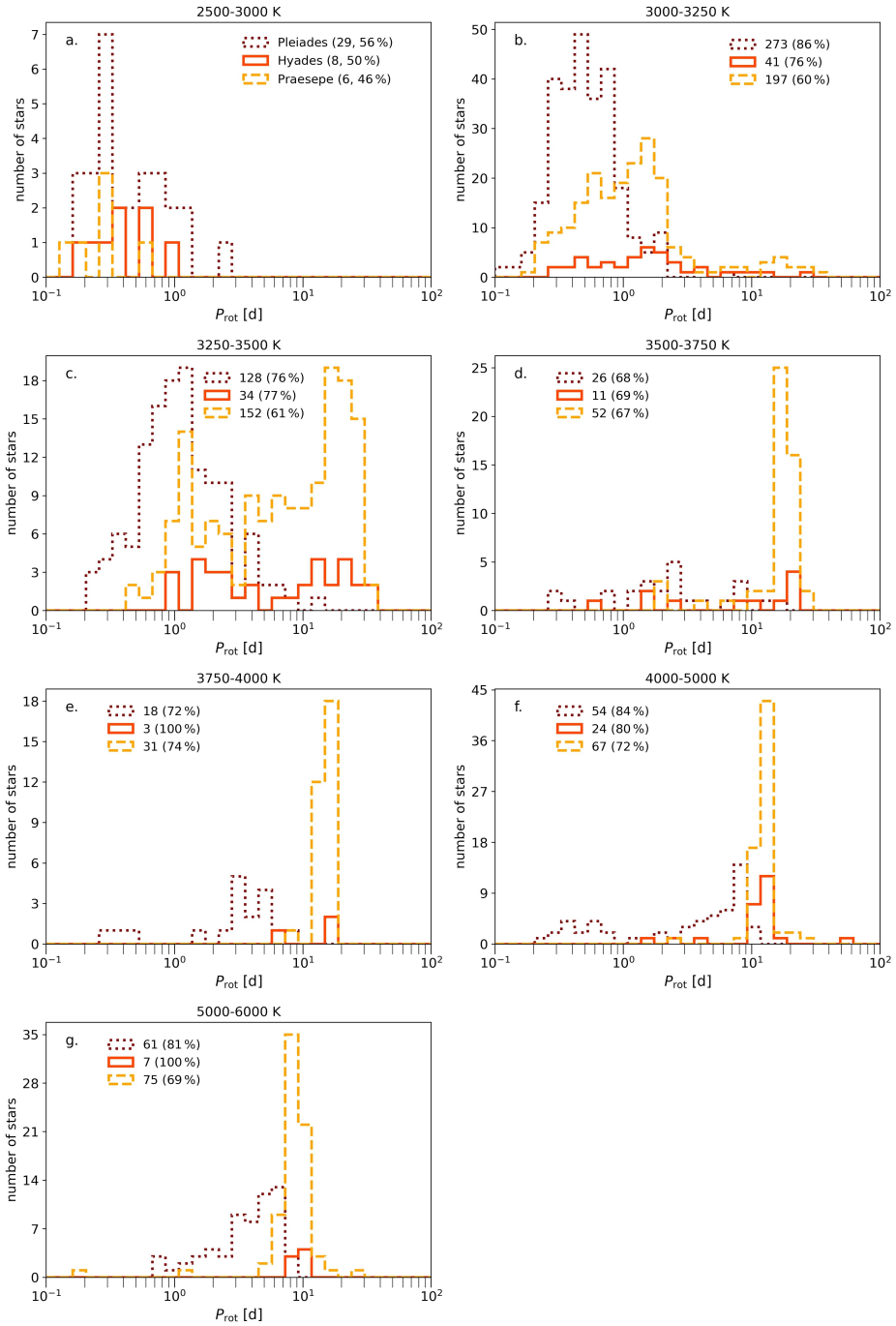

Figure 6.8: Rotation histograms for the cluster members that were searched for flares and had measured rotation periods P_{rot}. Rotation periods were taken from [Dou+19] for the Hyades (orange solid) and Praesepe (yellow dashed), and from [Reb+16] for the Pleiades (maroon dotted). The numbers and percentages in the legends in each panel denote the number of stars for which periods were given, and what fraction of the full sample that represented, respectively. The period distributions of Praesepe and the Hyades are consistent in all T_{eff} bins but the 3500 – 3750 K bin, where the distribution of the Hyades appears more similar to the younger Pleiades than the same-age Praesepe. However, the sample size for the Hyades in that bin is small (11 stars).

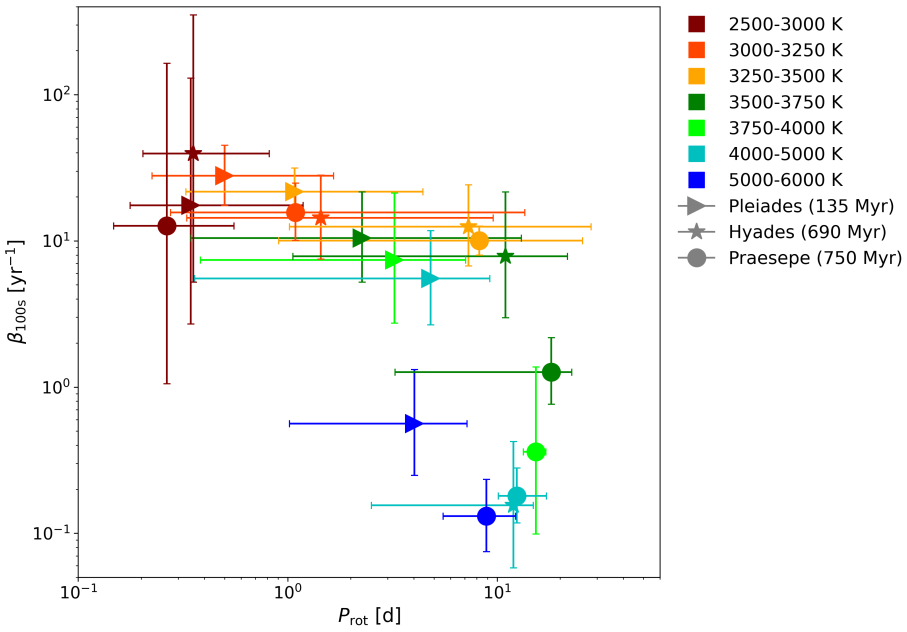

Figure 6.9: Flaring activity measure β_{100s} as a function of stellar rotation period P_{rot} (median value, and 5th to 95th percentiles of the distributions in Fig. 6.8). The saturated branch at high rotation rates and $\beta_{100s} \gtrapprox 5$ yr^{-1}, and the drop in activity around the 10 d boundary resemble analogous distributions for X-ray, Hα, and surface magnetic field strength. The additional dimensions are age (different symbols representing three open clusters), and T_{eff} (colors). At the ages of Hyades and Praesepe, the $T_{eff} \sim 3500 - 3750$ K stars are appear to be in the process of leaving the saturated branch, while the $T_{eff} \sim 3750 - 5000$ K stars already showed low activity levels. See Section 6.4.5 for a detailed discussion.

Wes+15]. In the 3500 – 3750 K temperature bin (see previous section), the median rotation rates changed as moderately as in the cooler bins. The Pleiades continued to spin down and gradually decreased in flaring activity. However, despite their similar ages, the stars in the Praesepe sample spun down more than those in the Hyades, and were lower in β_{100s} by almost an order of magnitude. At higher temperatures up to 5000 K, the Pleiades remained on the saturated activity branch declining only gradually, while both Hyades and Praesepe reappeared at much lower activity levels, indicating a mass-dependent activity transition that had occurred in the meantime.

In the highest mass bin (5000 – 6000 K) the stars in Praesepe remained at similar rotation rates and activity levels as the 4000 – 5000 K stars. The highest mass Pleiades appeared to be an outlier with intermediate flaring rates at relatively short rotation periods. Solar-type stars at ZAMS are expected to show a wide spread in activity. In the simulations by [JBG21], the slow and medium solar-type ZAMS rotators have left the saturated branch at 135 Myr, while the fast rotators remain highly active. As in the 3500 – 3750 K case, β_{100s} does not capture this intrinsic spread, but assumes similar activity levels for all stars in a given T_{eff}-age bin. As a consequence, we measured intermediate flaring rates instead of spanning the range

Table 6.4: Possible binary configurations for flaring old stars.

cluster	EPIC	median SpT	binary
M67	211434440	K1	K2 + M5.5
Ruprecht 147	219601739	G8	K1 + M6
Ruprecht 147	219610232	K0.5	K2 + M5.5
Ruprecht 147	219591752	M3	M3.5 + M3.5

from high to low activities. We expect that this limitation applies to a much lesser degree to the other $T_{\rm eff}$ and ages, because of the general agreement between the nearly coeval Hyades and Praesepe, and because the stars in each of these bins are predicted to be found either completely on the saturated branch, or to have left it without exceptions [JBG21].

6.4.6 M67 and Ruprecht 147: Possibly binaries

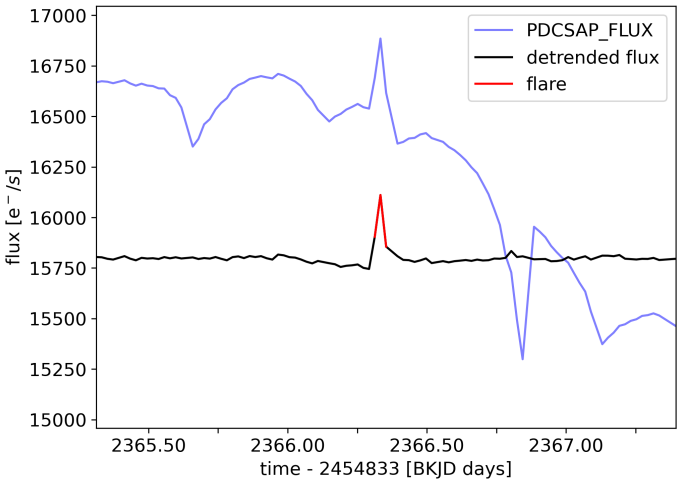

Figure 6.10: Single confirmed flare candidate in M67 on the K1 dwarf EPIC 211434440 (red line). Blue: Pre-search Data Conditioning (PDCSAP) flux, that is, the light curve before K2SC de-trending. Black: De-trended light curve that was searched for flares with `AltaiPony`. The amplitude of the flare is 2%, and the energy emitted in the Kepler band is $E_{\rm Kp} = 6.25 \cdot 10^{33}$ erg. The flare is small enough to be barely detectable, so its energy is uncertain, and most likely underestimated due to the low time sampling of the light curve.

We found eight and four flaring members in M67 and Ruprecht 147, respectively. Upon close inspection the majority were false positives, or occurred on multiple systems or evolved stars that were not properly filtered out. Most flares in these old clusters were detected on RS CVn binaries, cataclysmic binaries, spectroscopic binaries, and red giant stars. Excluding all these, we were left with one flare in M67 on an early K dwarf (Fig. 6.10). In Ruprecht 147, we excluded EPIC 219426848, a double-lined spectroscopic binary [Cur+13], and so narrowed down the list to a flare on a G8 star in Ruprecht 147, and four flares each on a K0.5 and an M3 star. For these stars, the multiplicity status was unknown. The uncertainty about the

stellar properties suggests a range of possible masses of the system. The mass budget could be calculated from the uncertainties on their radii R_* using the relations from [Eke+18]. In all cases, it was large enough that the stars in question could in principle be binary stars with mid-M dwarf companions that were too faint to be detected. We calculated hypothetic binary pairs for the cases where the primary mass was the smallest possible within 1σ on R_*. We give the median spectral type (SpT) of the target if it was a single star, and the spectral types of the possible binaries in Table 6.4.
After the manual inspection of the younger clusters we concluded that, while binaries and false positives were present in these clusters also, they were not the dominating source of flares. As multiplicity rates for low mass stars decrease from about 50% for F type stars [Rag+10] to 22% for L and T dwarfs [DK13], with M dwarfs showing somewhat higher multiplicity rates at about 27% [Win+19], we expect that the error introduced by unresolved binaries on our results was smaller for the cooler $T_{\rm eff}$ bins.

6.5 Discussion

The launch of the Kepler satellite in 2009 caused a surge in statistical flare studies, a trend that TESS will continue and expand. Comparing our results with these works [Lin+19; Lur+15; Rae+20; Shi+13b] and recent ground based surveys [CBH15; How+19] we found encouraging consistency but also some noteworthy discrepancies that we could not always trace back to their causes (Section 6.5.1). We discuss the disagreement between our FFDs and a gyrochronological model recently proposed for its parametrization as a function of mass and age (Section 6.5.2, [Dav+19]). We conclude the discussion with a reflection on the observational limitations of the representation of FFDs by power law distributions (Section 6.5.3), and the possibility of observing the maximum possible flare energy in our FFDs (Section 6.5.4).

6.5.1 Consistency with statistical flares studies

We found our results to be broadly consistent with previous work both on Kepler/K2 data, and ground based surveys in the optical regime, with some noteable exceptions. Fig. 6.11 presents the FFDs of the studies that we discuss in this context. Overall, we believe that the differences between individual results were rooted in a combination of astrophysical properties like age, mass, rotation speed, and the influence of selection criteria on the respective samples.
The FFDs of two fast rotating (0.26 and 0.71 days) M5 flare stars in an M5-M5-M8 triple system [Lur+15] were consistent with the FFDs of flares in the Pleiades, Praesepe, and Hyades in the 3000 – 3250 K bin. We also found that the FFDs of nearby K and M dwarfs, observed by Kepler/K2 within 200pc and 100pc, respectively, fell in the range between the Pleiades and Hyades/Praesepe FFDs in our sample [Lin+19].
The frequency of superflares at 10^{34} erg in the most active G-dwarfs and Sun-like stars in Kepler was once in 10–100 days, and every 440 years on average solar-type stars [Shi+13b]. Benchmarking on the flare detected on a K1 dwarf in M67 in the G to early K bin (5000-6000

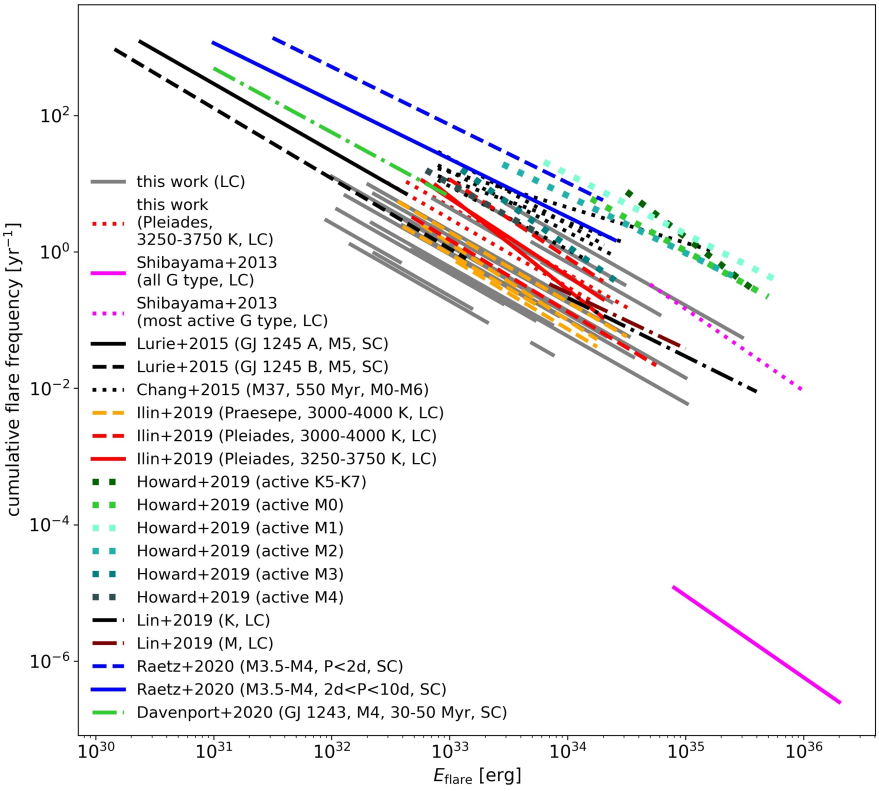

Figure 6.11: Comparison of FFDs found in different flare studies. Gray lines: FFDs from this work. The one-flare sample for 5000-6000 K in M67 is indicated as the shortest visible gray line. Red solid lines, and red and orange dashes: K2 long cadence light curves study of the Pleiades and Praesepe in four $T_{\rm eff}$ bins from 3000 to 4000 K each [Ili+19]. Magenta line and dots: Superflares on all G dwarfs in Kepler, and its most active subsample [Shi+13b]. Black line and dashes: Two M5 stars in an M5-M5-M8 triple system observed by Kepler [Lur+15]. Black dots: Flare study based on an MMT survey of the ~ 550 Myr old open cluster M37 [CBH15]. Dots in green and blue: Evryscope all-sky flare search on late K to mid M dwarfs [How+19]. Black and brown dash-dotted lines: K2 long-cadence study of K and M dwarfs within 200pc and 100pc [Lin+19]. Dark blue line and dashes: K2 short cadence light curves of M3.5-M4 dwarfs with known rotation periods below 2 d and between 2 and 10 d, respectively [Rae+20]. Green dash-dotted line: The 30 − 50 Myr old M4 flare star GJ 1243 exhibited a constant flaring activity for over a decade of intermittent space based observations with Kepler and TESS [DMH20]. In the studies that are based on Kepler or K2 observations, "SC" and "LC" denote the use of 1 minute and 30 minute cadence time series, respectively.

K), and accounting for the fraction of the total flare energy that the Kepler passband covers at a flare temperature of 10 000 K, we found the flaring rate at this energy to amount to about once every 100 years. Doing the same for the Pleiades stars yielded that ZAMS G to K dwarfs flare once per year at 10^{34} erg. Our young G-K stars therefore were less active than the active G dwarfs in [Shi+13b], while our solar-age G-K dwarfs appeared more active than in their results.

[How+19] monitored superflares on cool stars with bolometric energies above 10^{33} erg and

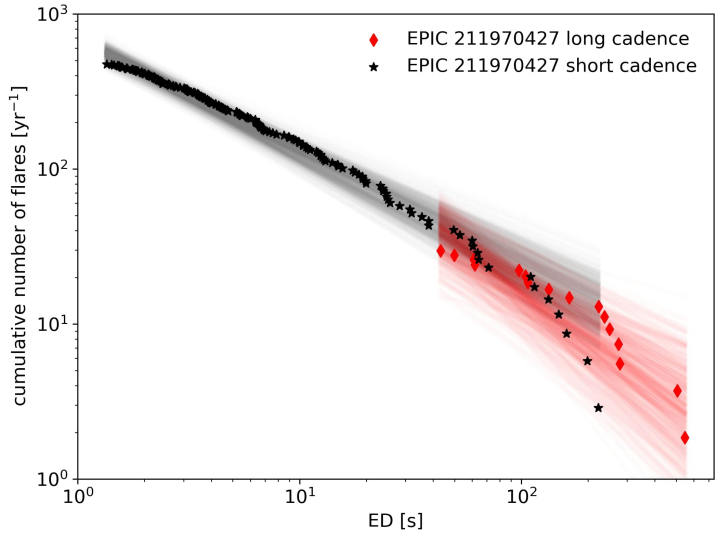

Figure 6.12: FFDs in *ED* for EPIC 211970427, an M3 dwarf in Praesepe that was observed in both short 1 minute cadence (campaigns 5, 18) and long 30 minute cadence (campaigns 5, 16, and 18). We detrended, and searched both light curve types for flares using the method described in Section 6.3.1. Red diamonds indicate flares found in the long cadence light curves, black stars are flares from the short cadence light curves. The red and black lines were randomly sampled from the posterior distributions of the power law fits to the long and short candence FFDs, respectively (see methods in Section 6.3.4).

up to 10^{36}erg. They found power law exponents $\sim$ 2 in FFDs resolved by spectral type. The activity levels for spectral types K5 to M4 were on average higher than in our sample. However, [How+19] only included stars that exhibited flares (active stars) into their FFDs, whereas we also accounted for the observing time of stars where no flares had been detected. Photometric flares observed by the MMT 6.5 telescope [Har+08] in the $\sim$ 550 Myr old open cluster M37 [CBH15] appeared on average more active than the Pleiades in our study for spectral types M0-M6. This could imply that flaring activity in these low mass stars peaked not at Pleiades age but at a later evolutionary stage.
Similarly, [Rae+20] pointed out that their fast rotating M1.5-M4.5 dwarfs appeared more active than the results for the Pleiades in [Ili+19] in the 3250 – 3750 K range. Our revised results remained consistent with [Ili+19] (Fig. 6.11). Both samples were comprised of flares with periods below 10 d. Rotation periods $P_{\rm rot}$ were given for 100% of the sample in [Rae+20], and for > 68% in our Pleiades subsample (Fig. 6.8).
We consider three plausible reasons for the discrepancy here. First, the M1.5-M4.5 dwarfs in [Rae+20] could be at an age at which stars show higher flaring activity than stars with the same rotation periods in the Pleiades. Second, there may be selection effects in the short cadence sample in [Rae+20] as compared to our sample. Targets for short cadence observations in K2 were not selected randomly from the underlying stellar population, but were filtered for a variety of properties that biased the final selection toward more active

stars. Third, our 3250 − 3750 K bin corresponds to spectral types M1-M3.5 rather than to M1.5-M4.5 [PM13]. So the $T_{\rm eff}$ bins chosen in [Rae+20] encompassed later, and therefore more active, spectral types. A resolution of this discrepancy must also take into account that the results for our Praesepe sample in the 3250 − 3750 K range were consistent with the slow rotators ($P_{\rm rot} \sim 32$ d) in [Rae+20].
Finally, we note that the difference in time sampling between our study (30 minute candence), and 1 minute cadence in [Rae+20] can most likely be ruled out as an explanation for the discrepancy. In Fig. 6.12, we show an example that illustrates that short cadence light curves used in [Rae+20], and long cadence light curves studied here yielded FFDs that were consistent withing uncertainties. There were no exactly matching events in the FFDs although a subset of the short cadence flares was detected in long cadence also for two main reasons. First, in long cadence, flare energy was typically underestimated [Yan+18]. Second, smaller flares were merged together if they occurred within a sufficently short time period. What looked like one flare in long cadence was sometimes resolved into two or more flares in short cadence.

6.5.2 Gyrochronological parametrization of flare frequency distributions

[Dav+19] derived a parametrization of the FFD arguments α and β as a function of mass and age using the Kepler flare catalog [Dav16], rotation periods from [MMA14], and the [MH08] gyrochrone model. We show the model power laws in Fig. 6.5 alongside our results. While the power law exponents appeared consistent with our estimates, the activity level in our sample was much lower than predicted by the model. A deviation was expected as the model was not designed to predict absolute ages. [Dav+19] noted a sample bias in their study toward more active stars. As discussed by the authors, their model overpredicted the superflaring rate of the average Sun-like sample from [Shi+13b] and more resembled the rate for their most active subsample. Moreover, the model was not designed to be applicable to flaring activity in the saturated regime of fast young rotators [Jac+20]. With our data we quantify the overestimation of flaring rates to be one to two orders of magnitude. Our results also suggest that the model overpredicts the activity level for old stars more than for younger stars (Fig. 6.5). We propose that future models include the mass-dependent drop in activity at $P_{\rm rot} \approx 10$ d (see Section 6.4.5), for instance, using a piecewise definition of the setup in [Dav+19] for stars with rotation rates above and below the 10 d threshold.

6.5.3 Universality of the power law exponent α

We found values for α to range from 1.84 to 2.39 (Table 6.3), with smaller numbers of flares in a FFD usually leading to values closer to the margins of this range, and FFDs that consisted of more than 50 flares being better constrained with $\alpha \sim 1.89 - 2.11$. Taking into account uncertainties and systematic errors resulting from the use of different power law fitting methods [MK09], the power law exponent $\alpha \sim 2$ appears to be similar for the majority of studies on flare statistics in the literature so far, irrespective of spectral type or age. To

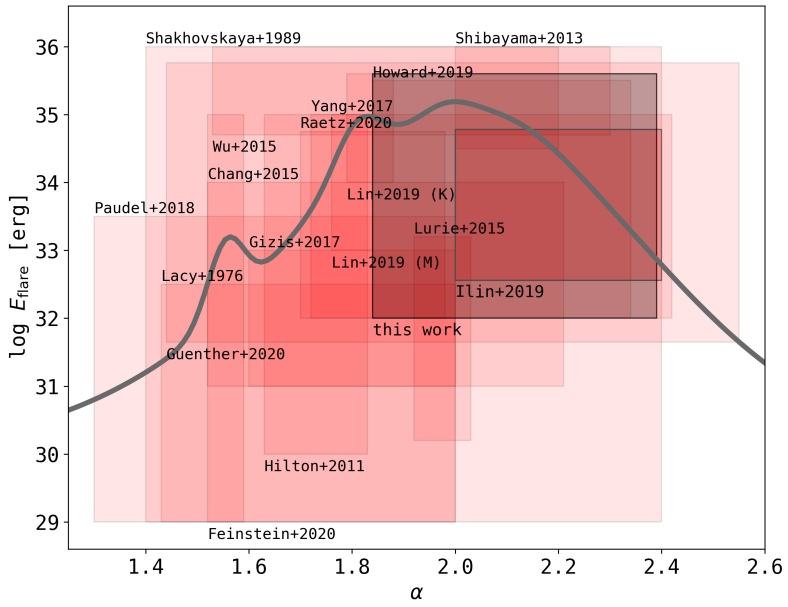

Figure 6.13: Literature overview over power law fits to FFDs. Red rectangles indicate the energy range in which flares were detected (height), and the range of values determined for the power law exponent α (width) including quoted uncertainties and superimposing the ranges for α from multiple FFDs if any. The references are anchored to the upper or lower left corner of the respective rectangle. The gray rectangle refers to this study. The gray line depicts the superposition of these results, representing each by a Gaussian fit with the range used as standard deviation, and weighted by the square root of the number of flares found in each study. [Ili+19] is shown with a dark outline. See Section 6.5.3 for details on the quoted works.

illustrate this, we searched the literature for studies where power laws were fit to FFDs of flares in the optical regime using different methods (Fig. 6.13).
[LME76] pioneered in statistical flare studies using observations of eight UV Ceti stars. [Sha89] analyzed monitoring data from several dozen active early K to late M dwarfs in the solar vicinity, the Orion, the Pleiades, the Hyades, and the Praesepe cluster. A number of studies focused on solar-type and G dwarfs stars in Kepler [Shi+13b; WIH15]. [Hil11] derived α from ground-based observations of M dwarfs. [Lur+15] determined α from Kepler short cadence light curves of two active M5 dwarfs in Kepler. [Yan+17] followed up on [Dav16] in searching the entire Kepler catalog for flares. [Lin+19] (M) and (K) were based on nearby M and K dwarf flares in K2 long cadence light curves. [Rae+20] studied short cadence M dwarfs with rotation periods in K2. [Giz+17] constructed an FFD for 22 flares on an M7 dwarf. [Pau+18] studied M6-L0 dwarfs in K2 short cadence data. [How+19] found over 500 superflares on 284 stars in the framework of the Evryscope all-sky survey. Photometric flares were observed by the MMT 6.5 telescope [Har+08] in the ~ 550 Myr old M37 open cluster [CBH15]. [Gün+20] took a first look to α as derived from stars observed during TESS Cycle 1. From their work we only use α derived from stars with 20 or more flare detections in Fig. 6.13. Finally, [Fei+20] used a convolutional neural network setup to detect flares in

nearby young moving groups, open clusters, OB associations, and star forming regions with ages between 1 and 800 Myr in TESS, finding relatively flat FFDs compared to [Gün+20]. While most studies consistently found values somewhat above or below $\alpha \approx 2$, the comparison would reveal unresolved systematic errors in all these studies, including our own, if α was truly universal for all FFDs. The determination of α using different methods without reliable uncertainty estimates across different studies makes it difficult to assess whether the spread in α from about 1.4 to 2.5 is physically motivated or not.
Addionally, for both low and high flare energies, the detection of flares is usually incomplete or contaminated. This is caused by finite time sampling, cosmic ray impact, and scatter in the light curve at the low end, and finite observation time at the high end (see Section 6.3.5). As long as these methodological and observational caveats apply, to answer the question about the universal nature of α proves very challenging.

6.5.4 Maximum flare energy

Spots can survive on the stellar surface from a few days to nearly a year [Dav15; Nam+17]. Complex spot geometry is correlated with the stongest X-class flares on the Sun [STZ00; Tor+17]. These observations support the idea that flares are associated with the presence of certain types of starspots, or more generally, certain types of active regions. Since we expect that there is a maximum flare energy a spot can produce, the underlying power law relation must break above some maximum value in any FFD. We tested a possible truncation of our FFDs using the Kolmogorov-Smirnov test for consistency with a power law distribution, followed by the exceedance statistic to test for a truncation of this power law as suggested by [MK09]. While most FFDs with $\geqslant 50$ flares were consistent with a power law distribution, we found no evidence for truncation in any of the $T_{\rm eff}$-age bins. This would imply that we did not sample the highest possible energies. Such a conclusion is plausible because flare energies higher than our observed maximum flare energies were detected on other stars (see Fig. 6.11, [How+19; Lin+19; Shi+13b; Tu+20]). In a few FFDs, we still noted a deviation from a single power law at the high energy end. This effect could be caused by the combination of stars with different flaring rates into a single distribution, which would violate the assumption of similarity between the stars in each bin (see Section 6.3.4).

6.6 Summary and conclusions

In this study, we investigated how flaring activity unfolded for different age and $T_{\rm eff}$ ranges anchoring the age to the membership in five open clusters. We found flaring activity to decrease from mid M dwarfs to G stars, and from ZAMS to solar age, except for stars later than M5, where activity increased from ZAMS to 690 Myr. We found indications of a mass- and rotation-dependent threshold age, above which stars depart from the saturated flaring activity branch.
Using multiple cluster membership studies we selected for high probability members, and drew from a host of multiband photometry catalogs and Gaia astrometry to determine $T_{\rm eff}$ and stellar luminosities. Keeping only targets with well-determined mass and age we

proceeded to search 3435 K2 long cadence light curves obtained for these stars throughout the K2 mission. We applied the open source software `K2SC` to remove rotational variability and instrumental effects. We developed the open source software `AltaiPony`, and used it to automatically detect and determine the properties of flare candidates. We vetted all flare candidates manually and discussed various sources of false positives and incompleteness on both the high and the low energy end of the FFDs. All in all, we searched 2111 stars in five open clusters, and found 3844 flares. Most flares originated in the Pleiades and Praesepe, several hundred were found in the Hyades, a handful in Ruprecht 147, and only one flare candidate appeared on a K1 dwarf in M67, although several flares were found in binary systems in both Ruprecht 147, and M67.

We fit power law functions to the FFDs of flares from stars in different age and $T_{\rm eff}$ bins. We found that the power law exponent α was consistent with previous work, and caution against interpreting apparent trends, especially when comparing across different studies.

Our results indicated that flaring activity declined with age, and did so faster for higher mass stars. We provide the measured flaring rates in Table 6.3 as a contribution to the endeavor of mapping the flaring-age-mass relation from pre-main sequence to main sequence turn-off, and from the onset of an outer convection zone in F type stars to the coolest brown dwarfs.

Our findings paint a picture of clear trends in the flaring evolution of GKM dwarfs on the main sequence. Regardless of varying methods employed for flare search and FFD analysis in previous studies we found encouraging consistency in flaring rates with both Kepler and K2 based work, and ground-based surveys. We noticed some differences, which we could not always resolve as being either systematic or astrophysical. We suggest that discrepancies between our results and flare studies that used rotation periods for their age estimates [Dav+19; Rae+20] could be explained by sample selection bias but may also point to limitations of rotation periods as an age indicator. Noteably, we found the flaring activity in M1-M2 dwarfs in Hyades and Praesepe to differ significantly despite their similar ages, while it was consistent for the two clusters for both higher and lower mass stars. We interpret this as a sign of a mass- and rotation-dependent transition from saturated to unsaturated activity levels: The flaring rates of higher mass stars at somewhat lower rotation periods had already declined substantially, while lower mass stars still resided in the saturated activity regime, and were spinning faster. We conclude that some discrepancies between our results and flare studies that used rotation periods for their age estimates could be explained by sample selection bias toward more active stars, but others may hint at limitations to using rotation as an age indicator without additional constraints from stellar activity.

The impact of flares from low mass stars on rocky exoplanets in the habitable zone is a key component to understanding the space weather environments in which life may develop on these objects. Flares are promising candidates for being a major source of high energy radiation [Air+20] that can fertilize the emergence of biological life or impede it if overdosed; it may sweep away or alter the composition of these planets' atmospheres, and even evaporate oceans full of surface water [SBJ16; Til+19]. Age-calibrated FFDs that trace the entire lifespan of planet hosting stars are indispensable ingredients to the assessment of planetary atmosphere survival under repeated flaring.

Although Kepler and K2 data were already used in more than 2 400 publications in 2018,

the public archive was still considered understudied [Bar+18]. It will remain a benchmark mission not only for exoplanet search, but also for various subfields in stellar astronomy, and flaring activity research, in particular. Results from the first year of operations of TESS indicate that the light curve quality delivered by the mission so far was well suited for statistical flare studies, too [DRD20; Fei+20; Gün+20]. The expected lifetime of TESS could be up to 20 years, in which case the number of high quality flare samples will soon outclass Kepler and K2 as the primary source of flares. The mission will vastly expand the treasury of light curves, leaving us optimistic that this work was only a first step toward a comprehensive flare rate evolution model.

Acknowledgements

EI is thankful to the anonymous referee for their detailed, constructive, and respectful report, Michael Gully-Santiago for invaluable advice in the development of `AltaiPony`, Ann-Marie Cody for helpful comments on K2 data, Nikoleta Ilić for assisting with code review, and Klaus Strassmeier for helpful remarks on the manuscript. EI acknowledges support from the German National Scholarship Foundation. JRAD acknowledges support from the DIRAC Institute in the Department of Astronomy at the University of Washington. The DIRAC Institute is supported through generous gifts from the Charles and Lisa Simonyi Fund for Arts and Sciences, and the Washington Research Foundation. This paper includes data collected by the Kepler mission and obtained from the MAST data archive at the Space Telescope Science Institute (STScI). Funding for the Kepler mission is provided by the NASA Science Mission Directorate. STScI is operated by the Association of Universities for Research in Astronomy, Inc., under NASA contract NAS 5–26555. We made use of data products from the Two Micron All Sky Survey, which is a joint project of the University of Massachusetts and the Infrared Processing and Analysis Center/California Institute of Technology, funded by the National Aeronautics and Space Administration and the National Science Foundation. The Pan-STARRS1 Surveys (PS1) and the PS1 public science archive have been made possible through contributions by the Institute for Astronomy of the University of Hawaii, the Pan-STARRS Project Office, the Max-Planck Society and its participating institutes, the Max Planck Institute for Astronomy, Heidelberg and the Max Planck Institute for Extraterrestrial Physics, Garching, The Johns Hopkins University, Durham University, the University of Edinburgh, the Queen's University Belfast, the Harvard-Smithsonian Center for Astrophysics, the Las Cumbres Observatory Global Telescope Network Incorporated, the National Central University of Taiwan, the Space Telescope Science Institute, the National Aeronautics and Space Administration under Grant No. NNX08AR22G issued through the Planetary Science Division of the NASA Science Mission Directorate, the National Science Foundation Grant No. AST-1238877, the University of Maryland, Eotvos Lorand University (ELTE), the Los Alamos National Laboratory, and the Gordon and Betty Moore Foundation. This research also made use of the Python packages `numpy` [Har+20], `pandas` [Reb+22], `astroML` [Ive+14; Van+12], `astropy` [Rob+13], `specmatch-emp` [YPB17], `bokeh` [Bok18], the cross-match service provided by CDS, Strasbourg; IMCCE's SkyBoT VO tool; data from the European Space Agency (ESA) mission *Gaia* (https://www.cosmos.esa.int/gaia),

processed by the *Gaia* Data Processing and Analysis Consortium (DPAC, https://www.cosmos.esa.int/web/gaia/dpac/consortium). Funding for the DPAC has been provided by national institutions, in particular the institutions participating in the *Gaia* Multilateral Agreement.

6.7 Appendix

6.7.1 Membership probabilities

To match catalogs on RA and declination we used the `astroML.crossmatch` tool for Python [Van+12].
For the studies with classifiers we assigned membership probabilities as follows. In [Gon16]:

$$\begin{aligned} p(M(\text{member})) &= 0.9, \\ p(BM(\text{binary member})) &= 0.9, \\ p(N(\text{nonmember})) &= 0.1, \\ p(SN(\text{single nonmember})) &= 0.1, \\ p(BN(\text{binary nonmember})) &= 0.1, \\ p(U(\text{unknown member})) &= 0.5. \end{aligned}$$

In [Cur+13]:

$$\begin{aligned} p(Y(\text{highest confidence member})) &= 0.9, \\ p(P(\text{possible/probable member})) &= 0.7, \\ p(N(\text{not likely/nonmember})) &= 0.7, \\ p(B(\text{photometry consistent with blue stragglers})) &= 0.0. \end{aligned}$$

In [Reb+17]:

$$\begin{aligned} p((\text{best})) &= 0.9, \\ p((\text{ok})) &= 0.6, \\ p((\text{else})) &= 0.1. \end{aligned}$$

Members from [Dou+17; Reb+16]; and [Col+18a] were assigned $p = 0.9$ if they appeared in the final catalog.
Table 6.5 gives an overview over different membership catalogs. Figure 6.14 shows membership probability histograms of the final sample broken down by membership source.

Table 6.5: Membership catalogs used in this work.

source	type	clusters covered	notes
[Cur+13]	classifier	Ruprecht 147	
[Dou+14]	probability	Hyades, Praesepe	meta study
[Gon16]	classifier	M67	
[Reb+16]	members list	Pleiades	meta study
[Reb+17]	classifier	Praesepe	meta study
[Dou+17]	members list	Praesepe	meta study
[Col+18a]	members list	Hyades†, Ruprecht 147, Pleiades, Praesepe	Gaia DR2
[Can+18]	probability	Ruprecht 147, Pleiades, Praesepe	Gaia DR2
[Gao18]	probability	M67	Gaia DR2
[Rei+18b]	probability	Hyades†	Gaia DR1
[Oli+18]	probability	Pleiades	Gaia DR2, DANCe
[Oli+19]	probability	Ruprecht 147	Gaia DR2, DANCe

Meta study: See references in the studies for additional membership information. DANCe: DANCe membership study project. Gaia DR1: The study used data from the first data release [Col+16a] of the Gaia mission [Col+16b]. Gaia DR2: The study used data from the second data release [Col+18b]. †Positions for Hyades were propagated to epoch 2000 using Gaia proper motions.

6.7.2 Cluster parameters

We compiled various age, distance, and metallicity values from the literature for the clusters in this study. Table 6.6 shows that most studies independently arrived at similar results for all our clusters. The adopted parameters are emphasized, and were chosen based on consistency with prior work, uncertainties provided with the results and the data used for the study (newer catalogs were preferred).

6.7.3 Solar system object detection with SkyBot

K2 photometry was heavily affected by crossings of solar system objects (SSOs), which consequently produced mimicking flare profiles in the light curves [Sza+15]. Independently, two of us visually verified the SSO-nature of 42 flaring light curve events by inspecting their corresponding TargetPixelFiles (TPF) using `lightkurve` [Lig+18]. Except for one occasion, we found all events to be known SSOs, both in the visual survey and automatically using SkyBot [Ber+16]. Subsequently, we ran SkyBot on the remaining catalog of flares to remove other false positive events caused by known SSOs. Visual inspections of TPFs were carried out for any SSO detected within 30" of its target star at mid-event time. This yielded additional 103 contaminated signals distributed among three subgroups, (i) 77 unambiguous SSO-contaminants verified through `lightkurve` (ii) 18 faint SkyBot-detections ($V \approx 20.4 - 23.8$) within ~ 3 pixels from the respective target star but visually unresolvable in the TPF, (iii) 8 occurrences in which both flare and SSO-crossing occurred during the given flare duration stated in the catalog. The latter should be dealt with caution due to a high risk of inaccurate catalog information altered by the presence of SSOs. Despite of discarding a total of 144 flare

Table 6.6: Non-exhaustive literature overview over OC parameters.

cluster	source	distance [pc]	age [Myr]	[Fe/H]
Pleiades	**adopted in this work:**	135.6	$135\pm^{25}_{25}$	-0.037 ± 0.026
	[Bos+19] [a]		$86.5\pm^{6}_{2.4}$	
	[Can+18]	135.6		
	[Gos+18]		$135\pm^{25}_{25}$	
	[Yen+18]	126.3	$141.3\pm^{170}_{100}$	
	[CD16]	139		
	[Net+16]			-0.01
	[Dah15]		$112\pm^{5}_{5}$	
	[Sch+15b]	130	120	
	[Con+14]			-0.037 ± 0.026
	[Mel+14]	136		
	[Bel+12]	135	125	
Hyades	**adopted in this work[b]:**		$690\pm^{160}_{100}$	0.13 ± 0.02
	[Col+18a]		$690\pm^{160}_{100}$	
	[Gos+18]		680	
	[Liu+16]			± 0.02
	[Net+16]			0.13
	[TJ05]			0.103 ± 0.008
	[SWP04]		650	0.15
	[Per+98]		$625\pm^{50}_{50}$	
Praesepe	**adopted in this work:**	185.5	$750\pm^{3}_{7}$	0.16
	[Bos+19]		$750\pm^{3}_{7}$	
	[Can+18]	185.5		
	[Gos+18]		590	
	[Yen+18]	183	$794\pm^{253}_{269}$	
	[Net+16]			0.16
	[Sch+15b]	187	832	
	[BRL13]			0.12
	[Bou+12]	160	630	
	[SWP04]	175	650	
Ruprecht 147	**adopted in this work:**	305	$2650\pm^{380}_{380}$	0.08 ± 0.07
	[Bra+18]			0.08 ± 0.07
	[Can+18]	305		
	[Col+18a]	309	$1995\pm^{404}_{257}$	
	[Tor+18]	283	$2650\pm^{380}_{380}$	
	[Cur16][c]			0.10 ± 0.02
	[Sch+15b]	270	1953	
	[Cur+13]	300	$3125\pm^{125}_{125}$	0.07 ± 0.03
M67	**adopted in this work:**	908	$3639\pm^{17}_{17}$	$-0.102 \pm .081$
	[Bos+19]		$3639\pm^{17}_{17}$	
	[Net+16]			0.03
	[Bar+16]		$4200\pm^{700}_{700}$	
	[Sch+15b]		$3428\pm^{147}_{72}$	
	[Con+14]			$-0.102 \pm .081$
	[Dia+12]	908	4300	
	[Öne+11]	880	4200	0.02
	[SWP04]		$4300\pm^{500}_{500}$	0.02 ± 0.06

[a] [Bos+19] noted some caveats for their isochronal ages, for which they used Gaia DR2 photometry. [b] We did not adopt a mean value for the Hyades distance because the cluster members are on average closer than 50 pc. [c] [Cur16] reanalysed HIRES spectra using an improved spectroscopic method as compared to [Cur+13].

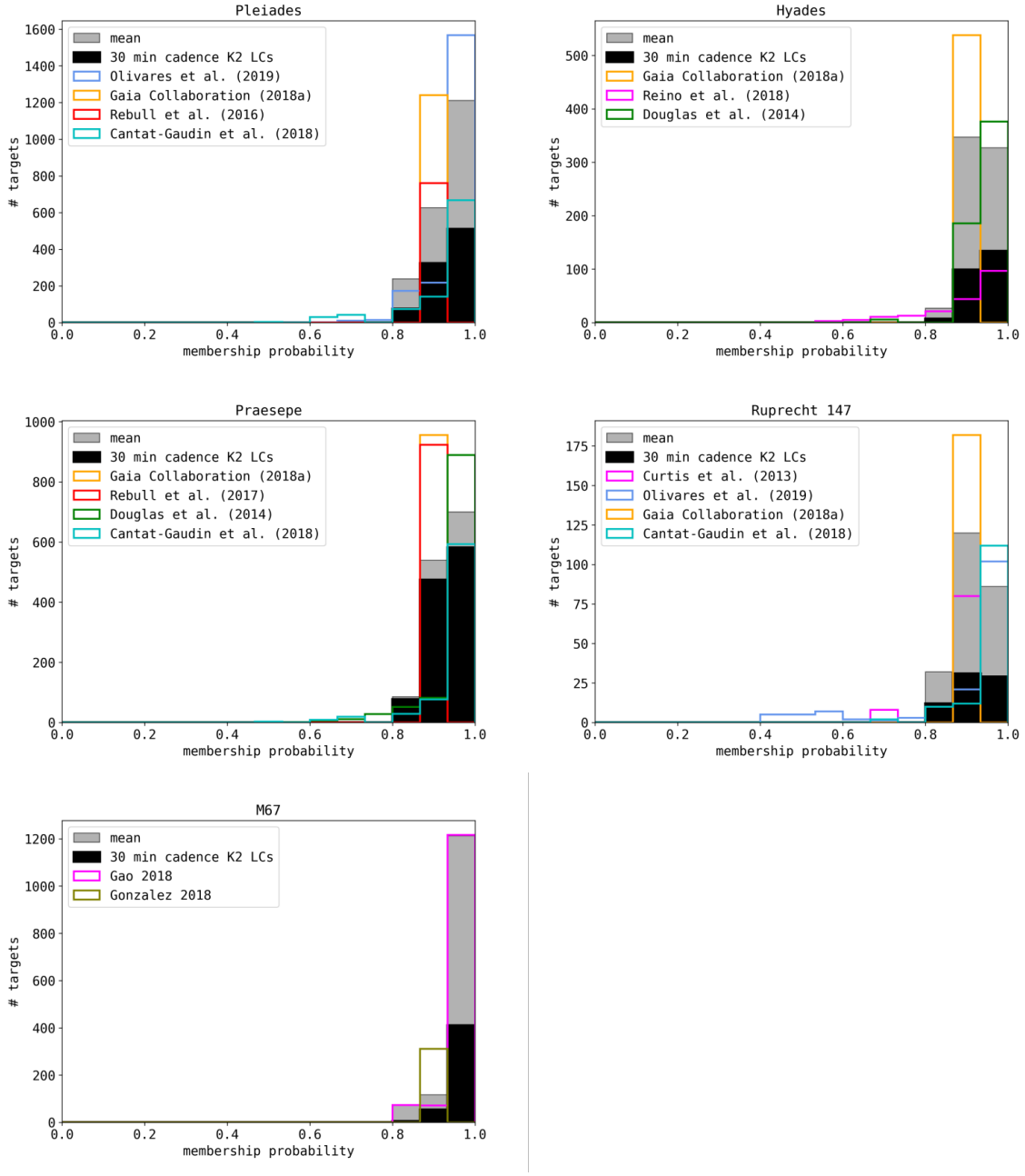

Figure 6.14: Open cluster membership histograms and selected targets. Each panel corresponds to the distribution of candidate members of the cluster indicated in the panel title. Membership catalogs are shown as step histograms (different colors). The mean membership probability distribution is a filled histogram (gray). For our study, we selected only stars with membership probabilities above 80% that were observed by K2 in long cadence mode (black filled histogram).

events, we expect additional contaminants by unknown SSOs to hide in the current sample.

This issue can partly be resolved by animating each TPF as demonstrated by Kristiansen et al. (in prep.).

6.7.4 Modified maximum likelihood estimatator

As a means to arrive at results efficiently, and as consistency check to the method derived from [Whe04] we fit α to the FFDs in ED and E_{Kp} space using a modified maximum likelihood estimatator (MMLE, [MK09]). The logarithm of the likelihood function $\mathcal{L}$ that had to be maximized was given by the authors in Eq. (8) in their manuscript:

$$\log \mathcal{L} = n \log(1 - \hat{\alpha}) - n \log\left(x_{\mathrm{max}}^{1-\hat{\alpha}} - x_{\mathrm{min}}^{1-\hat{\alpha}}\right) - \hat{\alpha} \sum_{i=1}^{n} \log x_i, \tag{6.9}$$

where x_i, x_{max}, and x_{min} were the detected flare energies, and the upper and lower limits for detection, respectively. n was the total number of flares. The estimate for α would be biased in practice because the value used for x_{max} would be the maximum energy that was measured, and not the underlying upper limit. The stabilization transformation suggested by the authors (Eq. (12) in [MK09]) was then applied to the solution for α to account for this bias:

$$\alpha = 1 + \frac{n}{n-2}(\hat{\alpha} - 1) \tag{6.10}$$

Using the MMLE method on the full sample of flares in E_{Kp} and ED space we obtained $\alpha_{\mathrm{erg}} = 1.97$ and $\alpha_{\mathrm{s}} = 2.06$, respectively, indicating a marginally flatter power law than the adopted [Whe04] model ($\alpha_{\mathrm{erg}} = 1.98$, $\alpha_{\mathrm{s}} = 2.1$).

7 Giant white-light flares on fully convective stars occur at high latitudes

Ilin, E.; Poppenhäger, K.; Schmidt, S. J.; Järvinen, S. P.; Newton, E. R.; Alvarado-Gómez, J. D.; Pineda, J. S.; Davenport, J. R. A.; Oshagh, M; & Ilyin, I.
Monthly Notices of the Royal Astronomical Society, Volume 507, Issue 2, Pages 1723–1745 (2021).
DOI: 10.1093/mnras/stab2159

Abstract

White-light flares are magnetically driven localized brightenings on the surfaces of stars. Their temporal, spectral, and statistical properties present a treasury of physical information about stellar magnetic fields. The spatial distributions of magnetic spots and associated flaring regions help constrain dynamo theories. Moreover, flares are thought to crucially affect the habitability of exoplanets that orbit these stars. Measuring the location of flares on stars other than the Sun is challenging due to the lack of spatial resolution. Here we present four fully convective stars observed with the Transiting Exoplanet Survey Satellite (TESS) that displayed large, long-duration flares in white-light which were modulated in brightness by the stars' fast rotation. This allowed us to determine the loci of these flares directly from the light curves. All four flares occurred at latitudes between 55° and 81°, far higher than typical solar flare latitudes. Our findings are evidence that strong magnetic fields tend to emerge close to the stellar rotational poles for fully convective stars, and suggest that the impact of flares on the habitability of exoplanets around small stars could be weaker than previously thought.

7.1 Introduction

Cool stars, i.e. stars with an outer convective envelope, are known to display a variety of magnetically driven phenomena, such as starspots, flares, and coronal mass ejections, collectively called magnetic activity [SZ08]. Sun-like stars possess a radiative core, and their magnetic activity is understood to be driven by a magnetic dynamo of the α-Ω type [Par55; Rob72]. For low-mass stars that are fully convective (spectral type M4V and later, [Sta+11]), a type of dynamo must be operating that does not require the presence of a radiative core. Surprisingly, the relation between rotation and magnetic activity for stars on either side of the fully-convective boundary is the same in both X-ray [WD16; Wri+18] and Hα [New+17] observations, suggesting that the dynamo operating in fully convective stars has a similar efficiency as the one in our Sun. One important difference between Sun-like stars and low-mass M dwarfs is that Sun-like stars spin down quickly, while M dwarfs remain fast rotators much longer [Irw+11; New+16]. Fast rotation fuels enhanced magnetic activity and

therefore frequent flaring, which is exploited in studies of stellar flares in M dwarf stars down to the bottom of the main sequence [Pau+18; RPS10; Sch+16a; Ste+06].

On the Sun, emerging magnetic fields drive flares, and stronger fields drive more energetic flares, making them highly localized markers of dynamic magnetic field concentrations [PF02]. In optical light curves, flares manifest as sudden brightenings that last between a few minutes and several hours. The onset of a flare is characterized by a fast rise in stellar flux which peaks in a sharp maximum, followed by an exponential, and then a more gradual, decay back toward the quiescent state.

The location of flares on the stellar surface constrains the surface field strength and topology, and tests predictions from stellar dynamo theories. On the Sun, the positions of large flares follow the cyclic latitude variations of sunspots [Zha+07]. The latter is known as the butterfly diagram, and is crucial to the understanding of the solar dynamo [Gne77]. Fast-rotating young solar-like stars and low mass stars have been predicted to form magnetic spots close to the rotational poles [Gas+13; Gra+00; SS92; Yad+15], and this prediction has been confirmed by spectroscopic and spectropolarimetric observations [e.g., Bar+15; Bar+17; Işı+18; Jär+07; Jär+08; Mar+06; SR98]. If these spots are co-spatial with large flares, they may be classified as intensely active regions with a dynamic local field configuration.

Differences in flaring region loci can also, at least partially, explain the variety seen in flare light curve morphologies. The convex shape of a flare light curve in X-rays on V773 Tau [Ski+97] could be well-described by rotational modulation. Later, effects of rotation and eclipses have been put forward as an explanation for unusual flare light curves multiple times [Joh+12; Mon+00; Ste+99]. However, only few examples of unambiguously located stellar flares exist to date [Pet+10; SF99; Wol+08].

Here, we present observations of four giant flares that occurred on fast-rotating fully convective dwarfs detected in photometry from the Transiting Exoplanet Survey Satellite (TESS, [Ric+15]). These flares are remarkable because they lasted longer than a full rotation period of the star so that the characteristic flare light curve was modulated by the flaring footpoint's movement in and out of view on the stellar surface. In Section 7.2, we describe our selection of both the stellar and the flare sample, and explain how we determined stellar properties for the promising candidates. In Section 7.7, we introduce a model of large flares with rotationally modulated light curves, show how we can use it to infer the latitude of the flaring regions, and discuss the assumptions made in the model. We fit our model to the observations, and present the inferred flaring region latitudes in Section 7.10. We briefly discuss quasiperiodic pulsations as an alternative model, place our results in the context of current research on stellar surface magnetic fields and dynamo thoeries for fully convective stars, and explore their implications for exoplanet habitability in Section 7.11. We conclude with a short summary and an outlook in Section 7.12.

7.2 Data

We started our systematic search for long-duration superflares on fully convective stars with the entire TESS archive. First, we used a color and brightness cut to restrict our search to fully convective nearby stars (Section 7.3). Second, we searched their 2 minute cadence

light curves for flares, and selected those candidate events where we could detect a rotation period that was shorter than the visible flare decay (Section 7.4). Our final sample consists of four giant flares on four stars with spectral types M5-M7 and rotation periods between 2.7 and 8.4 hours. Two stars in our sample lacked measurements of projected rotation velocity in the literature. For those we obtained high-resolution spectra (Section 7.5), so that we could determine the properties of all stars, including the inclination of the stellar rotation axis (Section 7.6).

7.3 Stellar sample and TESS light curves

We compiled a sample of nearby fully convective dwarf stars of spectral type M5 and later that were observed with TESS in the first two years of observations (Cycles 1 and 2). We selected bright stars with TESS magnitude < 15, which we crossmatched within 5 arcsec with nearby stars (parallax > 20 arcsec) in Gaia [Col+16b] DR2 [Col+18b]. We required good G and RP colour measurements, i.e., band flux divided by its error (`flux_over_error` in the Gaia catalog) > 10, and applied a color cut to select for fully convective stars. We applied $1.27 < G - RP < 1.75$, based on the relation between $G - RP$ band color and spectral type [Kim+19] derived from spectroscopically identified M and L dwarfs in the Sloan Digital Sky Survey [Yor+00] (SDSS). In total, we analysed 3,175 targets that were observed with TESS.

7.4 Flare sample

We searched for stars that displayed both long duration flares in their light curves, and clear rotational modulation outside of flares with a period shorter than the visible flare decay. Modulation of the flare itself was not a selection criterion. The typical TESS light curve spans one Sector, or 27 days, and we used only stars with 2-minute cadence data to ensure that we could fit the shapes of the superflares in sufficient detail. Our sample covers TESS Cycles 1 and 2, Sectors 1-26, encompassing both hemispheres above and below the ecliptic, that is, about 73 per cent of the whole sky [Ric+15]. We used the flare finding algorithm `AltaiPony` [Ili21] to detect flares on 6,291 light curves that were obtained for the 3,175 sample stars.

From the 17,646 automated flare detections we selected those with relative amplitudes above 20 per cent. For each light curve with at least one such flare we derived the Lomb-Scargle periodogram [Lom76; Sca82] using `lightkurve` [Lig+18] in order to determine the stellar rotation period as the signal with the highest peak and $SNR > 2.5$. For the promising cases, we compared the periodograms derived from the TESS light curves that were systematic corrected with the Presearch Data Conditioning pipeline [PDCSAP_FLUX, Jen+16], and those extracted from the raw flux (SAP_FLUX). We selected candidates where the measured flare duration was at least 15 per cent of the detected rotation period. The duration was chosen to ensure that we did not exclude the superflares that were split into multiple detections by `AltaiPony` due to rotational modulation. We arrived at this threshold

Table 7.1: Long-duration flares on small stars with complex shapes that indicate the presence of more than two superimposed events. These targets were excluded from the analysis.

TIC	Sector	P [h]	t_{start} [BTJD - 2457000 d]
441811894	18	5.13	1804.987685
441606549	20	4.49	1846.901948
298160985	14	6.90	1704.145163
260972843	5	6.83	1454.968234

by injecting model superflare events into simulated light curves with typical Gaussian noise levels, and recovering their properties using `AltaiPony` (see also Section 7.11.1).

7.4.1 Manual inspection of flare events

We identified 343 candidate events for superflares which we inspected visually. Out of those, in 19 cases the detected rotation period was a fluke in the periodogram where multiple peaks could not be separated into rotational and non-rotational signal. Some candidates were instrumental false positives (19), others were contaminations from Solar system objects that mimicked flare events (6), both of which could be disambiguated from the Target Pixel Files from which the light curves were extracted. The majority, however, were flares with total duration below one rotational period (291), partly because aliases in the periodogram suggested faster rotation, but mostly because the conservative 15 per cent relative flare duration threshold allows selection of short flares. Finally, four flares lasted for multiple rotation periods but exhibited a complex flare morphology that indicated the presence of more than two superimposed flares in each event (Table 7.1).

We observed four long duration superflares, i.e., flares with TESS band energies above 10^{33} erg, on fully convective M dwarf stars in the red-optical regime ("white-light") with TESS: TIC 277539431 (2MASS J10551532-7356091), TIC 452922110 (2MASS J08055713+0417035), TIC 44984200 (2MASS J08380224-5855583), and TIC 237880881 (2MASS J01180670-6258591), hereafter referred to as TIC 277, TIC 452, TIC 449, and TIC 237.

7.5 High-resolution spectra

We collected high-resolution spectra for two of our sample stars that did not have literature values for their projected rotation velocity $v \sin i$ available. TIC 449 and TIC 277 were observed with the High-Resolution Spectrograph [HRS, Cra+14] at the Southern African Large Telescope [SALT, BSM06] on February 08 and February 09 2020, respectively. The HRS provides spectra covering a wavelength range of $5,500-8,900$ Å in its red arm with a spectral resolution of about $40,000$ in our chosen medium-resolution mode. Since our targets have low effective temperatures, the bulk of the stellar emission was observed redwards of $7,000$ Å . The data were reduced with the PEPSI data reduction software [SIS18]. The reduction followed the standard steps of bias overscan, detection and subtraction, scattered light extraction from the inter-order space and subtraction, definition of échelle orders, optimal extraction of spectral orders, wave-length calibration, and a self-consistent continuum fit

to the full two-dimensional (2D) image of extracted orders. The one-dimensional spectra resulting from combining the échelle orders were used to infer the rotational line broadening as described in Section 7.6.5.

7.6 Stellar properties

Our goal was to simultaneously constrain the latitude (θ_f) of the superflare on the stellar surface together with its longitude, and underlying shape. In order to infer θ_f from the flare light curves we required reliable information about the stars on which they occurred (Table 7.2). Rotation periods ($P_{\rm rot}$) enter both the stellar inclination calculation, and the flare modulation model itself. Spectral types are needed to determine the luminosity of the stars, and from these the flare energies (E_f) and flaring region sizes (ω). Combining $P_{\rm rot}$ with stellar radius (R_*), and projected rotational velocity $v \sin i$, we could calculate the inclination i of the stellar rotation axes. Eventually, knowing i allows us to break the partial degeneracy between i and θ_f in the model fit.

7.6.1 Rotation periods

We calculated the uncertainty on $P_{\rm rot}$ by combining the results from sine fits to all available TESS light curves for each target assuming Gaussian uncertainties on the flux, and derived the posterior distributions for $P_{\rm rot}$ using the Python Markov Chain Monte Carlo (MCMC) sampler `emcee` [For+13]. The modulation was stable (Fig. 7.1), i.e., it did not show any sign of evolution in the phase-folded light curves of 1-3 consequent Sectors for each star. The resulting values for $P_{\rm rot}$ were then used in the inclination calculation, and the modulation model fits.

7.6.2 Spectral types

We adopted spectral types from previous work [Kir+16; Kra+14; Pha+17] that used low-resolution optical or IR spectroscopy for TIC 237, TIC 277, and TIC 449. For TIC 452, we compared a spectrum obtained from the FAST spectrograph at the Fred Lawrence Whipple Observatory to the [Boc+07] composite spectra. For TIC 277 and TIC 449, spectral types were also consistent with the literature values when comparing the SALT spectra to those in [Boc+07]. We selected the nearest stars within 5 arcsec of our targets in the Two Micron All-Sky Survey [2MASS, Skr+06] and Gaia DR2 databases in order to obtain optical and infrared photometry and distances from parallaxes.

7.6.3 Stellar quiescent flux

The absolute released flare flux determines the modelled size of the flaring region in the photosphere. However, the light curves provided by TESS did not have accurately calibrated absolute fluxes. We calculated absolute quiescent fluxes in the TESS band using stellar spectrophotometry, transforming the flux in Gaia G band to the TESS band. We first

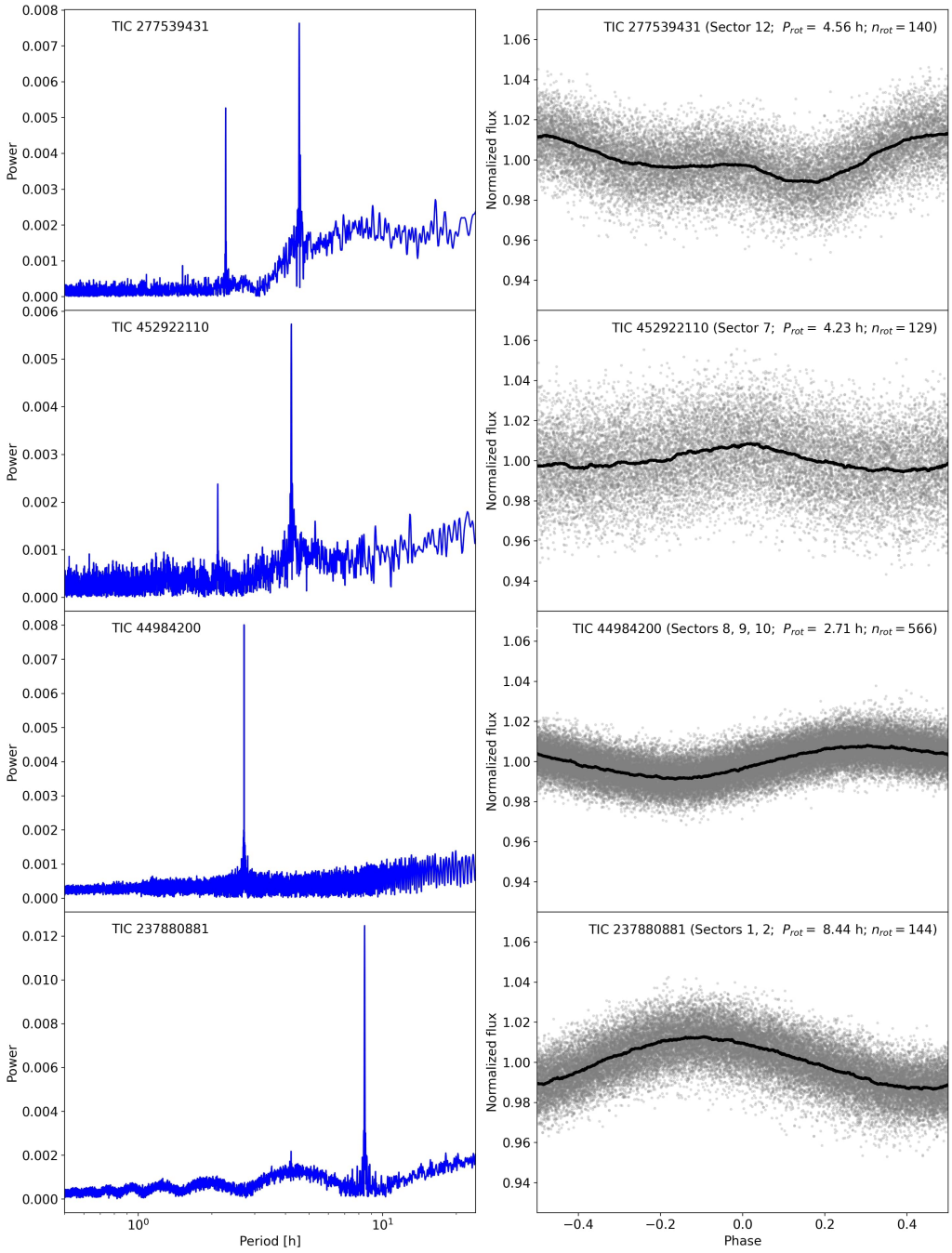

Figure 7.1: Left: Lomb-Scargle periodograms of the TESS light curves (PDCSAP_FLUX) of the four investigated stars. Right: phase folded light curve of the same stars as on the left, folded with their rotation periods P_{rot}. Grey dots: Light curve flux with outliers clipped at 3σ above the noise level. Black line: Rolling median, calculated using an 800 data points window. n_{rot} is the number of rotation periods covered by the data.

constructed representative spectra for each spectral type that covered the TESS-Gaia range ($\sim 3,500 - 11,000$ Å) by combining spectroscopic templates [Boc+07; Sch+14a] with the IR prism spectra from the Spex Prism Library [BM06; Bur+04; Bur+07; Bur+08; Bur14; Kir+10]. We then integrated over the Gaia G band filter response curve, and normalized the spectral energy distribution (SED) to the Gaia value. To obtain fluxes in TESS, we integrated over the response curve for TESS. The major uncertainty in the spectrophotometric fluxes was in the spectral type used to select the SED, so we assigned uncertainties to the fluxes with a difference of one spectral subclass based on typical differences in the literature, which is higher than uncertainties quoted within individual works. We then converted flux to luminosity using the Gaia distances.

7.6.4 Stellar radii

We calculated stellar radii based on the relationship between absolute K_S magnitude and radius for M dwarfs [Man+15]. The absolute K_S magnitude was calculated from the apparent K_S magnitude in 2MASS and the geometric Gaia DR2 distance of the stars [Bai+18]. The uncertainties in the reported radii are based on a combination of the scatter in the magnitude-radius relationship (~ 3 per cent) and the uncertainties on distance and K_S magnitude.

Systematic errors in the model fits may arise in the R_* calculation, which would affect the derived inclination, and relative size of the flaring region. Radii that are inflated by $\sim 12 - 14$ per cent compared to stellar structure models have been reported for both components of the rapidly rotating late M dwarf equal mass wide binary GJ 65 [Ker+16] which they attributed to youth and the suppression of convection due to strong magnetic fields. However, we determine the radii of our targets from absolute K_S magnitudes, with their distance being well known from Gaia DR2 data [Man+15]. This method is self-correcting for inflation because an M dwarf that is abnormally large will also have an absolute brightness that will be larger than for a non-inflated M dwarf.

7.6.5 Projected rotation velocity $v \sin i$

The inclination i of the stellar rotation axis is partially degenerate with the flare latitude θ_f. This ambiguity needs to be broken by an independent measurement of i, which we achieve by measuring the projected stellar rotation velocity $v \sin i$.

For two stars (TIC 452 and TIC 237) we used existing $v \sin i$ values [Kes+18; Kra+14]. The other two, TIC 449 and TIC 277, did not have existing $v \sin i$ measurements in the literature. For those, we used the collected SALT spectra (see Section 7.5) to determine the projected rotation velocity.

For the $v \sin i$ inference we used a technique that employs cross correlation functions (CCFs) of rotationally broadened template spectra to calibrate a relation between the FWHM of the CCF and $v \sin i$ [RJG12]. We calibrated the normalized CCFs using high-resolution optical CARMENES (Calar Alto high-Resolution search for M dwarfs with Exo-earths with Near-infrared and optical Echelle Spectrographs, [Qui+10]) spectra of CN Leo (M6), LP 731-058 (M6.5), and Teegarden's Star (M7). This was done to reduce bias in the $v \sin i$ values

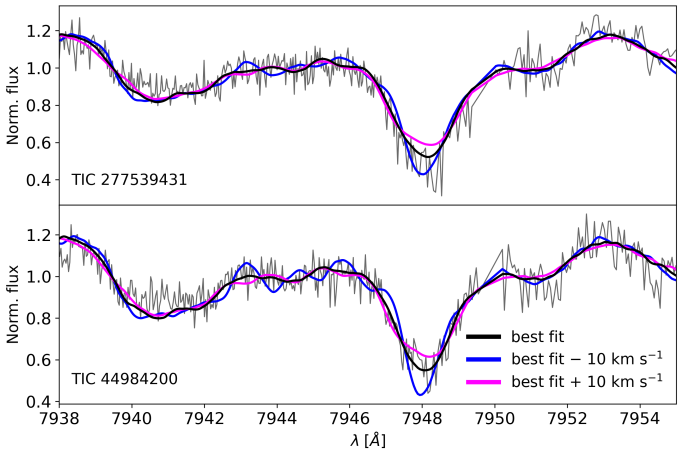

Figure 7.2: SALT spectra of TIC 277 (top panel) and TIC 449 (bottom panel), and rotationally broadened best-fitting template spectra. The black line is a template spectrum broadened with the best-fitting $v \sin i$ value obtained with the CCF technique. The magenta and blue lines show the same templates, but broadened with a 10 km s^{-1} higher and lower $v \sin i$ than the best-fitting solution, respectively.

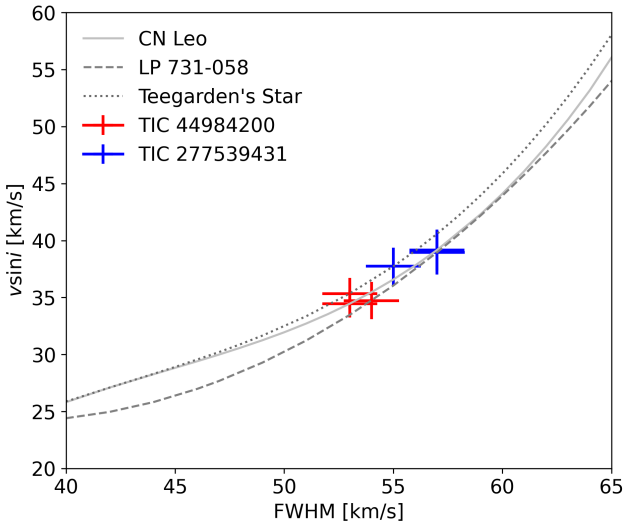

Figure 7.3: Projected rotational velocity $v \sin i$ derived from the SALT spectra of TIC 449 and TIC 277. Grey lines: Third order polynomial fits to the calibration functions for three template spectra. Red and blue crosses: Fitted FWHM from the cross-correlation functions of SALT spectra in the $7,938 - 7,955$Å region with uncertainties for TIC 449 and TIC 277. The fits indicate that the stars are rapidly rotating with $v \sin i$ of ~35 km s^{-1} and ~38 km s^{-1}, respectively.

derived with individual templates, and to account for uncertainty in the spectral types of the SALT targets. The template stars rotate at $v \sin i < 3$ km s^{-1} [Rei+18a]. We broadened these three template spectra using the `eniric` [NF19] software assuming a limb darkening coefficient $\epsilon = 0.6$ [Cla98] in the range from 1 to 60 km s^{-1} taking 1 km s^{-1} steps. Then we measured the FWHM of the CCFs to derive a calibration function for $v \sin i$ from the broadened templates.

In the selection of spectral regions, we started with suggestions for suitable wavelengths for low-mass stars in [Rei+18a] in the $7,410 - 8,700$ Å range that overlapped with our SALT spectra. We found the region $7,938 - 7,955$Å surrounding the Rb 7948Å line to be best suited for the chosen technique, and the spectra collected for our target stars (Fig. 7.2). This line is strong, shows isolated line wings, and is largely unaffected by telluric features. These properties make it sensitive to changes in $v \sin i$ in the $10 - 50$ km s^{-1} range, while in the other inspected regions the lines were blended, or much weaker, or both. We fit a third order polynomial to the calibration function, and used the fit to propagate the uncertainty on FWHM to the resulting $v \sin i$ values (Fig. 7.3). We found uncertainties on $v \sin i$ in the $1.2 - 1.9$ km s^{-1} range for individual pairs of templates and spectra, and no apparent trends with the spectral type of the templates, so that we treated the results as independent measurements. Averaging over the best-fit results for the pairs we arrived at uncertainties of 0.8 km s^{-1} for TIC 449 and 1.0 km s^{-1} for TIC 277 with Gaussian error propagation.

7.6.6 Stellar inclinations

We used the stellar rotation period $P_{\rm rot}$ and radius R_* along with the $v \sin i$ to infer the stellar inclination angle i. To account for the statistical dependence between equatorial velocity (determined from $P_{\rm rot}$ and R_*) and $v \sin i$, we used the framework of [MW20]. We used an MCMC sampler [GW10] to produce a posterior probability density for $\cos i$ given the measurements. We required $0 < \cos i < 1$, and assumed Gaussian priors on $v \sin i$, $P_{\rm rot}$ and R_*. The posteriors for i were non-Gaussian for the stars determined to be close to equator-on, but could be approximated by a double Gaussian fit which we subsequently used as an informative prior in the model fits (Fig. 7.4). We give the median and 68 per cent confidence interval as the best-fitting values and errors in Table 7.2, using the convention that $i < 90°$.

7.7 Methods

The presence (or absence) of a periodic modulation in the flare flux observed in the optical light curves in our sample can be modeled by a bright flaring region on the stellar surface that periodically, partially or fully, rotates in and out of view (Section 7.8, Fig. 7.5). We discuss the simplifications made in the design of the model (Section 7.9), such as assuming a 10,000 K flare temperature, a spherical cap as the shape of the flaring region, and a universal flare time evolution parametrization. We also motivate why we neglect differential rotation in our analysis, and why we assume that multi-peaked flares are co-spatial. Our assumptions do not pose considerable limitations on our conclusions. They may, however, partly explain

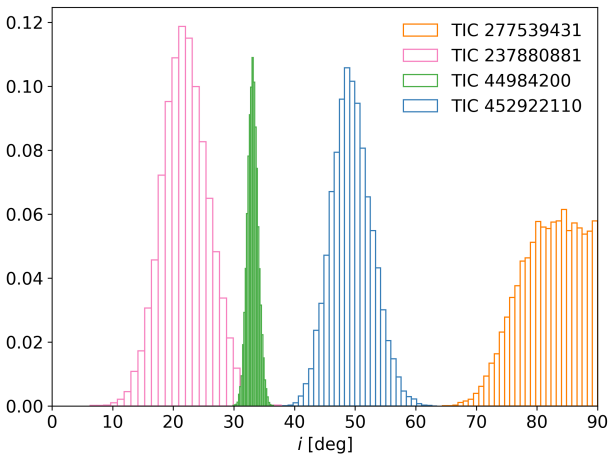

Figure 7.4: Posterior distributions of stellar inclination angles. Inclinations i were derived from $v \sin i$, K_s magnitude based stellar radii and rotation periods from TESS light curves using the method described in [MW20]. For all stars except for TIC 277 the uncertainties on i were well approximated as Gaussian, while the latter can be approximated with a superposition of two Gaussian distributions using the convention that $i < 90°$. Accurate constraints on i are crucial to the accuracy of the subsequent inference of the flare latitude θ_f because the morphology of a modulated flare is to some extent degenerate in i and θ_f.

the cases where the model could not capture all features of the flare light curve, such as deviations from the flare template near the peak.

7.8 The flare modulation model

While flaring regions on the Sun may take complicated shapes that grow, shrink, brighten and dim non-uniformly with time [AA08], the large flares typically observed on stars can be adequately represented in terms of the flare amplitude and the impulsive and gradual phase of the flare [e.g., Gün+20]. For our observed light curves, the integrated flux from these regions can be described as an empirical model flare ([Dav+14], hereafter [Dav+14]) that erupts from a circular region and is modulated by rotation. We chose to adapt the [Dav+14] empirical model by decoupling their $t_{1/2}$ in the first and second addend of their Eq. 4 into FWHM_i and FWHM_g for the impulsive and gradual flare phases, respectively. The model parametrizes the rise and the decay phases of the flare separately, as in Eqn. 1 and 4 in [Dav+14]. In its adapted form, it reads:

$$\begin{aligned} F_{rise} &= 1 + 1.941\,\mathrm{FWHM}_i - 0.175\,\mathrm{FWHM}_i^2 \\ &\quad -2.246\,\mathrm{FWHM}_i^3 - 1.125\,\mathrm{FWHM}_i^4 \end{aligned} \tag{7.1}$$

$$F_{decay} = 0.6890\,\mathrm{e}^{-1.600\,\mathrm{FWHM}_i} + 0.3030\,\mathrm{e}^{-0.2783\,\mathrm{FWHM}_g}. \tag{7.2}$$

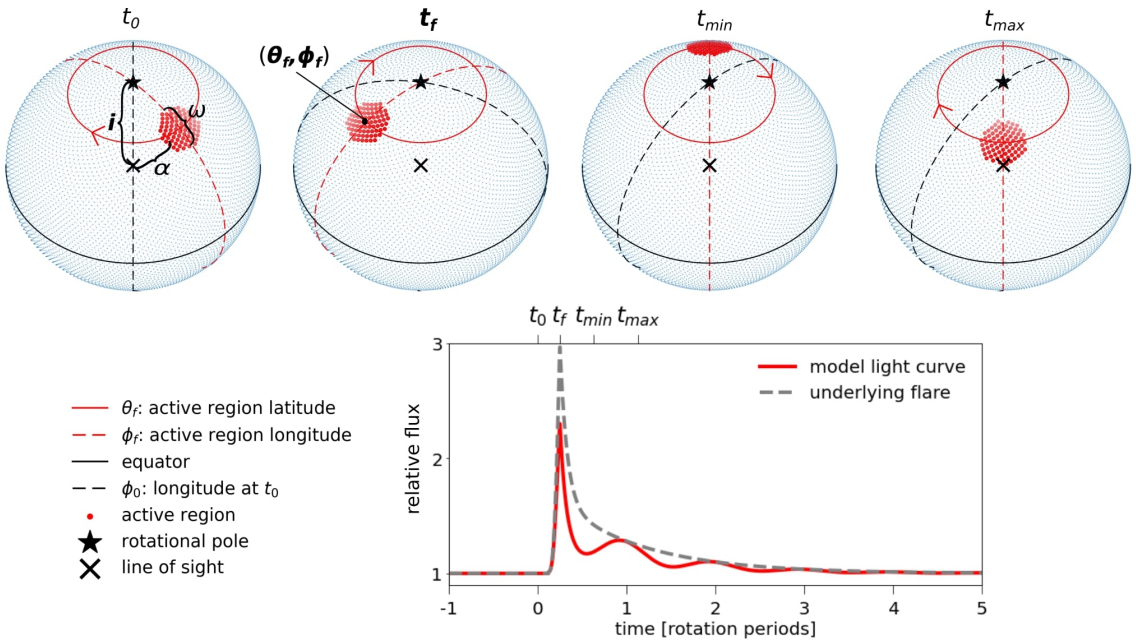

Figure 7.5: Flare modulation model. From left to right, the top row shows a clockwise rotating star (blue dots) with a flaring region (red dots), from the start of observation at t_0 to the peak flare time t_f, and further to the flaring region being rotated to the stellar far (t_{min}) and near (t_{max}) sides. The angular distance between the rotational pole (black star) and the intersection of the line of sight with the centre of the star (black cross) is the inclination i. α is the angular distance of the flaring region to the line of sight, and ω is the full opening angle of the circular flaring region. The depicted configuration results in the observed light curve (red line) in the bottom panel. The underlying flare model is shown as a grey dashed line in the same panel.

Our (3+3+1)-parameter model was fit using an MCMC method (Fig. 7.6). The first three parameters are the flare peak time t_f, the corresponding longitude ϕ_f, and the latitude θ_f, which define the timing of the flare and its location on the stellar surface. The other three are the relative flare amplitude A, FWHM_i, and FWHM_g, which determine the intrinsic shape of the light curve. The last parameter is the inclination i of the stellar rotation axis, which is constrained by independent observations. The geometric modulation is determined by i, θ_f and ϕ_f that we combined to give the distance of the flaring region from the limb. The model light curve was constructed in three steps:

1. Determine the size of the flaring region from the flare temperature T_f, and A, given the stellar radius R_* and luminosity L_*.

2. Split the flaring region into spatial elements (θ, ϕ) to calculate the spatially resolved rotational modulation of the flare flux.

3. Apply the modulation to the flare light curve and sum the spatial elements to obtain the model luminosity L_{model}.

7.8.1 Size of the flaring region

We modeled the flaring region, that is, the photospheric footpoint of the flaring magnetic loop, from which the white-light emission originates, as a uniformly bright spherical cap. Its position relative to the line of sight of the observer determined the morphology of the obtained flare light curve. We described the flare emission in the optical as a $T_f = 10,000$ K blackbody (see Section 7.9.1), and determined the specific flare flux $F_{f,s}(T_f)$ of the region by integrating its spectral energy distribution within the TESS band. The modulation is equal to the cosine of the incidence angle, known as geometrical foreshortening. The integration over the flaring region yields the maximum observable flare luminosity $L_{f,max}$, that is the flare luminosity of a flaring region centred on the line of sight (see grey lines in Fig. 7.6):

$$L_{f,max} = \pi R^2 F_{f,s}(T_f) \sin^2\left(\frac{\omega}{2}\right). \tag{7.3}$$

ω is the full opening angle of the cap which can take values between 0 and π. In the following, all reported flare parameters (FWHM_i, FWHM_g, A) refer to the flare as it would appear when fixed on the line of sight. $L_{f,max}$ is also the product of A with the quiescent stellar luminosity L_* in the TESS band:

$$L_{f,max} = A \cdot L_*. \tag{7.4}$$

Combining Eqn. 7.3 and 7.4 yields the angular radius $\omega/2$ of a circular region that produces a flare with a given amplitude A and temperature T_f on a star with radius R_* and quiescent luminosity L_*:

$$\omega/2 = \arcsin\left(\sqrt{\frac{A \cdot L_*}{\pi R_*^2 F_{f,s}(T_f)}}\right). \tag{7.5}$$

7.8.2 Rotational modulation and model luminosity

The flaring region with radius $\omega/2$ centred on (θ_f, ϕ_f) was represented by an ensemble of N evenly distributed spatial elements. It was assumed to emit uniformly, so each spatial element emitted the same fraction $F_f(t) = L_f(t)/N$ of $L_f(t)$ at any given time t during the flare. Before and after the flare the region emitted the average quiescent stellar flux. To model the maximum flare flux $F_f(t)$, we used the adapted [Dav+14] model.

For ease of calculation, we converted t to phase $\hat{t}$ in units of radian using the rotation rate of the star $\hat{t} = 2\pi(t - t_0)/P_{\mathrm{rot}}$ where t_0 marked the start time of the light curve that we selected for the model fit, and P_{rot} was the rotation period of the star.

Every spatial element emitted a modified flux $F_f(\theta, \phi, \hat{t})$ of its maximum flux $F_f(\hat{t})$ toward an observer at infinite distance. The modification was again given by the geometrical foreshortening with incidence angle α:

$$F_f(\theta, \phi, \hat{t}) = F_f(\hat{t}) \cos\alpha(\theta, \phi, \hat{t}). \tag{7.6}$$

α was the distance from the intersection point O of the line of sight with the centre of the star to every spatial element (θ, ϕ)

$$\alpha = \arccos\big(\sin\theta\cos i + \cos\theta\sin i\cos(\phi - \phi_0 - \hat{t})\big), \tag{7.7}$$

where ϕ_0 was the longitude that faced the observer at t_0.

To determine when a spatial element was behind the limb we calculated the visible rotation fraction D, i.e., the fraction of each stellar rotation during which the spatial element is visible to a distant observer. Applying the spherical law of cosines to the triangle between O, a point on the limb at a given latitude, and the rotational pole of the star we obtained

$$D = \frac{1}{\pi}\arccos\Big(-\tan\theta\tan\Big(\frac{\pi}{2} - i\Big)\Big). \tag{7.8}$$

Using D and ϕ_0 we defined a step function $d(\hat{t})$ that was 1 when the spatial element was visible, and 0 when it was hidden. Combining d with $F_f(\theta, \phi, \hat{t})$ we obtained the modulated flux of a spatial element in the flaring region

$$F_{model}(\theta, \phi, \hat{t}) = F_f(\theta, \phi, \hat{t})\, d(\theta, \phi, \hat{t}). \tag{7.9}$$

Finally, we calculated the model luminosity L_{model} as a function of $\hat{t}$ by summing up all spatial elements. For $N \to \infty$, L_{model} becomes the surface integral over the flaring region. In our fits, we used $N = 100$, motivated by the time resolution of TESS light curves in cases where the modeled flare is modulated with a high gradient, that is, when the impulsive flare peak is moving in or out of view at the limb. In all other cases, $N \approx 10$, or even $N = 1$ (for flares located close to the pole at low i) can be sufficient.

7.8.3 Fitting the model to the observed light curve

First, we masked the flare and fit the dominating starspot modulation and long-term trends in the light curve using Gaussian Process (GP, [RW06]) regression with `celerite2` [For+17; For18]. `celerite2` is a software that provides a library of covariance functions, or kernels, to use for GP regression on one-dimensional data sets like time series, and more specifically, light curves. Following [For+17], we chose a mixture of two kernels, called SHOTerm, which are derived starting from the dynamics of stochastically driven damped simple harmonic oscillators (SHOs) as a general model for stellar variability. The first is a RotationTerm, which is itself a mixture of two SHOTerm kernels with periods P_{rot} and $P_{\mathrm{rot}}/2$, and used to model the rotational variability. The second is a single SHOTerm that covers all other variability that may be present in the light curve. We obtained posterior distributions on the parameters using the same wide Gaussian priors ($\sigma = 2$) for all fits except for the prior on the rotation period in the RotationTerm kernel. There, we used the period P_{rot} obtained from the Lomb-Scargle periodogram as a prior (see Sections 7.6.1 and 7.4). We then subtracted the prediction for the light curve in the time interval of the masked flare to obtain the residual flare light curve to which we subsequently fit our model.

In a second step, we constructed a likelihood function assuming that the uncertainty in flux (quadratic addition of uncertainty from GP fit and PDCSAP_FLUX_ERR, termed "original uncertainty" from here on) was Gaussian. Our priors were uniform over the physically permissible ranges (> 0 for the flare parameters, $[0°, 360°]$ for the longitude of the flare, and $[-90°, 90°]$ for θ_f) for all parameters but i, for which we adopted empirical priors (see Section 7.6.6). Using the MCMC method [`emcee`, For+13] we determined the posterior distributions of the flare peak time t_f; the intrinsic flare properties FWHM_i, FWHM_g, and A; the location of the flaring region, θ_f and ϕ_f; and an updated distribution of the inclination i.

7.9 Model assumptions and their motivation

7.9.1 Flare emission in the optical is a 10 000 K blackbody

We assumed that the observed red-optical emission of our flares stems from a blackbody component at effective temperature $T_f \approx 10,000\,\mathrm{K}$, as is common in both the Sun and other low-mass stars [HF92; KMH18; Kow+13; Kre11]. Hotter temperatures have occasionally been reported for M dwarf superflares in the past [Fro+19; Rob+05]. Typically, the short, impulsive phase can be hotter than $\sim 10,000\,\mathrm{K}$, but cools rapidly to $\lessapprox 10,000\,\mathrm{K}$ where it emits during the longer, gradual phase [Fuh+08; How+20]. In our model, T_f primarily affects the size of the flaring region. A large region will be more smoothly modulated than a small bright kernel. If an initially hotter temperature with subsequent rapid cooling was present, our model would overestimate the size of the flaring region in the first few minutes of the flare decay, but the protracted gradual phase that characterizes long-duration superflares would be largely unaffected.

7.9.2 The flaring region is a spherical cap

We also assumed that the flaring region was a simple spherical cap on the stellar surface. White-light flares on the Sun take more complex shapes in general, such as pairs of non-circular footpoints, or crescent-shaped ribbons [HWM06]. The morphologies of active regions that are associated with the strongest flares are also the most complex [STZ00]. In particular, non-circular shapes may cause departures from our model when the region moves across the stellar limb, but less so when the region is fully in view. Moreover, effects like saturation of flare loops might violate the assumption that the flaring region is flat [HS18; JKH18]. However, unlike in solar observations, we can neglect limb darkening effects (see Appendix 7.13.2).

7.9.3 Flares follow the same time evolution parametrization

Flares often display a complex time evolution that does not follow the [Dav+14] empirical template. The majority of the largest flares are complex. Based on the $\sim 6,800$ flaring events that [Gün+20] detected in TESS M dwarf light curves, out of 10 per cent of the flares with the highest amplitudes ($A > 0.24$) more than 52 per cent were best fit with superpostions of two or more [Dav+14] flare templates, while in the other 90 per cent this fraction was only ~ 20 per cent.

Some flares cannot be resolved into superpositions of multiple classical flares ("unusual" flares). While we expect about one out of four flares to be complex [Dav+14; Gün+20; Haw+14], unusual flares are rare with about 1 per cent incidence rate [Dav+14].

The [Dav+14] model was derived from the flares found in Kepler light curves of GJ 1243, a frequently flaring dM4e star. We based our flare model on the empirical parametrization derived for this star. However, if the time evolution of the flare and the geometry of the flaring region deviate from our assumptions, we expect this to mostly affect the impulsive phase of the flare. To avoid overfitting the gradual decay phase of the flare which reveals more about the rotational modulation than the impulsive phase due to its relatively long duration, we made two adjustments. First, we chose to decouple the time scales for the impulsive and gradual phases. This is consistent with models that attribute different physical processes to the impulsive and gradual phases of flares [BG10]. Second, we increased the uncertainties on the flux above $A/2$ in each of the flares to 20 per cent of the flare-only flux, as shown in the bottom panels in Fig. 7.6. The number was an ad hoc choice aiming to permit relatively strong variability in the amplitude while preserving the overall shape of the flare.

7.9.4 Differential rotation effects are negligible

Differential rotation may in principle cause systematic errors in the inclination estimates. Assuming the predicted differential rotation $(\Omega_{equator} - \Omega_{pole})/\Omega_{bulk} \sim 0.02$ [Yad+15] for fully convective stars, derived inclinations would increase by about $0.5° - 5°$. Assuming complete degeneracy between i and θ_f, the flare latitudes would *move poleward* accordingly. The poleward shift would be at the high end of the estimate for flare latitutes that were initially

close to the pole, and at the low end for flares near the equator. However, fully convective stars do not appear to reach such strong differential rotation, instead observations indicate typical values about one order of magnitude lower [Bar+17]. Moreover, the degeneracy is only partial, because one can, for instance, distinguish a pole-on from an equator-on flare for a relatively broad range of inclinations, but less so for smaller differences in latitude (compare, for instance, the left- and rightmost columns in Fig. 7.9). Overall, as long as differential rotation is Sun-like, i.e. rotation is slower at the pole than at the equator, the real flare latitudes will be a bit closer to the poles than what we derive in this work.

Another effect of differential rotation would cause the rotation period derived from the light curve to differ from the rotation period at the latitude of the flare. The input period would be either too long or too short, resulting in a poor fit if an otherwise strong rotational modulation of the flare light curve is present. However, we observed no lag between between the minima of modulation and the spot induced variability.

7.9.5 Flare footpoints are co-spatial with the loci of magnetic field emergence

One caveat concerns the interpretation of the flare latitude as the locus of magnetic field emergence (see Section 7.1, and references therein): We cannot exclude that the region of white-light emission footpoints could have wandered across the stellar surface in the time between emergence and flare eruption. The distance between where the magnetic field concentration is at the time of flux emergence and at the time of white-light emission will depend on the duration of the build-up phase of the flare, and the conditions of the sub-surface plasma. Our stars show stable starspot configurations over timescales of multiple weeks to months which suggests that large scale spot evolution is very slow, but we cannot exclude more dynamic conditions on smaller scales.

7.10 Results

Polar spots have been observed in fast-rotating young Sun-like stars [Işı+18]. However, on the present-day Sun, sunspots, and the flares they are associated with, occur in a belt around the equator, and almost never at latitudes above 30°. We found all our selected flares at significantly higher latitudes around and above 55°.

We found four candidates with long-duration superflares, and shorter measurable rotation period P_{rot}: TIC 277 (Sector 12), TIC 449 (Sector 10), TIC 452 (Sector 7), and TIC 237 (Sector 1). They rotate so quickly ($P_{\mathrm{rot}} = 2.7 - 8.4$ h) that the observed white-light superflares last longer than a full rotation period on each star. Three of the four stars display strong flux modulation during the superflare decay *in phase with the stellar rotation.* This can most straightforwardly be explained by rotational modulation, with the flaring region rotating in and out of view on the stellar surface.

In Fig. 7.6 we show all investigated superflare light curves. The shape of the modulation contains information on the latitude of the flaring region: the combination of flare latitude and the inclination angle of the stellar rotation axis determine how long a flaring region is

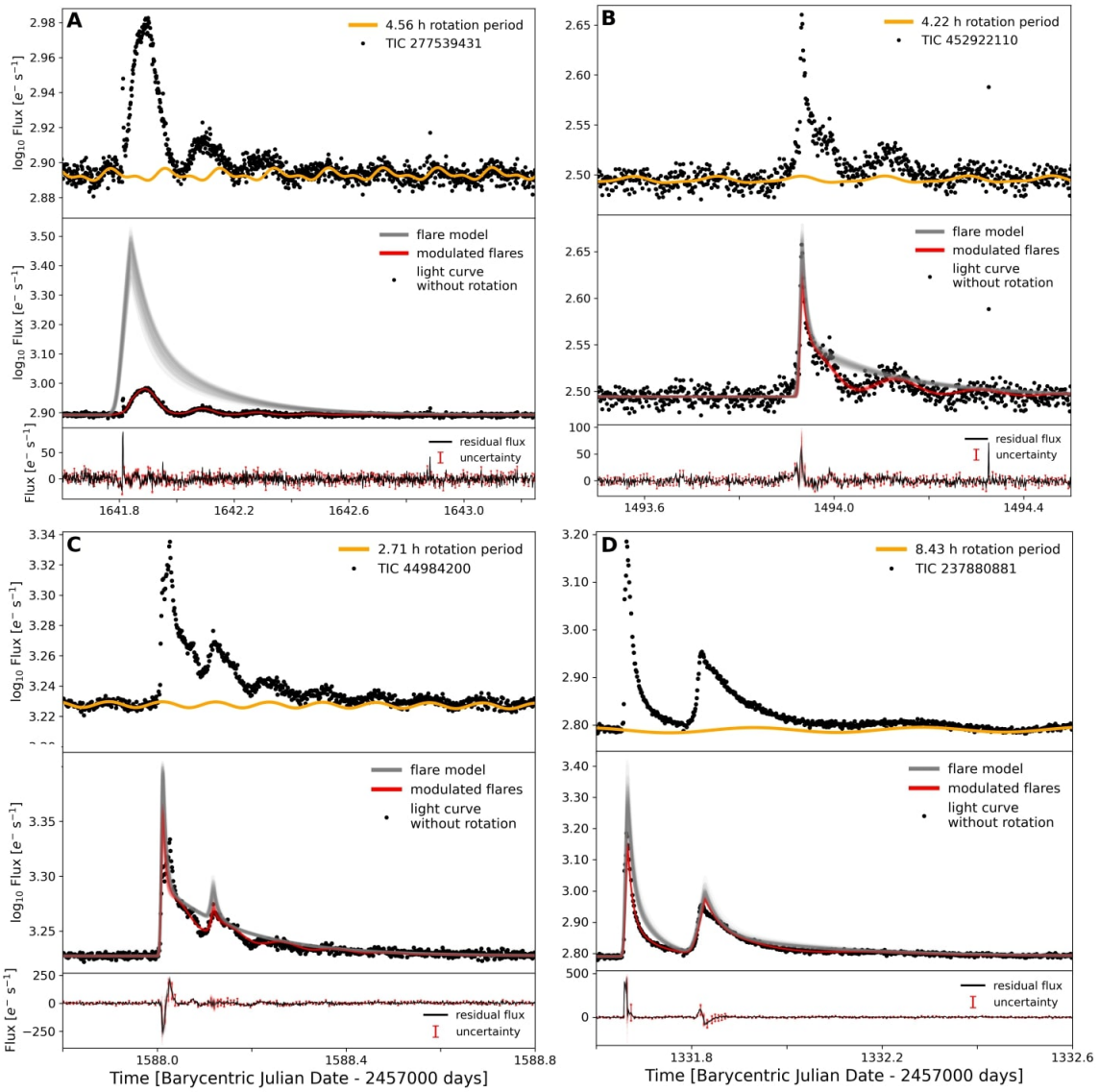

Figure 7.6: Giant flares on rapidly rotating stars. Each of the subfigures A-D shows one superflare on a fully-convective fast-rotating star that was visible for more than a full stellar rotation period. *Top panels.* Observed flare in the TESS light curve (PDCSAP_FLUX, black dots). Quiescent light curve fit incorporating long term trends and rotational variability from starspots (orange line). *Mid panels.* TESS light curve with rotational variability of the non-flaring photosphere removed (black dots). Samples from the posterior distribution of the fit to the modulated flare curve (red lines). Samples from the distribution of underlying flares without rotational modulation (grey lines). *Bottom panels.* Residual flux after subtracting rotational modulation and the model fit (black line). Flux uncertainty (red error bars). The flares in the subfigures A-C show clear modulation in phase with stellar rotation, while the flares in subfigure D remain nearly unaffected. We also constrain the longitude at which the flare occurs within a few percent uncertainty, e.g., in subfigure A, the longitude of the flare peak is about 230°, implying that it must have occurred behind the limb given the high inclination of the rotation axis.

Table 7.2: Properties, observations, and best-fitting results for stars with superflares. Stars with two flares are indexed 1 and 2 for the first and second flare in chronological order. Values in parentheses are the differences to the 84th (upper) and 16th (lower) percentiles, or else the 1-σ uncertainty. SpT: spectral type. K_S: 2MASS magnitude. d: Gaia distance. $P_{\rm rot}$: rotation period of the star. $v \sin i$: projected rotation velocity of the star. $R_*/R_\odot$: stellar radius measured in solar radii. i: updated posterior of the stellar inclination on the informative prior derived from $v \sin i$, $P_{\rm rot}$ and R_*. $\log_{10} E_f$: flare energy released in the TESS band. A: amplitude of the underlying flare as a fraction of quiescent flux. FWHM$_i$ and FWHM$_g$: impulsive and gradual full-width-at-half-maximum flux of the respective flare phases. θ_f: latitude of flaring region on the stellar surface.

	TIC 277	TIC 452	TIC 449 (2-flare)	TIC 237 (2-flare)
SpT	M7	M7	M6	M5
K_S (mag)	9.666 ± 0.024	10.865 ± 0.021	9.268 ± 0.021	10.636 ± 0.023
d (pc)	13.70 ± 0.11	22.03 ± 0.06	11.10 ± 0.03	46.01 ± 0.14
P (min)	273.618 ± 0.007	254.094 ± 0.054	162.694 ± 0.007	506.145 ± 0.020
$v \sin i$ (km s^{-1})	38.6 ± 1.0	29.7 ± 1.5	34.8 ± 0.8	14.4 ± 2.6
$R_*/R_\odot$	0.145 ± 0.004	0.137 ± 0.004	0.142 ± 0.004	0.275 ± 0.008
i (deg)	$87.0^{(+2.0)}_{(-2.4)}$	$49.2^{(+3.3)}_{(-3.3)}$	$33.1^{(+0.9)}_{(-0.9)}$	$21.3^{(+3.7)}_{(-3.9)}$
$\log_{10} E_{f,1}$ (erg)	$34.473^{(+0.067)}_{(-0.084)}$	$33.531^{(+0.024)}_{(-0.021)}$	$33.355^{(+0.006)}_{(-0.006)}$	$34.599^{(+0.034)}_{(-0.027)}$
A_1	$2.61^{(+0.45)}_{(-0.47)}$	$0.47^{(+0.04)}_{(-0.04)}$	$0.50^{(+0.01)}_{(-0.01)}$	$2.33^{(+0.24)}_{(-0.19)}$
FWHM$_{i,1}$ (min)	$103.5^{(+5.7)}_{(-5.4)}$	$21.0^{(+5.1)}_{(-3.4)}$	$14.5^{(+1.4)}_{(-2.3)}$	$18.2^{(+0.9)}_{(-0.8)}$
FWHM$_{g,1}$ (min)	$85.1^{(+2.4)}_{(-2.4)}$	$74.8^{(+6.3)}_{(-5.3)}$	$64.3^{(+1.1)}_{(-1.0)}$	$16.9^{(+0.6)}_{(-0.5)}$
$\log_{10} E_{f,2}$ (erg)	...	...	$31.994^{(+0.066)}_{(-0.075)}$	$34.670^{(+0.026)}_{(-0.013)}$
A_2	...	...	$0.08^{(+0.01)}_{(-0.01)}$	$0.60^{(+0.04)}_{(-0.03)}$
FWHM$_{i,2}$ (min)	...	...	$25.5^{(+4.0)}_{(-4.0)}$	$63.0^{(+2.5)}_{(-2.7)}$
FWHM$_{g,2}$ (min)	...	...	$3.9^{(+1.8)}_{(-2.3)}$	$93.6^{(+2.0)}_{(-2.0)}$
θ_f (deg)	$80.9^{(+0.5)}_{(-0.6)}$	$63.1^{(+3.5)}_{(-3.7)}$	$71.9^{(+1.1)}_{(-1.1)}$	$55.2^{(+5.1)}_{(-6.1)}$

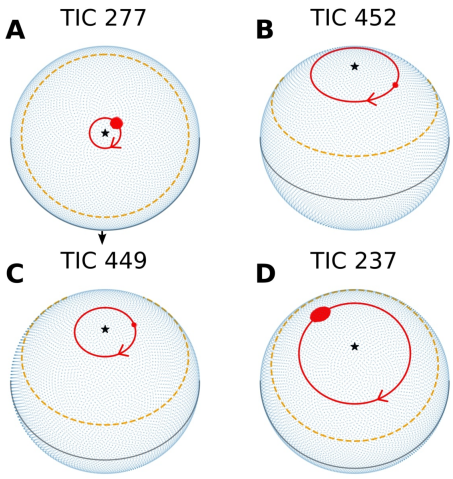

Figure 7.7: Loci of giant flares at flare peak time on the stellar surface, the subpanels correspond to those in Fig. 7.6. Red line: flare latitude. Red spot: active region, shown to scale. Orange dashed line: maximum typical solar flare latitude (30°). Black star: rotational pole of the star. Grey line: stellar equator. In sub-panel A, the flaring region is behind the limb. In sub-panels C and D the longitudes are those of the first flare on each star. TIC 277 (sub-panel A) is observed close to equator-on. For better visibility, we tilted the rotation axis by 90°. The observer's line of sight is indicated as black arrow.

visible as the star rotates. Similarly, unless the star is viewed strictly pole-on, the absence of flare modulation also contains latitude information, indicating that the flare occurs close enough to the rotational pole for the modulation to be indistinguishable from the noise, and that the pole is visible all the time; this is exploited for TIC 237 which displays much more subtle but still measurable rotational flare modulation.

We found that all four stars displayed their giant flares at high latitudes $\geq 55°$. In Table 7.2, we give the results for the marginalized posterior distributions of the model parameters, and in Fig. 7.7, we illustrate the inferred active regions loci at flare peak time on the stellar surface. The full posterior distributions can be viewed in detail in Appendix 7.13.3.

7.10.1 Model setups: single and double-flare, original and increased uncertainty around the flare peaks

The stars TIC 277 and TIC 452 both showed single modulated flares. The flares we detected on TIC 449 and TIC 237 were complex because they were better fit with a superposition of two flares than with a single flare (see Section 7.9.3).

TIC 237 displayed two flares in close sequence, both without apparent rotational modulation. We fitted this light curve under the assumption that both flares occurred at the same location, which is common on the Sun [Tör+11; Uch68; WC06] and proposed for other stars as well [Giz+17; Vid+16]. TIC 449 displayed excess flux indicating a secondary flare during the second rotation of the main event that was, however, less clear than in the case of TIC 237. A model with a single underlying flare for TIC 449 is unable to reproduce the shape of

the light curve through rotational modulation, in particular around the secondary peak. A model with two co-spatial flare events reproduces the light curve better.

Since flares often display complex evolution in the impulsive phase and the flare peak, we accommodated possible deviations from the flare template by increasing the uncertainty to 20 per cent of the excess flux around the peak (above $A/2$, see Section 7.9.3) for all flares except for TIC 277 where the flare peak most likely occurred behind the limb, and is therefore not observed (bottom panels in Fig. 7.6). This is motivated by the fact that our model is most sensitive to the (absence of) rotational modulation in the gradual decay phase. Deviations in the short impulsive phase, which our model cannot capture, however, can cause over-fitting of the template because they are more likely intrinsic to the flare than to effects of geometrical foreshortening.

We could improve or achieve consistent modelling of the modulated decay phase of the flare in all cases when we increased the uncertainties. In Appendix 7.13.1, we show the alternative fits with original uncertainties from the TESS light curves (Fig. 7.11, 7.12 A and B, 7.13). While we preferred the fits shown in Fig. 7.6, the inferred latitudes were overall high even in the solutions with higher amplitudes and stronger systematic deviations in residual flux ($> 48°$, see Table 7.3).

7.10.2 Star by star: model fits, alternative and disfavoured setups

TIC 277

TIC 277 (WISEA J105515.71-735611.3) is an M7 dwarf 13.7 pc away that rotates with a 4.56 hour period and is seen nearly equator-on. The superflare occurred at $\theta_f = \left(80.9^{+0.5}_{-0.6}\right)^\circ$ so that the flaring region was only briefly hidden from view during each rotation.

The flare peak occurred while the region was facing away from the observer (Fig. 7.6 A) at phase $\phi_f = 0.64 \pm 0.01$, and was a clear single flare event, so that we did not fit the model with alternative setups. Note that the center of the flaring region becomes visible around $\phi \sim 0.70$, while other parts of it stay behind the limb longer (at lower latitudes) or shorter (at higher latitudes).

The uncertainty on θ_f is small despite the relatively high uncertainty on inclination (Fig. 7.4). This is due to the sensitivity of the modulation model to flares that occur simultaneously close to the observed limb and to the rotational pole (see posterior probability distributions in Fig. 7.15). For the flare in TIC 277, the flare light curve morphology alone constrains the latitude to very high values even without knowing the inclination.

One possible caveat is the flare temperature. If the flare is visible throughout almost the entire rotation, which is the case for TIC 277, i can be considered a lower limit on θ_f, unless the flaring region is very large. The flaring region size depends on the flare temperature, which we here assumed to be 10, 000 K. If T_f were only 6, 500 K, the observed flare could be placed at about 70° latitude. However, this temperature would be more typical for less energetic solar flares [see Appendix in CK20, and references therein] than for stellar superflares, which are usually hotter (see Section 7.9.1). Similarly, a higher temperature could place the flaring region even closer to the poles.

TIC 452

TIC 452 (2MASS J08055713+0417035) is an M7 dwarf that has literature $v \sin i = (29.7 \pm 1.5)$ km s^{-1} [Kes+18], and a Gaia DR2 distance of 22 pc. A full rotation period of this star is 4.22 h, and the rotation axis is viewed at an inclination angle of about 49°. Its chromospheric activity places TIC 452 among active fast-rotating low-mass stars with saturated Hα luminosity [New+17]. Both the single flare fit with original (Fig. 7.11) and the preferred fit with increased uncertainties above $A/2$ (Fig. 7.6 B) consistently implied a flare latitude of $\approx 63°$.

In the remaining two stars, the simple model had to be adjusted to a more complex flare morphology.

TIC 449

TIC 449 (SCR J0838-5855) is an M6 dwarf 11.1 pc away rotating at $P_{\rm rot} = 2.71$ h. The flare on TIC 449 was visible for almost five rotation periods. While the flux appeared modulated, the flaring region never fully rotated out of view. The light curve strongly suggests the presence of a secondary flare. However, the burst in the second maximum could also stem from other complex flaring behaviour in the wake of the large event. We therefore fitted both a single- and a co-spatial two-flare solution to the light curve with increased and original uncertainties above $A/2$ (see Section 7.10.1). The first and second events are indexed accordingly in Tables 7.2 and 7.3.

The fit with the least systematic residual flux in the important gradual decay phase was achieved in the two-flare fit with increased peak uncertainties (Fig. 7.6 C) which indicated that the flares occurred at high latitudes at $(72 \pm 1)°$. Because of the contamination by complex behaviour in the secondary maximum the results of the fits were inconsistent with each other, but yielded high latitudes regardless: $(86 \pm 1)°$ for the two-flare fit with original uncertainties (Fig. 7.12 A), $(83 \pm 1)°$ for the single flare fit with original uncertainties (Fig. 7.12 B), and $(70 \pm 1)°$ for the single flare with increased uncertainties (Fig. 7.12 C). While a secondary flare is a likely scenario, other conceivable explanations include a flare region shape that deviates substantially from our circular simplification, or a cluster of > 2 flares.

TIC 237

Finally, TIC 237 (2MASS J01180670-6258591) was our earliest type star, an M5 dwarf at a distance of 46 pc with literature $v \sin i = (14.4 \pm 2.6)$ km s^{-1} [Kra+14]. TIC 237 is a probable member of the Tucana-Horologium association [Ujj+20], a young nearby moving group with age estimates spanning $4 - 45$ Myr [BMN15; Kra+14; Ujj+20].

The systematic deviation of the fit with original uncertainties, which implied $\theta_f \sim 48°$, was stronger in the decay phase (Fig. 7.13) than that with increased uncertainties on both peaks (Fig. 7.6 D), which suggests a flaring region latitude of $\left(55^{+5}_{-6}\right)°$.

In TIC 237, the flare modulation was very subtle yet measurable, in particular, in the decay phase of the second event. We show a close-up in Fig. 7.8, in which we placed the flaring region at 25° higher and lower latitudes relative to the best-fit solution, respectively.

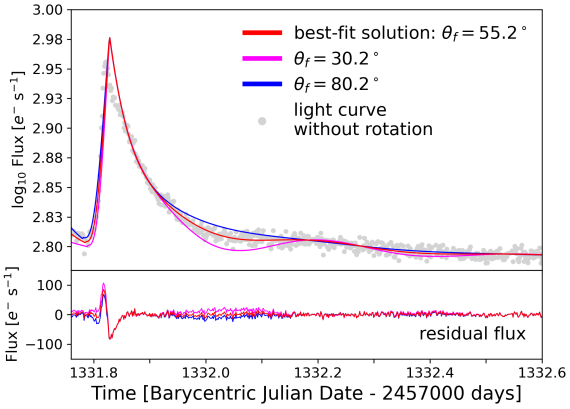

Figure 7.8: Close-up on the second event in the light curve of TIC 237. Upper panel. Grey dots: flare light curve with rotational variation removed. Red line: best-fit solution (see Table 7.2). Magenta and blue lines: best-fit solution with FWHM$_i$ and A adjusted to match the peak and impulsive decay phase of the flare while decreasing and increasing the flare latitude θ_f by 25°, respectively. Lower panel: residual flux for the three different models, color-coded as in the upper panel.

The observed modulation appears as an intermediate between stronger modulation at lower latitudes, and vanishing modulation closer to the pole. We cannot rule out that at least a fraction of the observed modulation is intrinsic to the flare. If all variation was intrinsic, the flare would reside on the pole. In a less extreme case, if there was a mixture of intrinsic variation and rotational modulation that gives the appearance of more rotational modulation than is actually present, the derived latitude would still be biased to lower values. The opposite case, where rotational modulation is masked by intrinsic variation, is less likely to occur: While variation that mimics rotational modulation can manifest as modulation with many different flare latitudes and longitudes, a variation that masks rotational modulation has much fewer degrees of freedom. We therefore suggest to give more credence to the lower error quoted for TIC 237 than the upper error. The same reasoning applies, albeit to a lesser degree, to the other three flares.

7.11 Discussion

The consistently high latitudes of the superflares studied in this work are significant, even though the sample size is small. If superflares were uniformly distributed across the stellar surface, the probability of finding all four superflares above 55° would be about 0.1 per cent, i.e. very unlikely, provided that our detection method is not biased towards finding preferentially high latitude flares (Section 7.11.1). If flares occurred at all latitudes θ_f equally, and all inclinations i were equally likely to be observed, purely geometric considerations imply that as many flares would be observed in the equatorial strip $[-26.4°, 26.4°]$ as in the complementing northern and southern polar caps taken together.

Superflares that last longer than a full rotation period of the star on fully convective M dwarfs are rare, with about one event per star per 120 years of continuous observation based

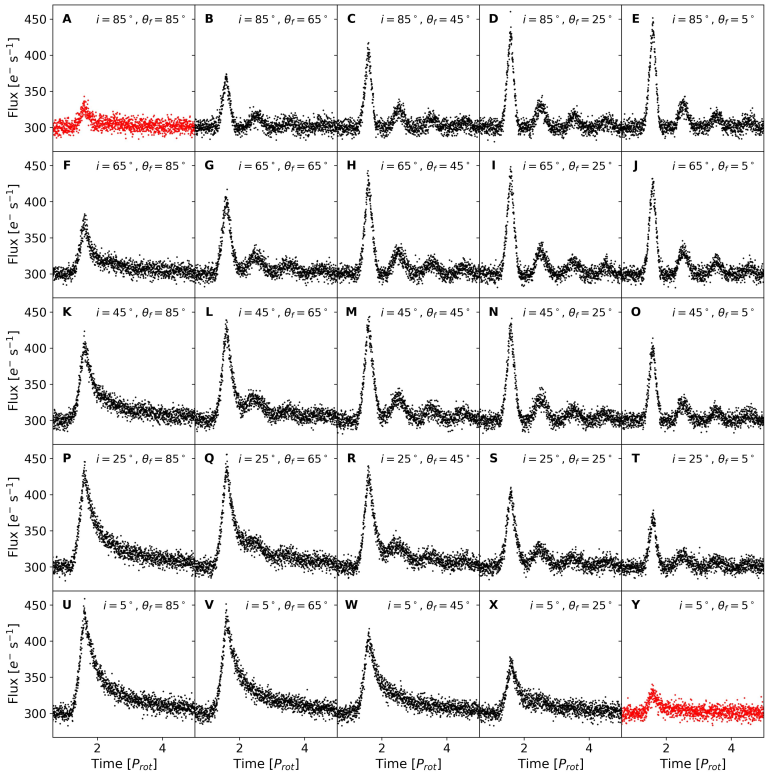

Figure 7.9: Light curves of a subset of 25 simulated multiperiod flares. Setup: Relative amplitude $A = 0.5$, FWHM_i =$\mathrm{FWHM}_g = 4P_{\mathrm{rot}}$, and 2 per cent Gaussian noise on a fictitious star with varying inclination i and flare latitude θ_f. Black scatter: recovered events (sub-panels B–X). Red scatter: missed events (sub-panels A and Y).

on our sample, and distinct from the quasiperiodic pulsations phenomenon (Section 7.11.2). Yet each event is an opportunity to probe the magnetic nature (Section 7.11.3) and the space weather conditions (Section 7.11.4) on these cool, ubiquitous stars.

7.11.1 Observing polar vs. equatorial rotationally modulated superflares

To test if our selection mechanism disfavours equatorial flares, we analysed the recovery efficiency of our pipeline on a grid of simulated flares that we injected into light curves with typical noise properties. To produce the synthetic light curves, we used our model to produce flares on a uniform grid of latitudes θ_f and inclinations i. We fixed the stellar properties and flare FWHM values ($\mathrm{FWHM}_i \equiv \mathrm{FWHM}_g$), and varied the underlying flare amplitude A and peak time t_f to capture the effects of photometric noise levels and the visibility of the flare peak on the detection probability and recovered properties. We show an example of 25 flares from this grid of model flares that occur at different combinations of i and θ_f in Fig. 7.9. The majority of flares shown in this example would have been recovered, except for events that remain attenuated for the entire duration of the event because they

occurred close the limb (red scatter). These can be both polar flares seen at high inclinations (Fig. 7.9 A), and equatorial flares seen at very low inclinations (Fig. 7.9 Y). Overall, our automated flare detection method (Section 7.4) did not show any bias towards polar over equatorial flare locations.

7.11.2 Quasiperiodic pulsations are ruled out

Rotational modulation is the preferred scenario for our observations because the period of the modulation matches the rotation period of the star. A different type of flare modulation, magnetohydrodynamic oscillations of plasma following strong flares, has been seen on the Sun [Asc+99; Nak+99] and some other stars [Lóp+16; Pil+14]. Such quasiperiodic pulsations have been mainly observed in coronal X-ray emission or in chromospherically active individual spectral lines [Mit+05; NO01; Sri+08] with periods ranging from a few and up to about 20 minutes [ID12]. White-light flare oscillations have been measured in a number of Sun-like and low-mass stars, but the detected periods were predominantly between 5 and 45 min, and none exceeded 100 min [Pug+16], remaining shorter than the shortest modulation period we found. In contrast, the flare modulation we report here is of the order of several hours, and is observed in white-light.

7.11.3 Stellar dynamos, magnetic field emergence, and polar spots

Large polar spots have long been suspected to exist on fully convective fast rotators, based on indirect methods such as (Zeeman) Doppler Imaging (DI or ZDI), which map spectral modulations to stellar surfaces [Bar+17; KBH17; Mor+08b; Mor+10]. Moreover, a number of simulations predict that strong magnetic fields emerge near the poles in fully convective fast rotators [Gas+13; WB16; Yad+15].

The body of knowledge on magnetic field configurations of rapidly rotating, fully convective stars is still small, not least because the targets are faint and atomic lines that are typically employed for these methods in earlier type stars fade out and the spectrum grows dominated by molecular signatures. However, magnetic fields of up to 7 kG have been reported from fully convective fast rotators [Shu+17], far above the equipartition values suggested by solar-type dynamo models [Pev+03]. The average value is about 5 kG as derived from molecular spectropolarimetry in a sample of nine M1 to M7 dwarfs [AB19]. Among the later M5-M7 dwarfs, cool spots appeared to occupy the majority of the stellar atmosphere, and at a greater depth than in the earlier types.

In ZDI maps of fully convective dwarfs with spectral types $\geq$ M4, a wide range of magnetic filling factors was observed [See+19]. This can be interpreted as manifestation of a bimodal dynamo with either strong bipolar or weak multipolar fields [Mor+10]. The strong bipolar branch is associated with fast rotation, a stable spot configuration, and little differential rotation [Gas+13], suggesting that the stars in our sample belong on this branch, and rotate as near-solid bodies.

Studies on individual stellar systems indicate the presence of both branches. V374 Peg (M4V, $P_{\rm rot} = 0.446$ d [New+16]), showed no dominating polar spot, and weak contrast small

spots on its surface at most [Mor+08b]. GJ 65 A and B, two rapidly rotating fully convective dwarfs with similar properties, revealed very different spot configurations [Bar+17]. While GJ 65 A appeared to have spots in a band around 30 − 40°, but also larger polar spots at 50 − 85°, observations of GJ 65 B are more consistent with extended spots at intermediate latitudes (50 − 56°) and no spots above 70°. GJ 791.2A (M4.5V, $P_{\rm rot}$ = 0.257 d, [New+16]) showed spots at all latitudes, but circumpolar spots were larger than those closer to the equator. The spot structure of LP 944-20 (M9V) could be reconstructured with a dominating large spot at 79°, and marginal detections of smaller spots at lower latitudes [Bar+15].

Finally, [Ber+17] reconstructed a magnetic field loop from giant flare-like bursts of the fast-rotating (2.84 h, [Hal+08]) M8.5 dwarf [Des+12] LSR J1835+3259, one of which appeared to be modulated by rotation. Lacking a precise stellar rotation axis inclination, they could not derive the latitude of the loop's footpoints. However, they recovered the geometry of the loops, and found that if the bursting region occupied ∼ 3 per cent of the stellar surface [Hal+15] – comparable to the sizes of flaring regions in our sample – its magnetic field strength could reach 10 kG.

In this context, our results are further evidence that in fully convective, rapidly rotating dwarfs, strong magnetic field concentrations may indeed emerge at latitudes that are closer to the rotational pole than to the equator, where they create active regions that can erupt in giant flares.

7.11.4 Implications for stellar space weather

Our findings are relevant to exoplanets; several thousand of such planets outside of the Solar System have been discovered up to now [Per18]. Planets residing in the habitable zones around their host stars, that is, orbital distances that allow for liquid water on the planetary surface, are of prime interest. The habitable zone is located close to the host star in the case of fully convective M dwarfs, enabling efficient detection of temperate planets, in comparison to more massive host stars. In order to characterize habitability of temperate planetary surfaces, the longevity and composition of exoplanetary atmospheres needs to be taken into account.

Numerical simulations have shown that flares and coronal mass ejections, which are directly associated with flares in the solar case [WH12], can erode or alter exoplanetary atmospheres, and cause loss of exoplanetary oceans [SBJ16; Til+19]. Our results suggest that the largest flares on such fully convective stars preferably occur at high latitudes. This decreases the flare energy that is received at the planetary habitable zone orbit, but will less affect X-ray and (E)UV emission (Section 7.11.4). Coronal mass ejections are thought to accompany stellar superflares [Dra+13; Ode+20]. However, in contrast to flares, they are only indirectly and rarely observed in stars to date [Mos+19]. If they can escape the strong magnetic field of the star [Alv+18] and propagate at large angles to the planetary orbital plane they would pose a lesser risk to their planets' environments than predicted under the assumption of a Sun-like low latitude distribution ([Til+19], Section 2.4., and our Section 7.11.4). These considerations assume that the planetary orbital plane and the stellar

equator are roughly aligned, which is not well understood for late-type systems (Section 7.11.4).

The impact of flares decreases with increasing flaring region latitude

With the present results, we have the opportunity to estimate the relative flux received by exoplanets, that are potentially hosted by these or similar stars, as a function of flare latitude. All else equal and assuming spin-orbit alignment, placing the flares in our sample at 45° or 80° latitude, the optical flux emitted in the direction of a distant observer in the orbital plane decreases by ∼ 30 and ∼ 85 per cent compared to the same event located near the equator. The exception is the first flare in the light curve of TIC 237 that, when placed at 80°, is visible for a larger fraction of the stellar rotation period due to the relatively large size of the active region. We show the typical relative attenuation of optical flux as a function of flare latitude in Fig. 7.10.

This comparison assumes that compact bright kernels in the stellar photosphere contribute the majority of the blackbody radiation to the flare events. This is true for most solar flares, but it is possible for superflares with particularly large flare region sizes ($\gtrapprox$ 2.5 per cent of the total stellar surface) to saturate the density in the flare loop arcades in the gradual decay phase such that they become optically thick and contribute significantly to, and may even become the dominant source of, white-light emission [HS18; JKH18]. Flare emission from a volume with considerable height, as it is proposed by [HS18], instead of a flat slab on the stellar surface may explain the residual flux in our model fits in the impulsive phase because geometrical foreshortening cannot be applied to an extended 3D loop. Yet the good overall agreement between our model and data in the gradual phase suggests that the flat circular kernel is a satisfactory approximation for the purpose of accurate latitude inference.

However, the more energetic (E)UV and X-ray emission is produced at higher altitudes on the Sun. Spectropolarimetric observations of a large flare on a late M dwarf suggest a similar stratification for the stellar case [Ber+17]. Furthermore, stellar coronae are optically thin, meaning that the X-ray photons originating from them are not subject to the self-shadowing effects that optical emission experiences near the stellar limb. The X-ray flux received by the planets may therefore be much less attenuated than the optical continuum appears in Fig. 7.10. Ultimately, an accurate assessment of flare radiation impact on habitable zone exoplanets will have to include the combined effects of flaring region location, strong magnetic fields, high density, and large pressure gradients in the compact atmospheres of late type stars and brown dwarfs on the 3D emission distribution of superflares.

Coronal mass ejections and energetic particle events

The majority of X-class flares on the Sun are associated with coronal mass ejections (CMEs, [CRZ17]). A similar correlation is expected for stellar superflares [Ode+20], but direct CME observations are missing to date [CO18], perhaps due to differences in the spectral signature between solar and stellar CMEs [Alv+19; Alv+20]. Solar energetic particle (EP) events typically carry a few percent of the energy of the CME they are associated with [Asc+17]. Extrapolating the power law relation between X-ray flux and solar EP

fluence to stellar superflares is poorly constrained so that stellar events may contain one to five orders of magnitude more energy than the largest EP events on the Sun [Her+19]. If stellar EP events associated with the most powerful flares are ejected from the star at high latitudes, as suggested by our observed flares, they may typically not collide with an exoplanet's atmosphere, rendering their effect on habitability smaller than for equatorial flares. However, such particles coming from CMEs and EPs might also be deflected towards the equatorial plane by a strong stellar dipole field [Kay+19]. The impact of particle events also hinges upon their ability to leave the stellar magnetosphere. In M dwarfs, there is evidence that CMEs and EPs may be suppressed by the large overarching dipole field that these stars often possess [Alv+18; Fra+19].

Key uncertainty: Spin-orbit alignment

All of the above assumes that exoplanetary orbital and their host stars' rotation axes are aligned. While there is statistical evidence for spin-orbit alignment in Kepler exoplanet hosts [Maz+15], cases of misaligned systems suggest that alignment is less common than one would expect from protoplanetary disk formation [Bou+18; Hjo+21; Lou+21; WF15]. For small planets around M dwarfs, however, only few measurements exist, all of which indicate spin-orbit alignment [Add+21; Hir+20; Pal+20; Ste+20]. Spin-orbit alignment in low-mass star systems with Earth-like planets is therefore not yet well understood, which ultimately limits our ability to assess the influence of flare emission direction on exoplanetary space weather.

7.12 Summary and conclusions

In a systematic analysis of fully convective stars observed with TESS, we detected four stars that displayed giant flares which were modulated in brightness by the stars' rapid rotation. The exceptional morphology of the modulation allowed us to directly localize these flares between 55° and 81° latitude on the stellar surface. Our findings are evidence that strong magnetic fields tend to emerge close to the rotational poles of fast-rotating fully convective stars, and suggest a reduced impact of these flares on exoplanet habitability.

Our search encompassed the first two years of TESS observations, during which one hemisphere per year was observed. By summer 2021, TESS will have completed its second full-sky scan that will give us the opportunity to put the conclusions of this work to test with more detections of long duration superflares.

The strength of our method lies in its complementarity to spectroscopy and spectropolarimetry not only with respect to the type of scientific information used to infer the stars' magnetic properties, but also regarding the time scales probed. Flares trigger sudden and drastic changes in the local magnetic field configuration. Space-based time series photometry can capture its effects with a few minutes or less resolution. In contrast, ground based (Z)DI reconstructs larger scale changes on time scales of hours and longer.

This work is a step towards understanding spatially constrained flare evolution on stars other than the Sun. Together with multiwavelength flare studies [Gua+19; Kow+13; Mae+21;

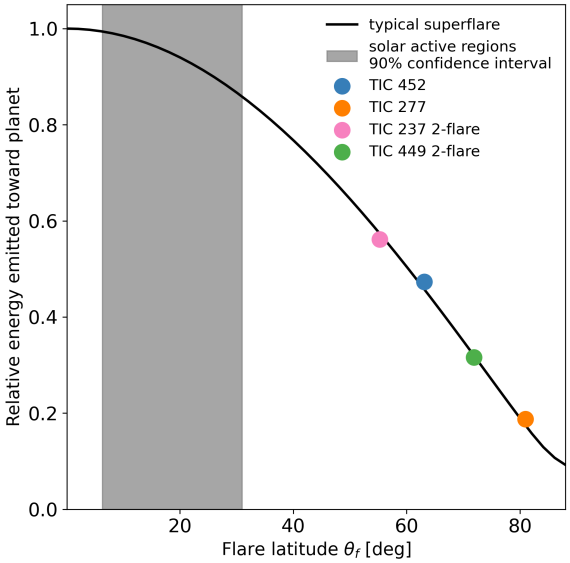

Figure 7.10: Attenuation of optical continuum emission from a flat flaring region as a function of flaring region latitude. Relative optical flare energy emitted in the ecliptic plane of a spin-orbit aligned star-planet system as a function of flare latitudes θ_f for a typical superflare (black line). Colored dots indicate the relative energies at the θ_f derived for the stars in this study. The thermal emission of large flares at high latitudes is significantly attenuated. The grey shaded region indicates the latitudes of 45 solar active regions that comprised less than 0.5 per cent of all active regions but produced about half of all X-class flares in solar activity cycles 21-23 [Che+11].

Nam+20] that provide insight into the propagation of flare events through the stellar atmosphere we may soon see the first fully empirical spatio-temporal flare reconstructions on low mass stars. Such models would help us understand the so far elusive relation between stellar flares, coronal mass ejections, and energetic particle events, and better assess the impact of stellar magnetic activity on the space weather environment of exoplanet systems.

Acknowledgements

The authors would like to thank Uwe Wolter for his thorough reading and constructive criticism that markedly improved the quality of this work. EI acknowledges support from the German National Scholarship Foundation. KP acknowledges support from the German *Leibniz Community* under grant P67/2018. JRAD acknowledges support from the DIRAC Institute in the Department of Astronomy at the University of Washington. The DIRAC Institute is supported through generous gifts from the Charles and Lisa Simonyi Fund for Arts and Sciences, and the Washington Research Foundation. This paper includes data collected with the TESS mission, obtained from the MAST data archive at the Space Telescope Science Institute (STScI). Funding for the TESS mission is provided by the NASA Explorer Program. STScI is operated by the Association of Universities for Research in Astronomy, Inc., under NASA contract NAS 5-26555. This study was enabled by the TESS guest observer program G022164 led by JSP, ERN, JRAD, SJS, and Adam Burgasser. This research has benefitted from the SpeX Prism Library, maintained by Adam Burgasser. We are thankful to Andrew Vanderburg for providing the code used to calculate the inclination probability distributions.

Some of the observations reported in this paper were obtained with the Southern African Large Telescope (SALT). This publication makes use of data products from the Two Micron All Sky Survey, which is a joint project of the University of Massachusetts and the Infrared Processing and Analysis Center/California Institute of Technology, funded by the National Aeronautics and Space Administration and the National Science Foundation. This work has made use of data from the European Space Agency (ESA) mission *Gaia* (https://www.cosmos.esa.int/gaia), processed by the *Gaia* Data Processing and Analysis Consortium (DPAC, https://www.cosmos.esa.int/web/gaia/dpac/consortium). Funding for the DPAC has been provided by national institutions, in particular the institutions participating in the *Gaia* Multilateral Agreement. Based on data from the CARMENES data archive at CAB (INTA-CSIC). This research also made use of the Python packages numpy, pandas astropy, and the cross-match service provided by CDS, Strasbourg.

Data availability

TESS light curves are publicly available through the Mikulski Archive for Space Telescopes (https://mast.stsci.edu/portal/Mashup/Clients/Mast/Portal.html). The Gaia data used in this work are publicly available through the Gaia archive (https://gea.esac.esa.int/archive/). Data from the 2MASS Point Source Catalogs is accessible through the Centre de Donnees astronomiques de Strasbourg (CDS) via the VizieR Service (http://vizier.u-strasbg.fr/cgi-bin/

Table 7.3: Best-fitting results for stars with rotationally modulated superflares that were ruled out or disfavoured. Description of the table rows is the same as in Table 7.2. "h. u." stands for **h**igh **u**ncertainties around the peak in the single flare fit to TIC 449. In the remaining fits, we kept the original uncertainties.

	TIC 452	TIC 449	TIC 449 (h. u.)	TIC 449 (2-flare)	TIC 237 (2-flare)
i (deg)	$49.2^{+3.3}_{-3.3}$	$33.1^{+0.8}_{-0.8}$	$33.1^{+0.8}_{-0.8}$	$33.1^{+0.8}_{-0.8}$	$25.0^{+4.3}_{-3.3}$
$\log_{10} E_{f,1}$ (erg)	$33.546^{+0.024}_{-0.021}$	$33.364^{+0.005}_{-0.005}$	$33.342^{+0.005}_{-0.005}$	$33.342^{+0.006}_{-0.006}$	$34.765^{+0.034}_{-0.024}$
A_1	$0.574^{+0.033}_{-0.027}$	$0.324^{+0.004}_{-0.004}$	$0.629^{+0.009}_{-0.009}$	$0.319^{+0.005}_{-0.004}$	$3.507^{+0.303}_{-0.180}$
$\mathrm{FWHM}_{i,1}$ (min)	$14.3^{+1.1}_{-0.9}$	$50.3^{+0.8}_{-0.8}$	$0.6^{+0.3}_{-0.3}$	$48.4^{+0.8}_{-0.8}$	$17.3^{+0.1}_{-0.1}$
$\mathrm{FWHM}_{g,1}$ (min)	$64.2^{+3.1}_{-3.0}$	$86.4^{+1.2}_{-1.2}$	$57.6^{+0.8}_{-0.8}$	$80.6^{+1.4}_{-1.4}$	$16.6^{+0.3}_{-0.3}$
$\log_{10} E_{f,2}$ (erg)	...	...	...	$32.277^{+0.023}_{-0.022}$	$34.712^{+0.030}_{-0.017}$
A_2	...	...	...	$0.069^{+0.003}_{-0.003}$	$0.660^{+0.047}_{-0.025}$
$\mathrm{FWHM}_{i,2}$ (min)	...	...	...	$42.9^{+3.3}_{-3.1}$	$58.0^{+1.2}_{-1.2}$
$\mathrm{FWHM}_{g,2}$ (min)	...	...	...	$16.1^{+2.5}_{-2.2}$	$96.1^{+1.6}_{-1.6}$
θ_f (deg)	$63.4^{+3.2}_{-3.5}$	$83.2^{+0.8}_{-0.8}$	$70.0^{+1.0}_{-1.0}$	$85.8^{+1.0}_{-1.0}$	$48.3^{+5.5}_{-4.8}$

VizieR?-source=II/246]). CARMENES spectra are publicly available through the CARMENES data archive (http://carmenes.cab.inta-csic.es/gto/jsp/reinersetal2018.jsp). SpeX Prism Library is available through http://www.browndwarfs.org/spexprism. Reduced SALT spectra ara available via Zenodo, under DOI:10.5281/zenodo.4332142. Low-resolution spectra obtained from the FAST spectrograph at the Fred Lawrence Whipple Observatory (used for spectral typing of TIC 452) will be made available online through the Dataverse (preparation of data release in progress, to be completed prior to acceptance). Python code including the flare modulation model, model fitting scripts, Gaussian Process regression scripts, scripts that were used to produce the figures and tables in this manuscript is publicly available through GitHub (https://github.com/ekaterinailin/MalachiteMountains). The code used to calculate the inclination probability distributions was provided by A. Vanderburg for use in this work and is available by request to the authors and with permission from A. Vanderburg.

7.13 Appendix

7.13.1 Alternative and disfavoured fits to the light curves

In our analysis we used different model setups to fit the light curves. The results we achieved using setups that we ruled out or disfavoured are summarized in Table 7.3, and illustrated in Figs. 7.11 7.12, and 7.13 for TIC 452, TIC 449, and TIC 237, respectively.

7.13.2 Limb darkening

The geometric flare modulation model does not account for limb darkening effects that can affect the shape of the modulated flare light curve. The effect increases with flare region size: The larger the fraction of the stellar disk that covered by the flaring region the more do differences in observed stellar flux across the disk take effect.

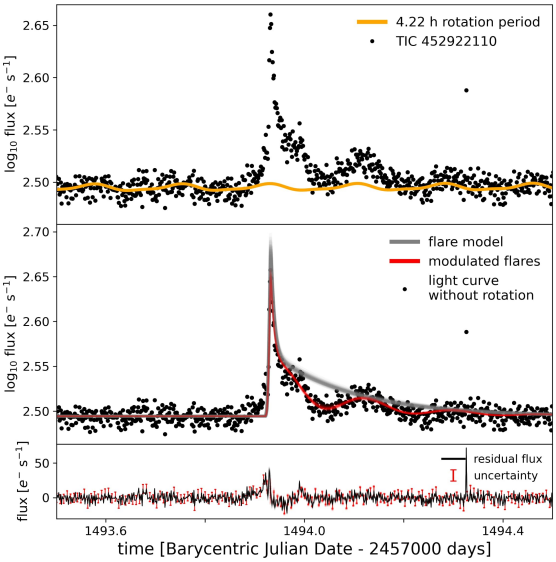

Figure 7.11: TIC 452: Single flare fit with original uncertainties. The fit yields a flare latitude of 63°, consistent with the fit in Fig. 7.6 B that adopts increased uncertainty on the flare peak.

In Fig. 7.14, we illustrate a scenario that represents the flare with the largest flaring region in our sample (first flare on TIC 237), which is comparable to some of the largest region sizes derived for flares on fully convective dwarfs in the literature [Sch+14b; Xin+21]. The effect is negligible compared to the noise in the light curves in our sample.

7.13.3 MCMC model fits

In Figs. 7.15–7.18, we show the posterior distributions for the MCMC fits with the best-fit results quoted in Table 7.2. The upper left density plot in each figure shows the partial degeneracy between θ_f and i, which is best seen in TIC 277 (Fig. 7.15), where the empirical prior for i was non-Gaussian. In the distributions for TIC 277, TIC 449, and TIC 237, there are some correlations worth noting:

The flare parameters A_1, $\mathrm{FWHM}_{i,1}$, and $\mathrm{FWHM}_{g,1}$ of the first event in TIC 449 (Fig. 7.17) are sensitive to the uncertainty on the flare peak time $t_{f,1}$, but the flare latitude is not affected. The tail in the distribution of $\mathrm{FWHM}_{g,2}$ suggests that the secondary flare could be fit with a single exponential in the decay phase.

In TIC 277, inclination and flare amplitude are correlated. Higher inclination implies stronger geometrical foreshortening. The distribution suggests that there are three particularly favorable solutions, depending on A, which seems counterintuitive at first. But since higher A implies a larger flaring region, we can interpret the solutions as combinations of different flare region sizes viewed at certain inclinations near the pole that result in comparable light curve morphologies.

Finally, in TIC 237, θ_f has a tail towards lower latitudes that correlates with higher flare amplitudes A_1 and A_2. However, as we can see in Fig. 7.8, rotational modulation in the decay

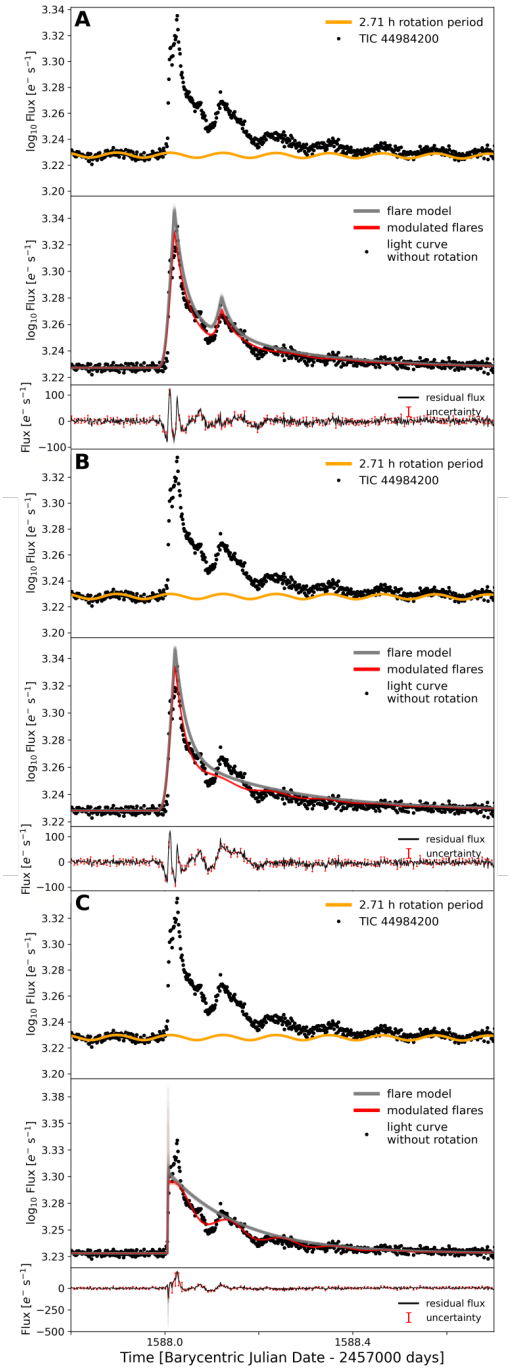

Figure 7.12: Alternative and ruled out fits to the long-duration flare on TIC 449. **A**: two-flare fit with original uncertainties. The rotational modulation in the decay phase is underestimated, leading to an overestimated flare latitude of $\sim 86°$. **B**: single flare fit with original uncertainties. This solution did not capture the secondary peak, or the degree of modulation in the decay phase. Solutions A and B were ruled out. **C**: single flare fit with increased uncertainties. Relaxing the constraints posed by the impulsive flare peak led to an improved fit of the secondary peak and the decay phase over the solution in B. The fit suggests $\theta_f \approx 70°$, $\sim 2°$ lower than our preferred estimate (Fig. 7.6 C).

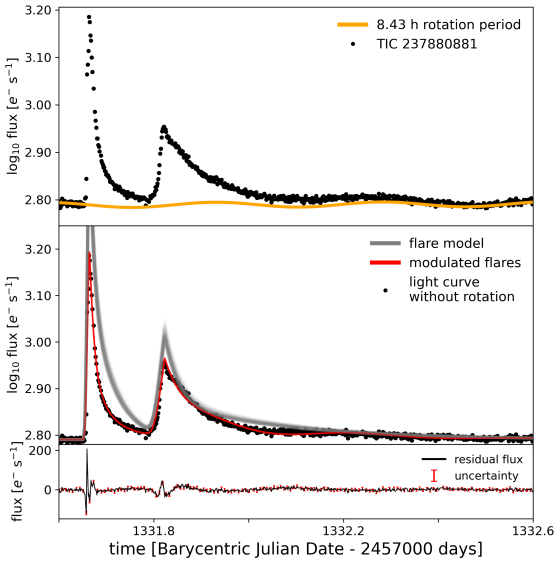

Figure 7.13: TIC 237: two-flare fit with original uncertainties. The decay phase of the second long duration flare is not well represented by the best fit solution, suggesting a rotational modulation that is too strong. This leads to an underestimated flare latitude of 48°. This solution was ruled out.

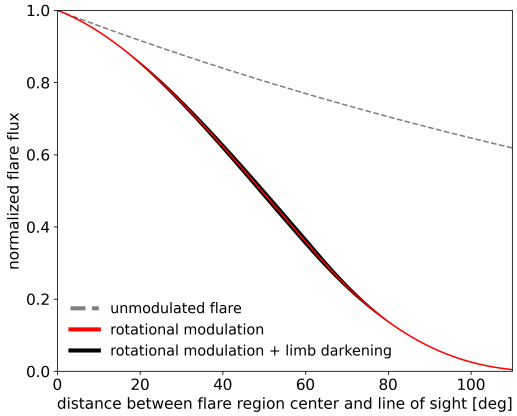

Figure 7.14: Linear limb darkening applied to an exponential decay of a large (angular radius of 30°) flaring region that moves across the equator from the line of sight to and over the limb. Grey dashed line: unmodulated exponential flare decay with an e-folding time scale equal to one full stellar rotation. Red line: geometric foreshortening applied to the unmodulated flare. Black area: Geometric foreshortening and linear limb darkening applied to unmodulated flare with limb darkening coefficients between 0.5 and 1.5.

phase of the event would become more and more pronounced with decreasing latitude, thereby breaking the partial degeneracy in A_1, A_2 and θ_f.

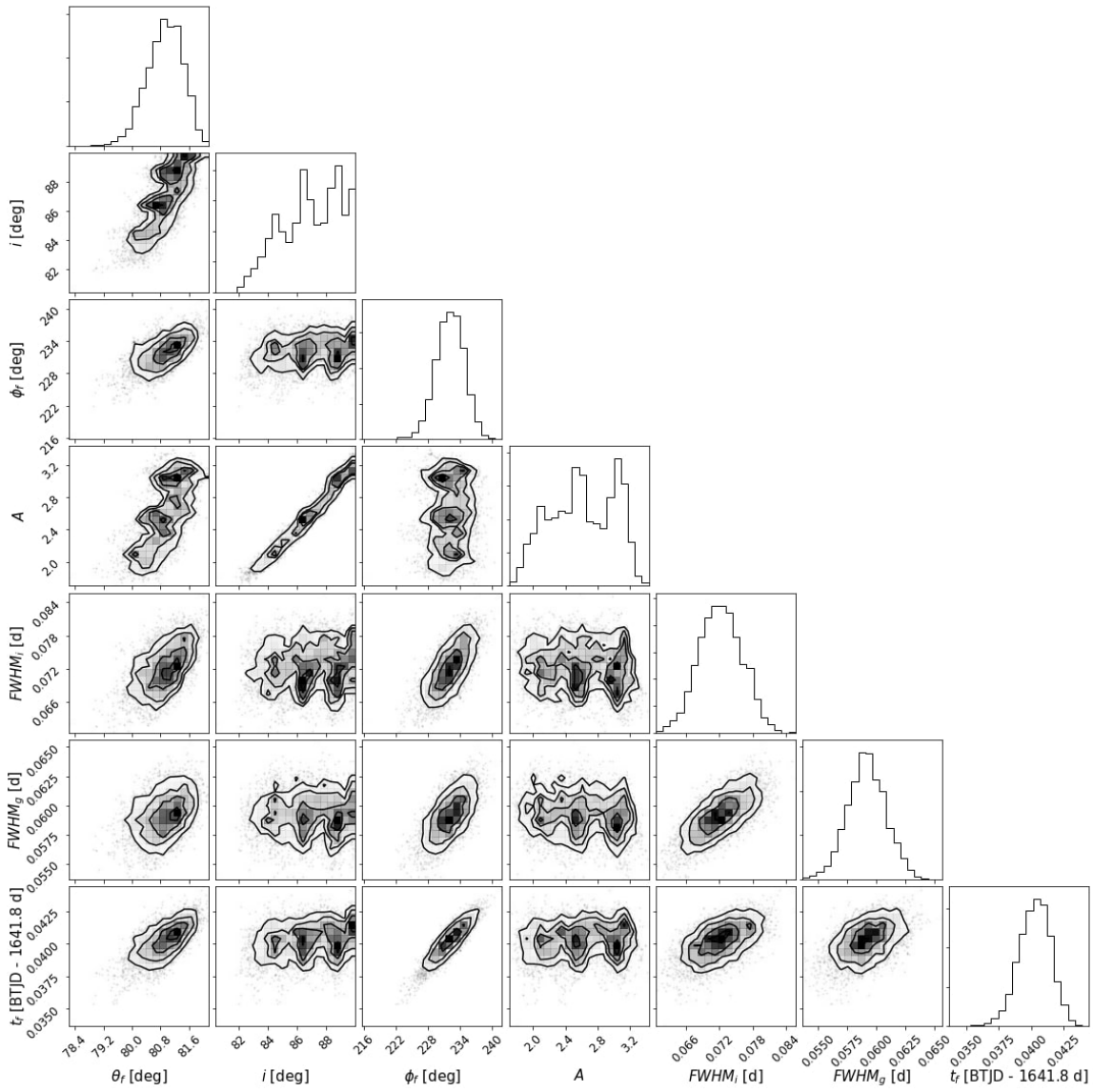

Figure 7.15: MCMC posterior distributions (density plots) and marginalized distributions (histograms) for the flare fit to the light curve of TIC 277 in Fig. 7.6 A.

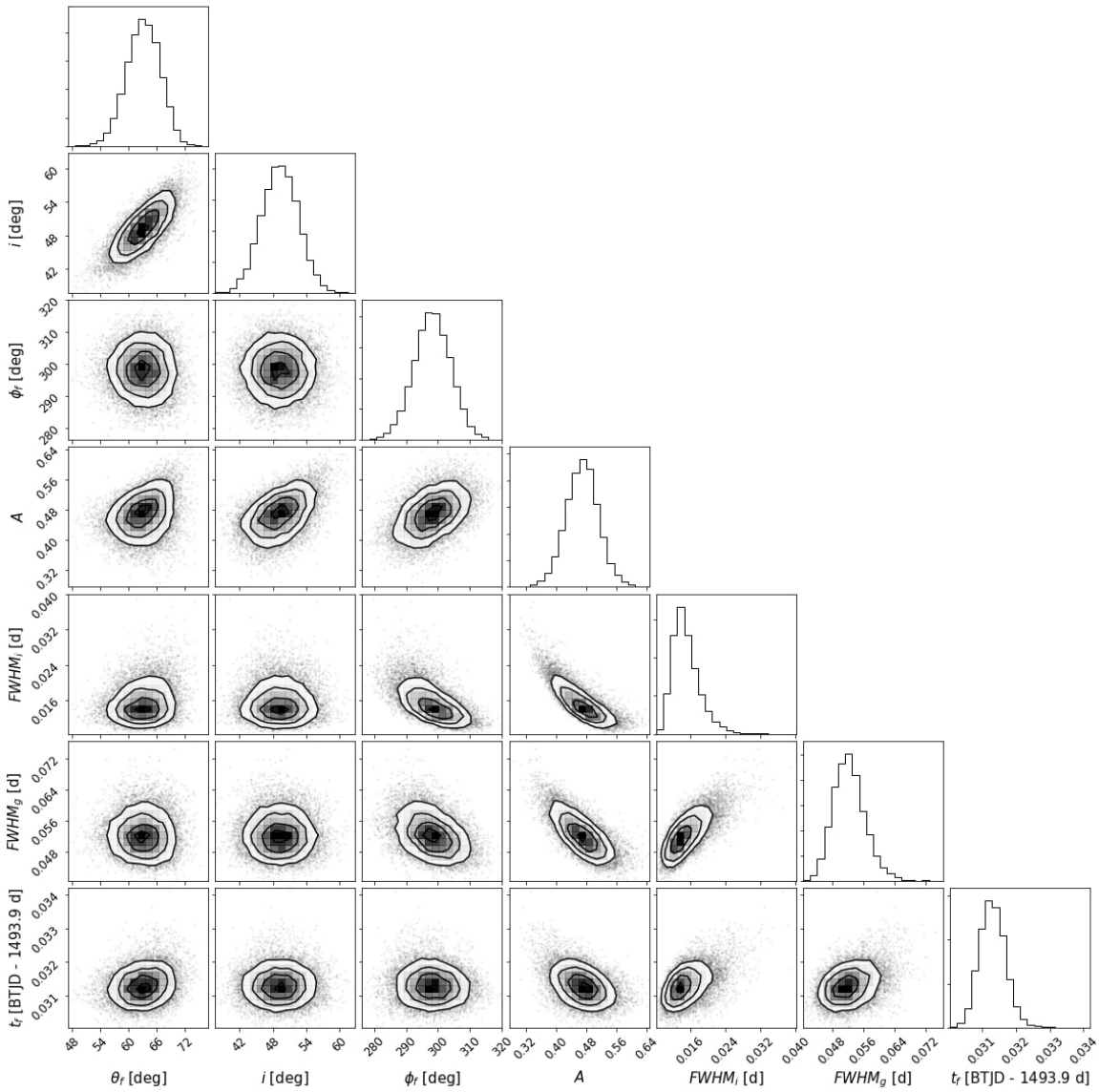

Figure 7.16: MCMC posterior distributions (density plots) and marginalized distributions (histograms) for the flare fit to the light curve of TIC 452 in Fig. 7.6 B.

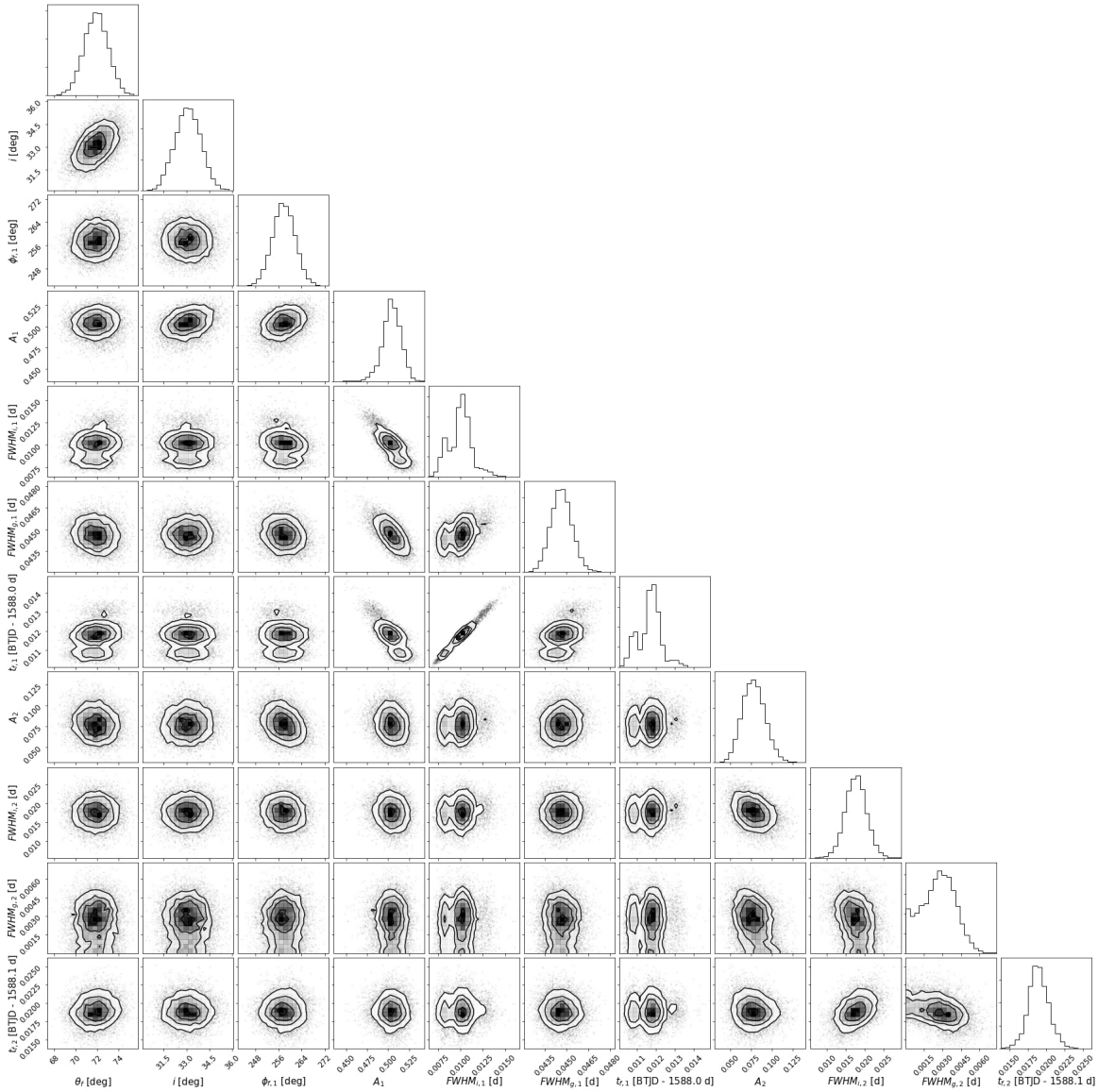

Figure 7.17: MCMC posterior distributions (density plots) and marginalized distributions (histograms) for the flare fit to the light curve of TIC 449 in Fig. 7.6 C.

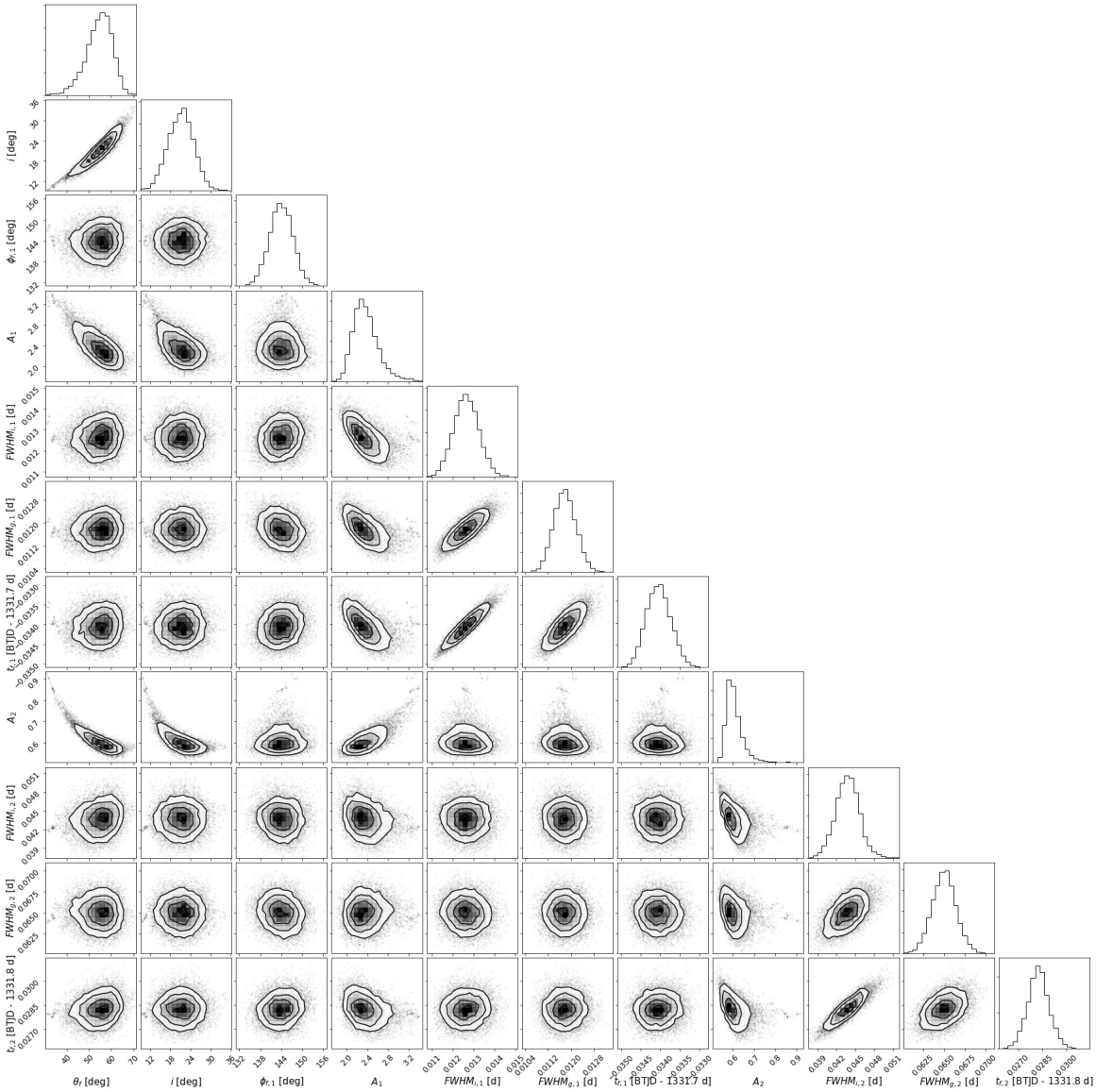

Figure 7.18: MCMC posterior distributions (density plots) and marginalized distributions (histograms) for the flare fit to the light curve of TIC 237 in Fig. 7.6 D.

8 Searching for flaring star-planet interactions in AU Mic TESS observations

Ilin, E. & Poppenhäger, K.
Monthly Notices of the Royal Astronomical Society, Volume 513, Isuue 3, Pages 4579-4586 (2022).
DOI: 10.1093/mnras/stac1232

Abstract

Planets that closely orbit magnetically active stars are thought to be able to interact with their magnetic fields in a way that modulates stellar activity. This modulation in phase with the planetary orbit, such as enhanced X-ray activity, chromospheric spots, radio emission, or flares, is considered the clearest sign of magnetic star-planet interaction (SPI). However, the magnitude of this interaction is poorly constrained, and the intermittent nature of the interaction is a challenge for observers. AU Mic is an early M dwarf, and the most actively flaring planet host detected to date. Its innermost companion, AU Mic b, is a promising target for magnetic SPI observations. We used optical light curves of AU Mic obtained by the Transiting Exoplanet Survey Satellite to search for signs of flaring SPI with AU Mic b using a customized Anderson-Darling test. In the about 50 days of observations, the flare distributions with orbital, rotational, and synodic periods were generally consistent with intrinsic stellar flaring. We found the strongest deviation ($p = 0.07,\ n = 71$) from intrinsic flaring with the orbital period of AU Mic b, in the high energy half of our sample ($ED > 1$ s). If it reflects the true SPI signal from AU Mic b, extending the observing time by a factor of $2 - 3$ will yield a $> 3\sigma$ detection. Continued monitoring of AU Mic may therefore reveal flaring SPI with orbital phase, while rotational modulation will smear out due to the star's strong differential rotation.

8.1 Introduction

Flares are electromagnetic explosions in the stellar corona that are driven by the dynamics of the surface magnetic fields [BG10]. They can be triggered intrinsically by the star in isolation, but also by magnetic star-planet interaction (SPI). In SPI flares, the event is induced by the re-connection of stellar and planetary magnetic field lines [FS19; Lan18; Sau+13]. For this to occur, the planet must revolve around the star in close orbit, so that it moves within the stellar Alfvén zone for at least a fraction of its orbit. When the planet is within the Alfvén zone, the magnetic field and the energy transported along the field lines as particles or waves can fall back on to the star, whereas outside of it it would be carried away by the stellar wind pressure.

Several studies of individual systems with close-in and eccentric Hot Jupiters report excess flaring in phase with the planet or close to periastron [Mag+15; Pil+11; Shk+05], but in light of many non-detections of excess flares in similar systems [Fig+16; FS19], flaring SPI remains an elusive phenomenon. One interpretation is that the interaction is so weak and intermittent that the system has to be observed for many orbits of the interacting planet before SPI flares become measurable against the background of intrinsic, stochastic flares [Lan09; Sau+13; Shk+08; Str+15].

Recently, AU Mic, an M0-M1 [Gai+14; PM13] pre-main sequence dwarf star, and a member of the β Pic young moving group, which is $16 - 29$ Myr old [BJ14; BJ16; BMN15; Mal+14; MB14; Mir+20; Shk+17], was discovered to be a favorable candidate for magnetic star-planet interactions [Kav+21]. The system hosts two planets in close orbits near a 2:1 mean-motion resonance, AU Mic b and AU Mic c [Mar+21; Pla+20], with masses $M_b = 11.7 \pm 5.0 M_\oplus$ and $M_c = 22.2 \pm 6.7 M_\oplus$ [Zic+22]. Several papers reported system parameters of AU Mic based on photometry from the Transiting Exoplanet Survey Satellite (TESS, [Ric+15]), the CHEOPS mission [Ben+21b], and HARPS [May+03] spectroscopy [Cal+21a; Gil+22; Pla+20; Zic+22], which are mutually compatible within uncertainties. In this work, we use the determinations by [Gil+22], who based their analysis on the complete TESS photometry.

AU Mic rotates at a 4.85 ± 0.03 d period [Gil+22], showing strong solar-like differential rotation, a strong, mostly poloidal large-scale magnetic field of > 400 G, and several activity indicators that vary in phase with the star's latitude-dependent rotation periods [Kle+21]. Optical light curves obtained by TESS confirm previous observations [KDL99; Red+02; Rob+01] that AU Mic is actively flaring [Mar+21].

AU Mic b is a Neptune-sized planet ($R_p = 4.19 \pm 0.24 R_\oplus$, [Gil+22]) that was first discovered using TESS photometry [Pla+20] with an orbital period of $P_{orb} \approx 8.46$ d [Gil+22]. The system shows strong transit timing variations, but the mean orbital period is consistent with the instantaneous P_{orb} [Sza+22] for the purpose of this study. [Kav+21] predict magnetic SPI with AU Mic b to be observable in the radio regime, a signal indicative of a phenomenon similar to the planet-moon interaction observed within the Jupiter-Io system [Sau+13]. [Kav+21] found that, based on reconstructions of AU Mic's magnetic field and mass loss rate, AU Mic b could reside in the sub-Alfvénic regime. If this is true, flaring SPI is also possible [Lan18]; a recent study even claimed to have visually identified hints of such an interaction in TESS data [CPM22]. In fact, AU Mic is the most actively flaring star among all currently known exoplanet hosts (Ilin et al. in prep.), implying that the footpoint of interaction may frequently pass regions where high magnetic tension has built up, and therefore trigger flares more easily than in other star-planet systems.

Two further reasons favor AU Mic in the search for flaring SPI: First, AU Mic b's orbit is not synchronized with the stellar rotation, so that confusion with rotational modulation of intrinsic flaring activity is unlikely. Second, the system is observed equator-on. The footpoint of interaction would therefore move in and out view of the observer regardless of its latitude on the star.

When observational biases are taken into account, the absence of flaring SPI signal can be informative, too. It favors models with strong stellar winds that produce a small Alfvén

zone [Kav+21]; weak planetary magnetic fields, and steady energy transfer channels between planet and star rather than eruptive, flaring ones (see Section 8.4).

In this work, we searched the TESS light curves of AU Mic for statistically reliable signs of flaring SPI. We present our light curve de-trending and flare finding method in Section 8.2.2, and the resulting flare catalog in Section 8.2.2. In Section 8.3, we show how we can combine flare samples from general time series measurements into a homogeneous data set, and apply this method to test whether flaring SPI signal is present in the TESS observations. The main result is shown in Table 8.2. We discuss our results and present our conclusions in Sections 8.4 and 8.5.

8.2 Data

8.2.1 TESS photometry

The Transiting Exoplanet Survey Satellite (TESS, [Ric+15]) is an all-sky mission that began operations in 2018, and completed its first full sky scan in April 2020. It is still observing at the time of writing, collecting nearly continuous photometric times series in the 600-1000 nm band for ~ 27 d in each observing Sector. Light curves of 232 763 stars observed in 2 min cadence in the first two years of operations (Sectors 1 to 26) are currently available on the Mikulski Archive for Space Telescopes[11]. From Sector 27 on, 1000 targets were observed at even higher 20 s cadence each Sector. AU Mic was observed in Sector 1 at a 2 min cadence, and in Sector 27 at a 20 s cadence. The light curves reveal strong rotational variability from starspots, vigorous flaring, and transits of two planets, AU Mic b and c [Mar+21; Pla+20].

8.2.2 Light curve de-trending and flare finding

Stellar light curves are time series of flux measurements that vary due to both astrophysical and instrumental effects. Flares are only one of many phenomena like spot variability, transits, eclipses, bursts and dips that can be detected in the data. Accurate automated flare detection algorithms are still challenging to design [Vid+21], not least due to this intrinsically heterogeneous morphology of light curves. We applied an iterative three-step algorithm to remove all but the variations caused by flares, and derived a realistic noise estimate (Section 8.2.2). We then used a σ-clipping procedure to mark flare candidates and calculate their properties (Section 8.2.2). The resulting flare catalog is presented in Section 8.2.2.

De-trending

Typical flare times range from a few minutes to a few hours, and rarely exceed one day in duration. Most stellar variability occurs on longer time scales, except for ultrafast rotational variability in some stars [Ili+21b]. The light curve de-trending presented here was implemented with a broad spectrum of Kepler [Bor+10] and TESS light curve types in mind. Our

11 as of Mar 16, 2022

method consists of three steps, each of which removed variability on decreasing time scales while preserving the flare signal:

1. We fit and subtract a third order spline function that goes through the start and end of any light curve portion that has no gaps longer than 2 h, and through an averaged flux point every 6 h in between[12]. This step removes long term trends as well as starspot variability on time scales of several days. If the light curve portion is shorter than 5 d, this step is skipped.

2. We iteratively remove strong periodic signal on time scales between 2 h and 5 d from the light curve. Each iteration first masks outlier points using a padded sigma-clipping procedure. For this step, single outliers above 3.5σ are masked as pure outliers. Series of $n > 1$ data points above 3.5σ are masked as flare candidates, and padded with rounded $\sqrt{n}$ masked points before the outliers to capture slow rise phases, and rounded $2\sqrt{n}$ after the series to capture a potential extended decay phase that flares often display. Then we calculate a Lomb-Scargle periodogram [Lom76; Sca82] for the light curve, and perform a least-square fit with a cosine function using the dominant frequency in the periodogram as a starting point. The cosine fit is then subtracted from the light curve. We iterate five times or until the dominant peak's signal-to-noise ratio drops below 1.

3. Finally, we again apply the padded outlier clipping, and smooth any remaining variability that is not sinusoidal, first with a 6 h and then with a 3 h window 3rd order Savitzky-Golay [SG64] filter implemented in `lightkurve` as `LightCurve.flatten`.

These three steps can sometimes miss the very edges of the light curve, leaving small exponential drops or rises in the flux that affect the quiescent flux level calculation and/or produce false positive flare detections. If the first or the last data point is a 1σ outlier in the de-trended light curve, we fit an exponential growth or decay function to these fringes.

Finally we estimate the noise in the de-trended light curve using a rolling standard deviation with a 2 h window after padding outliers in the aforementioned way, but now above 1.5σ[13]. We interpolated the masked outliers to arrive at a noise in the flare regions that is informed by the flux uncertainty in an adjacent light curve portion.

The result for the light curve in Sector 1 is shown in Fig. 8.1. This method is based on `AltaiPony` [Ili21], an open-source Python toolkit for flare-focused light curve analysis of Kepler and TESS data, and was inspired by the iterative approach in [Dav16], who searched the entire Kepler catalog for flares. We tested this method on a variety of synthetic and real light curves in the TESS and Kepler archives, so that it can be applied to a larger sample. We provide the de-trending module and an example script for the use of this method with TESS short cadence light curves in this project's Github repository[14].

12 30 h for stars less active than AU Mic
13 2.5σ for stars less active than AU Mic
14 https://github.com/ekaterinailin/flaring-spi/tree/master/notebooks, accessed June 4, 2022

Table 8.1: Confirmed flare events in the TESS light curves of AU Mic, sorted by orbital phase of AU Mic b. The remainder of the table is available in electronic form.

Sec.	t_s [BTJD]	t_f [BTJD]	orb. phase	a	ED [s]
27	2058.2378	2058.2526	0.001	0.007	3.48 ± 0.04
27	2058.2584	2058.2593	0.004	0.002	0.10 ± 0.01
27	2041.3551	2041.3572	0.006	0.002	0.23 ± 0.02
1	1330.4514	1330.4709	0.007	0.003	1.65 ± 0.03
27	2041.3690	2041.3734	0.008	0.003	0.70 ± 0.03
27	2041.6186	2041.6202	0.038	0.002	0.15 ± 0.02
27	2050.1252	2050.1259	0.043	0.003	0.10 ± 0.01
27	2050.1724	2050.1731	0.048	0.001	0.07 ± 0.01
1	1330.8028	1330.8250	0.049	0.002	1.72 ± 0.06
27	2058.7093	2058.7148	0.057	0.004	0.74 ± 0.03

Flare finding

We searched the de-trended light curves for flare candidates. For each light curve, we first find an iterative median, and then apply the threshold method introduced by [CBH15] that requires three consecutive positive outliers 3σ above median for a candidate detection. To these data points we then add subsequent data points until one of them falls below a 2σ above median threshold to avoid cutting off detectable parts of the flare decay phase. This series of data points is then flagged as a flare candidate. For each flare, the pipeline returns the flare start and end points, duration, amplitude, and equivalent duration (ED) with uncertainties. The ED is the integrated flare flux F_{flare} divided by the median quiescent flux F_0 of the star, integrated over the flare duration [Ger72]:

$$ED = \int \mathrm{d}t \, \frac{F_{flare}(t)}{F_0}. \tag{8.1}$$

We tested our flare-finding procedure on a range of both real and synthetic light curves that covers several typically observed spot-induced variability signal patterns, and that contains flare signatures between ones that barely exceed the detection threshold to the largest flares we typically observe. Since the light curve of AU Mic shows variability not only with rotation but also on shorter time scales comparable to those of flares, we confirmed all flare candidates by eye. In cases where the flare shape was not well captured by the algorithm, we manually corrected the flare duration by adding or subtracting data points to or from the detection. We treated the transit light curves of AU Mic b and c manually, too. Spot occultations by the transiting planet and small flares have similar shapes and time scales, so that we picked flares that occurred within transits directly by eye on a case by case basis.

Flare catalog

We confirmed 75 flares in Sector 1, and 114 flares in Sector 27 (see bottom panels in Fig. 8.1 for examples). We found more flares in Sector 27 because its six times higher observing

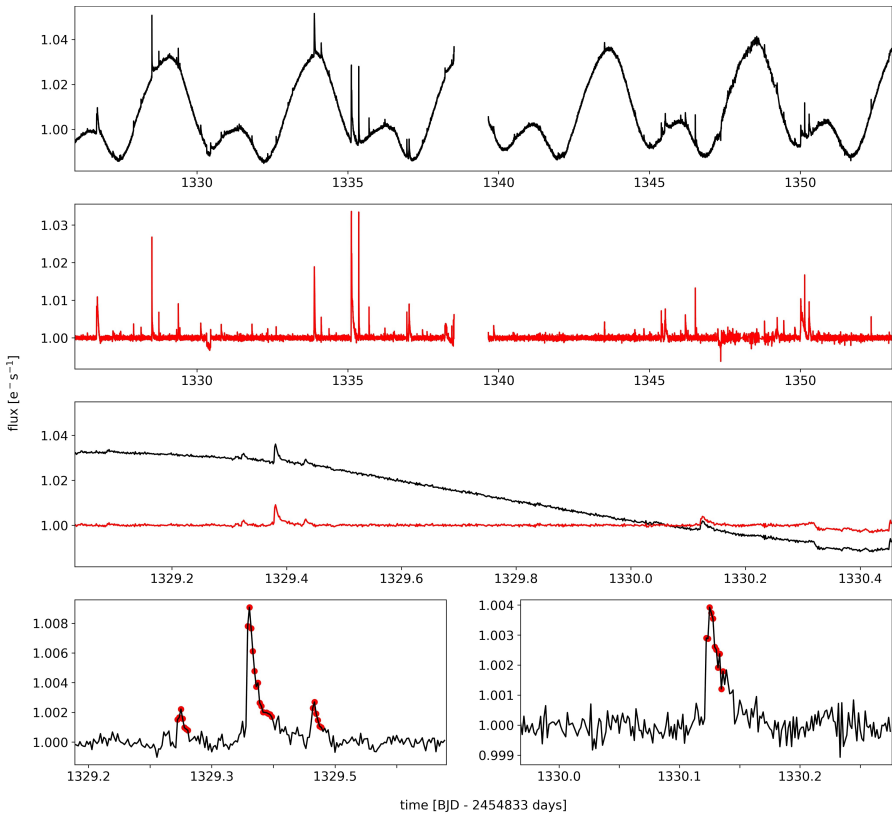

Figure 8.1: Subset of flares detected in the TESS light curve of AU Mic, Sector 1. Top panel: PDCSAP_FLUX light curve. Second panel from the top: De-trended light curve. Third panel from the top: section from the PDCSAP_FLUX (black) and de-trended (red) light curve. Two bottom panels: de-trended light curves of flares confirmed in the panel above. The red dots indicate the data points that mark the flares.

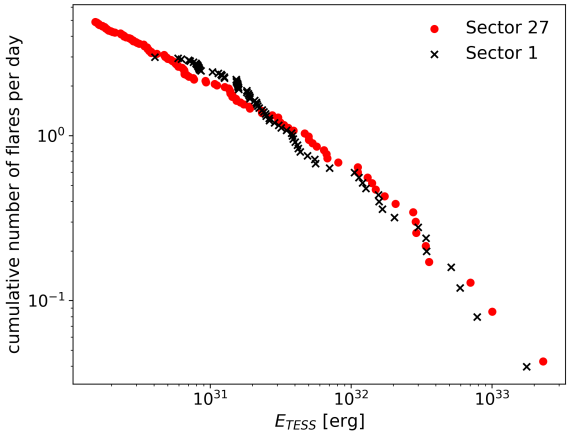

Figure 8.2: Cumulative flare frequency distributions (FFDs) obtained from the two TESS light curves of AU Mic. E_{TESS} is the flare energy emitted in the TESS band.

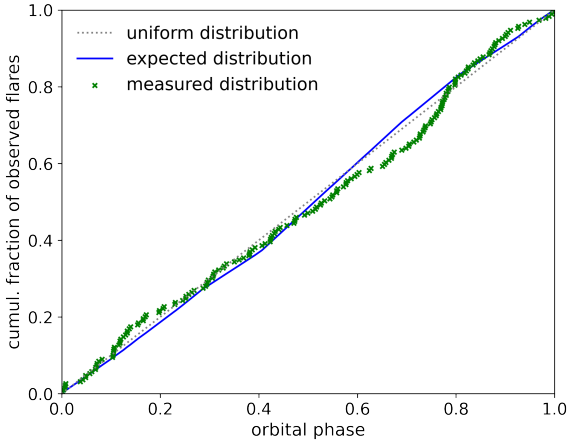

Figure 8.3: Cumulative distribution of the full sample of flares with orbital phase of AU Mic b (Sectors 1 and 27, green crosses). Phase 0 indicates the planet's transit mid-time. The underlying distribution is uniform (grey dotted line). In the data, however, it is modulated by gaps in the phase coverage and the different detection thresholds of the two light curves. The modulated distribution (blue line) is used as null hypothesis in the A-D test.

cadence lowers the detection threshold, which can be seen in the cumulative flare frequency distributions for both Sectors (Fig. 8.2). Overall, we confirmed fewer flares than reported by [Mar+21] who found 162 and 157 flares in Sector 1 and 27, respectively. However, we confirmed almost twice as many flares as [Gil+22]. We attribute these differences to the respective detection methods. [Mar+21] flagged single 2.5σ outliers as candidates, while we required three consecutive data points 3σ above the noise. [Gil+22] used a Bayesian template comparison method to detect probable candidates, which slides a Gaussian rise and exponential decay flare template over the data, and returns the probability of belonging to a flare for each data point. Therefore, their method selects flares that fit the template even if they are small, while our method is more senstive to flares that do not conform to the classical shape but misses flares that don't pass the sigma threshold. Table 8.1 lists the confirmed flare events with their respective start and finish times t_s and t_f, orbital phase of AU Mic b at t_s, amplitude a and ED.

8.3 Flare rate variation with rotational, orbital, and synodic phases

In analogy to solar flares, stellar flares are thought to occur in the vicinity of active regions on the stellar surface, where magnetic field lines emerge, and magnetic energy can accumulate. AU Mic is a young, extremely active flaring star that is covered with large active regions [KR20; LW94; Pla+20], and possibly a multitude of magnetic loops across the entire corona [CWM13].

Flares on early M dwarfs tend to occur randomly in the various active regions which cover the stellar surface [Doy+18; Doy+19]. A variation of flaring rate with stellar rotational

Table 8.2: Median p-values of the custom A-D tests for the orbital, rotational and synodic periods of AU Mic (and AU Mic b) calculated using 20 different start phases. Smallest p-value is boldfaced. There is no significant deviation from uniform flaring in time with either of the periods. n: number of flares in sample.

Sec.	sample	n	$p(P_{orb})$	$p(P_{rot})$	$p(P_{syn})$
both	$ED > 1$ s	71	**0.07**	0.79	0.37
	$ED < 1$ s	118	0.52	0.78	0.75
	total	189	0.21	0.57	0.43
1	$ED > 1$ s	38	0.27	0.71	0.48
	$ED < 1$ s	37	0.56	0.63	0.44
	total	75	0.20	0.64	0.71
27	$ED > 1$ s	33	0.44	0.11	0.48
	$ED < 1$ s	81	0.52	0.53	0.68
	total	114	0.53	0.24	0.68

phase can be caused by an extremely active region that rotates in and out of view of the observer. A very inactive region that suppresses flaring compared to the rest of the stellar surface is also conceivable, for instance in a region wherein the magnetic field is strong enough to sufficiently suppress convection that is required to produce flares. In both cases, flare rates would be elevated or decreased for a fixed fraction of the rotation period, which depends on the inclination of the star and the latitude of the active region. This signal is then smeared out by differential rotation [HL21]. Notably, a non-uniform rotational phase distribution of flares involves only the star.

When a magnetized planet that orbits inside the Alfvén surface of the star comes into play, it can introduce a deviation from a uniform flare distribution in time via magnetic star-planet interaction. The magnetic field lines that connect the star's to the planet's magnetic field channel energy from the planet to the star, that is then dissipated via flares. The footpoint of the connection field lines move across the stellar surface as the planet orbits the star. If the stellar properties at the location of these footpoints are negligible or sufficiently uniform not to affect the interaction, excess flares can be observed whenever the footpoint is in view, in phase with the orbital period P_{orb}. If, however, the stellar properties at the footpoint's location matter, this occurrence of excess flares will be modulated with the stellar rotation period P_{rot}. Then the relevant period is the synodic period P_{syn} [FS19], with

$$P_{syn} = \left| \frac{1}{P_{rot}} - \frac{1}{P_{orb}} \right|^{-1} . \tag{8.2}$$

In summary, if an inhomogeneous distribution of active regions on the stellar surface, or the interaction of AU Mic with the innermost planet takes place, triggering flares in the observable regime, the flaring rates in phase with P_{rot}, P_{orb} or P_{syn} will deviate from a uniform distribution. Our null hypothesis is that no rotational, orbital, or synodic dependence is present. We test if we have to reject this hypothesis using a customized Anderson-Darling test (A-D test, [AD52; Ste74]), a non-parametric goodness-of-fit test suited for continuous variables, such a flare frequencies. The A-D test is more sensitive to the ends of the distribu-

tion, i.e. phases near 0 or 1, than the more widely used Kolmogorov-Smirnov [Kol33; Smi48] test. Since the starting phase should ideally not affect the outcome of the test, we choose the A-D test.

With this method we can analyse N light curves that cover observing periods that do not overlap (to avoid double counting of flares), and each of which has the same flare detection threshold throughout the observing time of the light curve. It is permissible, however, that this threshold varies from light curve to light curve, as is the case in our data set for AU Mic.

After having searched all light curves for flares (see Section 8.2.2), we calculate the deviation from a uniform underlying flare rate distribution with orbital, rotational, and synodic phase each using a customized A-D test in six steps:

1. Calculate ϕ, the expected frequency distribution of flares per phase (expected distribution for short), using all valid data points in the de-trended light curves, taking into account the different observing cadences, and detection thresholds.

2. Sample N flare occurrence phases x_i with $i \in [1, N]$ from the expected distribution ϕ to get a distribution of flare phases, where N is the total number of flares in the data. This step generates a list of flares that are uniformly distributed across all phases, modulated only by the phase coverage of the observations, and the detection thresholds of the light curves. This list is a sample from the expected distribution we test against (see Fig. 8.3).

3. Repeat the previous step to obtain a large number of samples, and calculate the A-D statistic A^2 for each of them using the cumulative form $\hat{\phi}(x_i)$ of the expected distribution, where the x_i are sorted in ascending order.

$$A^2 = -N - \sum_{i=1}^{N} \frac{2i-1}{N} \Big(\log(\hat{\phi}(x_i)) + \log(1 - \hat{\phi}(x_{N+1-i})) \Big) \tag{8.3}$$

   In this study, we generated 10 000 samples for each test. We also varied the start phase of the distribution between 0 and 1 with a step size of 0.05. While the A-D test is less sensitive to the start phase than the K-S test, we still observed a scatter in the outcomes of the tests. We accounted for this by calculating the median of all start phase varied test results.

4. Take all N flare occurrence times from the TESS data, and derive their phases $x_{i,obs}$ with $i \in [1, N]$.

5. Sort all $x_{i,obs}$ by phase in ascending order using the same start phase as the expected distribution.

6. Finally, compare the A^2_{obs} value of the observed distribution of flare phases against the expected distribution of A^2, and calculate the significance level (p-value) of the difference.

The p-values for the A-D test obtained from the above procedure are shown in Table 8.2. No choice of Sector, energy split, or period resulted in a consistently significant deviation from uniform flaring in time. The strongest deviation from uniformity, a $\sim 1.5\sigma$ detection ($p = 0.07,\ n = 71$), is seen with P_{orb} in the flares whose energy exceeds $ED = 1$ s, that is, approximately $2.3 \cdot 10^{31}$ erg in the TESS band. The p-values in this subsample were consistently < 0.175 at all 20 start phases, which is not the case for any other subsample in Table 8.2.

The observed distribution of flares does not deviate significantly from a uniform distribution of flares with orbital or synodic period. [HL21] detected flaring periodicity in 3 out of 284 late K and M dwarfs observed with TESS, and concluded that it may be rare, difficult to detect, or both.

Because AU Mic is seen nearly equator-on, the non-detection with P_{rot} implies a uniform distribution of flares with stellar longitude. The spot structure evolved between Sector 1 and 27 [Mar+21], but during each Sector spot patterns were stable over several rotation periods of the star [Sza+21]. However, considering each Sector separately does not reveal a significant deviation from uniform flaring with longitude. This observation is consistent with most M dwarfs that were searched for rotational periodicity [Doy+18; Doy+19].

We also applied the above method to test for active longitudes excited by the close 4:7 P_{rot}:P_{orb} commensurability [Cal+21a; Sza+21] of AU Mic and AU Mic b. The excitation of resonant oscillations in the stellar magnetic field of close-in star-planet systems was predicted by [Lan22]. We found no significant deviation from uniformity with the resonance period $P_{rot}/4$. However, for the AU Mic system specifically, [Lan22] estimate that this excitation will not occur due to the planet's relatively large distance from its host, consistent with our result.

8.4 Discussion

If the tentative signal with orbital phase ($p = 0.07,\ n = 71$) truly stems from flaring SPI with AU Mic b, we can estimate the required observing time to confirm the detection. In our estimate, we doubled and tripled the sample by introducing one and two additional flares between each pair $(x_i, x_{i+1}),\ i \in [1, N]$, of real flares, placing them at equal distance from each other and smearing out the exact occurrence phase with a Gaussian with a standard deviation of $(x_{i+1} - x_i)/2$ and $(x_{i+1} - x_i)/3$, respectively. We executed the A-D test procedure from Section 8.3 on the new $2N$ sized flare distribution, sampling $2 \cdot 10^5$ and $3 \cdot 10^5$ A^2 values for each start phase, instead of 10^4, to obtain the critical values in the high significance tail of the A^2 distribution. Assuming that the structure of the phase distribution remains the same over time, doubling the sample size yields $p \approx 0.003$; tripling yields $p \approx 0.0008$. Therefore, since the deviation was found in the higher energy flares in our sample, monitoring AU Mic for another $50 - 100$ d with instruments with the same or somewhat lower photometeric precision and observing cadence as TESS may suffice to detect flaring SPI in this system with $> 3\sigma$ significance.

If the signal is a fluke in the data, the observed absence of flaring SPI signal can be explained in two ways – observational biases that impede detection, and physical reasons

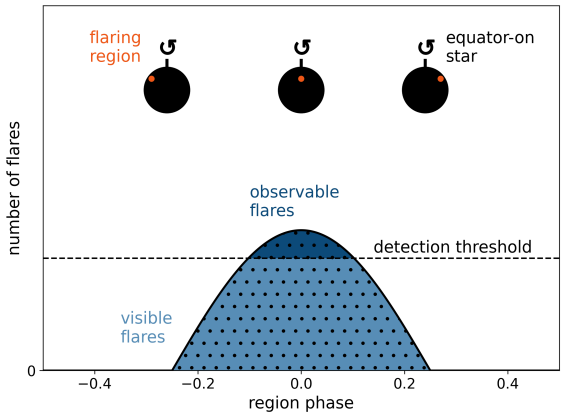

Figure 8.4: Number of flares produced by a single flaring region on the stellar surface at different phases of the region. The flares become visible (light blue area) when the region comes into view. However, they are not observable because the amplitude is geometrically foreshortened when the region is close to the limb. When the region approaches the center of the stellar disk, the flares' amplitude exceeds the detection threshold so that they can be observed (dark blue area). The phase can be the stellar rotation phase, the orbital phase of the planet, or the synodic phase of the star-planet system.

that prevent flaring SPI to occur in the first place. We consider three physical explanations first.

A first physical reason could be the unknown magnetic field of AU Mic b. It is possible that AU Mic b has no magnetic field that can interact with the stellar magnetic field to trigger flares [Lan18]. A magnetic dynamo driven by convective motion of conductive fluids in the interior of the rotating planet is the most efficient mechanism to produce the magnetic field strengths observed in Solar System planets. At the same time, planetary magnetic fields in the Solar System are diverse, which is thought to depend heavily on the internal structure and composition of the planet [Jon11; Ste03]. Only a few indirect measurements of exoplanet magnetic fields exist to date (e.g., [Ben+21a; Cau+19]). Therefore, it is difficult to predict the presence or the strength of AU Mic b's field based solely on mass and radius estimates.

Second, AU Mic b's orbit could be outside the Alfvén zone of AU Mic, either constantly or temporarily. Although the star has a strong magnetic field, a high mass loss rate may pull the Alfvén surface closer to the star [Kav+21], so that no energy can be channelled from the planet to the star. Following [Kav+21], the absence of SPI would suggest that the mass loss rate of AU Mic was closer to $1000\dot{M}_\odot$ than to $10\dot{M}_\odot$. This situation may change with evolving stellar cycle. [Iba+19] report a 5-year chromospheric activity cycle in AU Mic, but it is not clear how it affects mass loss.

Third, instead of via flares, energy may be transferred between planet and star gradually. [Shk+05; SWB03], and [Shk+08] observed evidence of chromospheric hot spots in several systems with close Hot Jupiter companions that could partially be explained in terms of magnetic SPI [Coh+11; Lan12]. It is not clear if flares and hot spots could be effects of the

same SPI reconnection event or instead represent separate channels. The chromospheric observations in Shkolnik et al. did not provide the observing cadence required to conclusively detect or exclude coincident flares in excess of intrinsic flaring activity.

Observational biases can also prevent the detection of flaring SPI. We discuss four possible biases here, all of which can be interpreted within Fig. 8.4:

First, the effect might simply be too weak. SPI flares may be triggered rarely, with only a handful of flares in our sample, which are not detectable with sufficient significance. This corresponds to fewer dots per area, i.e. flares per time, in Fig. 8.4.

Second, we may be looking into the wrong flare energy regime. Flaring SPI may manifest at low energies $< 10^{30}$ erg, i.e. below the detection threshold (no dark blue area in Fig. 8.4). If, on the contrary, SPI flares are triggered at very high energies, they may, again, occur too rarely to be observed within the given monitoring time.

Third, flaring activity could be elevated through flaring SPI, but manifest as excess flares across all longitudes. While the mechanism of flaring SPI is not well understood, we can imagine circumstances that create a large or spread-out SPI-induced flaring region, which would always be in view. Flaring region sizes increase with flare energy for intrinsic flares [How+20; Not+19; STZ00]. It is therefore conceivable that extreme amounts of released energy during SPI might manifest in large flaring regions. Another scenario is efficient transport of the released energy or the magnetic field perturbation within the stellar magnetosphere before erupting in a flare. This could result in a broad range of longitudes at which SPI flares occur. Alternatively, the magnetic field lines connecting planet and star could be arranged such that the locations they map to on the stellar surface are distributed in a broad longitudinal range.

Finally, flares triggered by the interaction might be frequent enough and have sufficiently high amplitudes to be detected if the flaring region was located close to the equator. Yet if the region was at high latitudes, flares would always appear geometrically foreshortened, and remain below the detection threshold.

However, if the tentative 1.5σ signal in the $ED > 1$ s flares (Table 8.2) indeed stems from flaring SPI, we may be limited mostly by the first observational bias, i.e., insufficient observing time. In this case, the flares triggered by the interaction are well above the detection threshold of TESS.

8.5 Summary and conclusions

Since SPI flares are expected to be morphologically identical to intrinsic stellar flares, a statistically significant orbital phase dependence of flaring behaviour is the closest we can currently get to detecting the effect directly. Using high cadence TESS observations of AU Mic, an early M dwarf with a close-in planet detected in 2020, we did not find any sign of flaring SPI.

The strength of the interaction is difficult to constrain in theory [Str+19], and multiple physical models of flaring SPI co-exist [Lan18; Sau+13]. Moreover, the orbit of AU Mic b is not yet synchronized with the stellar rotation period which may additionally lead to tidal interaction [CSM00]. Although AU Mic shows the largest number of flares detected among

all exoplanet hosts found by Kepler and TESS to date, we conclude that most of them are manifestations of intrinsic stellar activity.

We do not rule out that, as time series observations of AU Mic accumulate with TESS, and soon PLATO [Rau+14], SPI-triggered flares can be detected with high significance. We found the strongest deviation ($p = 0.07,\ n = 71$) from intrinsic flaring with the orbital period P_{orb} of AU Mic b, in the high energy half of our flare sample ($ED > 1$ s). We estimate that extending the observing time by a factor of $2 - 3$ will yield a $> 3\sigma$ detection, if the temporal structure of the signal is preserved over time. We argue that long gaps on time scales of months to years betweeen consecutive light curves will average out rotational variability signal as the spot structure evolves, but will leave a P_{orb}-dependent SPI signal intact. In contrast, a persisting absence of flaring SPI would support models that favor an Alfvén zone inside AU Mic b's orbit; strong winds; weak planetary magnetic fields; or a more gradual energy transfer between planet and host.

In an upcoming study, we will apply the methods of flare finding and orbital phase analysis presented here to a large sample of star-planet systems with known close-in planets. This will increase the total number of orbits covered, and probe the effects of orbital distance and star-planet mass ratio on the presence and intensity of flaring SPI.

Acknowledgements

The authors would like to thank Gyula M. Szabó for comments that improved the quality of this work. EI would like to thank Florian U. Jehn for advice on data visualization. EI acknowledges support from the German National Scholarship Foundation. KP acknowledges support from the German Leibniz Community under grant P67/2018. We made use of the Python packages numpy [Har+20] and pandas [McK10; Reb+22], as well as GNU Parallel [Tan18]. This project made use of computational systems and network services at the American Museum of Natural History supported by the National Science Foundation via Campus Cyberinfrastructure Grant Award #1827153 (CC* Networking Infrastructure: High Performance Research Data Infrastructure at the American Museum of Natural History). This research has made use of the SIMBAD database, operated at CDS, Strasbourg, France [Wen+00]. This paper includes data collected with the TESS mission, obtained from the MAST data archive at the Space Telescope Science Institute (STScI). Funding for the TESS mission is provided by the NASA Explorer Program. STScI is operated by the Association of Universities for Research in Astronomy, Inc., under NASA contract NAS 5-26555.

Data Availability

TESS light curves are publicly available through the Mikulski Archive for Space Telescopes (https://mast.stsci.edu/portal/Mashup/Clients/Mast/Portal.html). The python scripts and modules used to perform the statistical analysis and generate the figures in this work as well as the full versions of Tables 6.2 and 8.2 can be found on Github (https://github.com/ekaterinailin/flaring-spi).

9 AltaiPony - Flare science in Kepler, K2 and TESS light curves

Ilin, E.
Journal of Open Source Software, Volume 6, Isuue 2845 (2021).
DOI: 10.21105/joss.02845

Summary

Flares are unmistakeable signs of stellar magnetic activity, and a key to our understanding of stellar properties and evolution. They are violent explosions that penetrate all layers of a star's atmosphere, and enhance its overall brightness by up to orders of magnitude within minutes. We observe flares as distinct signatures in time series of stellar photometric observations that we call light curves. Flaring rates and energies provide unique insights into the nature of the stars that produce them.

Space missions like Kepler [Koc+10], K2 [How+14], and TESS [Ric+15] have collected light curves of tens of thousands of flaring stars, for time spans ranging from several weeks to multiple years. As TESS continues to gather high-cadence data, we developed `AltaiPony` to aid astronomers who require accurately characterized flare samples for their research. `AltaiPony` is a toolbox for statistical flares studies on photometric time series from these missions, including flare search and characterization, a framework to determine the algorithm's efficiency, and statistical analysis of flaring rates along with extensive documentation and Jupyter-based tutorials.

Figure 9.1: Official `AltaiPony` logo. Credit: Elizaveta Ilin.

9.1 Functionality

`AltaiPony` is based on `lightkurve` [Lig+18], and can access most methods that are implemented in it, which makes it an accessible tool for new users who are already familiar with the software. `lightkurve` is a versatile Python package for light curve handling that

includes visualization, basic tools for de-trending, transit detection, and asteroseismology. It is the most widely used software for handling Kepler, K2, and TESS data. `AltaiPony` inherits its main class `FlareLightCurve` directly from `lightkurve`'s `Lightkurve`, and its mission-specific derivatives.

`AltaiPony` was designed to be used by astronomers as a one stop shop solution that covers the essential steps of a typical flare study. We begin with adaptations of common de-trending tools like the Savitzky-Golay filter from `lightkurve.flatten()`, and `K2SC` [APP16]. We tailored them to preserve flare signal, while removing astrophysical and instrumental variability. `FlareLightCurve.detrend()` also allows users to add their own custom de-trending functions.

After de-trending, `FlareLightCurve.find_flares()` returns the occurrence times, amplitudes, durations, and relative energies of all flares above a defined noise threshold in the residual light curve using an adjustable iterative sigma-clipping procedure to identify candidate events as series of positive outliers [Dav16].

Usually, the measured flare amplitudes and durations differ systematically from their intrinsic properties due to the astrophysical and instrumental characteristics of the light curves in which they were found. Therefore, `AltaiPony` features an injection-recovery pipeline for synthetic flares that quantifies the cumulated effects of noise patterns, time sampling, de-trending and flare finding procedure of choice. `FlareLightCurve.sample_flare_recovery()` generates the synthetic data and performs the full flare search. The resulting sample can be used to determine the recovery probability and energy bias of candidate events in the original light curve. Flare frequency distributions (FFDs), that is, the rates f of flares above a given energy E follow a power law:

$$f(>E) = \frac{\beta}{\alpha - 1} E^{-\alpha+1} \tag{9.1}$$

The free parameters α and β are essential indicators of stellar magnetic activity. To estimate their values and uncertainties for a given sample of flares, `AltaiPony` provides the analysis class `FFD`. It includes a fully Bayesian framework [Whe04] that combines the power law nature of FFDs, and the exponential flare waiting times to predict flare frequencies, and uses `emcee` [For+13] to sample from the posterior distribution using the Markov Chain Monte Carlo method. As a fast alternative, we also implemented a modified maximum likelihood estimator [MK09] for α, and a least-squares fit to β with bootstrapped uncertainties.

9.2 Other software

Other software packages for flare science in the field offer alternative methods, as well as complementing functions. `Appaloosa` [Dav16] was designed with Kepler light curves in mind. `Appaloosa` is this software's predecessor as many of its functions, such as the empirical flare model `aflare`, have been ingested into `AltaiPony`. `stella` [FMA20] uses Convolutional Neural Networks to find flares and return their detection probabilities in TESS light curves. For individual events, `allesfitter` [GD21] offers a Bayesian framework to fit multiple aspects of stellar variability at once, including flares.

9.3 Applications

`AltaiPony` has already been used in peer-reviewed publications to study flaring activity as a function of stellar age, mass, and rotation in K2 open cluster members [Ili+19; Ili+21a], and TESS light curves of ultrafast rotating M dwarfs [RDD20]. The software remains under active development.

Acknowledgements

EI acknowledges valuable contributions from Michael Gully-Santiago and Geert Barentsen, who offered advice and hands-on support in the early development stages of the project. EI is thankful to Yori Fournier for helpful comments on the paper and for his support while bringing the software to maturity.

10 Looking ahead

In the past decade, Kepler and TESS revolutionized our understanding of star-planet systems, and highlighted the role of flares. The flare studies they enabled until now, including those in this thesis, are only the tip of the iceberg. We now know that flares are ubiquitous and self-similar on low mass stars across all spectral types, ages, and flare energies. They influence the magnetic main sequence evolution of stars, and shape the evolution of planetary habitability. We do not yet understand all or even most of the underlying reasons and mechanisms, but with TESS' continuing its second extended mission until 2025[15], and perhaps even further, we can expect to illuminate some of them.

Combing the data taken by Kepler and TESS, in 2025, we will, for the first time, be able to search long-term changes in flaring activity, such as cycles, on a 15-year baseline. We will also be able to measure the flaring activity levels of stars in the evolutionary stage of the Sun, that only rarely show flares above the detection threshold. The large number of flares collected on more active stars could constrain the flare frequency distribution enough to conclusively assess its debated contribution to coronal heating on the main sequence. The unusual flares we don't yet grasp the physics of will become easier to interpret the more statistically reliable the sample of such events becomes. In Chapter 8, I have shown that the robust detection of planet-induced flaring interactions could be just a few light curves away. Finally, the declining flaring activity in the brown dwarf regime will become more accessible. This will allow us to probe the important transition in atmospheric and magnetic structure from stellar-type flaring activity to planet-like auroral emission. In the following project, we use the spatio-temporal confinement of flares observed by TESS to expand our capability to localize flares on the stellar surface.

10.1 Mapping small scale magnetic fields with flares

Rare flares, such as those in Chapter 7, will be more routinely detected. Between 4 and 8 rotationally modulated energetic flares on rapidly rotating stars are captured during each full-sky scan of TESS [IPA21]. Until 2025, we will detect a total of ~ 15-30 precisely localizable large flares, increasing the current sample by a factor of 3-5. In upcoming work, we will identify and localize these flares, but also complement the sample by a much more comprehensive approach to measuring the latitudes of flaring regions.

We have developed a method that can be used on all stars with known rotation period, and at least a few flares per light curve. Compared to Chapter 7, this new technique neither requires that the flares are very energetic, nor that the star rotates very fast. To constrain the number and positions of active latitudes, we use only the flare occurrence times relative to the rotational phase of the star. The waiting times between consecutive flares follow a distribution that depends on the number of active regions and their latitudes. This allows us to tell whether the star possesses a low active latitude with a dominating flare productive region like the Sun, or whether there are instead more evenly distributed regions across the stellar surface (Fig. 10.1). We are preparing to use this method both on individual stars with known inclinations, and ensembles of stars without them.

15 https://heasarc.gsfc.nasa.gov/docs/tess/second-extended.html, accessed on May 1st, 2022

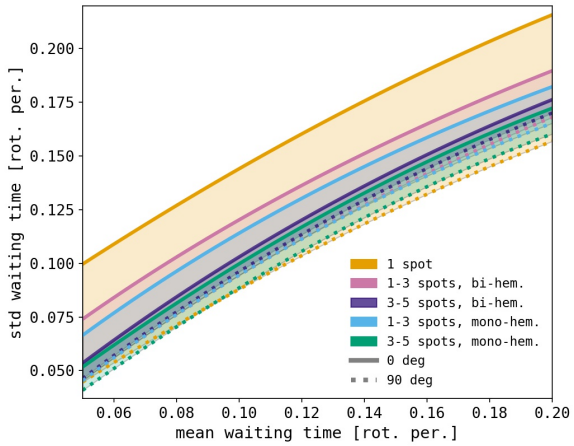

Figure 10.1: How to infer flaring region latitude using only flare timing: In an ensemble of about $10^2 - 10^3$ randomly oriented stars with similar magnetic properties, calculate the mean μ and standard deviation σ of the waiting times between two subsequent flares. The values depend on the number (e.g., 1, 1-3, 3-5) and location of the flaring region(s), i.e. their latitude and whether they occur on one or both hemispheres (mono- or bi-hemispheric). The colored areas show where combinations of μ and σ can fall for each configuration. The solid and dotted lines show which combinations correspond to equator-on and pole-on flaring regions, respectively, with all other latitudes gradually increasing in between (not shown).

Together with the method devised in Chapter 7, this new approach will allow us to map the locations of flares on the stellar surface with decreasing rotation period, and better understand how the topology of small scale magnetic fields evolves with stellar rotation. The latitudes at which flares emerge on fast rotators are much higher than on the Sun (Fig. 10.2). Filling in the observational gap for intermediate rotators will place important constraints on the stellar dynamo that produces these flaring regions, and quantify what fraction of particles associated with large flares would hit or miss the planets orbiting in the equatorial plane of the star.

This can all be done using almost exclusively data from Kepler and TESS. One of the stars studied in Chapter 7, however, made a convincing case for in depth follow-up in a different wavelength regime, as the next Section will show.

10.2 Coronal structure at the bottom of the main sequence

If we walk down the mass spectrum from solar-type stars to Earth-like planets, the magnetospheres of mid-to-late M and early L dwarfs will appear most alien to us. Those stars and brown dwarfs no longer possess partially ionized stellar atmospheres described in Section 2, but do not yet present the cool, familiar ones of Jupiter and Earth. The nature of their atmospheres is poorly understood. Some specimen already present auroral emission, others still flare, and many exhibit both phenomena [Ber+17; Hal+15; LME76; Mac+21; Zic+19]. One of the stars in Chapter 7 falls squarely into this regime, and shows an exceptional combination of magnetic structure and geometry that allows us to study its corona directly. From the large flare we saw in its TESS data, we know that strong

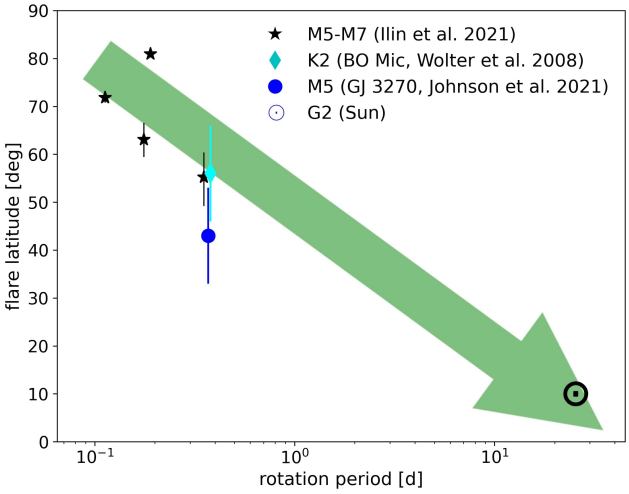

Figure 10.2: Flare latitude as a function of stellar rotation period. Hypothesis (green arrow): As the star spins down, the locations of flares move towards the equator.

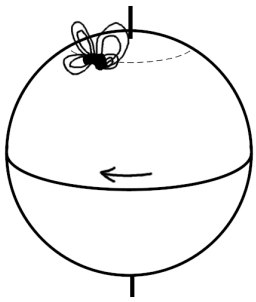

Figure 10.3: Sketch of TIC 277's coronal loops extending above the photospheric footpoint of an actively flaring region, localized in Chapter 7. The loop (partially) moves behind the limb as the star rotates, so that its height and temperature stratification can be inferred from X-ray spectroscopy. Credit: Katja Poppenhäger (2021).

and dynamic magnetic fields emerge close to its rotational pole. Moreover, the star's rotation axis is seen nearly equator-on, so that the region of emergence comes in and out of view as the star spins. The region's strong magnetic fields are believed to extend far into the star's corona. In an upcoming project, we will monitor this star in X-rays for two full rotations with the XMM-Newton space telescope [Jan+01]. We expect to directly observe the partial or full occultation of these large coronal loops by the stellar disk (Fig. 10.3), and infer, for the first time, their size and temperature stratification directly from observations.

10.3 Final remarks

Moving into unprecedented observational regimes such as done by Kepler and TESS promises the discovery of new territory. Incremental progress is easier to predict than a transformational discovery, and improvements in engineering are easier to foresee than a scientific paradigm shift. We can often reasonably extrapolate the expected trend by adding observational, material and computational resources. We are witnessing the growing ecosystem of open source software, mostly in Python, of which `AltaiPony` is one of many examples, but also the introduction of new programming languages to astronomy, like Julia[16]. We use machine learning techniques to aid with the processing, and analysis of petabytes of observations (e.g., [Col+18b; Fei+19; Mas+19]). Large astronomical archives are produced by unprecedented efforts to realize the high signal-to-noise, homogeneous, long-term monitoring of the entire sky. The Gaia Collaboration is releasing its third iteration of positions, velocities, and spectra for over 1.8 billion objects the summer this thesis is completed [Tor+21]. The James Webb Space Telescope (JWST, [Gar+06]), that will scan the sky in the infrared for the next decade, recently sent its first high-resolution images back to Earth [Ces22]. The PLATO mission [Rau+14], scheduled to launch in 2026, will succeed Kepler and TESS. The exponentially

16 https://juliaastro.github.io/dev/index.html, accessed May 1, 2022

dropping costs of launching mass into Earth's orbit will further increase the use of CubeSats or SmallSats [SET20], compact telescopes for targeted and uninterrupted space-based monitoring of, among other targets, nearby star-planet systems.

In one or another form, all these missions will observe flares whenever they target low mass stars. Understanding the influence of flares on the infrared band of JWST, or the astrometric, radial velocity and spectral information obtained from stars in their flaring state with Gaia is crucial to disentangle flaring activity from the desired planetary, or stellar, signal. But as this thesis has shown by the example of Kepler and TESS, flares are never only interferers. They are just as often putting a unique spotlight on the phenomena we want to study (e.g., [Che+21]).

In the upcoming decades, we will perhaps not only see the interaction of flares (and the particles they eject) with planets, and witness exo-space weather in action. We might even observe their interplay with moons orbiting extrasolar planets [Kip+22], as well as their impact on the interplanetary medium and the entire astrosphere. We will find even rarer flares, with higher energies than ever observed before, and use high cadence observation of flares to study magnetic structures that are so small that only in-situ observation would be able to spatially resolve them directly. With the aid of simultaneous, coordinated observations in multiple electromagnetic bands, we will be able to resolve the full spatio-temporal evolution of individual flares and CMEs.

All these speculations are still known unknowns, discoveries that are already on the horizon. It is, however, just a tiny fraction of what is beyond our range of vision. We can expect to learn surprising things when studying flares. There is a vast territory of unknown unknowns waiting to be discovered.

Acknowledgments

I had a great time with this piece of work. I felt like I had the best equipment with me to dive into the vast scientific waters with curiosity, and no second thoughts whatsoever. Almost every bit of the result you see here echoes the great advising, feedback, support and empowerment of my supervisor Katja. Without you, I would not only lack a lot in terms of astrophysical skill, but also many tricks of the trade, strategic thinking, and the confidence to explore new ideas. Most importantly, you are living proof to me that I need not ever lose the joy in doing research. You have left me hungry for more. Sarah, you sparked this hunger in the first place. I vividly remember you giving me the "welcome to flares"-talk to this day, and many other great science chats since then. As you see, I am still hooked. Jim, your curiosity and visionary thinking remind me to think an order of magnitude bigger, whenever I think I've gone too big. Ruth, without your encouragement, I would not have attempted my first theoretical work. The pandemic put our time together too late in my doctorate to include the result into the bulk of this thesis. It certainly deserves more than just a mention. Julián, your dedication to detail and accuracy leaves a wonderful imprint on my writing. Nikoleta, Laura, Grace, Vada, Matthias, Engin, Victoria, Rocio – you made the Humboldt-Haus a great place to hang around. Andrea, thank you for the Friday PhD chats that I was always looking forward to during the home office times. Lucy, you have a special place in my heart. Thank you for pulling me out from under the rock with so much patience, for the great time in Boulder, and, of course, the AOTWs. Joel, Sam, Isabel – thank you for offering me glimpses into your work, your ideas, the lively discussions, and the *absolutely* vital fun times. Thank you for the wisdom of experience you openly shared, Martin, Heike, Klaus, and Sydney.

Without my parents, who left their home country for a better future with my seven year old self and my toddler sister, I would never have had the immense privilege to write this thesis. The difficulty of the never ending, simultaneous processes of emigration and immigration cannot be overestimated. Without Jens, Lucas, Franzi, Michi, Laura and Jonas I might not have so joyfully plunged into physics after school. And without Bramdal and Kevin (with honorable mentions to the ZERO) I might have gone crazy over Landau, Lifschitz, and Co. Tom, you are the fuzzy black shadow who paradoxically keeps brightening the long days of reading, writing, and coding. Isabelle, it was a pleasure to discover space weather in Oslo with you, and I am looking forward to see you leaving this galaxy soon. Lena, your, somehow still wonderfully gentle, 120% in everything always inspire me to challenge myself, and they still do. Philipp, Andrea, Klaus – thank you for the opportunity to explore. Thank you, Pascal, for making my pursuit of fundamental research a conscious decision. Thank you, Max, Florian Z., Katha, and Birte, for listening to my stellar rants in between community building calls. Thank you, Nick, for the alien, the ephemeral, and the rebellious. Farina, thank you for the burrito, the therapy, the walks and the dancing, the crushing of the patriarchy between our fingers. Peter, thank you for the warm-hearted rationalism, the depth, the strategy and nuance in everything. Florian, your compassion rubbed off on me.

Bibliography

[22] *Space Weather Impacts | NOAA / NWS Space Weather Prediction Center*. 2022. URL: https://www.swpc.noaa.gov/impacts (visited on 04/28/2022) (p. 19).

[AA08] Aschwanden and Aschwanden. **Solar Flare Geometries. I. The Area Fractal Dimension**. *ApJ* 674 (2008). 530–543 (p. 82).

[AB15] Afram and Berdyugina. **Molecules as magnetic probes of starspots**. *AA* 576 (2015). A34 (p. 8).

[AB19] Afram and Berdyugina. **Complexity of magnetic fields on red dwarfs**. *AA* 629 (2019). A83 (p. 96).

[AD52] Anderson and Darling. **Asymptotic Theory of Certain Goodness of Fit Criteria Based on Stochastic Processes**. *Ann. Math. Stat.* 23:2 (1952). 193–212 (p. 118).

[Add+21] Addison et al. **The Youngest Planet to Have a Spin-Orbit Alignment Measurement AU Mic b**. *AJ* 162 (2021). 137 (p. 99).

[Agü+18] Agüeros et al. **A New Look at an Old Cluster: The Membership, Rotation, and Magnetic Activity of Low-mass Stars in the 1.3 Gyr Old Open Cluster NGC 752**. *ApJ* 862 (2018). 33 (p. 13).

[Air+17] Airapetian et al. **How Hospitable Are Space Weather Affected Habitable Zones? The Role of Ion Escape**. *ApJ* 836 (2017). L3 (pp. 3, 20).

[Air+20] Airapetian et al. **Impact of space weather on climate and habitability of terrestrial-type exoplanets**. *IJAsB* 19 (2020). 136–194 (p. 65).

[Alv+18] Alvarado-Gómez et al. **Suppression of Coronal Mass Ejections in Active Stars by an Overlying Large-scale Magnetic Field: A Numerical Study**. *ApJ* 862 (2018). 93 (pp. 97, 99).

[Alv+19] Alvarado-Gómez et al. **Coronal Response to Magnetically Suppressed CME Events in M-dwarf Stars**. *ApJ* 884 (2019). L13 (p. 98).

[Alv+20] Alvarado-Gómez et al. **Tuning the Exospace Weather Radio for Stellar Coronal Mass Ejections**. *ApJ* 895 (2020). 47 (pp. 20, 98).

[Alv+22] Alvarado-Gómez et al. **Simulating the Space Weather in the AU Mic System: Stellar Winds and Extreme Coronal Mass Ejections**. *ApJ* 928 (2022). 147 (pp. 19, 20).

[AM20] Atri and Mogan. **Stellar flares versus luminosity: XUV-induced atmospheric escape and planetary habitability**. *MNRAS: Letters* 500:1 (2020). L1–L5 (p. 20).

[Ama+20] Amazo-Gómez et al. **Inflection point in the power spectrum of stellar brightness variations. III. Facular versus spot dominance on stars with known rotation periods**. *AA* 642 (2020). A225 (p. 8).

[And+18] Andrae et al. **Gaia Data Release 2. First stellar parameters from Apsis**. *AA* 616 (2018). A8 (pp. 39, 40).

[And+19] Anders et al. **Photo-astrometric distances, extinctions, and astrophysical parameters for Gaia DR2 stars brighter than G = 18**. *AA* 628 (2019). A94 (pp. 39, 40).

[Anf+13] Anfinogentov et al. **The Decaying Long-period Oscillation of a Stellar Megaflare**. *ApJ* 773 (2013). 156 (p. 27).

[APP16] Aigrain et al. **K2SC: flexible systematics correction and detrending of K2 light curves using Gaussian process regression**. *MNRAS* 459 (2016). 2408–2419 (pp. 36, 43, 126).

[Arc22] Archive. *Exoplanet and Candidate Statitics*. 2022. URL: https://exoplanetarchive.ipac.caltech.edu/docs/counts_detail.html (visited on 04/08/2022) (p. 17).

[Asc+17] Aschwanden et al. **Global Energetics of Solar Flares. V. Energy Closure in Flares and Coronal Mass Ejections**. *ApJ* 836 (2017). 17 (pp. 10, 98).

[Asc+99] Aschwanden et al. **Coronal Loop Oscillations Observed with the Transition Region and Coronal Explorer**. *ApJ* 520 (1999). 880–894 (pp. 27, 96).

[Asc15] Aschwanden. **Thresholded Power law Size Distributions of Instabilities in Astrophysics**. *ApJ* 814 (2015). 19 (p. 47).

[Auv+09] Auvergne et al. **The CoRoT satellite in flight: description and performance**. *AA* 506:1 (2009). 411 (p. 24).

[Bag+09] Baglin et al. **CoRoT: Description of the Mission and Early Results**. *Proc. of the Transiting Planets Conference* 253 (2009). 71–81 (p. 24).

[Bai+13] Bailer-Jones et al. **The Gaia astrophysical parameters inference system (Apsis). Pre-launch description**. *AA* 559 (2013). A74 (p. 39).

[Bai+18] Bailer-Jones et al. **Estimating Distance from Parallaxes. IV. Distances to 1.33 Billion Stars in Gaia Data Release 2**. *AJ* 156 (2018). 58 (p. 79).

[Bar+15] Barnes et al. **Starspot Distributions on Fully Convective M Dwarfs: Implications for Radial Velocity Planet Searches**. *ApJ* 812 (2015). 42 (pp. 74, 97).

[Bar+16] Barnes et al. **Rotation Periods for Cool Stars in the 4 Gyr old Open Cluster M67, The Solar-Stellar Connection, and the Applicability of Gyrochronology to at least Solar Age**. *ApJ* 823 (2016). 16 (pp. 11, 38, 69).

[Bar+17] Barnes et al. **Surprisingly different star-spot distributions on the near equal-mass equal-rotation-rate stars in the M dwarf binary GJ 65 AB**. *MNRAS* 471 (2017). 811–823 (pp. 14, 74, 88, 96, 97).

[Bar+18] Barentsen et al. **Kepler's Discoveries Will Continue: 21 Important Scientific Opportunities with Kepler & K2 Archive Data** (2018) (p. 66).

[Bar03] Barnes. **On the Rotational Evolution of Solar- and Late-Type Stars, Its Magnetic Origins, and the Possibility of Stellar Gyrochronology**. *ApJ* 586 (2003). 464–479 (pp. 11, 13, 34, 49).

[Bar10] Barnes. **A Simple Nonlinear Model for the Rotation of Main-sequence Cool Stars. I. Introduction, Implications for Gyrochronology, and Color-Period Diagrams**. *ApJ* 722 (2010). 222–234 (pp. 12, 14).

[BB17] Brun and Browning. **Magnetism, dynamo action and the solar-stellar connection**. *LRSP* 14:1 (2017). 4 (p. 6).

[BB22] Brady and Bean. **Assessing the Transiting Exoplanet Survey Satellite's Yield of Rocky Planets Around Nearby M Dwarfs**. *AJ* 163 (2022). 255 (p. 18).

[BB55] Babcock and Babcock. **The Sun's Magnetic Field, 1952-1954**. *ApJ* 121 (1955). 349 (p. 6).

[BB88] Bessell and Brett. **JHKLM Photometry: Standard Systems, Passbands, and Intrinsic Colors**. *PASP* 100 (1988). 1134 (p. 39).

[Bec+12] Beck et al. **Fast core rotation in red-giant stars as revealed by gravity-dominated mixed modes**. *Nature* 481 (2012). 55–57 (p. 13).

[Bec15] Beck. **Magnetic fields in spiral galaxies**. *AAR* 24 (2015). 4 (p. 6).

[Bel+12] Bell et al. **Pre-main-sequence isochrones - I. The Pleiades benchmark**. *MNRAS* 424 (2012). 3178–3191 (pp. 37, 69).

[Ben+18] Benomar et al. **Asteroseismic detection of latitudinal differential rotation in 13 Sun-like stars**. *Science* 361 (2018). 1231–1234 (p. 6).

[Ben+21a] Ben-Jaffel et al. **Signatures of strong magnetization and a metal-poor atmosphere for a Neptune-sized exoplanet**. *NatAs* (2021). 1–13 (p. 121).

[Ben+21b] Benz et al. **The CHEOPS mission**. *Exp. Ast.* 51 (2021). 109–151 (p. 112).

[Ben16] Benz. **Flare Observations**. *LRSP* 14:1 (2016). 2 (pp. 9, 10).

[Ber+06] Berthier et al. **SkyBoT, a new VO service to identify Solar System objects**. *Proc. of the Astronomical Data Analysis Software and Systems XV Conference* 351 (2006). 367 (p. 43).

[Ber+16] Berthier et al. **Prediction of transits of Solar system objects in Kepler/K2 images: an extension of the Virtual Observatory service SkyBoT**. *MNRAS* 458 (2016). 3394–3398 (pp. 43, 68).

[Ber+17] Berdyugina et al. **First Detection of a Strong Magnetic Field on a Bursty Brown Dwarf: Puzzle Solved**. *ApJ* 847 (2017). 61 (pp. 97, 98, 130).

[Ber06] Berger. **Radio Observations of a Large Sample of Late M, L, and T Dwarfs: The Distribution of Magnetic Field Strengths**. *ApJ* 648 (2006). 629–636 (pp. 12, 14, 34).

[BG10] Benz and Güdel. **Physical Processes in Magnetically Driven Flares on the Sun, Stars, and Young Stellar Objects**. *ARAA* 48 (2010). 241 (pp. 9, 34, 87, 111).

[BG94] Benz and Güdel. **X-ray/microwave ratio of flares and coronae**. *AA* 285 (1994). 621 (p. 14).

[Big64] Bigg. **Influence of the Satellite Io on Jupiter's Decametric Emission**. *Nature* 203:4949 (1964). 1008–1010 (p. 20).

[BJ14] Binks and Jeffries. **A lithium depletion boundary age of 21 Myr for the Beta Pictoris moving group**. *MNRAS* 438 (2014). L11–L15 (p. 112).

[BJ16] Binks and Jeffries. **Spectroscopic confirmation of M-dwarf candidate members of the Beta Pictoris and AB Doradus Moving Groups**. *MNRAS* 455 (2016). 3345–3358 (p. 112).

[BLP16] Buzasi et al. **Rotation, activity, and stellar obliquities in a large uniform sample of Kepler solar analogs**. *JSWSC* 6 (2016). A38 (p. 13).

[BM06] Burgasser and McElwain. **Resolved Spectroscopy of M Dwarf/L Dwarf Binaries. I. DENIS J220002.05-303832.9AB**. *AJ* 131 (2006). 1007–1014 (pp. 42, 79).

[BMN15] Bell et al. **A self-consistent, absolute isochronal age scale for young moving groups in the solar neighbourhood**. *MNRAS* 454 (2015). 593–614 (pp. 93, 112).

[Boc+07] Bochanski et al. **Low-Mass Dwarf Template Spectra from the Sloan Digital Sky Survey**. *AJ* 133 (2007). 531–544 (pp. 42, 77, 79).

[Boc+10] Bochanski et al. **The Luminosity and Mass Functions of Low-mass Stars in the Galactic Disk. II. The Field**. *AJ* 139 (2010). 2679–2699 (p. 42).

[Bok18] Bokeh Development Team. **Bokeh: Python library for interactive visualization**. manual. 2018. URL: https://bokeh.pydata.org/en/latest/ (p. 66).

[Boo+17] Booth et al. **An improved age-activity relationship for cool stars older than a gigayear**. *MNRAS* 471 (2017). 1012–1025 (pp. 13, 34).

[Boo+20] Booth et al. **Chromospheric emission of solar-type stars with asteroseismic ages**. *MNRAS* 491 (2020). 455–467 (p. 34).

[Bor+10] Borucki et al. **Kepler Planet-Detection Mission: Introduction and First Results**. *Science* 327 (2010). 977 (pp. 4, 17, 24, 113).

[Bos+19] Bossini et al. **Age determination for 269 Gaia DR2 open clusters**. *AA* 623 (2019). A108 (pp. 37, 38, 69).

[Bot19] Boteler. **A 21st Century View of the March 1989 Magnetic Storm**. *SpWea* 17:10 (2019). 1427–1441 (p. 19).

[Bou+12] Boudreault et al. **Astrometric and photometric initial mass functions from the UKIDSS Galactic Clusters Survey - III. Praesepe**. *MNRAS* 426 (2012). 3419–3434 (pp. 37, 69).

[Bou+14] Bouvier et al. **Angular Momentum Evolution of Young Low-Mass Stars and Brown Dwarfs: Observations and Theory**. *Proc. of the Protostars and Planets V Conference* (2014) (p. 5).

[Bou+17] Bourrier et al. **Reconnaissance of the TRAPPIST-1 exoplanet system in the Lyman-alpha line**. *AA* 599 (2017). L3 (p. 12).

[Bou+18] Bourrier et al. **Orbital misalignment of the Neptune-mass exoplanet GJ 436b with the spin of its cool star**. *Nature* 553 (2018). 477–480 (p. 99).

[Bou+22] Bouma et al. **A 38 Million Year Old Neptune-sized Planet in the Kepler Field**. *AJ* 163 (2022). 121 (p. 25).

[Boy+13] Boyajian et al. **Stellar Diameters and Temperatures. III. Main-sequence A, F, G, and K Stars: Additional High-precision Measurements and Empirical Relations**. *ApJ* 771 (2013). 40 (pp. 39, 40).

[Bra+18] Bragaglia et al. **The chemical composition of the oldest nearby open cluster Ruprecht 147**. *AA* 619 (2018). A176 (pp. 37, 69).

[BRL13] Boesgaard et al. **The Chemical Composition of Praesepe (M44)**. *ApJ* 775 (2013). 58 (p. 69).

[Bro08] Browning. **Simulations of Dynamo Action in Fully Convective Stars**. *ApJ* 676 (2008). 1262–1280 (p. 12).

[Bru+17] Brun et al. **On Differential Rotation and Overshooting in Solar-like Stars**. *ApJ* 836 (2017). 192 (p. 14).

[Bry+20] Bryson et al. **The Occurrence of Rocky Habitable-zone Planets around Solar-like Stars from Kepler Data**. *AJ* 161:1 (2020). 36 (p. 18).

[BSM06] Buckley et al. **Completion and commissioning of the Southern African Large Telescope**. *Proc. of the SPIE Conference Series* 6267 (2006). 62670Z (p. 76).

[BSR22] Bogner et al. **Effects of flares on the habitable zones of M dwarfs accessible to TESS planet detections**. *AN* 343 (2022). e10079 (p. 28).

[Bur+04] Burgasser et al. **The 2MASS Wide-Field T Dwarf Search. III. Seven New T Dwarfs and Other Cool Dwarf Discoveries**. *AJ* 127 (2004). 2856–2870 (pp. 42, 79).

[Bur+07] Burgasser et al. **Discovery of a High Proper Motion L Dwarf Binary: 2MASS J15200224-4422419AB**. *ApJ* 658 (2007). 557–568 (pp. 42, 79).

[Bur+08] Burgasser et al. **Subtle Signatures of Multiplicity in Late-type Dwarf Spectra: The Unresolved M8.5 + T5 Binary 2MASS J03202839-0446358**. *ApJ* 681 (2008). 579–593 (pp. 42, 79).

[Bur+10] Burgasser et al. **SpeX Spectroscopy of Unresolved Very Low Mass Binaries. I. Identification of 17 Candidate Binaries Straddling the L Dwarf/T Dwarf Transition**. *ApJ* 710 (2010). 1142–1169 (p. 42).

[Bur14] Burgasser. **The SpeX Prism Library: 1000+ low-resolution, near-infrared spectra of ultracool M, L, T and Y dwarfs**. *Proc. of the Astronomical Society of India Conference Series* 11 (2014). 7–16 (p. 79).

[Cal+21a] Cale et al. **Diving Beneath the Sea of Stellar Activity: Chromatic Radial Velocities of the Young AU Mic Planetary System**. *AJ* 162 (2021). 295 (pp. 112, 120).

[Cal+21b] Callingham et al. **The population of M dwarfs observed at low radio frequencies**. *NatAs* 5:12 (2021). 1233–1239 (p. 14).

[Can+18] Cantat-Gaudin et al. **A Gaia DR2 view of the open cluster population in the Milky Way**. *AA* 618 (2018). A93 (pp. 36–38, 68, 69).

[Car+07] Caramazza et al. **X-ray flares in Orion low-mass stars**. *AA* 471:2 (2007). 645–654 (p. 15).

[Car01] Carpenter. **Color Transformations for the 2MASS Second Incremental Data Release**. *AJ* 121 (2001). 2851–2871 (p. 39).

[Car33] Carroll. **The spectroscopic determination of stellar rotation and its effect on line profiles**. *MNRAS* 93 (1933). 478–507 (p. 5).

[Car59] Carrington. **Description of a Singular Appearance seen in the Sun on September 1, 1859**. *MNRAS* 20 (1859). 13–15 (p. 23).

[Cau+19] Cauley et al. **Magnetic field strengths of hot Jupiters from signals of star-planet interactions**. *NatAs* 3 (2019). 1128–1134 (pp. 21, 121).

[CB97] Chabrier and Baraffe. **Structure and evolution of low-mass stars**. *AA* 327 (1997). 1039 (p. 12).

[CBE07] Cranmer et al. **Self-consistent Coronal Heating and Solar Wind Acceleration from Anisotropic Magnetohydrodynamic Turbulence**. *ApJS* 171 (2007). 520–551 (p. 8).

[CBH15] Chang et al. **Photometric Study on Stellar Magnetic Activity. I. Flare Variability of Red Dwarf Stars in the Open Cluster M37**. *ApJ* 814 (2015). 35 (pp. 35, 46, 59–61, 63, 115).

[CD16] Chelli and Duvert. **Pseudomagnitude distances: Application to the Pleiades cluster**. *AA* 593 (2016). L18 (p. 69).

[Ces22] Cesari. *NASA's Webb In Full Focus, Ready for Instrument Commissioning – James Webb Space Telescope*. en-US. 2022. URL: https://blogs.nasa.gov/webb/2022/04/28/nasas-webb-in-full-focus-ready-for-instrument-commissioning/ (visited on 05/01/2022) (p. 131).

[Cha+16] Chambers et al. **The Pan-STARRS1 Surveys**. *arXiv:1612.05560* (2016) (p. 38).

[Cha+17] Chadney et al. **Effect of stellar flares on the upper atmospheres of HD 189733b and HD 209458b**. *AA* 608 (2017). A75 (p. 20).

[Che+11] Chen et al. **Statistical properties of superactive regions during solar cycles 19-23**. *AA* 534 (2011). A47 (p. 100).

[Che+21] Chen et al. **Persistence of flare-driven atmospheric chemistry on rocky habitable zone worlds**. *NatAs* 5 (2021). 298–310 (pp. 20, 132).

[Cho+16] Cho et al. **Comparison of Damped Oscillations in Solar and Stellar X-Ray flares**. *ApJ* 830 (2016). 110 (p. 27).

[Chr21] Christensen-Dalsgaard. **Solar structure and evolution**. *LRSP* 18 (2021). 2 (p. 5).

[CK20] Castellanos Durán and Kleint. **The Statistical Relationship between White-light Emission and Photospheric Magnetic Field Changes in Flares**. *ApJ* 904 (2020). 96 (p. 92).

[Cla+02] Clarke et al. **Ultraviolet emissions from the magnetic footprints of Io, Ganymede and Europa on Jupiter**. *Nature* 415 (2002). 997–1000 (p. 21).

[Cla+18] Clarke et al. **Flare Activity of Wide Binary Stars with Kepler**. *ApJ* 853 (2018). 59 (p. 35).

[Cla98] Claret. **Very low mass stars: non-linearity of the limb-darkening laws**. *AA* 335 (1998). 647–653 (p. 81).

[CO18] Crosley and Osten. **Low-frequency Radio Transients on the Active M-dwarf EQ Peg and the Search for Coronal Mass Ejections**. *ApJ* 862 (2018). 113 (p. 98).

[Coh+11] Cohen et al. **The Dynamics of Stellar Coronae Harboring Hot Jupiters. I. A Time-dependent Magnetohydrodynamic Simulation of the Interplanetary Environment in the HD 189733 Planetary System**. *ApJ* 733 (2011). 67 (p. 121).

[Col+16a] Collaboration et al. **Gaia Data Release 1. Summary of the astrometric, photometric, and survey properties**. *AA* 595 (2016). A2 (p. 68).

[Col+16b] Collaboration et al. **The Gaia mission**. *AA* 595 (2016). A1 (pp. 38, 68, 75).

[Col+18a] Collaboration et al. **Gaia Data Release 2. Observational Hertzsprung-Russell diagrams**. *AA* 616 (2018). A10 (pp. 67–69).

[Col+18b] Collaboration et al. **Gaia Data Release 2. Summary of the contents and survey properties**. *AA* 616 (2018). A1 (pp. 36–39, 68, 75, 131).

[Col+22] Colombo et al. **Hot Jupiters accreting onto their parent stars: Effects on the stellar activity**. *AN* 343 (2022). e10096 (p. 21).

[Com19] Committee. *The Nobel Prize in Physics 2019*. en-US. 2019. URL: https://www.nobelprize.org/prizes/physics/2019/summary/ (visited on 04/08/2022) (p. 17).

[Con+14] Conrad et al. **A RAVE investigation on Galactic open clusters. I. Radial velocities and metallicities**. *AA* 562 (2014). A54 (pp. 37, 69).

[CP06] Chen and Priest. **Transition-Region Explosive Events: Reconnection Modulated by p-Mode Waves**. *Sol. Phys.* 238 (2006). 313–327 (p. 27).

[CPM22] Colombo et al. **Short term variability of DS Tuc A observed with TESS** (2022) (pp. 28, 112).

[Cra+14] Crause et al. **Performance of the Southern African Large Telescope (SALT) High Resolution Spectrograph (HRS)**. *Proc. of the Ground-based and Airborne Instrumentation for Astronomy V Conference* 9147 (2014). 91476T (p. 76).

[Cru+03] Cruz et al. **Meeting the Cool Neighbors. V. A 2MASS-Selected Sample of Ultracool Dwarfs**. *AJ* 126 (2003). 2421–2448 (p. 42).

[Cru+04] Cruz et al. **2MASS J05185995-2828372: Discovery of an Unresolved L/T Binary**. *ApJ* 604 (2004). L61–L64 (p. 42).

[CRZ17] Compagnino et al. **A Statistical Study of CME Properties and of the Correlation Between Flares and CMEs over Solar Cycles 23 and 24**. *Sol. Phys.* 292 (2017). 5 (pp. 20, 98).

[CS02] Carlsson and Stein. **Dynamic Hydrogen Ionization**. *ApJ* 572 (2002). 626–635 (pp. 5, 8).

[CSM00] Cuntz et al. **On Stellar Activity Enhancement Due to Interactions with Extrasolar Giant Planets**. *ApJ* 533 (2000). L151–L154 (p. 122).

[Cur+13] Curtis et al. **Ruprecht 147: The Oldest Nearby Open Cluster as a New Benchmark for Stellar Astrophysics**. *AJ* 145 (2013). 134 (pp. 11, 13, 36, 38, 58, 67–69).

[Cur+19] Curtis et al. **A Temporary Epoch of Stalled Spin-down for Low-mass Stars: Insights from NGC 6811 with Gaia and Kepler**. *ApJ* 879 (2019). 49 (pp. 11, 13, 14).

[Cur+20] Curtis et al. **When Do Stalled Stars Resume Spinning Down? Advancing Gyrochronology with Ruprecht 147**. *ApJ* 904 (2020). 140 (p. 14).

[Cur16] Curtis. **Ruprecht 147 and the Quest to Date Middle-Aged Stars**. PhD thesis. 2016. (pp. 13, 69).

[CVV06] Casas et al. **Solar Rotation in the 17th century**. *Sol. Phys.* 234:2 (2006). 379–392 (p. 5).

[CWM13] Cranmer et al. **Constraining a Model of Turbulent Coronal Heating for AU Microscopii with X-Ray, Radio, and Millimeter Observations**. *ApJ* 772 (2013). 149 (p. 117).

[CWO20] Chang et al. **Photometric flaring fraction of M dwarf stars from the SkyMapper Southern Survey**. *MNRAS* 491 (2020). 39–50 (p. 34).

[Dah15] Dahm. **Reexamining the Lithium Depletion Boundary in the Pleiades and the Inferred Age of the Cluster**. *ApJ* 813 (2015). 108 (pp. 37, 69).

[Dav+12] Davenport et al. **Multi-wavelength Characterization of Stellar Flares on Low-mass Stars Using SDSS and 2MASS Time-domain Surveys**. *ApJ* 748 (2012). 58 (pp. 15, 44).

[Dav+14] Davenport et al. **Kepler Flares. II. The Temporal Morphology of White-light Flares on GJ 1243**. *ApJ* 797 (2014). 122 (pp. 25, 46, 82, 85, 87).

[Dav+19] Davenport et al. **The Evolution of Flare Activity with Stellar Age**. *ApJ* 871 (2019). 241 (pp. 13, 34, 35, 46, 49, 51, 55, 59, 62, 65).

[Dav15] Davenport. **Spots and Flares: Stellar Activity in the Time Domain Era**. PhD thesis. 2015. (pp. 34, 64).

[Dav16] Davenport. **The Kepler Catalog of Stellar Flares**. *ApJ* 829 (2016). 23 (pp. 24, 25, 27, 34, 46, 62, 63, 114, 126).

[DC11] Durante and Cucinotta. **Physical basis of radiation protection in space travel**. *RvMP* 83 (2011). 1245–1281 (p. 19).

[DC15] Dressing and Charbonneau. **The Occurrence of Potentially Habitable Planets Orbiting M Dwarfs Estimated from the Full Kepler Dataset and an Empirical Measurement of the Detection Sensitivity**. *ApJ* 807 (2015). 45 (pp. 3, 18).

[Des+12] Deshpande et al. **Intermediate Resolution Near-infrared Spectroscopy of 36 Late M Dwarfs**. *AJ* 144 (2012). 99 (p. 97).

[Deu58] Deutsch. **Harmonic Analysis of the Periodic Spectrum Variables**. *Proc. of the Electromagnetic Phenomena in Cosmical Physics Conference* 6 (1958). 209 (p. 8).

[Dia+12] Dias et al. **Fitting isochrones to open cluster photometric data. II. Nonparametric open cluster membership likelihood estimation and its application in optical and 2MASS near-IR data**. *AA* 539 (2012). A125 (pp. 37, 38, 69).

[DK13] Duchêne and Kraus. **Stellar Multiplicity**. *ARAA* 51:1 (2013). 269–310 (p. 59).

[DL09] Donati and Landstreet. **Magnetic Fields of Nondegenerate Stars**. *ARAA* 47:1 (2009). 333–370 (p. 6).

[DMH20] Davenport et al. **10 Years of Stellar Activity for GJ 1243**. *AJ* 160 (2020). 36 (p. 60).

[Doi+10] Doi et al. **Photometric Response Functions of the Sloan Digital Sky Survey Imager**. *AJ* 139 (2010). 1628–1648 (p. 42).

[Don+00] Donati et al. **Surface differential rotation and prominences of the Lupus post T Tauri star RX J1508.6-4423**. *MNRAS* 316 (2000). 699–715 (p. 13).

[Don+97] Donati et al. **Spectropolarimetric observations of active stars**. *MNRAS* 291 (1997). 658–682 (p. 6).

[Dou+14] Douglas et al. **The Factory and the Beehive. II. Activity and Rotation in Praesepe and the Hyades**. *ApJ* 795 (2014). 161 (pp. 13, 36, 37, 68).

[Dou+17] Douglas et al. **Poking the Beehive from Space: K2 Rotation Periods for Praesepe**. *ApJ* 842 (2017). 83 (pp. 36, 37, 67, 68).

[Dou+19] Douglas et al. **K2 Rotation Periods for Low-mass Hyads and a Quantitative Comparison of the Distribution of Slow Rotators in the Hyades and Praesepe**. *ApJ* 879 (2019). 100 (pp. 55, 56).

[Doy+18] Doyle et al. **Investigating the rotational phase of stellar flares on M dwarfs using K2 short cadence data**. *MNRAS* 480 (2018). 2153–2164 (pp. 117, 120).

[Doy+19] Doyle et al. **Probing the origin of stellar flares on M dwarfs using TESS data sectors 1-3**. *MNRAS* 489 (2019). 437–445 (pp. 117, 120).

[Doy+22] Doyle et al. **The puzzling story of flare inactive ultra fast rotating M dwarfs - I. Exploring their magnetic fields**. *MNRAS* 512 (2022). 979–988 (p. 14).

[Dra+13] Drake et al. **Implications of Mass and Energy Loss due to Coronal Mass Ejections on Magnetically Active Stars**. *ApJ* 764 (2013). 170 (pp. 8, 14, 20, 97).

[DRD20] Doyle et al. **Superflares and variability in solar-type stars with TESS in the Southern hemisphere**. *MNRAS* 494 (2020). 3596–3610 (p. 66).

[Dun61] Dungey. **Interplanetary Magnetic Field and the Auroral Zones**. *PhRvL* 6:2 (1961). 47–48 (p. 19).

[Ehr+15] Ehrenreich et al. **A giant comet-like cloud of hydrogen escaping the warm Neptune-mass exoplanet GJ 436b**. *Nature* 522 (2015). 459–461 (p. 19).

[Eke+18] Eker et al. **Interrelated main-sequence mass-luminosity, mass-radius, and mass-effective temperature relations**. *MNRAS* 479 (2018). 5491–5511 (p. 59).

[Enc22] Encyclopaedia. *The Extrasolar Planet Encyclopaedia — Catalog Listing*. 2022. URL: http://exoplanet.eu/catalog/ (visited on 04/08/2022) (p. 17).

[Fei+19] Feinstein et al. **eleanor: An Open-source Tool for Extracting Light Curves from the TESS Full-frame Images**. *PASP* 131 (2019). 094502 (p. 131).

[Fei+20] Feinstein et al. **Flare Statistics for Young Stars from a Convolutional Neural Network Analysis of TESS Data**. *AJ* 160 (2020). 219 (pp. 11, 25, 27, 34, 49, 63, 66).

[Fei+22] Feinstein et al. **Testing Self-organized Criticality across the Main Sequence Using Stellar Flares from TESS**. *ApJ* 925 (2022). L9 (p. 27).

[Fig+16] Figueira et al. **Is the activity level of HD 80606 influenced by its eccentric planet?** *AA* 592 (2016). A143 (p. 112).

[Fil+15] Filippazzo et al. **Fundamental Parameters and Spectral Energy Distributions of Young and Field Age Objects with Masses Spanning the Stellar to Planetary Regime**. *ApJ* 810 (2015). 158 (p. 42).

[Fin+16] Finkbeiner et al. **Hypercalibration: A Pan-STARRS1-based Recalibration of the Sloan Digital Sky Survey Photometry**. *ApJ* 822 (2016). 66 (p. 39).

[Fin+19] Finley et al. **Solar Angular Momentum Loss over the Past Several Millennia**. *ApJ* 883 (2019). 67 (p. 13).

[Fin+20] Finley et al. **The Solar Wind Angular Momentum Flux as Observed by Parker Solar Probe**. *ApJ* 902 (2020). L4 (p. 13).

[Fla+18] Flaccomio et al. **A multi-wavelength view of magnetic flaring from PMS stars**. *AA* 620 (2018). A55 (p. 24).

[FMA20] Feinstein et al. **stella: Convolutional Neural Networks for Flare Identification in TESS**. *JOSS* 5 (2020). 2347 (p. 126).

[Fol+18] Folsom et al. **The evolution of surface magnetic fields in young solar-type stars II: the early main sequence (250-650 Myr)**. *MNRAS* 474 (2018). 4956–4987 (p. 13).

[Fol+20] Folsom et al. **Circumstellar environment of 55 Cancri. The super-Earth 55 Cnc e as a primary target for star-planet interactions**. *AA* 633 (2020). A48 (p. 21).

[Fol15] Foley. **The Role of Plate Tectonic-Climate Coupling and Exposed Land Area in the Development of Habitable Climates on Rocky Planets**. *ApJ* 812 (2015). 36 (p. 18).

[For+13] Foreman-Mackey et al. **emcee: The MCMC Hammer**. *PASP* 125 (2013). 306 (pp. 77, 86, 126).

[For+17] Foreman-Mackey et al. **Fast and Scalable Gaussian Process Modeling with Applications to Astronomical Time Series**. *AJ* 154 (2017). 220 (p. 86).

[For18] Foreman-Mackey. **Scalable Backpropagation for Gaussian Processes using Celerite**. *RNAAS* 2 (2018). 31 (p. 86).

[Fra+19] Fraschetti et al. **Stellar Energetic Particles in the Magnetically Turbulent Habitable Zones of TRAPPIST-1-like Planetary Systems**. *ApJ* 874 (2019). 21 (pp. 20, 99).

[Fri+21] Fritzewski et al. **A detailed understanding of the rotation-activity relationship using the 300 Myr old open cluster NGC 3532**. *AA* 656 (2021). A103 (pp. 11, 13).

[Fro+19] Froning et al. **A Hot Ultraviolet Flare on the M Dwarf Star GJ 674**. *ApJ* 871 (2019). L26 (pp. 10, 44, 86).

[FS19] Fischer and Saur. **Time-variable Electromagnetic Star-Planet Interaction: The TRAPPIST-1 System as an Exemplary Case**. *ApJ* 872 (2019). 113 (pp. 28, 111, 112, 118).

[Fuh+08] Fuhrmeister et al. **Multiwavelength observations of a giant flare on CN Leonis. I. The chromosphere as seen in the optical spectra**. *AA* 487:1 (2008). 293–306 (pp. 15, 86).

[Ful+17] Fulton et al. **The California-Kepler Survey. III. A Gap in the Radius Distribution of Small Planets**. *AJ* 154 (2017). 109 (p. 19).

[Gai+14] Gaidos et al. **Trumpeting M dwarfs with CONCH-SHELL: a catalogue of nearby cool host-stars for habitable exoplanets and life**. *MNRAS* 443 (2014). 2561–2578 (p. 112).

[Gao18] Gao. **A Machine-learning-based Investigation of the Open Cluster M67**. *ApJ* 869 (2018). 9 (pp. 36, 38, 68).

[Gar+03] García-Alvarez et al. **Simultaneous optical and X-ray observations of flares and rotational modulation on the RS CVn binary HR 1099 (V711 Tau) from the MUSICOS 1998 campaign**. *AA* 397 (2003). 285–303 (p. 15).

[Gar+06] Gardner et al. **The James Webb Space Telescope**. *Space Sci. Rev.* 123 (2006). 485–606 (p. 131).

[Gas+13] Gastine et al. **What controls the magnetic geometry of M dwarfs?** *AA* 549 (2013). L5 (pp. 12, 74, 96).

[GB93] Guedel and Benz. **X-Ray/Microwave Relation of Different Types of Active Stars**. *ApJ* 405 (1993). L63 (p. 14).

[GCH17] Giles et al. **A Kepler study of starspot lifetimes with respect to light-curve amplitude and spectral type**. *MNRAS* 472 (2017). 1618–1627 (p. 11).

[GCM21] Gaudi et al. **The Demographics of Exoplanets**. *arXiv:2011.04703* (2021) (pp. 17, 18).

[GD21] Günther and Daylan. **Allesfitter: Flexible Star and Exoplanet Inference from Photometry and Radial Velocity**. *ApJS* 254 (2021). 13 (p. 126).

[Ger72] Gershberg. **Some results of the cooperative photometric observations of the UV Cet-type flare stars in the years 1967 71**. *ApSS, Volume 19, Issue 1, pp.75-92* 19:1 (1972). 75 (pp. 3, 24, 44, 45, 115).

[Gib+20] Gibbs et al. **EDEN: Sensitivity Analysis and Transiting Planet Detection Limits for Nearby Late Red Dwarfs**. *AJ* 159 (2020). 169 (p. 24).

[Gil+17] Gillon et al. **Seven temperate terrestrial planets around the nearby ultracool dwarf star TRAPPIST-1**. *Nature* 542 (2017). 456–460 (p. 18).

[Gil+22] Gilbert et al. **Flares, Rotation, and Planets of the AU Mic System from TESS Observations**. *AJ* 163 (2022). 147 (pp. 112, 117).

[Giz+13] Gizis et al. **Kepler Monitoring of an L Dwarf I. The Photometric Period and White Light Flares**. *ApJ* 779 (2013). 172 (pp. 10, 34).

[Giz+17] Gizis et al. **K2 Ultracool Dwarfs Survey. II. The White Light Flare Rate of Young Brown Dwarfs**. *ApJ* 845 (2017). 33 (pp. 63, 91).

[Gne77] Gnevyshev. **Essential features of the 11-year solar cycle**. *Sol. Phys.* 51 (1977). 175–183 (p. 74).

[Gon+94] Gonzalez et al. **What is a geomagnetic storm?** *JGR: Space Physics* 99:A4 (1994). 5771–5792 (p. 19).

[Gon16] Gonzalez. **Variability among stars in the M 67 field from Kepler/K2-Campaign-5 light curves**. *MNRAS* 459 (2016). 1060–1068 (pp. 36, 38, 67, 68).

[Gos+18] Gossage et al. **Age Determinations of the Hyades, Praesepe, and Pleiades via MESA Models with Rotation**. *ApJ* 863 (2018). 67 (pp. 37, 69).

[Gra+00] Granzer et al. **Distribution of starspots on cool stars. II. Pre-main-sequence and ZAMS stars between 0.4 and 1.7 solar masses**. *AA* 355 (2000). 1087–1097 (p. 74).

[Gre+19] Green et al. **A 3D Dust Map Based on Gaia, Pan-STARRS 1, and 2MASS**. *ApJ* 887 (2019). 93 (p. 39).

[Gre18] Green. **dustmaps: A Python interface for maps of interstellar dust**. *JOSS* 3 (2018). 695 (p. 39).

[Gua+19] Guarcello et al. **Simultaneous Kepler/K2 and XMM-Newton observations of superflares in the Pleiades**. *AA* 622 (2019). A210 (p. 99).

[Gue+16] Guerrero et al. **On the Role of Tachoclines in Solar and Stellar Dynamos**. *ApJ* 819 (2016). 104 (pp. 12, 14).

[Gün+20] Günther et al. **Stellar Flares from the First TESS Data Release: Exploring a New Sample of M Dwarfs**. *AJ* 159 (2020). 60 (pp. 11, 24, 25, 28, 34, 63, 64, 66, 82, 87).

[GW10] Goodman and Weare. **Ensemble samplers with affine invariance**. *CAMCoS* 5 (2010). 65–80 (p. 81).

[Hal+08] Hallinan et al. **Confirmation of the Electron Cyclotron Maser Instability as the Dominant Source of Radio Emission from Very Low Mass Stars and Brown Dwarfs**. *ApJ* 684 (2008). 644–653 (p. 97).

[Hal+15] Hallinan et al. **Magnetospherically driven optical and radio aurorae at the end of the stellar main sequence**. *Nature* 523 (2015). 568–571 (pp. 97, 130).

[Hal+21] Hall et al. **Weakened magnetic braking supported by asteroseismic rotation rates of Kepler dwarfs**. *NatAs* 5 (2021). 707–714 (p. 14).

[Hal08] Hale. **On the Probable Existence of a Magnetic Field in Sun-Spots**. *ApJ* 28 (1908). 315 (p. 6).

[Har+08] Hartman et al. **Deep MMT Transit Survey of the Open Cluster M37. I. Observations and Cluster Parameters**. *ApJ* 675 (2008). 1233–1253 (pp. 61, 63).

[Har+19] Hardegree-Ullman et al. **Kepler Planet Occurrence Rates for Mid-type M Dwarfs as a Function of Spectral Type**. *AJ* 158 (2019). 75 (p. 18).

[Har+20] Harris et al. **Array programming with NumPy**. *Nature* 585:7825 (2020). 357–362 (pp. 66, 123).

[Har+21] Harbach et al. **Stellar Winds Drive Strong Variations in Exoplanet Evaporative Outflow Patterns and Transit Absorption Signatures**. *ApJ* 913 (2021). 130 (p. 19).

[Haw+14] Hawley et al. **Kepler Flares. I. Active and Inactive M Dwarfs**. *ApJ* 797 (2014). 121 (pp. 25, 87).

[Haz+22] Hazra et al. **The impact of coronal mass ejections and flares on the atmosphere of the hot Jupiter HD189733b**. *MNRAS* 509 (2022). 5858–5871 (p. 20).

[Her+19] Herbst et al. **From solar to stellar flare characteristics. On a new peak size distribution for G-, K-, and M-dwarf star flares**. *AA* 621 (2019). A67 (pp. 20, 99).

[HF92] Hawley and Fisher. **X-Ray–heated Models of Stellar Flare Atmospheres: Theory and Comparison with Observations**. *ApJS* 78 (1992). 565 (pp. 34, 44, 86).

[HFR90] Houdebine et al. **Dynamics of flares on late-type dMe stars. I. Flare mass ejections and stellar evolution.** *AA* 238 (1990). 249 (p. 15).

[Hil+10] Hilton et al. **M Dwarf Flares from Time-resolved Sloan Digital Sky Survey Spectra**. *AJ* 140 (2010). 1402–1413 (pp. 15, 34).

[Hil11] Hilton. **The Galactic M Dwarf Flare Rate**. PhD thesis. 2011. (p. 63).

[Hir+20] Hirano et al. **Limits on the Spin-Orbit Angle and Atmospheric Escape for the 22 Myr Old Planet AU Mic b**. *ApJ* 899 (2020). L13 (p. 99).

[Hjo+21] Hjorth et al. **A backward-spinning star with two coplanar planets**. *PNAS* 118 (2021). 2017418118 (p. 99).

[HL21] Howard and Law. **EvryFlare. IV. Detection of Periodicity in Flare Occurrence from Cool Stars with TESS**. *ApJ* 920 (2021). 42 (pp. 118, 120).

[HM22] Howard and MacGregor. **No Such Thing as a Simple Flare: Substructure and Quasi-periodic Pulsations Observed in a Statistical Sample of 20 s Cadence TESS Flares**. *ApJ* 926 (2022). 204 (pp. 25, 27).

[Hon+18] Honda et al. **Time-resolved spectroscopic observations of an M-dwarf flare star EV Lacertae during a flare**. *PASJ* 70 (2018). 62 (p. 15).

[How+14] Howell et al. **The K2 Mission: Characterization and Early Results**. *PASP* 126 (2014). 398 (pp. 24, 35, 125).

[How+19] Howard et al. **EvryFlare. I. Long-term Evryscope Monitoring of Flares from the Cool Stars across Half the Southern Sky**. *ApJ* 881 (2019). 9 (pp. 15, 34, 46, 59–61, 63, 64).

[How+20] Howard et al. **EvryFlare. II. Rotation Periods of the Cool Flare Stars in TESS across Half the Southern Sky**. *ApJ* 895 (2020). 140 (pp. 11, 13, 15, 34, 49, 86, 122).

[How+85] Howard et al. **Coronal mass ejections: 1979-1981**. *JGR* 90 (1985). 8173–8192 (p. 20).

[HS18] Heinzel and Shibata. **Can Flare Loops Contribute to the White-light Emission of Stellar Superflares?** *ApJ* 859 (2018). 143 (pp. 87, 98).

[HSR91] Haisch et al. **Flares on the Sun and other stars**. *ARAA* 29 (1991). 275–324 (p. 34).

[Hut81] Hut. **Tidal evolution in close binary systems**. *AA* 99 (1981). 126 (p. 5).

[HWM06] Hudson et al. **White-Light Flares: A TRACE/RHESSI Overview**. *Sol. Phys.* 234 (2006). 79–93 (p. 87).

[Iba+19] Ibañez Bustos et al. **First long-term activity study of AU Microscopii: a possible chromospheric cycle**. *MNRAS* 483 (2019). 1159–1167 (p. 121).

[ID12] Inglis and Dennis. **The Relationship between Hard X-Ray Pulse Timings and the Locations of Footpoint Sources during Solar Flares**. *ApJ* 748 (2012). 139 (p. 96).

[Ili+19] Ilin et al. **Flares in open clusters with K2 . I. M 45 (Pleiades), M 44 (Praesepe), and M 67**. *AA* 622 (2019). A133 (pp. 11, 27, 35, 37, 38, 42, 46, 47, 53, 60, 61, 63, 127).

[Ili+21a] Ilin et al. **Flares in open clusters with K2. II. Pleiades, Hyades, Praesepe, Ruprecht 147, and M 67**. *AA* 645 (2021). A42 (pp. 11, 27, 127).

[Ili+21b] Ilin et al. **Giant white-light flares on fully convective stars occur at high latitudes**. *MNRAS* 507 (2021). 1723–1745 (p. 113).

[Ili21] Ilin. **AltaiPony - Flare science in Kepler, K2 and TESS light curves**. *JOSS* 6:62 (2021). 2845 (pp. 25, 42, 75, 114).

[IPA21] Ilin et al. **Localizing flares to understand stellar magnetic fields and space weather in exo-systems**. *AN* 343:4 (2021) (p. 129).

[IPH22] Ilic et al. **Tidal star-planet interaction and its observed impact on stellar activity in planet-hosting wide binary systems**. *MNRAS* 513 (2022). 4380–4404 (p. 20).

[Irw+11] Irwin et al. **On the Angular Momentum Evolution of Fully Convective Stars: Rotation Periods for Field M-dwarfs from the MEarth Transit Survey**. *ApJ* 727 (2011). 56 (pp. 12, 14, 73).

[Ish+91] Ishida et al. **Flare Event Statistics on Uv-Ceti Type Stars**. *ApSS* 182:2 (1991). 227–240 (p. 24).

[Işı+18] Işık et al. **Forward modelling of brightness variations in Sun-like stars. I. Emergence and surface transport of magnetic flux**. *AA* 620 (2018). A177 (pp. 74, 88).

[Ive+14] Ivezić et al. **Statistics, Data Mining, and Machine Learning in Astronomy**. Princeton University Press, 2014. URL: https://ui.adsabs.harvard.edu/abs/2014sdmm.book.....I (visited on 03/12/2022) (p. 66).

[Jac+19] Jackman et al. **Detection of a giant flare displaying quasi-periodic pulsations from a pre-main-sequence M star by the Next Generation Transit Survey**. *MNRAS* 482 (2019). 5553–5566 (p. 27).

[Jac+20] Jackman et al. **NGTS clusters survey - II. White-light flares from the youngest stars in Orion**. *MNRAS* 497 (2020). 809–817 (pp. 24, 62).

[Jac+21] Jackman et al. **Stellar flares detected with the Next Generation Transit Survey**. *MNRAS* 504 (2021). 3246–3264 (p. 24).

[Jan+01] Jansen et al. **XMM-Newton observatory. I. The spacecraft and operations**. *AA* 365 (2001). L1–L6 (p. 131).

[Jär+07] Järvinen et al. **EK Draconis. Magnetic activity in the photosphere and chromosphere**. *AA* 472:3 (2007). 887–895 (p. 74).

[Jär+08] Järvinen et al. **Magnetic activity on V889 Herculis. Combining photometry and spectroscopy**. *AA* 488:3 (2008). 1047–1055 (p. 74).

[JBG21] Johnstone et al. **The active lives of stars: A complete description of the rotation and XUV evolution of F, G, K, and M dwarfs**. *AA* 649 (2021). A96 (pp. 13, 57, 58).

[JC19] Jardine and Collier Cameron. **Slingshot prominences: nature's wind gauges**. *MNRAS* 482 (2019). 2853–2860 (p. 13).

[Jef+11] Jeffries et al. **Investigating coronal saturation and supersaturation in fast-rotating M-dwarf stars**. *MNRAS* 411 (2011). 2099–2112 (pp. 11, 13).

[Jen+16] Jenkins et al. **The TESS science processing operations center**. *Proc. of the Software and Cyberinfrastructure for Astronomy IV Conference* 9913 (2016). 99133E (p. 75).

[Jes+19] Jess et al. **Statistical Signatures of Nanoflare Activity. I. Monte Carlo Simulations and Parameter-space Exploration**. *ApJ* 871 (2019). 133 (p. 15).

[JKH18] Jejčič et al. **High-density Off-limb Flare Loops Observed by SDO**. *ApJ* 867 (2018). 134 (pp. 87, 98).

[Joh+12] Johnstone et al. **The soft X-ray light curves of partially eclipsed stellar flares**. *MNRAS* 419 (2012). 29–38 (p. 74).

[Joh+15] Johnstone et al. **The Evolution of Stellar Rotation and the Hydrogen Atmospheres of Habitable-zone Terrestrial Planets**. *ApJ* 815 (2015). L12 (p. 20).

[Joh+21] Johnson et al. **Simultaneous photometric and CARMENES spectroscopic monitoring of fast-rotating M dwarf GJ 3270. Discovery of a post-flare corotating feature**. *AA* 651 (2021). A105 (p. 15).

[Jon11] Jones. **Planetary Magnetic Fields and Fluid Dynamos**. *AnRFM* 43 (2011). 583–614 (pp. 6, 121).

[Kan+22] Kanodia et al. **High-resolution Near-infrared Spectroscopy of a Flare around the Ultracool Dwarf vB 10**. *ApJ* 925 (2022). 155 (p. 15).

[Kas+02] Kashyap et al. **Flare Heating in Stellar Coronae**. *ApJ* 580 (2002). 1118–1132 (p. 15).

[Kav+19] Kavanagh et al. **MOVES - II. Tuning in to the radio environment of HD189733b**. *MNRAS* 485 (2019). 4529–4538 (p. 21).

[Kav+21] Kavanagh et al. **Planet-induced radio emission from the coronae of M dwarfs: the case of Prox Cen and AU Mic**. *MNRAS* 504 (2021). 1511–1518 (pp. 112, 113, 121).

[Kay+19] Kay et al. **Frequency of Coronal Mass Ejection Impacts with Early Terrestrial Planets and Exoplanets around Active Solar-like Stars**. *ApJ* 886 (2019). L37 (p. 99).

[KBH17] Kuzmychov et al. **First Spectropolarimetric Measurement of a Brown Dwarf Magnetic Field in Molecular Bands**. *ApJ* 847 (2017). 60 (p. 96).

[KDL99] Katsova et al. **New Insights into the Large 1992 July 15-17 Flare on AU Microscopii: The First Detection of Posteruptive Energy Release on a Red Dwarf Star**. *ApJ* 510 (1999). 986–998 (p. 112).

[Ker+16] Kervella et al. **The red dwarf pair GJ65 AB: inflated, spinning twins of Proxima. Fundamental parameters from PIONIER, NACO, and UVES observations**. *AA* 593 (2016). A127 (p. 79).

[Kes+18] Kesseli et al. **Magnetic Inflation and Stellar Mass. II. On the Radii of Single, Rapidly Rotating, Fully Convective M-Dwarf Stars**. *AJ* 155 (2018). 225 (pp. 79, 93).

[Kes+19] Kesseli et al. **Radii of 88 M Subdwarfs and Updated Radius Relations for Low-metallicity M-dwarf Stars**. *AJ* 157 (2019). 63 (pp. 39, 40).

[KF14] Kerr and Fletcher. **Physical Properties of White-light Sources in the 2011 February 15 Solar Flare**. *ApJ* 783 (2014). 98 (p. 44).

[KHM91] Kirkpatrick et al. **A Standard Stellar Spectral Sequence in the Red/Near-Infrared: Classes K5 to M9**. *ApJS* 77 (1991). 417 (p. 34).

[Kho+04] Khodachenko et al. **Collisional and viscous damping of MHD waves in partially ionized plasmas of the solar atmosphere**. *AA* 422 (2004). 1073 (p. 8).

[Kho+07] Khodachenko et al. **Coronal Mass Ejection (CME) Activity of Low Mass M Stars as An Important Factor for The Habitability of Terrestrial Exoplanets. I. CME Impact on Expected Magnetospheres of Earth-Like Exoplanets in Close-In Habitable Zones**. *Astrobiology* 7 (2007). 167–184 (p. 19).

[Kim+19] Kiman et al. **Exploring the Age-dependent Properties of M and L Dwarfs Using Gaia and SDSS**. *AJ* 157 (2019). 231 (p. 75).

[Kip+22] Kipping et al. **An exomoon survey of 70 cool giant exoplanets and the new candidate Kepler-1708 b-i**. *NatAs* 6 (2022). 367–380 (p. 132).

[Kir+10] Kirkpatrick et al. **Discoveries from a Near-infrared Proper Motion Survey Using Multi-epoch Two Micron All-Sky Survey Data**. *ApJS* 190 (2010). 100–146 (pp. 42, 79).

[Kir+16] Kirkpatrick et al. **The AllWISE Motion Survey, Part 2**. *ApJS* 224 (2016). 36 (p. 77).

[Kle+16] Kleint et al. **Continuum Enhancements in the Ultraviolet, the Visible and the Infrared during the X1 Flare on 2014 March 29**. *ApJ* 816 (2016). 88 (p. 44).

[Kle+21] Klein et al. **Investigating the young AU Mic system with SPIRou: large-scale stellar magnetic field and close-in planet mass**. *MNRAS* 502 (2021). 188–205 (p. 112).

[Kle+22] Klein et al. **One year of AU Mic with HARPS - II. Stellar activity and star-planet interaction**. *MNRAS* 512 (2022). 5067–5084 (p. 21).

[KMH18] Kowalski et al. **The Evolution of T = 10,000 K Blackbody-Like Continuum Radiation in the Impulsive Phase of dMe Flares**. Proc. of the 20th Cambridge Workshop on Cool Stars, Stellar Systems and the Sun. arXiv:1810.07226, 2018. URL: https://ui.adsabs.harvard.edu/abs/2018csss.confE..42K (visited on 03/24/2022) (p. 86).

[Koc+10] Koch et al. **Kepler Mission Design, Realized Photometric Performance, and Early Science**. *ApJ* 713 (2010). L79–L86 (pp. 34, 35, 125).

[Kol+21] Kolotkov et al. **Multi-wavelength quasi-periodic pulsations in a stellar superflare**. *ApJL* 923:2 (2021). L33 (p. 27).

[Kol33] Kolmogorov. **Sulla determinazione empirica di una lgge di distribuzione**. *Inst. Ital. Attuari, Giorn.* 4 (1933). 83–91 (p. 119).

[Kow+10] Kowalski et al. **A White Light Megaflare on the dM4.5e Star YZ CMi**. *ApJ* 714 (2010). L98–L102 (p. 15).

[Kow+13] Kowalski et al. **Time-resolved Properties and Global Trends in dMe Flares from Simultaneous Photometry and Spectra**. *ApJS* 207:1 (2013). 15 (pp. 9, 10, 15, 34, 44, 86, 99).

[KR20] Kochukhov and Reiners. **The Magnetic Field of the Active Planet-hosting M Dwarf AU Mic**. *ApJ* 902 (2020). 43 (p. 117).

[Kra+14] Kraus et al. **A Stellar Census of the Tucana-Horologium Moving Group**. *AJ* 147 (2014). 146 (pp. 77, 79, 93).

[Kra67] Kraft. **Studies of Stellar Rotation. V. The Dependence of Rotation on Age among Solar-Type Stars**. *ApJ* 150 (1967). 551 (p. 12).

[Kre11] Kretzschmar. **The Sun as a star: observations of white-light flares**. *AA* 530 (2011). A84 (pp. 10, 44, 86).

[Kul+14] Kulow et al. **Ly α Transit Spectroscopy and the Neutral Hydrogen Tail of the Hot Neptune GJ 436b**. *ApJ* 786 (2014). 132 (p. 19).

[KWR93] Kasting et al. **Habitable Zones around Main Sequence Stars**. *Icarus* 101 (1993). 108–128 (pp. 3, 19).

[KWW12] Kippenhahn et al. **Stellar Structure and Evolution**. Springer Berlin Heidelberg, 2012. ISBN: 978-3-642-30304-3. URL: https://ui.adsabs.harvard.edu/abs/2012sse..book.....K (visited on 04/05/2022) (p. 5).

[Lam+03] Lammer et al. **Atmospheric Loss of Exoplanets Resulting from Stellar X-Ray and Extreme-Ultraviolet Heating**. *ApJ* 598 (2003). L121–L124 (p. 19).

[Lan09] Lanza. **Stellar coronal magnetic fields and star-planet interaction**. *AA* 505:1 (2009). 339–350 (p. 112).

[Lan12] Lanza. **Star-planet magnetic interaction and activity in late-type stars with close-in planets**. *AA* 544 (2012). A23 (p. 121).

[Lan18] Lanza. **Close-by planets and flares in their host stars**. *AA* 610 (2018). A81 (pp. 21, 111, 112, 121, 122).

[Lan22] Lanza. **A model for spin-orbit commensurability and synchronous starspot activity in stars with close-by planets**. *AA* 658 (2022). A195 (p. 120).

[Law+15] Law et al. **Evryscope Science: Exploring the Potential of All-Sky Gigapixel-Scale Telescopes**. *PASP* 127 (2015). 234 (pp. 24, 34).

[LB15] Luger and Barnes. **Extreme Water Loss and Abiotic O2Buildup on Planets Throughout the Habitable Zones of M Dwarfs**. *Astrobiology* 15 (2015). 119–143 (p. 3).

[Lec+12] Lecavelier des Etangs et al. **Temporal variations in the evaporating atmosphere of the exoplanet HD 189733b**. *AA* 543 (2012). L4 (p. 34).

[Lee+17] Lee et al. **A rotating protostellar jet launched from the innermost disk of HH 212**. *NatAs* 1 (2017). 0152 (p. 5).

[Lee+18] Lee et al. **Unveiling a magnetized jet from a low-mass protostar**. *Nat. Comm.* 9:1 (2018). 4636 (p. 5).

[Lei+20] Leitzinger et al. **A census of coronal mass ejections on solar-like stars**. *MNRAS* 493 (2020). 4570–4589 (p. 20).

[Let18] Letzter. *A Solar Storm Detonated U.S. Navy Mines During the Vietnam War*. en. 2018. URL: https://www.scientificamerican.com/article/a-solar-storm-detonated-u-s-navy-mines-during-the-vietnam-war/ (visited on 04/15/2022) (p. 19).

[LFS10] Liefke et al. **Multiwavelength observations of a giant flare on CN Leonis. III. Temporal evolution of coronal properties**. *AA* 514 (2010). A94 (p. 15).

[Lig+18] Lightkurve Collaboration et al. **Lightkurve: Kepler and TESS time series analysis in Python**. *ASCL* (2018). ascl:1812.013 (pp. 43, 68, 75, 125).

[Lin+19] Lin et al. **A Comparative Study of the Magnetic Activities of Low-mass Stars from M-type to G-type**. *ApJ* 873 (2019). 97 (pp. 45, 46, 59, 60, 63, 64).

[Lin+21] Lin et al. **EDEN: Flare Activity of the Nearby Exoplanet-hosting M Dwarf Wolf 359 Based on K2 and EDEN Light Curves**. *AJ* 162 (2021). 11 (p. 24).

[Lin17] Linsky. **Stellar Model Chromospheres and Spectroscopic Diagnostics**. *ARAA* 55:1 (2017). 159–211 (p. 8).

[Liu+16] Liu et al. **The Hyades open cluster is chemically inhomogeneous**. *MNRAS* 457 (2016). 3934–3948 (p. 69).

[LM16] Lanza and Mathis. **Tides and angular momentum redistribution inside low-mass stars hosting planets: a first dynamical model**. *CMDA* 126 (2016). 249–274 (pp. 5, 20).

[LME76] Lacy et al. **UV Ceti stars: statistical analysis of observational data**. *ApJS* 30 (1976). 85–96 (pp. 34, 63, 130).

[Lom76] Lomb. **Least-Squares Frequency Analysis of Unequally Spaced Data**. *ApSS* 39:2 (1976). 447–462 (pp. 75, 114).

[Lóp+16] López-Santiago et al. **Star-disk interaction in classical T Tauri stars revealed using wavelet analysis**. *AA* 590 (2016). A7 (p. 96).

[Lor+18] Lorenzo-Oliveira et al. **The Solar Twin Planet Search. The age-chromospheric activity relation**. *AA* 619 (2018). A73 (p. 34).

[Lor+19] Lorenzo-Oliveira et al. **Constraining the evolution of stellar rotation using solar twins**. *MNRAS* 485 (2019). L68–L72 (p. 14).

[Lou+21] Louden et al. **Hot Stars with Kepler Planets Have High Obliquities**. *AJ* 161 (2021). 68 (p. 99).

[Loy+18a] Loyd et al. **HAZMAT. IV. Flares and Superflares on Young M Stars in the Far Ultraviolet**. *ApJ* 867 (2018). 70 (p. 44).

[Loy+18b] Loyd et al. **The MUSCLES Treasury Survey. V. FUV Flares on Active and Inactive M Dwarfs**. *ApJ* 867 (2018). 71 (pp. 20, 34).

[LPS16] Lorenzo-Oliveira et al. **The age-mass-metallicity-activity relation for solar-type stars: comparisons with asteroseismology and the NGC 188 open cluster**. *AA* 594 (2016). L3 (p. 34).

[Lu+19] Lu et al. **Magnetic Activities of M-type Stars Based on LAMOST DR5 and Kepler and K2 Missions**. *ApJS* 243 (2019). 28 (p. 55).

[Lu+21] Lu et al. **Gyro-kinematic Ages for around 30,000 Kepler Stars**. *AJ* 161 (2021). 189 (pp. 11, 13).

[Lug+16] Luger et al. **EVEREST: Pixel Level Decorrelation of K2 Light Curves**. *AJ* 152 (2016). 100 (p. 36).

[Lug+18] Luger et al. **An Update to the EVEREST K2 Pipeline: Short Cadence, Saturated Stars, and Kepler-like Photometry Down to Kp = 15**. *AJ* 156 (2018). 99 (p. 36).

[Lur+15] Lurie et al. **Kepler Flares III: Stellar Activity on GJ 1245A and B**. *ApJ* 800 (2015). 95 (pp. 35, 53, 59, 60, 63).

[Luy49] Luyten. **New stars with proper motions exceeding 0.5" annually**. *AJ* 55 (1949). 15 (pp. 23, 24).

[LW94] Linsky and Wood. **High-Velocity Plasma in the Transition Region of AU Microscopii: Evidence for Magnetic Reconnection and Saturated Heating during Quiescent and Flaring Conditions**. *ApJ* 430 (1994). 342 (p. 117).

[Mac+21] MacGregor et al. **Discovery of an Extremely Short Duration Flare from Proxima Centauri Using Millimeter through Far-ultraviolet Observations**. *ApJ* 911 (2021). L25 (pp. 15, 130).

[Mac22] MacGregor. **The Proxima Cen Campaign - A Multi-Wavelength Picture of Stellar Flaring**. Proc. of the Fifty Years of the Skumanich Relations Conference. 2022. URL: https://ui.adsabs.harvard.edu/abs/2022fysr.confE..43M (visited on 04/25/2022) (p. 15).

[Mae+12] Maehara et al. **Superflares on solar-type stars**. *Nature* 485 (2012). 478–481 (p. 34).

[Mae+15] Maehara et al. **Statistical properties of superflares on solar-type stars based on 1-min cadence data**. *Earth, Planets and Space* 67 (2015). 59 (p. 27).

[Mae+17] Maehara et al. **Starspot activity and superflares on solar-type stars**. *PASJ* 69 (2017). 41 (pp. 11, 13, 44).

[Mae+21] Maehara et al. **Time-resolved spectroscopy and photometry of M dwarf flare star YZ Canis Minoris with OISTER and TESS: Blue asymmetry in the H alpha line during the non-white light flare**. *PASJ* 73 (2021). 44–65 (pp. 15, 99).

[Mag+15] Maggio et al. **Coordinated X-Ray and Optical Observations of Star-Planet Interaction in HD 17156**. *ApJ* 811 (2015). L2 (pp. 21, 112).

[Mal+14] Malo et al. **BANYAN. IV. Fundamental Parameters of Low-mass Star Candidates in Nearby Young Stellar Kinematic Groups—Isochronal Age Determination using Magnetic Evolutionary Models**. *ApJ* 792 (2014). 37 (p. 112).

[Man+15] Mann et al. **How to Constrain Your M Dwarf: Measuring Effective Temperature, Bolometric Luminosity, Mass, and Radius**. *ApJ* 804 (2015). 64 (pp. 39, 42, 79).

[Man+16] Mann et al. **Erratum: How to Constrain Your M Dwarf: Measuring Effective Temperature, Bolometric Luminosity, Mass, and Radius (ApJ, 804, 64)**. *ApJ* 819 (2016). 87 (pp. 39, 40, 42).

[Mar+06] Marsden et al. **Surface differential rotation and photospheric magnetic field of the young solar-type star HD 171488 (V889 Her)**. *MNRAS* 370 (2006). 468–476 (p. 74).

[Mar+21] Martioli et al. **New constraints on the planetary system around the young active star AU Mic. Two transiting warm Neptunes near mean-motion resonance**. *AA* 649 (2021). A177 (pp. 18, 112, 113, 117, 120).

[Mas+08] Massi et al. **Interacting coronae of two T Tauri stars: first observational evidence for solar-like helmet streamers**. *AA* 480:2 (2008). 489 (p. 20).

[Mas+19] Masci et al. **The Zwicky Transient Facility: Data Processing, Products, and Archive**. *PASP* 131 (2019). 018003 (p. 131).

[Mat+15] Matt et al. **The Mass-dependence of Angular Momentum Evolution in Sun-like Stars**. *ApJ* 799 (2015). L23 (p. 12).

[May+03] Mayor et al. **Setting New Standards with HARPS**. *The Messenger* 114 (2003). 20–24 (p. 112).

[May+11] Mayor et al. **The HARPS search for southern extra-solar planets XXXIV. Occurrence, mass distribution and orbital properties of super-Earths and Neptune-mass planets**. *arXiv:1109.2497* (2011) (p. 18).

[Maz+15] Mazeh et al. **Photometric Amplitude Distribution of Stellar Rotation of KOIs—Indication for Spin-Orbit Alignment of Cool Stars and High Obliquity for Hot Stars**. *ApJ* 801 (2015). 3 (p. 99).

[MB14] Mamajek and Bell. **On the age of the beta Pictoris moving group**. *MNRAS* 445 (2014). 2169–2180 (p. 112).

[McK10] McKinney. **Data Structures for Statistical Computing in Python**. *Proceedings of the 9th Python in Science Conference* (2010). 56–61 (p. 123).

[ME19] Metcalfe and Egeland. **Understanding the Limitations of Gyrochronology for Old Field Stars**. *ApJ* 871 (2019). 39 (p. 14).

[Mei+15] Meibom et al. **A spin-down clock for cool stars from observations of a 2.5-billion-year-old cluster**. *Nature* 517 (2015). 589–591 (p. 11).

[Mel+14] Melis et al. **A VLBI resolution of the Pleiades distance controversy**. *Science* 345 (2014). 1029–1032 (p. 69).

[MH08] Mamajek and Hillenbrand. **Improved Age Estimation for Solar-Type Dwarfs Using Activity-Rotation Diagnostics**. *ApJ* 687 (2008). 1264–1293 (pp. 55, 62).

[MHB92] Mullan et al. **Transient Periodicities in X-Ray–active Red Dwarfs: First Results from Mount Cuba and Interpretation with an Oscillating Loop Model**. *ApJ* 391 (1992). 265 (p. 27).

[MHF16] Mazeh et al. **Dearth of short-period Neptunian exoplanets: A desert in period-mass and period-radius planes**. *AA* 589 (2016). A75 (pp. 18, 19).

[Mir+20] Miret-Roig et al. **Dynamical traceback age of the beta Pictoris moving group**. *AA* 642 (2020). A179 (p. 112).

[Mir93] Mirzoyan. **Flare stars and the evolution of red dwarf stars**. *Astrophysics* 36 (1993). 170–191 (p. 35).

[Mit+05] Mitra-Kraev et al. **The first observed stellar X-ray flare oscillation: Constraints on the flare loop length and the magnetic field**. *AA* 436:3 (2005). 1041–1047 (p. 96).

[MK09] Maschberger and Kroupa. **Estimators for the exponent and upper limit, and goodness-of-fit tests for (truncated) power-law distributions**. *MNRAS* 395 (2009). 931–942 (pp. 45, 62, 64, 71, 126).

[MK16] Matsakos and Königl. **On the Origin of the Sub-Jovian Desert in the Orbital-period-Planetary-mass Plane**. *ApJ* 820 (2016). L8 (p. 18).

[MMA14] McQuillan et al. **Rotation Periods of 34,030 Kepler Main-sequence Stars: The Full Autocorrelation Sample**. *ApJS* 211 (2014). 24 (pp. 13, 62).

[MMN02] Massi et al. **Periodic radio flaring on the T Tauri star V 773 Tauri**. *AA* 382 (2002). 152–156 (p. 20).

[Mof74] Moffett. **UV Ceti flare stars: observational data**. *ApJS* 29 (1974). 1–42 (pp. 24, 25).

[MOH20] MacGregor et al. **Properties of M Dwarf Flares at Millimeter Wavelengths**. *ApJ* 891:1 (2020). 80 (p. 15).

[Mon+00] Montmerle et al. **Rotation and X-Ray Emission from Protostars**. *ApJ* 532 (2000). 1097–1110 (p. 74).

[Mon+19] Mondrik et al. **An Increased Rate of Large Flares at Intermediate Rotation Periods for Mid-to-late M Dwarfs**. *ApJ* 870 (2019). 10 (pp. 34, 49).

[Mor+08a] Morin et al. **Large-scale magnetic topologies of mid M dwarfs**. *MNRAS* 390 (2008). 567–581 (p. 6).

[Mor+08b] Morin et al. **The stable magnetic field of the fully convective star V374 Peg**. *MNRAS* 384 (2008). 77–86 (pp. 6, 96, 97).

[Mor+10] Morin et al. **Large-scale magnetic topologies of late M dwarfs***. *MNRAS* 407 (2010). 2269–2286 (pp. 6, 96).

[Mor+17] Morris et al. **The Starspots of HAT-P-11: Evidence for a Solar-like Dynamo**. *ApJ* 846 (2017). 99 (p. 8).

[Mor+18] Morris et al. **Possible Bright Starspots on TRAPPIST-1**. *ApJ* 857:1 (2018). 39 (p. 8).

[Mor20] Morris. **A Relationship between Stellar Age and Spot Coverage**. *ApJ* 893 (2020). 67 (p. 11).

[Mos+19] Moschou et al. **The Stellar CME-Flare Relation: What Do Historic Observations Reveal?** *ApJ* 877 (2019). 105 (pp. 20, 97).

[MQ95] Mayor and Queloz. **A Jupiter-mass companion to a solar-type star**. *Nature* 378:6555 (1995). 355–359 (pp. 17, 18).

[MR13] Mathis and Remus. **Tides in Planetary Systems and in Multiple Stars: a Physical Picture**. *Lecture Notes in Physics, Berlin Springer Verlag* 857 (2013). 111–147 (pp. 5, 20).

[MS81] Moss and Smith. **Stellar rotation and magnetic stars**. *Reports on Progress in Physics* 44:8 (1981). 831–891 (p. 5).

[Muñ+15] Muñoz-Jaramillo et al. **Small-scale and Global Dynamos and the Area and Flux Distributions of Active Regions, Sunspot Groups, and Sunspots: A Multi-database Study**. *ApJ* 800 (2015). 48 (p. 8).

[Mur+22] Murray et al. **A Study of Flares in the Ultra-Cool Regime from SPECULOOS-South**. *MNRAS* (2022) (p. 12).

[MW20] Masuda and Winn. **On the Inference of a Star's Inclination Angle from its Rotation Velocity and Projected Rotation Velocity**. *AJ* 159 (2020). 81 (pp. 81, 82).

[Nak+06] Nakariakov et al. **Quasi-periodic modulation of solar and stellar flaring emission by magnetohydrodynamic oscillations in a nearby loop**. *AA* 452:1 (2006). 343 (p. 27).

[Nak+99] Nakariakov et al. **TRACE observation of damped coronal loop oscillations: Implications for coronal heating**. *Science* 285 (1999). 862–864 (pp. 27, 96).

[Nam+17] Namekata et al. **Statistical Studies of Solar White-light Flares and Comparisons with Superflares on Solar-type Stars**. *ApJ* 851 (2017). 91 (p. 64).

[Nam+20] Namekata et al. **Optical and X-ray observations of stellar flares on an active M dwarf AD Leonis with the Seimei Telescope, SCAT, NICER, and OISTER**. *PASJ* 72 (2020). 68 (pp. 15, 101).

[Nam+21] Namekata et al. **Probable detection of an eruptive filament from a superflare on a solar-type star**. *NatAs* (2021). 1–8 (p. 15).

[Net+16] Netopil et al. **On the metallicity of open clusters. III. Homogenised sample**. *AA* 585 (2016). A150 (pp. 37, 55, 69).

[New+16] Newton et al. **The Rotation and Galactic Kinematics of Mid M Dwarfs in the Solar Neighborhood**. *ApJ* 821 (2016). 93 (pp. 73, 96, 97).

[New+17] Newton et al. **The H alpha Emission of Nearby M Dwarfs and its Relation to Stellar Rotation**. *ApJ* 834 (2017). 85 (pp. 11, 13, 55, 73, 93).

[NF19] Neal and Figueira. **Eniric: Extended NIR Information Content**. *JOSS* 4:37 (2019). 1053 (p. 81).

[NO01] Nakariakov and Ofman. **Determination of the coronal magnetic field by coronal loop oscillations**. *AA* 372 (2001). L53–L56 (p. 96).

[Not+19] Notsu et al. **Do Kepler Superflare Stars Really Include Slowly Rotating Sun-like Stars?—Results Using APO 3.5 m Telescope Spectroscopic Observations and Gaia-DR2 Data**. *ApJ* 876 (2019). 58 (pp. 15, 27, 34, 122).

[Noy+84] Noyes et al. **Rotation, convection, and magnetic activity in lower main-sequence stars**. *ApJ* 279 (1984). 763–777 (p. 12).

[NV20] Netto and Valio. **Stellar magnetic activity and the butterfly diagram of Kepler-63**. *AA* 635 (2020). A78 (p. 8).

[Ode+17] Odert et al. **Stellar coronal mass ejections - I. Estimating occurrence frequencies and mass-loss rates**. *MNRAS* 472 (2017). 876–890 (p. 34).

[Ode+20] Odert et al. **Stellar coronal mass ejections - II. Constraints from spectroscopic observations**. *MNRAS* 494 (2020). 3766–3783 (pp. 97, 98).

[OJA20] Olson et al. **Oceanographic Considerations for Exoplanet Life Detection**. *ApJ* 895:1 (2020). 19 (p. 18).

[OL18] Owen and Lai. **Photoevaporation and high-eccentricity migration created the sub-Jovian desert**. *MNRAS* 479 (2018). 5012–5021 (p. 18).

[Olá+21] Oláh et al. **Toward the true number of flaring giant stars in the Kepler field. Are their flaring specialities associated with their being giant stars?** *AA* 647 (2021). A62 (p. 27).

[Oli+18] Olivares et al. **The seven sisters DANCe. IV. Bayesian hierarchical model**. *AA* 617 (2018). A15 (pp. 36, 37, 68).

[Oli+19] Olivares et al. **Ruprecht 147 DANCe. I. Members, empirical isochrone, luminosity, and mass distributions**. *AA* 625 (2019). A115 (pp. 38, 68).

[Ols15] Olson. **Houston, We Have a Narrative: Why Science Needs Story**. Chicago, IL: University of Chicago Press, 2015. ISBN: 978-0-226-27084-5. (Visited on 06/02/2022) (p. 29).

[OM16] Owen and Mohanty. **Habitability of terrestrial-mass planets in the HZ of M Dwarfs - I. H/He-dominated atmospheres**. *MNRAS* 459 (2016). 4088–4108 (p. 19).

[Öne+11] Önehag et al. **M67-1194, an unusually Sun-like solar twin in M67**. *AA* 528 (2011). A85 (pp. 38, 69).

[OW15] Osten and Wolk. **Connecting Flares and Transient Mass-loss Events in Magnetically Active Stars**. *ApJ* 809 (2015). 79 (pp. 14, 20).

[Owe19] Owen. **Atmospheric Escape and the Evolution of Close-In Exoplanets**. *AREPS* 47 (2019). 67–90 (p. 19).

[Pac13] Pace. **Chromospheric activity as age indicator. An L-shaped chromospheric-activity versus age diagram**. *AA* 551 (2013). L8 (p. 34).

[Pal+20] Pallé et al. **Transmission spectroscopy and Rossiter-McLaughlin measurements of the young Neptune orbiting AU Mic**. *AA* 643 (2020). A25 (p. 99).

[Par55] Parker. **Hydromagnetic Dynamo Models**. *ApJ* 122 (1955). 293 (pp. 6, 73).

[Par57] Parker. **Sweet's Mechanism for Merging Magnetic Fields in Conducting Fluids**. *JGR* 62 (1957). 509–520 (p. 9).

[Pau+18] Paudel et al. **K2 Ultracool Dwarfs Survey. III. White Light Flares Are Ubiquitous in M6-L0 Dwarfs**. *ApJ* 858 (2018). 55 (pp. 34, 63, 74).

[Pau+19] Paudel et al. **K2 Ultracool Dwarfs Survey - V. High superflare rates on rapidly rotating late-M dwarfs**. *MNRAS* 486 (2019). 1438–1447 (p. 23).

[Pau+20] Paudel et al. **K2 Ultracool Dwarfs Survey - VI. White light superflares observed on an L5 dwarf and flare rates of L dwarfs**. *MNRAS* 494 (2020). 5751–5760 (pp. 27, 34).

[PD12] Parnell and De Moortel. **A contemporary view of coronal heating**. *Philos. Trans. R. Soc. of London Series A* 370 (2012). 3217–3240 (p. 8).

[Per+98] Perryman et al. **The Hyades: distance, structure, dynamics, and age**. *AA* 331 (1998). 81–120 (pp. 37, 69).

[Per18] Perryman. **The Exoplanet Handbook**. 2nd ed. Cambridge University Press, 2018. ISBN: 978-1-108-41977-2. (Visited on 03/28/2022) (p. 97).

[Pet+10] Peterson et al. **A large coronal loop in the Algol system**. *Nature* 463 (2010). 207–209 (p. 74).

[Pev+03] Pevtsov et al. **The Relationship Between X-Ray Radiance and Magnetic Flux**. *ApJ* 598 (2003). 1387–1391 (p. 96).

[PF02] Priest and Forbes. **The magnetic nature of solar flares**. *AAR, Volume 10, Issue 4, pp. 313-377 (2002).* 10:4 (2002). 313 (pp. 9, 34, 74).

[Pha+17] Phan-Bao et al. **Detection of lithium in nearby young late-M dwarfs**. *AA* 600 (2017). A19 (p. 77).

[PHM13] Petigura et al. **Prevalence of Earth-size planets orbiting Sun-like stars**. *PNAS* 110 (2013). 19273–19278 (p. 18).

[Pil+11] Pillitteri et al. **X-Ray Activity Phased with Planet Motion in HD 189733?** *ApJ* 741 (2011). L18 (pp. 21, 112).

[Pil+14] Pillitteri et al. **The Corona of HD 189733 and its X-Ray Activity**. *ApJ* 785 (2014). 145 (pp. 21, 96).

[Pil+22] Pillitteri et al. **X-ray variability of HD 189733 across eight years of XMM-Newton observations**. *AA* 660 (2022). A75 (pp. 15, 21).

[Pin+22] Pinamonti et al. **HADES RV Programme with HARPS-N at TNG XV. Planetary occurrence rates around early-M dwarfs**. *arXiv:2203.04648* (2022) (p. 18).

[Piz+03] Pizzolato et al. **The stellar activity-rotation relationship revisited: Dependence of saturated and non-saturated X-ray emission regimes on stellar mass for late-type dwarfs**. *AA* 397 (2003). 147–157 (p. 55).

[Pla+20] Plavchan et al. **A planet within the debris disk around the pre-main-sequence star AU Microscopii**. *Nature* 582:7813 (2020). 497–500 (pp. 18, 112, 113, 117).

[PM13] Pecaut and Mamajek. **Intrinsic Colors, Temperatures, and Bolometric Corrections of Pre-main-sequence Stars**. *ApJS* 208 (2013). 9 (pp. 5, 42, 51, 62, 112).

[PS11] Poppenhaeger and Schmitt. **A Correlation Between Host Star Activity and Planet Mass for Close-in Extrasolar Planets?** *ApJ* 735 (2011). 59 (p. 21).

[Pud+07] Pudritz et al. **Disk Winds, Jets, and Outflows: Theoretical and Computational Foundations**. Proc. of the Protostars and Planets V Conference. arXiv:astro-ph/0603592, 2007. (Visited on 05/25/2022) (p. 5).

[Pug+16] Pugh et al. **Statistical properties of quasi-periodic pulsations in white-light flares observed with Kepler**. *MNRAS* 459 (2016). 3659–3676 (p. 96).

[Que+18] Queiroz et al. **StarHorse: a Bayesian tool for determining stellar masses, ages, distances, and extinctions for field stars**. *MNRAS* 476 (2018). 2556–2583 (p. 39).

[Qui+10] Quirrenbach et al. **CARMENES: Calar Alto high-resolution search for M dwarfs with exo-earths with a near-infrared Echelle spectrograph**. *Proc. of the Ground-based and Airborne Instrumentation for Astronomy III Conference* 7735 (2010). 773513 (p. 79).

[Rae+20] Raetz et al. **Rotation-activity relations and flares of M dwarfs with K2 long- and short-cadence data**. *AA* 637 (2020). A22 (pp. 11, 13, 27, 49, 59–63, 65).

[Rag+10] Raghavan et al. **A Survey of Stellar Families: Multiplicity of Solar-type Stars**. *ApJS* 190 (2010). 1–42 (p. 59).

[Ram+21] Ramsay et al. **Transiting Exoplanet Survey Satellite (TESS) Observations of Flares and Quasi-Periodic Pulsations from Low-Mass Stars and Potential Impact on Exoplanets**. *Sol. Phys.* 296 (2021). 162 (p. 27).

[Ram+22] Ramsay et al. **The Puzzling Story of Flare Inactive Ultra Fast Rotating M dwarfs. II. Searching for radial velocity variations**. *MNRAS* 511:2 (2022). 2755–2764 (pp. 14, 25).

[Rau+14] Rauer et al. **The PLATO 2.0 mission**. *Exp. Ast.* 38 (2014). 249–330 (pp. 24, 123, 131).

[RCV09] Rayner et al. **The Infrared Telescope Facility (IRTF) Spectral Library: Cool Stars**. *ApJS* 185 (2009). 289–432 (p. 42).

[RDD20] Ramsay et al. **TESS observations of southern ultrafast rotating low-mass stars**. *MNRAS* 497 (2020). 2320–2326 (pp. 25, 127).

[Reb+06] Rebull et al. **A Correlation between Pre-Main-Sequence Stellar Rotation Rates and IRAC Excesses in Orion**. *ApJ* 646 (2006). 297–303 (p. 5).

[Reb+16] Rebull et al. **Rotation in the Pleiades with K2. I. Data and First Results**. *AJ* 152 (2016). 113 (pp. 5, 36, 37, 55, 56, 67, 68).

[Reb+17] Rebull et al. **Rotation of Late-type Stars in Praesepe with K2**. *ApJ* 839 (2017). 92 (pp. 36, 37, 67, 68).

[Reb+22] Reback et al. *Pandas 1.4.2*. 2022. DOI: 10.5281/zenodo.6408044. URL: https://zenodo.org/record/6408044 (visited on 04/29/2022) (pp. 66, 123).

[Red+02] Redfield et al. **A Far Ultraviolet Spectroscopic Explorer Survey of Late-Type Dwarf Stars**. *ApJ* 581 (2002). 626–653 (p. 112).

[Rei+18a] Reiners et al. **The CARMENES search for exoplanets around M dwarfs. High-resolution optical and near-infrared spectroscopy of 324 survey stars**. *AA* 612 (2018). A49 (p. 81).

[Rei+18b] Reino et al. **A Gaia study of the Hyades open cluster**. *MNRAS* 477 (2018). 3197–3216 (pp. 36, 37, 68).

[Rei+22] Reiners et al. **Magnetism, rotation, and nonthermal emission in cool stars – Average magnetic field measurements in 292 M dwarfs**. *arXiv:2204.00342* (2022) (pp. 11–13).

[Rei12] Reiners. **Observations of Cool-Star Magnetic Fields**. *LRSP* 9 (2012). 1 (p. 6).

[Ric+15] Ricker et al. **Transiting Exoplanet Survey Satellite (TESS)**. *JATIS* 1 (2015). 014003 (pp. 4, 17, 24, 34, 74, 75, 112, 113, 125).

[Rim+18] Rimmer et al. **The origin of RNA precursors on exoplanets**. *Sci. Adv.* 4 (2018). eaar3302 (p. 20).

[RJG12] Reiners et al. **A Catalog of Rotation and Activity in Early-M Stars**. *AJ* 143 (2012). 93 (p. 79).

[Rob+01] Robinson et al. **Far-Ultraviolet Observations of Flares on the dM0e Star AU Microscopii**. *ApJ* 554 (2001). 368–382 (p. 112).

[Rob+05] Robinson et al. **GALEX Observations of an Energetic Ultraviolet Flare on the dM4e Star GJ 3685A**. *ApJ* 633 (2005). 447–451 (p. 86).

[Rob+13] Robitaille et al. **Astropy: A community Python package for astronomy**. *AA* 558 (2013). A33 (p. 66).

[Rob72] Roberts. **Kinematic Dynamo Models**. *Philos. Trans. R. Soc. of London Series A* 272 (1972). 663–698 (p. 73).

[Rod+20] Rodríguez Martínez et al. **A Catalog of M-dwarf Flares with ASAS-SN**. *ApJ* 892 (2020). 144 (p. 34).

[Rod74] Rodono. **Short-lived Flare Activity of the Hyades Flare Star H XI 2411**. *AA* 32 (1974). 337 (p. 27).

[RPS10] Robrade et al. **Quiescent and flaring X-ray emission from the nearby M/T dwarf binary SCR 1845-6357**. *AA* 513 (2010). A12 (pp. 34, 74).

[RW06] Rasmussen and Williams. **Gaussian Processes for Machine Learning**. MIT Press, 2006. ISBN: 13 978-0-262-18253-9. URL: https://ui.adsabs.harvard.edu/abs/2006gpml.book.....R (visited on 03/24/2022) (p. 86).

[RWK89] Rice et al. **Mapping stellar surfaces by Doppler imaging : technique and application.** *AA* 208 (1989). 179 (p. 8).

[RWS04] Rebull et al. **Stellar Rotation in Young Clusters: The First 4 Million Years**. *AJ* 127 (2004). 1029–1051 (p. 5).

[Saa94] Saar. **New Infrared Measurements of Magnetic Fields on Cool Stars**. *Proc. of the Infrared Sol. Phys. Conference* 154 (1994). 493 (p. 6).

[Sad+16] Saders et al. **Weakened magnetic braking as the origin of anomalously rapid rotation in old field stars**. *Nature* 529 (2016). 181–184 (p. 14).

[San+13] Sanchis-Ojeda et al. **Kepler-63b: A Giant Planet in a Polar Orbit around a Young Sun-like Star**. *ApJ* 775 (2013). 54 (p. 8).

[San+14] Sanchis-Ojeda et al. **A Study of the Shortest-period Planets Found with Kepler**. *ApJ* 787 (2014). 47 (p. 18).

[Sau+13] Saur et al. **Magnetic energy fluxes in sub-Alfvénic planet star and moon planet interactions**. *AA* 552 (2013). A119 (pp. 20, 111, 112, 122).

[SBJ16] Shields et al. **The habitability of planets orbiting M-dwarf stars**. *Phys. Rep.* 663 (2016). 1 (pp. 18, 65, 97).

[Sca+13] Scandariato et al. **A coordinated optical and X-ray spectroscopic campaign on HD 179949: searching for planet-induced chromospheric and coronal activity**. *AA* 552 (2013). A7 (p. 21).

[Sca82] Scargle. **Studies in astronomical time series analysis. II. Statistical aspects of spectral analysis of unevenly spaced data.** *ApJ* 263 (1982). 835–853 (pp. 75, 114).

[Sch+10] Schmidt et al. **Colors and Kinematics of L Dwarfs from the Sloan Digital Sky Survey**. *AJ* 139 (2010). 1808–1821 (p. 42).

[Sch+14a] Schmidt et al. **Calibrating Ultracool Dwarfs: Optical Template Spectra, Bolometric Corrections, and Chi Values**. *PASP* 126 (2014). 642 (pp. 42, 79).

[Sch+14b] Schmidt et al. **Characterizing a Dramatic Delta V -9 Flare on an Ultracool Dwarf Found by the ASAS-SN Survey**. *ApJ* 781 (2014). L24 (pp. 19, 23, 103).

[Sch+15a] Schmidt et al. **BOSS Ultracool Dwarfs. I. Colors and Magnetic Activity of M and L Dwarfs**. *AJ* 149 (2015). 158 (pp. 19, 34, 42).

[Sch+15b] Scholz et al. **Global survey of star clusters in the Milky Way. IV. 63 new open clusters detected by proper motions**. *AA* 581 (2015). A39 (pp. 37, 38, 69).

[Sch+16a] Schmidt et al. **ASASSN-16ae: A Powerful White-light Flare on an Early-L Dwarf**. *ApJ* 828 (2016). L22 (pp. 34, 74).

[Sch+16b] Schunker et al. **Asteroseismic inversions for radial differential rotation of Sun-like stars: ensemble fits**. *AA* 586 (2016). A79 (p. 13).

[Sch+19] Schmidt et al. **The Largest M Dwarf Flares from ASAS-SN**. *ApJ* 876 (2019). 115 (p. 34).

[Sch+20] Scheucher et al. **Proxima Centauri b: A Strong Case for Including Cosmic-Ray-induced Chemistry in Atmospheric Biosignature Studies**. *ApJ* 893 (2020). 12 (p. 20).

[Sch+98] Schou et al. **Helioseismic Studies of Differential Rotation in the Solar Envelope by the Solar Oscillations Investigation Using the Michelson Doppler Imager**. *ApJ* 505 (1998). 390–417 (p. 6).

[Sch14] Schmidt. **Examining the age/activity relationship of Ultracool Dwarfs with Gaia**. *Memorie della Societa Astronomica Italiana* 85 (2014). 741 (p. 42).

[Sch62] Schatzman. **A theory of the role of magnetic activity during star formation**. *Annales d'Astrophysique* 25 (1962). 18 (p. 11).

[SDJ91] Soderblom et al. **The Chromospheric Emission–Age Relation for Stars of the Lower Main Sequence and Its Implications for the Star Formation Rate**. *ApJ* 375 (1991). 722 (p. 34).

[See+17] See et al. **Studying stellar spin-down with Zeeman-Doppler magnetograms**. *MNRAS* 466 (2017). 1542–1554 (pp. 6, 13).

[See+19] See et al. **Estimating Magnetic Filling Factors from Zeeman-Doppler Magnetograms**. *ApJ* 876 (2019). 118 (pp. 6, 13, 96).

[Seg+10] Segura et al. **The Effect of a Strong Stellar Flare on the Atmospheric Chemistry of an Earth-like Planet Orbiting an M Dwarf**. *Astrobiology* 10 (2010). 751–771 (p. 20).

[Ser+91] Serio et al. **Dynamics of flaring loops. I - Thermodynamic decay scaling laws**. *AA* 241:1 (1991). 197 (p. 15).

[SET20] Serjeant et al. **The future of astronomy with small satellites**. *NatAs* 4 (2020). 1031–1038 (p. 132).

[SF99] Schmitt and Favata. **Continuous heating of a giant X-ray flare on Algol**. *Nature* 401 (1999). 44–46 (p. 74).

[SG64] Savitzky and Golay. **Smoothing and Differentiation of Data by Simplified Least Squares Procedures**. *Anal. Chem.* 36:8 (1964). 1627–1639 (p. 114).

[SGW15] Silburt et al. **A Statistical Reconstruction of the Planet Population around Kepler Solar-type Stars**. *ApJ* 799 (2015). 180 (p. 18).

[Sha+14] Shappee et al. **The Man behind the Curtain: X-Rays Drive the UV through NIR Variability in the 2013 Active Galactic Nucleus Outburst in NGC 2617**. *ApJ* 788 (2014). 48 (p. 34).

[Sha+20] Shapiro et al. **Inflection point in the power spectrum of stellar brightness variations. I. The model**. *AA* 633 (2020). A32 (p. 8).

[Sha89] Shakhovskaia. **Stellar flare statistics — Physical consequences**. *Sol. Phys.* 121 (1989). 375–386 (p. 63).

[Shi+13a] Shibata et al. **Can Superflares Occur on Our Sun?** *PASJ* 65 (2013). 49 (p. 15).

[Shi+13b] Shibayama et al. **Superflares on Solar-type Stars Observed with Kepler. I. Statistical Properties of Superflares**. *ApJS* 209 (2013). 5 (pp. 11, 42, 44, 45, 59, 60, 62–64).

[Shk+05] Shkolnik et al. **Hot Jupiters and Hot Spots: The Short- and Long-Term Chromospheric Activity on Stars with Giant Planets**. *ApJ* 622 (2005). 1075–1090 (pp. 21, 112, 121).

[Shk+08] Shkolnik et al. **The On/Off Nature of Star-Planet Interactions**. *ApJ* 676 (2008). 628–638 (pp. 21, 112, 121).

[Shk+17] Shkolnik et al. **All-sky Co-moving Recovery Of Nearby Young Members (ACRONYM). II. The beta Pictoris Moving Group**. *AJ* 154 (2017). 69 (p. 112).

[Shu+17] Shulyak et al. **Strong dipole magnetic fields in fast rotating fully convective stars**. *NatAs* 1 (2017). 0184 (pp. 3, 96).

[Shu+19] Shulyak et al. **Magnetic fields in M dwarfs from the CARMENES survey**. *AA* 626 (2019). A86 (p. 3).

[Shu77] Shu. **Self-similar collapse of isothermal spheres and star formation.** *ApJ* 214 (1977). 488–497 (p. 5).

[Sil+10] Silva-Valio et al. **Properties of starspots on CoRoT-2**. *AA* 510 (2010). A25 (p. 8).

[SIS18] Strassmeier et al. **PEPSI deep spectra. I. The Sun-as-a-star**. *AA* 612 (2018). A44 (p. 76).

[SKD00] Schaefer et al. **Superflares on Ordinary Solar-Type Stars**. *ApJ* 529 (2000). 1026–1030 (p. 34).

[Ski+97] Skinner et al. **ASCA Observations of the Barnard 209 Dark Cloud and an Intense X-Ray Flare on V773 Tauri**. *ApJ* 486 (1997). 886–902 (p. 74).

[Skr+06] Skrutskie et al. **The Two Micron All Sky Survey (2MASS)**. *AJ* 131 (2006). 1163–1183 (pp. 38, 77).

[Sku72] Skumanich. **Time Scales for Ca II Emission Decay, Rotational Braking, and Lithium Depletion**. *ApJ* 171 (1972). 565 (pp. 10, 11).

[SL18] Shkolnik and Llama. **Signatures of Star-Planet Interactions**. Handbook of Exoplanets. Springer International Publishing AG, 2018. (Visited on 03/23/2022) (p. 20).

[SMD06] Schwadron et al. **Relationship between Solar Wind and Coronal Heating: Scaling Laws from Solar X-Rays**. *ApJ* 642 (2006). 1173–1176 (p. 8).

[Smi48] Smirnov. **Table for Estimating the Goodness of Fit of Empirical Distributions**. *Ann. Math. Stat.* 19:2 (1948). 279–281 (p. 119).

[SOH21] Spake et al. **The Posttransit Tail of WASP-107b Observed at 10830 Å**. *AJ* 162 (2021). 284 (p. 19).

[SP13] Saders and Pinsonneault. **Fast Star, Slow Star; Old Star, Young Star: Subgiant Rotation as a Population and Stellar Physics Diagnostic**. *ApJ* 776 (2013). 67 (p. 12).

[SP15] Somers and Pinsonneault. **Rotation, inflation, and lithium in the Pleiades**. *MNRAS* 449 (2015). 4131–4146 (p. 11).

[Spr02] Spruit. **Dynamo action by differential rotation in a stably stratified stellar interior**. *AA* 381 (2002). 923–932 (p. 6).

[SPZ22] Schaefer et al. **Discovery of extreme, roughly-daily superflares on the recurrent nova V2487 Oph**. *MNRAS* (2022) (p. 27).

[SR98] Strassmeier and Rice. **Doppler imaging of stellar surface structure. VI. HD 129333 = EK Draconis: a stellar analog of the active young Sun**. *AA* 330 (1998). 685–695 (pp. 6, 8, 74).

[Sri+08] Srivastava et al. **Observation of multiple sausage oscillations in cool post-flare loop**. *MNRAS* 388 (2008). 1899–1903 (p. 96).

[SS92] Schuessler and Solanki. **Why rapid rotators have polar spots.** *AA* 264 (1992). L13–L16 (p. 74).

[St +00] St Cyr et al. **Properties of coronal mass ejections: SOHO LASCO observations from January 1996 to June 1998**. *JGR* 105 (2000). 18169–18186 (p. 20).

[Sta+11] Stassun et al. **The M4 Transition: Toward a Comprehensive Understanding of the Transition into the Fully Convective Regime**. *Proc. of 16th Cambridge Workshop on Cool Stars, Stellar Systems, and the Sun* 448 (2011). 505 (p. 73).

[Ste+06] Stelzer et al. **Simultaneous optical and X-ray observations of a giant flare on the ultracool dwarf LP 412-31**. *AA* 460:2 (2006). L35–L38 (pp. 34, 74).

[Ste+16] Stelzer et al. **A path towards understanding the rotation-activity relation of M dwarfs with K2 mission, X-ray and UV data**. *MNRAS* 463 (2016). 1844–1864 (pp. 13, 55).

[Ste+20] Stefansson et al. **The Habitable Zone Planet Finder Reveals a High Mass and Low Obliquity for the Young Neptune K2-25b**. *AJ* 160 (2020). 192 (p. 99).

[Ste+99] Stelzer et al. **Rotational modulation of X-ray flares on late-type stars: T Tauri stars and Algol**. *AA* 344 (1999). 154–162 (p. 74).

[Ste03] Stevenson. **Planetary magnetic fields**. *EPSL* 208:1-2 (2003). 1–11 (p. 121).

[Ste74] Stephens. **EDF statistics for goodness of fit and some comparisons**. *JASA* 69:347 (1974). 730–737 (p. 118).

[Str+15] Strugarek et al. **Magnetic Games between a Planet and Its Host Star: The Key Role of Topology**. *ApJ* 815 (2015). 111 (pp. 21, 112).

[Str+16] Strugarek et al. **The Puzzling Dynamos of Stars: Recent Progress With Global Numerical Simulations**. *Proc. of the IAU* 12:S328 (2016). 1–11 (p. 6).

[Str+19] Strugarek et al. **Chasing Star-Planet Magnetic Interactions: The Case of Kepler-78**. *ApJ* 881 (2019). 136 (pp. 21, 122).

[Str30] Struve. **On the axial rotation of stars.** *ApJ* 72 (1930). 1–18 (p. 5).

[Stu+84] Sturrock et al. **Energy Release in Solar Flares**. *Sol. Phys.* 94 (1984). 341–357 (p. 15).

[STZ00] Sammis et al. **The Dependence of Large Flare Occurrence on the Magnetic Structure of Sunspots**. *ApJ* 540 (2000). 583–587 (pp. 64, 87, 122).

[Sve76] Svestka. **Solar Flares**. Springer-Verlag Berlin Heidelberg, 1976. ISBN: 90-277-0662-X. (Visited on 03/23/2022) (p. 9).

[SWB03] Shkolnik et al. **Evidence for Planet-induced Chromospheric Activity on HD 179949**. *ApJ* 597 (2003). 1092–1096 (p. 121).

[Swe58] Sweet. **The Neutral Point Theory of Solar Flares**. 6 (1958). 123 (p. 9).

[SWP04] Salaris et al. **The age of the oldest Open Clusters**. *AA* 414 (2004). 163–174 (p. 69).

[SWP98] Salaris et al. **The Hyades: distance, structure, dynamics, and age**. *AA* 331 (1998). 81–120 (pp. 37, 38).

[SZ08] Schrijver and Zwaan. **Solar and stellar magnetic activity**. Vol. 34. Cambridge University Press, 2008 (p. 73).

[Sza+15] Szabó et al. **Main-belt Asteroids in the K2 Engineering Field of View**. *AJ* 149 (2015). 112 (p. 68).

[Sza+21] Szabó et al. **The changing face of AU Mic b: stellar spots, spin-orbit commensurability, and transit timing variations as seen by CHEOPS and TESS**. *AA* 654 (2021). A159 (p. 120).

[Sza+22] Szabó et al. **Transit timing variations of AU Microscopii b and c**. *AA* 659 (2022). L7 (p. 112).

[TA22] Toriumi and Airapetian. **Universal Scaling Laws for Solar and Stellar Atmospheric Heating**. *ApJ* 927 (2022). 179 (p. 8).

[Taj08] Tajika. **Snowball Planets as a Possible Type of Water-Rich Terrestrial Planet in Extrasolar Planetary Systems**. *ApJ* 680 (2008). L53 (p. 3).

[Tan18] Tange. **GNU Parallel 2018**. eng. Ole Tange, 2018. ISBN: 978-1-387-50988-1. DOI: 10.5281/zenodo.1146014. URL: https://zenodo.org/record/1146014 (visited on 12/15/2021) (p. 123).

[Til+19] Tilley et al. **Modeling Repeated M Dwarf Flaring at an Earth-like Planet in the Habitable Zone: Atmospheric Effects for an Unmagnetized Planet**. *Astrobiology* 19 (2019). 64–86 (pp. 20, 28, 34, 65, 97).

[TJ05] Taylor and Joner. **A Catalog of Temperatures and Red Cousins Photometry for the Hyades**. *ApJS* 159 (2005). 100–117 (p. 69).

[TL18] Tyson and Lang. **Accessory to war: The unspoken alliance between astrophysics and the military**. WW Norton & Company, 2018 (p. 19).

[Tör+11] Török et al. **A Model for Magnetically Coupled Sympathetic Eruptions**. *ApJ* 739 (2011). L63 (p. 91).

[Tor+17] Toriumi et al. **Magnetic Properties of Solar Active Regions That Govern Large Solar Flares and Eruptions**. *ApJ* 834 (2017). 56 (p. 64).

[Tor+18] Torres et al. **Eclipsing Binaries in the Open Cluster Ruprecht 147. I. EPIC 219394517**. *ApJ* 866 (2018). 67 (pp. 37, 38, 69).

[Tor+21] Torra et al. **Gaia Early Data Release 3. Building the Gaia DR3 source list - Cross-match of Gaia observations**. *AA* 649 (2021). A10 (p. 131).

[TSD15] Testa et al. **Stellar activity and coronal heating: an overview of recent results**. *Philos. Trans. R. Soc. of London Series A* 373 (2015). 20140259–20140259 (p. 8).

[Tsu+04] Tsurutani et al. **Properties of slow magnetic clouds**. *JASTP* 66 (2004). 147–151 (p. 20).

[Tu+20] Tu et al. **Superflares on Solar-type Stars from the First Year Observation of TESS**. *ApJ* 890 (2020). 46 (p. 64).

[Uch68] Uchida. **Propagation of Hydromagnetic Disturbances in the Solar Corona and Moreton's Wave Phenomenon**. *Sol. Phys.* 4 (1968). 30–44 (p. 91).

[Ujj+20] Ujjwal et al. **Analysis of Membership Probability in Nearby Young Moving Groups with Gaia DR2**. *AJ* 159 (2020). 166 (p. 93).

[URP21] Uzsoy et al. **Radius and Mass Distribution of Ultra-short-period Planets**. *ApJ* 919 (2021). 26 (p. 18).

[Van+12] VanderPlas et al. **Introduction to astroML: Machine learning for astrophysics**. In: *Proceedings of Conference on Intelligent Data Understanding*. eprint: arXiv:1411.5039, 2012, 47–54 (pp. 66, 67).

[Van+16] Van Cleve et al. **That's How We Roll: The NASA K2 Mission Science Products and Their Performance Metrics**. *PASP* 128 (2016). 075002 (pp. 26, 36).

[VB17] Vidotto and Bourrier. **Exoplanets as probes of the winds of host stars: the case of the M dwarf GJ 436**. *MNRAS* 470 (2017). 4026–4033 (pp. 13, 19).

[VC16] Van Cleve and Caldwell. **Kepler Instrument Handbook**. Tech. rep. 2016, 1. URL: https://ui.adsabs.harvard.edu/abs/2016ksci.rept....1V (visited on 03/22/2022) (p. 42).

[Ved+20] Vedantham et al. **Coherent radio emission from a quiescent red dwarf indicative of star–planet interaction**. *NatAs* 4:6 (2020). 577–583 (p. 21).

[Ven+16] Venot et al. **Influence of Stellar Flares on the Chemical Composition of Exoplanets and Spectra**. *ApJ* 830 (2016). 77 (p. 20).

[Vid+13] Vidotto et al. **Effects of M dwarf magnetic fields on potentially habitable planets**. *AA* 557 (2013). A67 (p. 20).

[Vid+14] Vidotto et al. **Stellar magnetism: empirical trends with age and rotation**. *MNRAS* 441 (2014). 2361–2374 (pp. 13, 55).

[Vid+15] Vidotto et al. **On the environment surrounding close-in exoplanets**. *MNRAS* 449 (2015). 4117–4130 (p. 19).

[Vid+16] Vida et al. **Investigating magnetic activity in very stable stellar magnetic fields. Long-term photometric and spectroscopic study of the fully convective M4 dwarf V374 Pegasi**. *AA* 590 (2016). A11 (pp. 15, 91).

[Vid+21] Vida et al. **Finding flares in Kepler and TESS data with recurrent deep neural networks**. *AA* 652 (2021). A107 (p. 113).

[Vid21] Vidotto. **The evolution of the solar wind**. *LRSP* 18 (2021). 3 (p. 13).

[VJ14] Vanderburg and Johnson. **A Technique for Extracting Highly Precise Photometry for the Two-Wheeled Kepler Mission**. *PASP* 126 (2014). 948 (p. 36).

[Vog+00] Vogt et al. **Six New Planets from the Keck Precision Velocity Survey**. *ApJ* 536 (2000). 902–914 (p. 17).

[Vog+02] Vogt et al. **Ten Low-Mass Companions from the Keck Precision Velocity Survey**. *ApJ* 568 (2002). 352–362 (p. 17).

[VR18] Vida and Roettenbacher. **Finding flares in Kepler data using machine-learning tools**. *AA* 616 (2018). A163 (p. 25).

[VSD17] Van Doorsselaere et al. **Stellar Flares Observed in Long-cadence Data from the Kepler Mission**. *ApJS* 232 (2017). 26 (p. 25).

[Wal+11] Walkowicz et al. **White-light Flares on Cool Stars in the Kepler Quarter 1 Data**. *AJ* 141 (2011). 50 (pp. 25, 27, 34).

[Wal22] Walters. *Solar storm: SpaceX to lose up to 40 out of 49 Starlink satellites after geomagnetic burst*. en. Section: Science. 2022. URL: https://www.express.co.uk/news/science/1563074/solar-storm-elon-musk-space-x-latest-news-starlink-satellites-flare-ont (visited on 04/15/2022) (p. 19).

[Wat+13] Watanabe et al. **Emission Height and Temperature Distribution of White-light Emission Observed by Hinode/SOT from the 2012 January 27 X-class Solar Flare**. *ApJ* 776 (2013). 123 (p. 44).

[WB16] Weber and Browning. **Modeling the Rise of Fibril Magnetic Fields in Fully Convective Stars**. *ApJ* 827 (2016). 95 (pp. 12, 96).

[WC06] Wheatland and Craig. **Including Flare Sympathy in a Model for Solar Flare Statistics**. *Sol. Phys.* 238 (2006). 73–86 (p. 91).

[WC11] Wedemeyer-Böhm and Carlsson. **Non-equilibrium calcium ionisation in the solar atmosphere**. *AA* 528 (2011). A1 (p. 5).

[WD16] Wright and Drake. **Solar-type dynamo behaviour in fully convective stars without a tachocline**. *Nature* 535 (2016). 526–528 (p. 73).

[WD67] Weber and Davis. **The Angular Momentum of the Solar Wind**. *ApJ* 148 (1967). 217–227 (p. 11).

[Wen+00] Wenger et al. **The SIMBAD astronomical database. The CDS reference database for astronomical objects**. *AAS* 143 (2000). 9–22 (p. 123).

[Wes+11] West et al. **The Sloan Digital Sky Survey Data Release 7 Spectroscopic M Dwarf Catalog. I. Data**. *AJ* 141 (2011). 97 (pp. 3, 19, 42).

[Wes+15] West et al. **An Activity-Rotation Relationship and Kinematic Analysis of Nearby Mid-to-Late-Type M Dwarfs**. *ApJ* 812 (2015). 3 (p. 57).

[WF15] Winn and Fabrycky. **The Occurrence and Architecture of Exoplanetary Systems**. *ARAA* 53 (2015). 409–447 (p. 99).

[WH12] Webb and Howard. **Coronal Mass Ejections: Observations**. *LRSP* 9 (2012). 3 (p. 97).

[Whe+18] Wheatley et al. **The Next Generation Transit Survey (NGTS)**. *MNRAS* 475 (2018). 4476–4493 (p. 24).

[Whe00] Wheatland. **The Origin of the Solar Flare Waiting-Time Distribution**. *ApJ* 536 (2000). L109–L112 (p. 23).

[Whe01] Wheatland. **Rates of Flaring in Individual Active Regions**. *Sol. Phys.* 203:1 (2001). 87–106 (p. 23).

[Whe04] Wheatland. **A Bayesian Approach to Solar Flare Prediction**. *ApJ* 609 (2004). 1134–1139 (pp. 23, 45, 71, 126).

[WIH15] Wu et al. **A Study of Variability in the Frequency Distributions of the Superflares of G-type Stars Observed by the Kepler Mission**. *ApJ* 798 (2015). 92 (p. 63).

[Wij+09] Wijn et al. **Small-Scale Solar Magnetic Fields**. *Space Sci. Rev.* 144 (2009). 275–315 (p. 8).

[Win+19] Winters et al. **The Solar Neighborhood. XLV. The Stellar Multiplicity Rate of M Dwarfs Within 25 pc**. *AJ* 157 (2019). 216 (p. 59).

[Wol+08] Wolter et al. **Doppler imaging an X-ray flare on the ultrafast rotator BO Mic. A contemporaneous multiwavelength study using XMM-Newton and VLT**. *AA* 478:1 (2008). L11–L14 (pp. 15, 74).

[Woo+14] Wood et al. **Evidence for a Weak Wind from the Young Sun**. *ApJ* 781 (2014). L33 (p. 13).

[Woo+21] Wood et al. **New Observational Constraints on the Winds of M dwarf Stars**. *ApJ* 915 (2021). 37 (pp. 8, 13).

[Wri+11] Wright et al. **The Stellar-activity-Rotation Relationship and the Evolution of Stellar Dynamos**. *ApJ* 743 (2011). 48 (pp. 11, 13, 14, 55).

[Wri+12] Wright et al. **The Frequency of Hot Jupiters Orbiting nearby Solar-type Stars**. *ApJ* 753 (2012). 160 (p. 18).

[Wri+18] Wright et al. **The stellar rotation-activity relationship in fully convective M dwarfs**. *MNRAS* 479 (2018). 2351–2360 (pp. 11, 13, 14, 73).

[WSR18] Winn et al. **Kepler-78 and the Ultra-Short-Period planets**. *New Astron. Rev.* 83 (2018). 37–48 (p. 18).

[Wu+22] Wu et al. **Broadening and Redward Asymmetry of H alpha Line Profiles Observed by LAMOST during a Stellar Flare on an M-type Star**. *ApJ* 928 (2022). 180 (p. 15).

[Xin+21] Xin et al. **A dR of 9.5 mag Superflare of an Ultracool Star Detected by the SVOM/GWAC System**. *ApJ* 909 (2021). 106 (pp. 19, 103).

[Yad+15] Yadav et al. **Explaining the Coexistence of Large-scale and Small-scale Magnetic Fields in Fully Convective Stars**. *ApJ* 813:2 (2015). L31 (pp. 12, 74, 87, 96).

[Yan+17] Yang et al. **The Flaring Activity of M Dwarfs in the Kepler Field**. *ApJ* 849 (2017). 36 (pp. 34, 63).

[Yan+18] Yang et al. **Do Long-cadence Data of the Kepler Spacecraft Capture Basic Properties of Flares?** *ApJ* 859 (2018). 87 (pp. 46, 47, 62).

[Yen+18] Yen et al. **Reanalysis of nearby open clusters using Gaia DR1/TGAS and HSOY**. *AA* 615 (2018). A12 (pp. 37, 69).

[YL19] Yang and Liu. **The Flare Catalog and the Flare Activity in the Kepler Mission**. *ApJS* 241 (2019). 29 (pp. 24, 43).

[Yor+00] York et al. **The Sloan Digital Sky Survey: Technical Summary**. *AJ* 120 (2000). 1579–1587 (p. 75).

[YPB17] Yee et al. **Precision Stellar Characterization of FGKM Stars using an Empirical Spectral Library**. *ApJ* 836 (2017). 77 (pp. 42, 66).

[Zah77] Zahn. **Tidal friction in close binary systems**. *AA* 57 (1977). 383 (p. 5).

[Zal+19] Zaleski et al. **Differential rotation of Kepler-71 via transit photometry mapping of faculae and starspots**. *MNRAS* 484 (2019). 618–630 (p. 8).

[Zal+20] Zaleski et al. **Activity and differential rotation of the early M dwarf Kepler-45 from transit mapping**. *MNRAS* 492 (2020). 5141–5151 (p. 8).

[Zar98] Zarka. **Auroral radio emissions at the outer planets: Observations and theories**. *JGR: Planets* 103:E9 (1998). 20159–20194 (p. 20).

[ZD21] Zhu and Dong. **Exoplanet Statistics and Theoretical Implications**. *ARAA* 59 (2021) (p. 18).

[Zee97] Zeeman. **The Effect of Magnetisation on the Nature of Light Emitted by a Substance**. *Nature* 55:1424 (1897). 347–347 (p. 6).

[Zel+21] Zeldes et al. **Flares Big and Small: a K2 and TESS View of ASAS-SN Superflares**. *arXiv:2109.04501* (2021) (p. 25).

[Zha+07] Zhang et al. **Longitudinal distribution of major solar flares during 1975 2005**. *ASR* 40 (2007). 970–975 (p. 74).

[Zic+19] Zic et al. **ASKAP detection of periodic and elliptically polarized radio pulses from UV Ceti**. *MNRAS* 488 (2019). 559–571 (p. 130).

[Zic+22] Zicher et al. **One year of AU Mic with HARPS - I. Measuring the masses of the two transiting planets**. *MNRAS* 512 (2022). 3060–3078 (p. 112).